Numerical Simulation of Shear Driven Wetting

Numerische Simulation schergetriebener Benetzung

Zur Erlangung des akademischen Grades Doktor-Ingenieur (Dr.-Ing.)
eingereichte Dissertation von Daniel Rettenmaier aus Günzburg
Tag der Einreichung: 12.11.2018
Tag der mündlichen Prüfung: 16.01.2019
Darmstadt — D 17

1. Gutachten: Prof. Dr. C. Tropea
2. Gutachten: Prof. Dr. D. Bothe

TECHNISCHE
UNIVERSITÄT
DARMSTADT

GRADUATE SCHOOL
computational engineering

Numerical Simulation of Shear Driven Wetting
Numerische Simulation schergetriebener Benetzung

Genehmigte Dissertation von Daniel Rettenmaier aus Günzburg

1. Gutachten: Prof. Dr. C. Tropea
2. Gutachten: Prof. Dr. D. Bothe

Tag der Einreichung: 12.11.2018
Tag der Prüfung: 16.01.2019

Darmstadt — D 17

Erklärung zur Dissertation

Hiermit versichere ich, die vorliegende Dissertation gemäß §22 Abs. 7 APB der TU Darmstadt ohne Hilfe Dritter und nur mit den angegebenen Quellen und Hilfsmitteln angefertigt zu haben. Alle Stellen, die Quellen entnommen wurden, sind als solche kenntlich gemacht worden. Diese Arbeit hat in gleicher oder ähnlicher Form noch keiner Prüfungsbehörde vorgelegen.

Mir ist bekannt, dass im Falle eines Plagiats (§38 Abs.2 APB) ein Täuschungsversuch vorliegt, der dazu führt, dass die Arbeit mit 5,0 bewertet und damit ein Prüfungsversuch verbraucht wird. Abschlussarbeiten dürfen nur einmal wiederholt werden.

Bei der abgegebenen Thesis stimmen die schriftliche und die zur Archivierung eingereichte elektronische Fassung gemäß §23 Abs. 7 APB überein.

Darmstadt, den 10. August 2019

(D. Rettenmaier)

Publications

Ideas, results and figures have prevoiusly been published in the following:

Journal papers:

Rettenmaier, D., Deising, D., Ouedraogo, Y., Gjonaj, E., De Gersem, H., Bothe, D., Tropea, C., and Marschall, H. (2019). Load Balanced 2D and 3D Adaptive Mesh Refinement in OpenFOAM. *SoftwareX*. under review

Thammanna Gurumurthy, V., Rettenmaier, D., Roisman, I. V., Tropea, C., and Garoff, S. (2018). Computations of spontaneous rise of a rivulet in a corner of a vertical square capillary. *Colloids and Surfaces A: Physicochemical and Engineering Aspects*, 544:118 – 126

Conference contributions:

Rettenmaier, D., Deising, D., Marschall, H., and Tropea, C. (2016). Kontaktlinien-Modellierung in einer algebraischen Volume-Of-Fluid Methode auf unstrukturierten Gittern mit OpenFOAM. In *Jahrestreffen der ProcessNet-Fachgruppen Agglomerations- und Schüttguttechnik, Computational Fluid Dynamics und Mehrphasenströmungen*

Rettenmaier, D., Marschall, H., and Tropea, C. (2017). 3D simulation of pinning of droplets on tilted surfaces with openfoam. In *3rd International Conference on Numerical Methods in Multiphase Flows (ICNMMF-III)*

Thammanna Gurumurthy, R., Rettenmaier, D., Roisman, I. V., Tropea, C., and Garoff, S. (2018b). Spontaneous rise of rivulets in square capillaries. In *14th Zsigmondy Colloquium of the German Colloid Society*

Thammanna Gurumurthy, R., Rettenmaier, D., Roisman, I. V., Tropea, C., and Garoff, S. (2018c). Spontaneous rise of rivulets in square capillaries. In *93th American Chemical Society Colloid and Surface Science Symposium in Pennsylvania*

Seiler, P. M., Rettenmaier, D., Roisman, I. V., and Tropea, C. (2018a). Shear driven drop propagation and breakup on a solid substrate. In *32st Conference of the European Colloid and Interface Society, Ljubljana, Slowenia, September 2018*

Rettenmaier, D., Deising, D., Ouedraogo, Y., Gjonaj, E., De Gersem, H., Bothe, D., Tropea, C., and Marschall, H. (2018). Load balanced 2D and 3D Adaptive Mesh Refinement. In *6th OpenFOAM Conference 2018*

Thammanna Gurumurthy, R., Rettenmaier, D., Roisman, I. V., Tropea, C., and Garoff, S. (2018a). Spontaneous imbibition and forced wetting in closed square capillaries and open rectangular grooves. In *AIChE Annual Meeting in Pittsburgh, PA*

Co-supervised students' theses:

Müller, P. (2016). *Simulation von Tropfenbewegung auf schiefen Platten in Scherströmung*. Bachelor thesis, Technical University Darmstadt

Ren, L. (2017). Simulation of Drops in Turbulent Channel Flow. Master thesis, Institut for Fluid Mechanics and Aerodynamics, Technical University Darmstadt

Haspel, P. (2017). Simulation of Drops and Rivulets in Shear Flow. Master thesis, Institut for Fluid Mechanics and Aerodynamics, Technical University Darmstadt

Hasenzahl, M. T. (2018). Simulation of Drop Motion in Turbulent Channel Flow. Master thesis, Institut for Fluid Mechanics and Aerodynamics, Technical University Darmstadt

Acknowledgements

During the last four years, I had the pleasure to be supported by my family, numerous friends, colleagues, and students. I would like to thank these people for making this work possible.

At first, I would like to express my gratitude to Prof. Dr. **Cameron Tropea**, who, while always being confident in my abilities, gave me the exceptional opportunity to learn and research under his supervision at the Institute for Fluid Mechanics and Aerodynamics of the Technical University Darmstadt, be part of the Graduate School Computational Engineering and be associated to the SFB 1194 - Interaction between Transport and Wetting Processes. I would further like to thank Prof. Dr. **Dieter Bothe** for taking on the role of my second supervisor and initiating the fruitful cooperation with Dr. **Holger Marschall** at the research area of Mathematical Modeling and Analysis at TU Darmstadt.

Special thanks go to my academic twin **Patrick Seiler**, who did the experimental counterpart to this numerical study. Endless discussions, motivating words and solid experiments have been invaluable for this research. To my fellow numerical research colleagues and in particular Daniel Deising, Yun Ouedraogo, Benjamin Franz, Christiane Schlawitschek, Achim Bender, Thomas Antritter, and Vignesh Thammanna, who have shared many of their insights, gave valuable feedback on the numerical framework and helped out whenever necessary. Thank you for being part of the last years!

I feel much respect and gratitude for Nicklas Linder, Daniel Deising, Samuel Chang, Anja Lippert, Stefan Batzdorf, Christian Kunkelmann, Edin Beberovic, Ahmand Baniabldelruhman, and Tyler Voskuilen for their scientific work, which led the way for my own research.

It was a pleasure to co-supervise the excellent students' thesis of Phillip Müller, Liu Ren, Philip Haspel, and Max Hasenzahl. Their work has been facilitating many of the interesting findings of this study. Especially their feedback on the numerical framework is very much appreciated.

For the meticulous proofreading, I want to thank Johannes, Clara, Franz, Jürgen, Maria, Martin, Vignesh, Benjamin, Sagun, Christopher, Max, Philip, Cameron and Dieter.

This work is dedicated to my lovely wife Julia and my son Michael. Your patients, all your efforts and sacrifices during the last years contributed greatly to the persistence required to finish this work.

This research was financially supported by the German Scientific Foundation (DFG) in the framework of the Graduate School of Computational Engineering. Calculations for this research were conducted on the Lichtenberg high-performance computer of the TU Darmstadt.

Abstract

In this thesis, a simulation framework is built that is able to accurately predict forced wetting on complex geometry in turbulent shear flow. To optimize functionalities and to increase the safety of industrial applications such as in printing, coating or the exterior water management of vehicles it is necessary to properly understand the motion of drops and rivulets in shear flow. For this purpose, the specific interplay of multi-phase flows, three-phase contact line dynamics, and turbulent flow fields on a multitude of length and time scales are to be modeled and discretized in such a way that complex geometries are representable. The sensitivity of the drop and rivulet motion on small length scales is the main motivation of this study since a detailed description of wetting phenomena on large-scale applications is necessary but not affordable. To develop the required simplifying models, all necessary models for a detailed description of the complex physical interplay are implemented and validated in the present study.

The numerical framework is based on the Volume of Fluid method within OpenFOAM to describe the multi-phase flow. To simulate wetting, a variety of models regarding the surface tension and the contact line dynamics, including the contact angle hysteresis, have been implemented and validated successfully. One of two elaborate turbulence models has been chosen because of its compatibility with the multi-phase flow description. This hybrid turbulence model is based on a Reynolds Average Navier Stokes method and a Large Eddy Simulation method, which provides a flexible compromise between accuracy and computational resources. Furthermore, to cope with the multitude of length scales, the high-performance techniques Adaptive Mesh Refinement and Dynamic Load Balancing have been significantly enhanced within this work to ensure a stable and efficient as well as highly parallelizable computation. All incorporated models have been implemented based on an unstructured mesh, which allows for the representation of complex geometries.

Kurzfassung

Das Ziel der vorliegenden Dissertation ist die numerische Simulation von Benetzung in turbulenter Scherströmung und bei komplexen geometrischen Verhältnissen. Zur Optimierung der Funktionalität und der Sicherheit industrieller Anwendungen wie z. B. im Druck, bei Beschichtungen oder bei Verschmutzungen am Fahrzeug soll die Bewegung von Tropfen und Rinnsalen in Scherströmung vollständig verstanden werden. Dabei müssen der Mehrphasen-Strömung, der dynamischen Drei-Phasen Kontaktlinie, der turbulenten Strömung und einer Vielzahl von Längen- und Zeitskalen bei der Modellierung und Diskretisierung so Rechnung getragen werden, dass auch komplexe Geometrien abgebildet werden können. Die hohe Sensitivität bezgl. der Prozesse auf kleinen Skalen auf die Tropfen und Rinnsalbewegung motiviert diese Arbeit, da in der großskaligen Anwendung eine detaillierte Beschreibung der kleinen Skalen notwendig wäre, aber nicht möglich ist. Um vereinfachende Modelle zu entwickeln, wurde in dieser Arbeit ein Strömungslöser implementiert, in dem alle notwendigen Modelle für eine detaillierte Beschreibung der vielfältigen physikalischen Effekte eingebunden sind.

In OpenFOAM wird die Mehrphasenströmung mithilfe der Volume of Fluid Methode beschrieben. An diese Methode wurde eine Reihe von Modellen für die Oberflächenspannung, die Kontaktliniendynamik und die Kontaktwinkel-Hysterese gekoppelt, mit experimentellen Daten validiert und die vielversprechendste Kombination ausgewählt. Diese Modelle bilden die Basis für eine akkurate Simulation der Benetzung. Hinsichtlich der Kompatibilität der Turbulenzmodelle mit der verwendeten Mehrphasenströmungsmethodik wurde ein Hybridmodell ausgewählt, welches dynamisch und lokal die Turbulenzmodellierung der günstigen aber ungenauen Reynolds Average Navier Stokes Methode und der teuren aber genauen Large Eddy Simulations Methode blendet. Um eine Vielzahl an zugrundeliegenden Längenskalen parallel und ressourcenschonend auflösen zu können, wurde die adaptive Gitterverfeinerung und dynamische Lastverteilung in OpenFOAM signifikant verbessert. Alle genannten Methoden sind so implementiert, dass eine Darstellung komplexer Geometrien mit Hilfe der unstrukturierten Gitterrepresentätion möglich ist.

In particular, the key scenarios of wetting found in the exterior water management of vehicles have been simulated and compared with well-defined experiments. Simulations of drop impact, as well as drop and rivulet motion on inclined plates, match with a variety of experimental setups in literature. Critical characteristics, such as the incipient motion of drops, the cornering of the drop tails and the meandering of rivulets also match experimental findings very well. Moreover, in shear flow, the simulation of the incipient motion of drops is in accordance with experiments and a developed theoretical model. Finally, the interaction of a moving drop in turbulent shear flow with a microchannel further confirms the predictive capabilities of the numerical framework even for complex geometries.

Simulationen der Schlüsselszenarien von Tropfenaufprall und Tropfen- und Rinnsalbewegung am Auto werden im Rahmen dieser Arbeit mit wohl-definierten Experimenten verglichen. Tropfen- und Rinnsalbewegung auf geneigten Ebenen stimmen mit den Simulationen dieser Arbeit überein. Dabei werden die charakteristische Startbewegung der Tropfen, die Hinterkante bewegter Tropfen, sowie das Mäandern von Rinnsalen hervorragend getroffen. Auch in Scherströmung lässt sich die Startbewegung eines Tropfens vorhersagen, wobei die Ergebnisse der Experimente, Simulation und eines hier präsentierten theoretischen Modells sehr gut übereinstimmen. Die Interaktion der Tropfenbewegung in turbulenter Scherströmung mit komplexer Geometrie bestätigt in einer abschließenden Untersuchung die hervorragenden prädiktiven Eigenschaften der ausgewählten Modelle und Methoden.

Contents

Nomenclature

Abbreviation	Description	Abbreviation	Description
AMR	Adaptive Mesh Refinement	LES	Large Eddy Simulation
CFD	Computational Fluid Dynamic	LS	Level-Set
CSF	Continuouse Surface Force	RANS	Reynolds-Averaged Navier-Stokes
DLB	Dynamic Load Balancing	S-CLSVOF	Simple Coupled Level-Set Volume of Fluid
DSB	Density Scaled Balanced	VLES	Very Large Eddy Simulation
FEM	Finite Element Method	VOF	Volume of Fluid
FVM	Finite Volume Method	WALE	Wall Adaptive Local Eddy

Symbol	Description	Unit
A	Amplitude	–
Bo	Bond number	–
Ca	Capillary number	–
C	Constant	–
D	Diameter	m
$\boldsymbol{f}$	Local volume force vector	$\mathrm{kg\,m/s^2}$
f	Frequency	$1/\mathrm{s}$
	Elliptic relaxation parameter	$1/\mathrm{s}$
F	Resolution dependent blending function	–
$\boldsymbol{g}$	Gravitational acceleration	$\mathrm{m/s^2}$
G	Filter kernel	–
h	Height of topological feature, drop height	m
H	Domain or channel height	m
$\boldsymbol{I}$	Unity tensor	–
k	Kinetic energy	$\mathrm{m^2/s^2}$
	Parameter to account for 3D contact line	$\mathrm{m^2/s^2}$
l	Length scale, drop length	m
L	Domain Length	m
$\mathbf{n}$	Normalized vector	–
p	Pressure	Pa
P	Turbulent production	Pa
R, r	Radius	m
	Base length of two dimensional sheared drop	m
Re	Reynolds number	–
s	Curvlinear coordinate	m
S	Surface area	$\mathrm{m^2}$
t, T	Time	s
u, $\boldsymbol{u}$	Velocity	m/s
$\bar{U}$	Mean velocity	m/s
v	Normal velocity scale	$\mathrm{m/s^2}$
V	Volume	$\mathrm{m/s^2}$
$W(x)$	Lambert function	–
We	Weber number	–
x, y, z	Kartesian Coordinates	–

Greek symbol	Description	Unit
α	Volume fraction of liquid phase in cell	–
β	Tilting angle	$^\circ$
Γ	Level-Set scaling parameter, Diffusion constant	–
δ	Boundary layer thickness, distance	m
	Kronecker delta, Dirac delta	–
Δ	Indication of small but finite parameter	–
ϵ	Dissipation rate	m^2/s^3
	Interface thickness	m
ζ	Velocity scale ratio	–
η	Dynamic viscosity	kg/ms
θ	Contact angle	$^\circ$
κ	Interface curvature, Wavenumber	1/m
λ	Wave length, slip length	m
ν	Kinematik viscosity	m^2/s
Ξ	Additional terms due to spacial filtering of the interface	kg/m^2s
ϱ	Density	kg/m^3
σ	Surface tension	kg/s^2
τ	Stress tensor	kg/ms^2
ψ	Level-Set function	kg/m^3
	Angle in respect to x-axis	$^\circ$
Ω	Domain	–

Subscript	Description
0	Large eddy length scale, initial point in time
A	Advancing
app	Aparent ontact angle
ad	Adhesion
c	cell center
cl	Contact line
d	Dynamic
e	Equilibrium
f	Face of a cell
K	Kolmogorov scales - smallest turbulent scales
m	Micro
num	Numerical correction of contact angle by Afkhami
R	Receeding
s	Shear, drag
p	Point in cell center
us	Unsteady
w	Wall
λ	Slip length, wave length
τ	Wall friction

Superscript	Description
+	Normalized and dimensionless variable
+, G	Domain with one fluid, gas
-, L	Domain with other fluid, liquid

1 Introduction

Figure 1.1: Wind tunnel experiment of a rain ride at 80 km/h visualized with fluorescent water (picture taken from Feldmann et al. (2018) and Seiler et al. (2018a)).

In printing, coating, spray cooling, herbicide treatment, fuel engines, and many more industrial applications, *wetting*, the displacement of a fluid with contact to a second phase, in the form of *drops*, *rivulets* or *thin films* is of utmost importance. During the last decades, the *fluid-fluid interface* has been under considerable investigation especially at the *three-phase contact line*, at which the fluid-fluid interface makes contact with a solid phase. Contact line related phenomena are yet to be fully understood. In capillary-driven flows, the *surface tension* is the dominating force and a *pinning* phenomenon is observed, known from raindrops adhering to windows. In this case, gravity counteracts the pinning force, eventually inducing a movement of larger drops. Considering a vehicle driving in rain (see Figure 1.1), drops in *shear flow* not only form thin films and rivulets but pose a safety hazard on the side window or mirror, where the sight of the driver might be impaired (Hagemeier et al., 2011). A better understanding and the ability to predict the underlying phenomena can lead to improvements for all the above-mentioned applications by providing feedback on functionality early on in the design process. For the prediction of wetting on complex surfaces and in turbulent shear flow, several challenges are to be met.

Considering exterior automotive water management, the wide range of influential length scales, several meters of a car down to nanometers at the contact line, poses one of numerous challenges for predicting wetting on surfaces using numerical simulations. A balance between computational effort, accuracy, and cut-off lengths has to be carefully discussed.

The second challenge is the accurate modeling of dynamic wetting, which is rich in physical effects at the contact line, including pinning of the contact line, *hysteretic* effects and a material, a length scale, and a velocity dependent *contact angle*. The contact angle forms between the solid surface and the fluid-fluid interface (Blake, 2006, Gao et al., 2018). The accurate description of the contact line is closely related to the fluid-fluid interface. Herein, the discrete representation of the two-phase interface, the related surface tension and *interface curvature* is a thriving research field (Popinet, 2018).

Most industrial applications deal with *turbulent flow*, which is considered the third involved research area of this study. Again, several magnitudes of length and time scales play an equally important role, and the interaction of turbulence and multi-phase interfaces are yet to be fully understood (Ketterl and Klein, 2018).

Furthermore, the *complex geometry* of surfaces in industrial applications has implications on the above other challenges since it introduces even more length and time scales, affects the contact line motion (Manukyan, 2013), and leads to even more requirements of turbulence models (Liu et al., 2019). Moreover, to describe complex geometries, the discrete

representation of the domain is required to be unstructured, which again has implications on the two-phase interface representation.

While the ultimate goal of this study is to predict liquid movement and distribution on complex surfaces using numerical simulations, experimental investigations are still imperative, on the one hand as inspiration for lacking analytic models, and on the other hand, necessary as a *validation* reference for simulations. Recent experiments by Seiler et al. (2018b) accompany this study, closing a gap in literature on drop motion in a defined turbulent channel flow and providing a perfect validation reference for the numerical framework developed in this study.

Due to the variety of physical phenomena and necessary models and methods associated with wetting, a state of the art review is included in each section. A general introduction to physical principles and governing equations is given in Chapter 2. In the present study, the mentioned challenges are tackled by improvements of the multi-phase solver `interFoam` of OpenFOAM, introduced in Chapter 3. The underlying Volume of Fluid method to capture the two-phase interface is implemented on an unstructured grid and allows for complex surfaces and very accurate simulations as long as a sufficient spatial and temporal discretization is used. On the other hand, a high spatial and temporal resolution limits the focus of this study to domains that measure a few centimeters as well as to several seconds of simulation time. To ease the handling of multiple scales, the high-performance techniques *Adaptive Mesh Refinement* and *Dynamic Load Balancing* are improved in OpenFOAM Rettenmaier et al. (2019). A library for different interface representations as well as state of the art contact line models are implemented in a single modular solver. Different turbulence models are compared with a focus on the compatibility with the two-phase interface description. With success, all models are meticulously validated by available analytic solutions or experiments using simplistic problem-related setups of increasing complexity. With a trusted setup, mobile and immobile contact lines of drops and rivulets are investigated numerically on tilted plate experiments in Chapter 4. Here, the incipient motion of a drop on an inclining plate, its subsequent motion, as well as rivulet meandering, is simulated with a close match to experimental observations. In Chapter 5, simulations of incipient drop motion in *laminar* shear flow pave the way to the main focus of this study: simulations of drop motion in *turbulent* channel flow. Drop oscillations and incipient motion is compared to experiments. The drop interaction with complex surfaces in shear flow is briefly outlined in Section 5.3. The overall good results, the modular structure and the good performance of the numerical framework make this study a solid foundation for future investigations on forced wetting in shear flow and complex geometries.

The relation of this study to a selection of corresponding literature is given in the following. Linder et al. (2015) introduced the contact line pinning boundary condition in three dimensions within a Volume of Fluid framework in OpenFOAM. The present study builds on this pinning model and adds the high-performance techniques Adaptive Mesh Refinement and Load Balancing as well as an enhanced interface description and turbulence modeling to the work of Linder. In the academic in-house code FS3D, also based on the Volume of Fluid method, a similar set of contact line models was implemented by Lippert (2016), including pinning of the contact line. The difference to the present study is the underlying structured mesh, limiting the geometrical complexity, and a focus on temperature driven Marangoni flows without shear flow. Maurer (2017) simulated the incipient motion of drops in turbulent shear flow with the Volume of Fluid method in OpenFOAM with a focus on the effects of a vibrating surface on the point of incipient motion. Besides the use of a different hysteresis model by Park and Kang (2012), no turbulence model is specified. Furthermore, the above mentioned additional high-performance techniques and enhanced interface description would be beneficial to Maurer's work. Inspired by automotive applications, Dianat et al. (2017b) performed simulations of drops in laminar shear flow over grooves without considering contact angle hysteresis. In the same field, Spruß (2016) performed experiments and simulations using PowerFlow, a Lattice-Boltzmann-based solver for the prediction of rivulets in shear flow considering neither the influence of hysteresis nor dynamic contact angles. Among others, Ade et al. (2017) simulate the exterior water management in turbulent shear flow. For the application on full-scale geometries, the complexity is reduced by a hybrid model which transitions between Lagrangian particle tracking of water drops and the transformation of such into a film representation at contact with the wall.

2 Physical background

Governing equations of physics in shear driven wetting are presented in this chapter. The fluid flow is described from a continuum mechanics perspective. The shear flow might become turbulent, which is an area of research on its own due to its industrial importance and the wide range of time and length scales necessary to describe turbulent flow. Two immiscible fluid phases form an interface, which in contact with a third solid phase meet at a three-phase contact line. The motion of such contact line is called wetting, which is yet to be fully understood and modeled, again, due to a large range of influential length scales and material as well as flow parameters.

2.1 Fluid flow

This study considers Newtonian fluids at length scales much greater than the molecular size, which allows a continuum mechanics modeling approach presented in the local formulation

$$\frac{\partial \rho}{\partial t} + \nabla \cdot (\rho \boldsymbol{u}) = 0, \tag{2.1}$$

$$\frac{\partial (\rho \boldsymbol{u})}{\partial t} + \nabla \cdot (\rho \boldsymbol{u} \otimes \boldsymbol{u}) = \nabla \cdot \boldsymbol{T} + \boldsymbol{f}. \tag{2.2}$$

Therein $\boldsymbol{T}$ is the material dependent stress tensor and $\boldsymbol{f}$ stands for volume force densities. Both equations are coupled by the velocity $\boldsymbol{u}$ and the density ρ. Because of the incompressible nature of the investigated flows with characteristic velocities of up to $U_{\text{shear}} \leq 20$ m/s resulting in low Mach numbers $Ma = U_{\text{shear}}/c_{\text{air}} < 0.06$ with the speed of sound in air $c_{\text{air}} = 331$ m/s, the density is assumed to remain constant, simplifying the continuity equation (2.1) to

$$\nabla \cdot \boldsymbol{u} = 0. \tag{2.3}$$

For Newtonian fluids, the stress tensor $\boldsymbol{T}$ can be written as

$$\boldsymbol{T} = -\Big(p + \frac{2}{3}\mu \nabla \cdot \boldsymbol{u}\Big)\boldsymbol{I} + \mu\big[\nabla \boldsymbol{u} + (\nabla \boldsymbol{u})^T\big] \tag{2.4}$$

and simplified with (2.3) to

$$\boldsymbol{T} = -p\boldsymbol{I} + \mu\big[\nabla \boldsymbol{u} + (\nabla \boldsymbol{u})^T\big], \tag{2.5}$$

in which p is the pressure, μ the dynamic viscosity and $\boldsymbol{I}$ the unity tensor. Including the simplified stress tensor in the momentum equation and assuming constant viscosity, the Navier-Stokes equation is written with the kinematic viscosity ν as

$$\frac{\partial \boldsymbol{u}}{\partial t} + (\boldsymbol{u} \cdot \nabla)\boldsymbol{u} = -\frac{\nabla p}{\rho} + \nu \Delta \boldsymbol{u} + \boldsymbol{f}. \tag{2.6}$$

The volume force term $\boldsymbol{f}$ includes, for example, the force $\boldsymbol{f_g}$ due to gravitational acceleration as well as the later introduced force due to surface tension in a so called one-field formulation.

2.2 Turbulent flow

"Turbulence is a three-dimensional time dependent motion in which vortex stretching causes velocity fluctuations to spread to all wavelengths between a minimum determined by viscous forces and a maximum determined by the boundary conditions. It is the usual state of fluid motion except at low Reynolds numbers." (Bradshaw, 2013)

Turbulence plays a role in industrial devices such as pipes, pumps, turbines, automotive aerodynamics to name just a few. Laminar and turbulent flow regimes are both described by the Navier-Stokes equations (see Section 2.1) and can be distinguished by the Reynolds number (1883)

$$Re = \frac{UL}{\nu}, \tag{2.7}$$

with the kinematic viscosity ν, the characteristic length L, and the velocity U. It compares the inertial forces to the viscous forces. The critical Reynolds number varies from problem to problem. Commonly known are the thresholds of $Re_{\text{cr}} \approx 2300$, 2×10^5, 5×10^5 for the flow in a pipe, around a cylinder, and on a flat plate, respectively. These values are, however, also dependent on flow properties and roughness of the surface. For very calm inflow conditions, laminar pipe flow has been observed for up to $Re_{\text{cr}} \approx 4 \times 10^5$ (Spurk, 2013). In channel flow, the characteristic length is the channel height H.

In the following subsections, the transition of large energy-containing eddies down to dissipative scales is explained together with a quantification of the scale extrema. This section concludes with an introduction of near-wall models that simplify the description of channel flow.

2.2.1 The energy cascade

The decay of large eddies into smaller ones (see Figure 2.1) is called the energy cascade. It is first mentioned by Richardson in 1920 and further investigated by Kolmogorov (1941) who postulates three hypotheses.

- Big vortices are determined only by the boundary conditions and the characteristic length scales of the problem. Their eddies are anisotropic and carry a significant amount of the kinetic energy, embodying the most influential flow scales.
- Eddies in the inertial range gradually lose the dependency on the boundary conditions and kinetic energy with a decreasing length scale. The scales are determined by the dissipation rate ϵ independently of the kinematic viscosity ν.
- The dissipating scales are fully dominated by viscosity ν and the dissipation rate ϵ. The smallest, dissipative eddies are of local character as they lost all dependencies to the large scales.

2.2.2 Turbulent scales

The energy cascade enforces the wide range of time and length scales necessary to describe turbulent flow. The kinetic turbulent energy k and the dissipation rate ϵ are used to define the large energy-containing length l_0, time τ_0, and velocity u_0 scales

$$l_0 = \frac{k^{3/2}}{\epsilon}, \quad \tau_0 = \frac{k}{\epsilon}, \quad u_0 = k^{1/2}. \tag{2.8}$$

Kolmogorov's hypotheses suggests that the anisotropy of the large scales diminishes while the eddies break into smaller ones down to a point, where the directionality and the geometric information of the large eddies is totally lost. Conse-

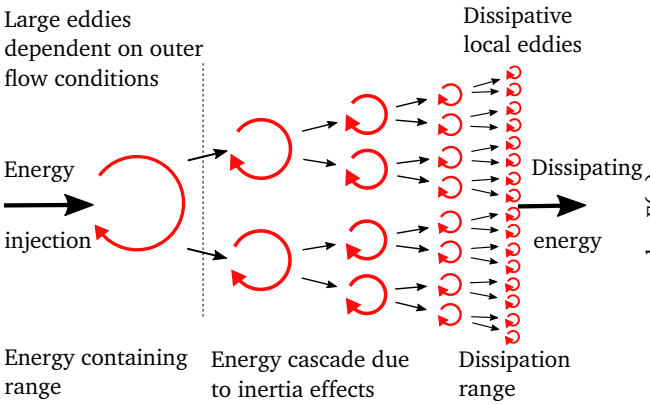

Figure 2.1: Energy cascade: Big eddies break down to smaller ones and dissipate (redrawn from Kondratyuk (2017)).

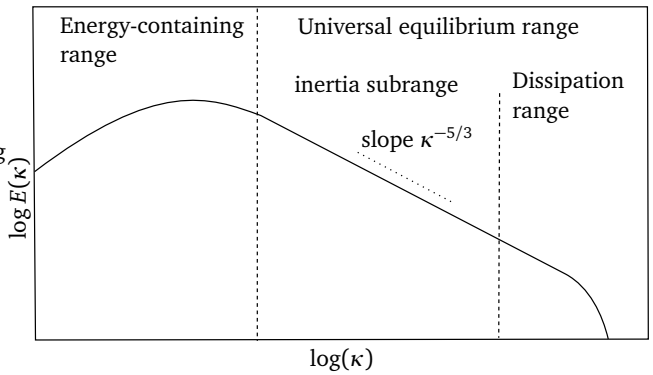

Figure 2.2: Energy spectrum: Smaller scales contain less energy (redrawn from Kondratyuk (2017)).

quently, the small scales are of universal character. Their magnitude can be estimated with the kinematic viscosity ν and the dissipation rate ϵ by

$$l_K = \left(\frac{\nu^3}{\epsilon}\right)^{1/4}, \quad \tau_K = \left(\frac{\nu}{\epsilon}\right)^{1/2} \text{ and } u_K = (\nu\epsilon)^{1/4}. \tag{2.9}$$

With the length l_K, time τ_K and velocity u_K, a Reynolds number of $Re = l_K u_K/\nu = 1$ is formed. The small Reynolds number indicates that this length scale regime is dominated by both viscosity and inertia.

The relation between the Kolmogorov and the large scales yields

$$\frac{l_K}{l_0} \sim Re^{-3/4}, \quad \frac{u_K}{u_0} \sim Re^{-1/4}, \quad \frac{\tau_K}{\tau_0} \sim Re^{-1/2}, \tag{2.10}$$

with $\epsilon = u_0^3/l_0$. For higher Reynolds numbers, the difference between both scales will increase.

2.2.3 Turbulent energy spectrum

Considering the energy cascade, Kolmogorov showed that the energy $E(\lambda)$ depends on the wavelength λ (see Figure 2.2). It is divided in the energy-containing, the inertial and the dissipation range. The energy in the inertial range follows the (5/3)-law

$$E(\lambda) \propto \lambda^{-5/3}. \tag{2.11}$$

For low Reynolds numbers, the (5/3) slope only persists of a short range since the span between the large and dissipative scales is small. With higher Reynolds numbers this span increases and with it the length of the (5/3) slope. The universal equilibrium range is defined as the combined inertia and dissipation range.

The different scales and dependencies on ϵ, k, and ν are of great importance in turbulence models (see Section 3.7). For a derivation and further details of turbulent energy and scales refer to Pope (2000).

2.2.4 Wall treatment

In many applications, such as in pipe flows or around vehicles, the turbulent flow is bound by an impermeable solid wall. Therefore, the accurate wall treatment of turbulence is of high importance. Fluctuations in the vicinity of the wall

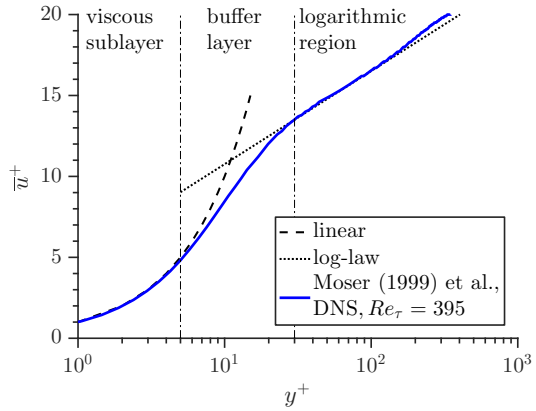

Figure 2.3: Turbulent velocity profile near a wall.

are damped in the normal direction to the wall, resulting in a higher energy of tangential fluctuations. The resulting anisotropy at the wall vanishes with increasing distance to the wall.

The flow at the wall is dominated by molecular and turbulent viscosity and often described in terms of the wall shear stress τ_w and the wall friction velocity u_τ to the result

$$u_\tau = \sqrt{\frac{\tau_w}{\varrho}}, \quad \text{with } \tau_w = \mu \frac{\partial u}{\partial y}\bigg|_w . \tag{2.12}$$

With these quantities of the flow in the turbulent boundary layer, the universal character can be described in dimensionless quantities such as the normalized distance to the wall y^+, the normalized velocity u^+ and the wall friction Reynolds number Re_τ

$$y^+ = \frac{u_\tau y}{\nu}, \quad u^+ = \frac{u}{u_\tau}, \quad Re_\tau = \frac{u_\tau \delta}{\nu} . \tag{2.13}$$

In a fully developed channel flow, half of the channel height is equal to the boundary layer thickness δ.

At the wall, three different regions are found as shown in Figure 2.3.

- In the **viscous sublayer** ($y^+ < 5$) the molecular viscosity dominates the flow and the velocity profile is linear, comparable to a laminar Couette profile

$$u^+ = y^+ . \tag{2.14}$$

- The **buffer layer** ($5 \leq y^+ \leq 30$) is a transition region in which the molecular and the turbulent viscosity are of the same magnitude.

- In the **log-law region** ($30 < y^+$) the molecular viscosity is negligible compared to the turbulent viscosity and the mean velocity profile can be expressed as

$$u^+ = \frac{1}{\kappa} \ln(y^+) + B \quad \text{with } \kappa = 0.4,\ B \approx 5 . \tag{2.15}$$

For further details refer to Pope (2000). Different wall functions used for simulations are explained in Section 3.6.4.

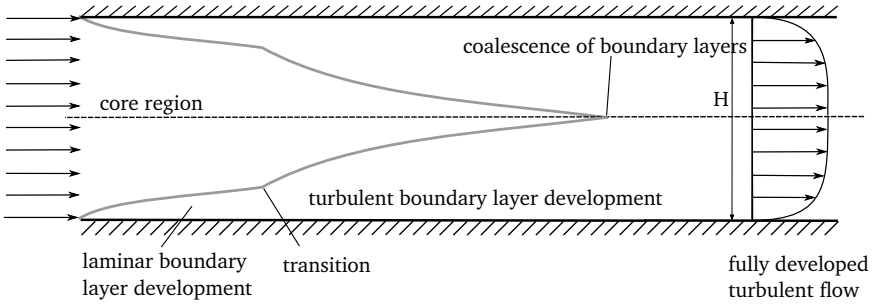

Figure 2.4: Unfolding of a fully developed turbulent channel flow (redrawn from Güttler (2017)).

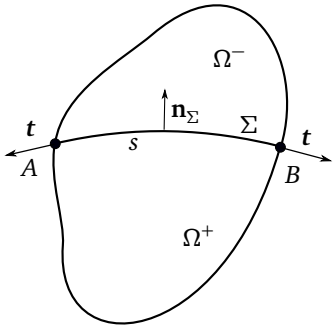

Figure 2.5: Control volume Ω with a curved interface Σ between two fluids (Ω^+, Ω^-), which results in surface tension that acts tangential to the curve.

2.2.5 Turbulent channel flow

In a channel, the turbulent inflow field develops a laminar boundary layer at the walls with the transition to a turbulent boundary layer after a certain stream length for Reynolds numbers above Re_{cr}. With increasing stream length, the boundary layers thicken until they meet at a point after which a fully developed turbulent flow field is formed (see Figure 2.4). The Reynolds numbers are calculated with the kinematic viscosity ν, the channel height H and $H/2$ together with the mean velocity $\bar{U}$, and the wall friction velocity u_τ

$$Re = \frac{\bar{U}H}{\nu}, \quad Re_\tau = \frac{Hu_\tau}{2\nu}. \tag{2.16}$$

In this study, a fully developed and two-dimensional Hagen-Poiseuille flow is simulated, according to experiments by Seiler et al. (2018b). The channel width ($W = 200\,\mathrm{mm}$) in the experiment in contrast to the height $H = 15\,\mathrm{mm}$, allows for the assumption of a two-dimensional flow since the secondary flow motion of the side walls and corners are negligible considering the drop motion of a millimeter-sized drop in the mid of the channel. Furthermore, the channel length assures fully developed turbulence even for low Reynolds numbers of $Re = 3000$.

2.3 Multi-phase flow

The Navier-Stokes equations introduced in Section 2.1 also apply for a system with multiple immiscible and incompressible fluids without phase-change, as considered here. In each phase, the material properties such as the density ϱ and viscosity ν are assumed to be smooth functions in time and space. Between two phases Ω^+ and Ω^-, a material interface Σ forms that is here considered as massless and of zero thickness. To couple the Navier-Stokes equations of each phase, jump conditions need to be formulated, which account for the discontinuity of the material parameters as well as the pressure and velocity. A quantity ψ is defined on the control volume Ω at a time t

$$\psi(t, \Omega) = \int_{\Omega \setminus \Sigma} \phi(t, \boldsymbol{x})\,\mathrm{d}x + \int_{\Sigma \cap \Omega} \phi_\Sigma(t, \boldsymbol{x})\,\mathrm{d}o\,. \tag{2.17}$$

To express a jump condition of the quantity ψ on the interface at the position $\boldsymbol{x}_\Sigma$, the interface is approached on arbitrary paths from both phases

$$[\![\psi]\!] = \lim_{h \to 0} \underbrace{\psi\left(\boldsymbol{x}_\Sigma + h\boldsymbol{n}_\Sigma\right)}_{\psi^-(\boldsymbol{x}_\Sigma, t)} - \underbrace{\psi\left(\boldsymbol{x}_\Sigma - h\boldsymbol{n}_\Sigma\right)}_{\psi^+(\boldsymbol{x}_\Sigma, t)}. \tag{2.18}$$

Thereby, the interface normal $\boldsymbol{n}_\Sigma$ is oriented into Ω^-. The mass balance at the interface can be written as

$$[\![\varrho(\boldsymbol{u}-\boldsymbol{u}_\Sigma)]\!]\cdot\boldsymbol{n}_\Sigma = 0\,. \tag{2.19}$$

The interface velocity is denoted as $\boldsymbol{u}_\Sigma$ and the interface normal as $\boldsymbol{n}_\Sigma$. Equation (2.19) reduces to

$$[\![\boldsymbol{u}]\!]\cdot\boldsymbol{n}_\Sigma = 0 \tag{2.20}$$

assuming a material interface, no mass at the interface, and a flow without phase-change. In addition, a no-slip condition at the interface $[\![\boldsymbol{u}_{||}]\!] = 0$ is enforced within this work, which combines with equation (2.20) to $[\![\boldsymbol{u}]\!] = 0$.

To conserve momentum, the stress at a material interface without phase-change reads as

$$\left[\!\left[\varrho\,\boldsymbol{u}\otimes(\boldsymbol{u}-\boldsymbol{u}_\Sigma) + p\boldsymbol{I} - \mu\left[\nabla\boldsymbol{u} + (\nabla\boldsymbol{u})^T\right]\right]\!\right]\cdot\boldsymbol{n}_\Sigma = \boldsymbol{f}_\Sigma\,, \tag{2.21}$$

where $\boldsymbol{f}_\Sigma$ denotes the surface force density. Assuming a constant surface tension σ, the surface force density can be written as

$$\boldsymbol{f}_\Sigma = \sigma\kappa\boldsymbol{n}_\Sigma\,, \tag{2.22}$$

with the curvature of the interface κ. A detailed derivation of the jump-condition can be found in Brennen (2013). A derivation of the surface tension from thermodynamic potentials is first given in the pioneering works of Gibbs (1928). Surface tension can be described as the reversible work of forming a unit area of interface in equilibrium. It is a partial derivative of the Gibbs free interface energy G of the surface area A_Σ at constant temperatures ϑ and pressures p valid in for homogeneous macrosystems

$$\sigma = \left(\frac{\partial G}{\partial A_\Sigma}\right)_{\vartheta,p}\,. \tag{2.23}$$

Surface tension forces in multi-phase systems are part of our every day live. Interfaces with surface tension tend to minimize the surface area which is e.g. the reason for spherical drop shapes.

2.4 Wetting and contact line dynamics

The contact of a two-phase interface with a third phase defines the three-phase contact line. This contact line accounts for a variety of physical effects such as the ability of drops to stick on a window or the coffee stain phenomenon. Wetting is the displacement of one fluid by another, typically liquid by air. The displacement might be forced by an external force such as a shear flow or gravity, or might happen spontaneously to gain a state closer to equilibrium (Butt et al., 2004). In industrial applications, a deep understanding is necessary to optimize wetting processes such as the reduction of herbicides (Knoche, 1994), curtain coating (Eral et al., 2013), ink-jet printing (Singh et al., 2009), spray cooling (Kim, 2007), anti-icing airfoil systems (Antonini et al., 2011), water transport in fuel cells (Hao and Cheng, 2009) and the water management on vehicles (Hagemeier et al., 2011).

The contact line motion is observed by Dussan et al. (1974) and Chen et al. (1997) to be a rolling motion other than a sliding motion, which is however usually assumed in continuum mechanics modeling. Huh and Scriven (1971) show, that in such a model, the application of a no-slip boundary condition at a solid wall leads to a non-integrable stress singularity at the contact line. In fact, the continuum mechanics assumption does not hold at the contact line because of the relevance of molecular length scales. With the practical continuum mechanics approach, a physical description

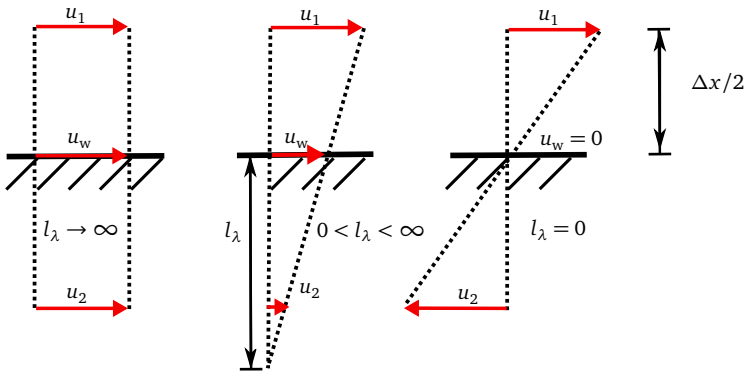

Figure 2.6: Definition of the slip-length l_λ by the flow velocity u_1 at a distance $\Delta x/2$ to the wall and at the wall u_w.

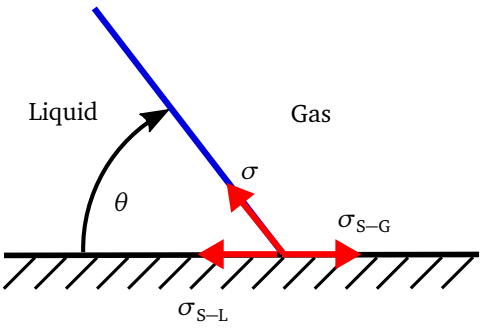

Figure 2.7: Contact angle defined by the surface tensions between the three phases.

requires a relaxation of this singularity.

A variety of mechanisms are reviewed by Bonn et al. (2009), such as Navier-slip models (Navier, 1823, Huh and Scriven, 1971), surface roughness (Hocking, 1976), mesoscopic precursor films De Gennes and Hervet (1984), evaporation and condensation Wayner (1993), shear thinning (Weidner and Schwartz, 1994), diffusive interface (Seppecher, 1996), molecular films Eres et al. (2000), and normal stress models (Boudaoud, A., 2007).

In this study, the Navier-Slip model by Navier (1823) is implicitly used to allow for slippage, which is proportional to the strain rate at the wall

$$\boldsymbol{u}|_{y=0} = -\boldsymbol{u}_w = l_\lambda \frac{\partial \boldsymbol{u}}{\partial x}\Big|_{y=0}, \tag{2.24}$$

where $\boldsymbol{u}_w$ is the velocity at the wall as shown in Figure 2.6. The slip length is expected to be of a molecular length scale near the contact line (Cox, 1986).

2.4.1 Contact angle

As shown in Figure 2.7, the contact angle θ is measured inside the denser fluid between the two-phase interface and the solid. In the absence of external forces, the minimization of the Gibbs free energy yields the equilibrium contact angle θ_e defined by the balance between the surface tensions of the solid and liquid σ_{S-L}, the solid and gas σ_{S-G} and the liquid and gas σ. Young (1805) formulated the relation

$$\sigma_{S-L} = \sigma_{S-G} + \sigma \cos\theta_e \,. \tag{2.25}$$

This contact angle definition is valid for any phase combination. In this study, however, only solid-liquid-gas combinations are considered. Hence, the contact angle depends on the combination of materials. Furthermore, a dependence of the contact angle on the contact line velocity needs to be taken into account. Hoffman (1975) measured the contact angle of different fluids in a glass capillary for a wide range of velocities. His experiments yield

$$\theta_d = f_{Hoff}\left[Ca + f_{Hoff}^{-1}(\theta_e)\right]. \tag{2.26}$$

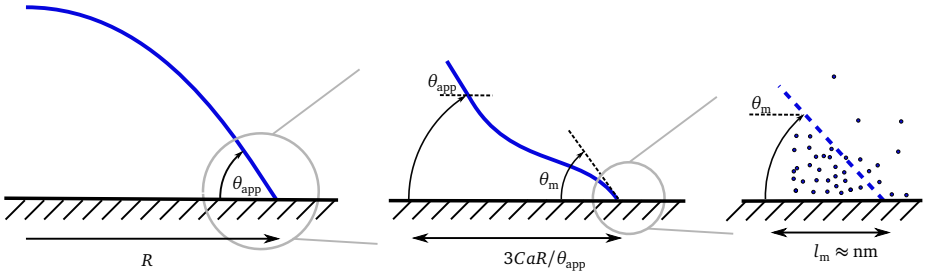

Figure 2.8: Different scales describing the contact line. The apparent contact angle θ_{app} is measured in a range of $10-100\,\mu$m, whereas the microscopic contact angle θ_m is defined by molecular length scales (redrawn from Lippert (2016)).

Since Hoffman gave no expression for f_{Hoff} several other authors have made suggestions that are summarized in Kistler (1993) which includes the Kistler model. The Capillary number relates the viscous forces to the surface tension

$$Ca = \frac{\varrho\, \nu U}{\sigma}, \tag{2.27}$$

and can also be interpreted as the dimensionless contact line velocity. Another approach is the formulation of an out-of-balance Young force

$$\frac{\cos\theta_d - \cos\theta_e}{\cos\theta_e} = f(Ca), \tag{2.28}$$

as given by Jiang et al. (1979) and Bracke et al. (1989). Both matched the function $f(Ca)$ empirically. The contact angle measured by the experimentalist with a resolution of approximately $100\,\mu$m is called the *apparent contact angle* θ_{app} and forms the largest of three length scales describing the contact line, as shown in Figure 2.8.

Besides the empirical models, several theoretical approaches are known to describe the contact angle: the hydrodynamic theory, the molecular kinetic theory, and the interface formation models.

The hydrodynamic theory is based on considerations of corner flow dominated by dissipation (Huh and Scriven, 1971) and relates the microscopic contact angle θ_m to an intermediate region ($3CaR/\theta_{app} \approx 10^{-3}$) contact angle θ_d. Models bridging the microscopic and the intermediate contact angle are expressed in the form

$$f(\theta_d, V) - f(\theta_m, \Upsilon) = Ca \ln\frac{\epsilon_d}{\epsilon_m}, \tag{2.29}$$

in which Υ denotes the viscosity ratio of the inner and outer fluid, ϵ_m a microscopic length scale, ϵ_d a non-universal intermediate length scale, and R the distance between the wall and the application point of the contact angle. Neglecting the gas-viscosity, the function $f(\theta, 0)$ is defined by

$$f(\theta) = \int_0^\theta \frac{x - \sin x \cos x}{2\sin x}\,\mathrm{d}x\,. \tag{2.30}$$

A solution to equation (2.30) is given among others by Voinov (1976)

$$\theta_d^3 = \theta_m^3 + Ca \ln\frac{\epsilon_d}{\epsilon_m}, \tag{2.31}$$

which is valid for small Capillary numbers $Ca \ll 1$. This model has been revisited by Dussan (1976) and Cox (1986). Shen and Ruth (1998) criticize this model revealing a discrepancy to experimental findings near the contact line $< 10\,\mu$m,

pointing out, that the microscopic contact angle θ_m is also velocity dependent. Furthermore, the contact line itself is not part of the solution, as it is cut off (Shikhmurzaev, 2007, Sprittles and Shikhmurzaev, 2013).

Models derived from molecular kinetic theory go back to the work of Glasstone et al. (1941) and determine the motion of the contact line by the statistical dynamics of the molecules near the three-phase contact line (Blake, 2006). While the correct parametrization of the model is difficult, results are as good as considering models based on hydrodynamic theory.

The interface formation model is derived by Shikhmurzaev (1993, 1997, 2007). They are based on non-equilibrium thermodynamics with interfacial mass densities and describe the dissipation during the creation and destruction of the interface during contact line motion. This dissipation is added to the dissipation in standard hydrodynamic channels. The model links the microscopic dynamic contact angle directly to the flow and allows for a description of high Capillary numbers found in high-speed coating. For low Capillary and Reynolds numbers this model reduces to a form similar to hydrodynamic theory models. A short review on the interface formation model is given in Blake (2006).

In the present study, only empirical and hydrodynamic theory models are considered since they are well established and require only the equilibrium contact angle and a length scale as parametrization. Despite the dependence on the contact line velocity, the contact angle depends further on temperature, since it is directly related to the temperature dependent surface tension (Batzdorf, 2015). Besides that, the surface roughness and chemical contamination also influence the contact angle by forming a contact angle hysteresis (De Gennes, 1985).

2.4.2 Contact angle hysteresis

Measuring the contact angle of a drop in equilibrium does not yield the equilibrium contact angle θ_e but a range between the receding θ_R and advancing θ_A contact angle $\theta_R < \theta_e < \theta_A$, depending on the measurement setup and the history of the contact angle formation. The range between θ_R and θ_A is defined as contact angle hysteresis. The contact line is found to be immobile for contact angles within the contact angle hysteresis, this state is described as a pinned contact line. In literature, the modeling of the contact angle hysteresis does not always include pinning. The name hysteresis refers to an influence of the wetting history. One can imagine a symmetrical drop which is pumped up until the contact line just moved. For the same critical volume, the contact line will have a different length before and after the contact line motion. Also, the static contact angles will be different. Reducing the drop volume again, the contact line will stay pinned until a lower critical volume is reached before it retraces. Thus, wetting states depend on the history, however, the characteristic material parameters are not history dependent as long as materials are not considered to age. In Figure 2.9 the Kistler model is extended by applying the advancing and receding angle as an equilibrium contact angle to model the contact angle hysteresis. Such an approach can be found among others in Roisman et al. (2008) and Linder (2015).

The influence of roughness on wetting has already been described by Wenzel (1936) and later by Shuttleworth and Bailey (1948), Eick et al. (1975), Huh and Mason (1977) and De Gennes (1985). A simplified view of a two-dimensional roughness in Figure 2.10 shows the difference of the apparent contact angle θ_{app} that can be measured e.g. with a camera resolution of $20\,\mu$m. On the contrary, the microscopic contact angle θ_m con only be measured with a finer resolution of the size of the roughness e.g. $2\,\mu$m. For a static interface, depending on the position of the surface, different apparent contact angles θ_{app} within the contact angle hysteresis are measured. On real surfaces, the contact angle hysteresis might also depend on the interface normal direction (Johnson and Dettre, 1993). Chemical heterogeneities of a surfaces have a similar effect (De Gennes, 1985).

In conclusion of the description of multi-phase flows, the interaction with a wall requires additional models to cover the contact line motion. The dynamic contact angle models, as well as an extension to describe the contact angle hysteresis and pinning, have been presented. The aspired flow complexity of wetting on complex car surfaces cannot yet be described by analytic models. To describe and understand such involved flows, a three-dimensional numerical simulation

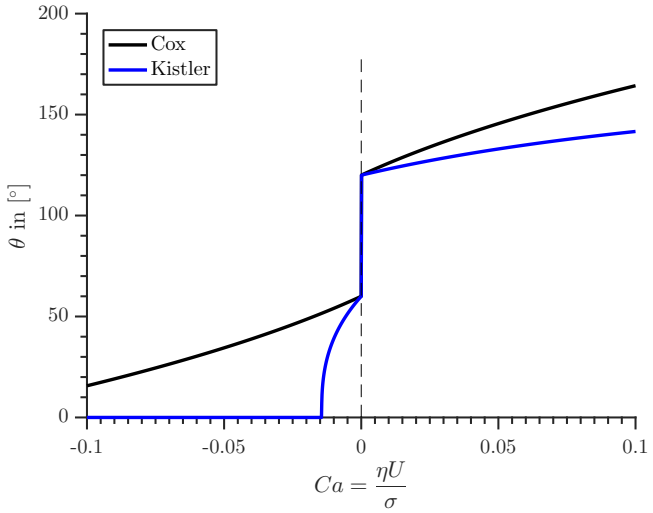

Figure 2.9: Contact angle dependency on the contact line velocity with hysteresis, showing an advancing and receding contact angle of $\theta_A = 120°$ and $\theta_R = 60°$. Cox's dynamic contact angle model is derived from hydrodynamic theory whereas Kistler's model is empirical.

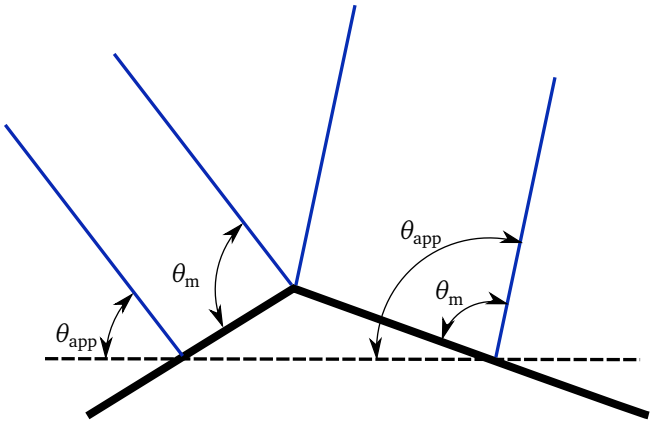

Figure 2.10: Roughness as a cause for the apparent contact angle θ_{app} that differs from the microscopic contact angle θ_m. Depending on the local contact line position on the roughness, the interface orientation changes with a microscopic contact angle θ_m, which is is assumed to be constant.

complements experimental observations. With this goal in mind, a numerical framework is developed within the present study that covers the outlined physics.

3 Numerical framework

The numerical framework to describe wetting on complex geometries and in turbulent shear flow has to meet several requirements that are not yet matched by any available framework found in literature. Considering the simulation of automotive exterior water management the outstanding challenges are the multi-scale problem, the accurate interface discretization, the dynamic contact line description, the combination of multi-phase models and turbulence models and finally the complex surface geometry. All of these challenges are tackled in the framework presented in this Chapter, with the objective to build a sound combination of models which focus rather on accuracy than the coverage of the largest length scales. An extensive validation is presented, so that future investigations can rely on this study.

This study builds upon version 5.x of OpenFOAM (Open Field Operation and Manipulation), a comprehensive open source C++ library for computational continuum mechanics, including CFD (Jasak, 1996, Weller et al., 1998, Jasak, 2009, Moukalled et al., 2016). It distinguishes itself from other open source Computational Fluid Dynamic (CFD) software by a modular code structure, where modules (linear solvers, interpolation schemes, physical models, etc.) are implemented following the Strategy Design Pattern. It is this strict layered software design which makes OpenFOAM extensible to clients/users in a straight-forward manner.

Maintainability is achieved by generic programming: extensive use of templates enables operations on different data types using the same methods without code duplication. Along with operator overloading, this allows devising tailored top-level CFD code, which closely mimics the mathematical language in continuum modeling, i.e. partial differential equations. Further flexibility is achieved by using the Runtime Type Selection (RTS) mechanism: following the Factory Design Pattern, OpenFOAM allows instantiation of an object in the class hierarchy during runtime of the software by the user, changing entries in a configuration file (dictionary). Such strict distinction between interface and library use is held up throughout the library in order to hide implementation details for the sake of usability and readability at top-level.

As for parallelism, communication details are isolated from library use at top-level by a software interface layer which works as parallel communication wrapper with a standard interface so as to allow every top-level code to be written without any specific parallelization requirements. This way, the same lines of code operate in serial and parallel execution. Inter-processor communication is established as a boundary condition, meaning each cell is uniquely allocated to separate processors in a zero-halo-layer approach, without duplicating cell data next to processor boundaries.

In the following, the numerical methodology of the Finite Volume Method in combination with the Volume of Fluid method is outlined. Then, developments in the high-performance techniques Adaptive Mesh Refinement (AMR) and Dynamic Load Balancing (DLB) are presented. These methods enable the description of wetting within multiple scales on an unstructured geometry. To achieve an accurate description of wetting, state of the art interface and contact line dynamic models are implemented in a modular framework. Furthermore, these models are validated with experiments and analytical solutions of increasing complexity. Moreover, to describe drop and rivulet motion in turbulent shear flow, a hybrid turbulence model has been enhanced to work with multiple phases. Simulation results of this model are compared to a well-known large eddy method. Finally, an optimal set of models is selected to perform accurate large-scale wetting simulations of drops and rivulets in turbulent shear flow and on complex geometry.

3.1 Finite Volume Method

The physical models introduced in the previous chapter require a proper discretization, which transforms the partial differential, presented in Chapter 2, into algebraic equations evaluated at discrete locations. Two-phase interfaces are

most prominently described within the Finite Volume Method (FVM), which enforces conservation by design. The domain is discretized by a finite number control volumes called cells that form arbitrary polyhedrons defined by its planar faces and a center point.
The flow, in and out of cells, is formulated as a face-centered flux and match the sources within the cell. The local balance of a general conservation equation with a transient (I), a convective (II), and a diffusive (III) and a source (IV) term is exemplarily formulated, wherein Γ represents a diffusion constant

$$\underbrace{\frac{\partial \Phi}{\partial t}}_{\text{I}} + \underbrace{\nabla \cdot (\boldsymbol{u}\Phi)}_{\text{II}} - \underbrace{\nabla \cdot (\Gamma \nabla \Phi)}_{\text{III}} = \underbrace{\dot{\Phi}}_{\text{IV}}. \tag{3.1}$$

Integrating this equation over a control volume V and applying the theorem of Gauss leads to

$$\iiint_V \frac{\partial \Phi}{\partial t} dV + \iint_S \Phi \boldsymbol{u} d\boldsymbol{S} - \iint_S \Gamma \nabla \phi d\boldsymbol{S} = \iiint_V \dot{\Phi} dV. \tag{3.2}$$

Approximating the integrals by discrete expressions, equation (3.2) can be written as

$$\left(\frac{\partial \Phi}{\partial t}\right)_P V_p + \sum_f \Phi_f \boldsymbol{u}_f \boldsymbol{S}_f + \sum_f \Gamma_f (\nabla \Phi)_f \boldsymbol{S}_f = \dot{\Phi}_P V_P, \tag{3.3}$$

where P is the enumerator representing the center of a control volume and f the cell face index. In a next step, the expressions at the faces have to be interpolated by the values at the center points P of the control volumes, since the field information is stored only there. The transient term is a function of the time step Δt and is approximated with Φ at the center point P of one or more earlier time steps. In explicit discretizations the approximation includes the current or earlier time steps

$$\frac{\partial \Phi}{\partial t} \approx f\left(\Delta t, \phi^{(n)}, \phi^{(n-1)}, \phi^{(n-2)}, \dots\right). \tag{3.4}$$

Hundreds of different spatial and temporal discretization schemes exist to approximate cell- and face-centered as well as temporal values. In this thesis second-order accurate schemes are used with an exception solving the volume fraction transport equation, which can only be solved with first order accuracy. For an overview on the Finite Volume Method and discretization schemes refer to Schäfer (2006) and Hirsch (2007). To find OpenFOAM specific implementation details and notations regarding FVM see Weller (2005) and Marschall (2011). Jasak (1996) and Juretic and Gosman (2010) elaborate on the truncation errors of the discretization schemes on unstructured meshes.

3.2 High-performance techniques

The high-performance techniques Adaptive Mesh Refinement (AMR) and Dynamic Load Balancing (DLB) are key for the scope of this study to cover the multi-scale problem of wetting on automotive surfaces in necessary detail. Therefore, these techniques are used and significantly enhanced within the framework of OpenFOAM in order to effectively tackle the above challenges. These enhancements are published in Rettenmaier et al. (2019), where all implementation details are given, which are summarized here with the objective

- to set out the main ingredients of AMR and DLB in the object-oriented fabric of OpenFOAM software,
- to enhance existing work on two-dimensional (2D) and axisymmetric (2.5D) refinement by Baniabedalruhman (2015)

- as well as to enhance existing work on DLB by Voskuilen (2014), and combine it with the improvements in AMR.

The parallel computational simulation of transient transport processes in science and engineering frequently poses a major challenge, that is using computational resources efficiently while at the same time maintaining high accuracy of the numerical solution throughout the computation. Transport processes often involve moving regions of interest, which migrate through the domain and deform dynamically over time. There is a demand to fully resolve fine transient solution features within these regions in order to decrease numerical errors. Examples in engineering applications are flame fronts, detonation shocks or fluid interfaces (Berger and Colella, 1989).

Nowadays, Computational Fluid Dynamics (CFD) software typically relies on distributed-memory parallel computer architectures for all medium and large-scale computations. In modern CFD simulation software, the commonly underlying Finite Volume Method (FVM) is required to support dynamic unstructured computational meshes of general topology to cope with complex solution domains of varying shape. Under these demands, it has become established practice to utilize a collocated (pseudo-staggered) variable arrangement on the computational mesh, where the values of transport variables are stored in cell centers (volume fields), while the cell-face centers hold information on the fluxes and interpolated cell values (surface fields). Parallelization is accomplished almost exclusively in domain decomposition mode, i.e. a large loop over cell-faces of the mesh is split up and processed by many processor cores, which are referred to as processors in the following.

Several commercial and academic CFD solver libraries already feature Adaptive Mesh Refinement (AMR) such as in Jasak (1996), Vuong et al. (2008), Schwing et al. (2013), Fondelli et al. (2015), Adams et al. (2015) as well as Dynamic Load Balancing (DLB) by Flaherty et al. (1997), Vandriessche and Roose (1995), Misaka et al. (2017). Simulations using the AMR and DLB framework made available in Rettenmaier et al. (2019) have already been employed in Deising et al. (2018) and Thammanna Gurumurthy et al. (2018).

First, new multi-refinement criteria improvements and AMR in 2D and 3D are covered. Then, the basics of the DLB algorithm are explained. In both subsections, Figure 3.1 guides through the structure of the most relevant classes and might help the interested reader who wants to dive into the implementation itself for further details. At last, validation results are presented.

3.2.1 Adaptive mesh refinement

To dynamically obtain high accuracy where locally necessary, while allowing lower accuracy where acceptable, the h-adaptivity approach is used in AMR. Thus far, OpenFOAM has only supported AMR for hexahedral cells in 3D.

Octree Cell Refinement

In 3D cases, hexahedral cells are split using an octree structure where a so-called refinement level is associated with each cell. A cell is refined by cutting it into eight child cells with 36 faces of which 12 are internal to the parent cell (see Figure 3.2a). Neighbors to the refined cells will change from hexahedral to polyhedral cells with more than six faces. The pseudo-staggered approach in OpenFOAM relies on two locations for defining mesh related fields: *volume fields* represent values on cell centers and *surface fields* on face centers. The handling of surface fields in combination with AMR suffers from three major problems in the current OpenFOAM versions: the lack of consistent interpolation between values of refined and unrefined cells, wrong face addressing of newly created faces during refinement, and sign-flipping of non-flux surface fields. Solutions for this problems are outlined in the following.

Mapping is the interpolation of fields between parent and refined child cells. Mapping of cell-centered volume fields is implemented in a straightforward and conservative manner. In a cell refinement step, child cells receive the cell-centered

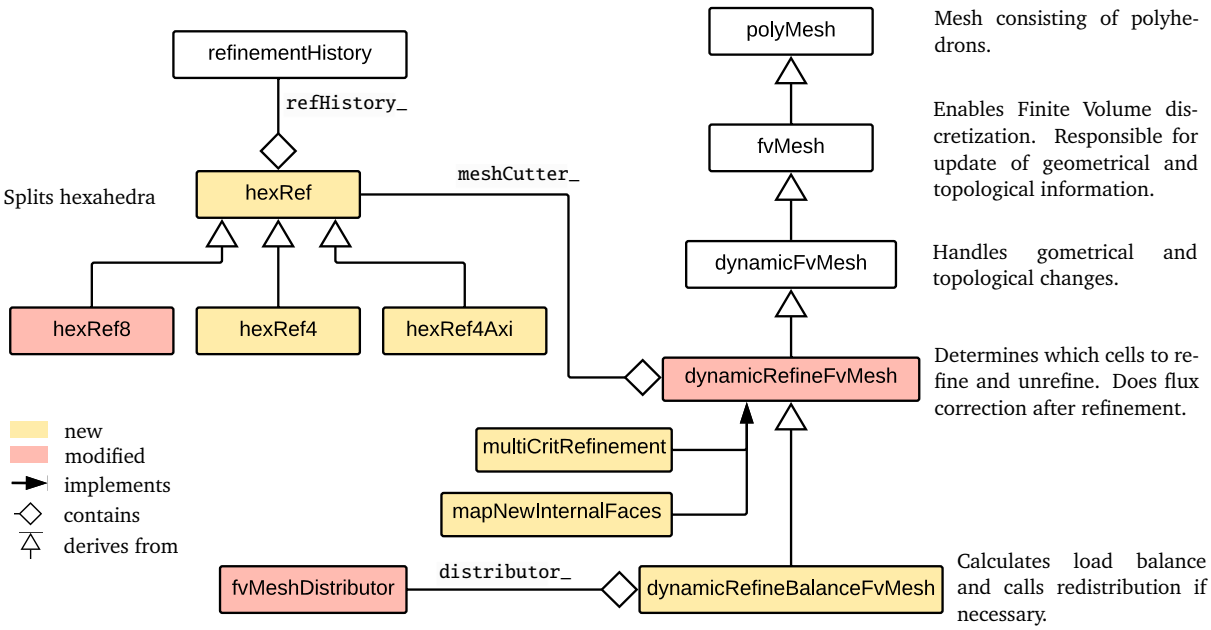

Figure 3.1: UML diagram that shows the newly implemented classes for Dynamic Load Balancing and 2D, as well as 2.5D Adaptive Mesh Refinement, in yellow. Already existing classes with necessary changes are marked in red.

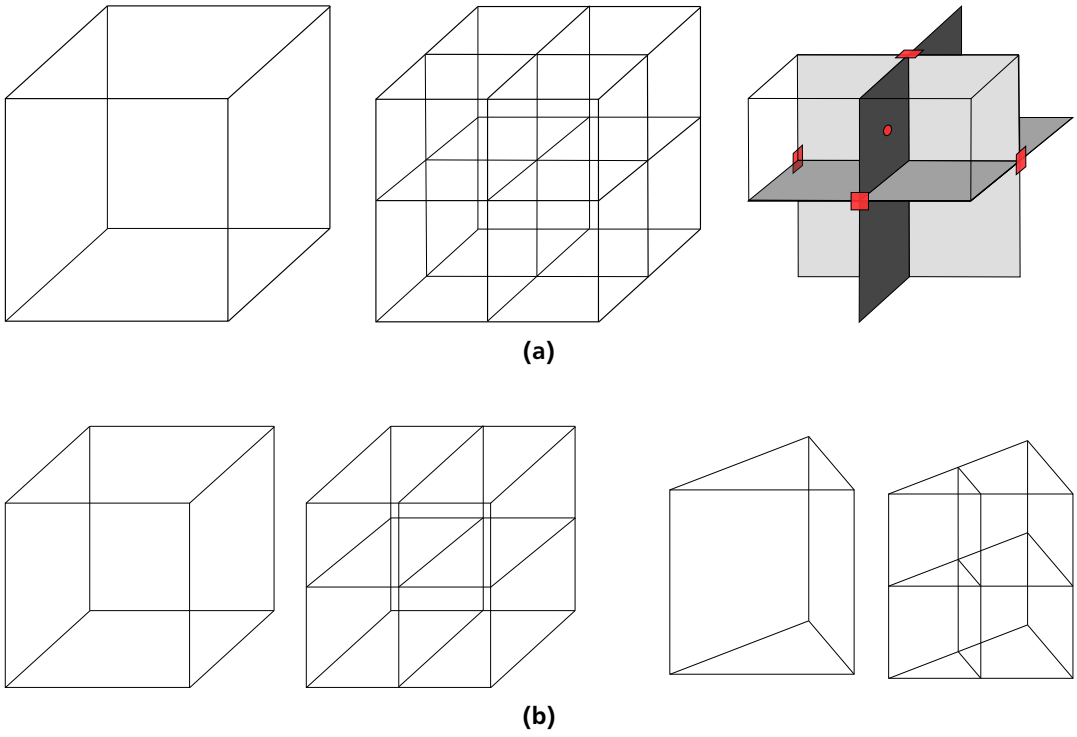

Figure 3.2: a) Octree refinement of a hexahedral cell creates 12 internal faces. Values of surface fields (round) are interpolated from the values of the adjacent master faces (squares) which is exemplarily shown for one internal face. b) Quadtree refinement of hexahedral cells and prism cells. The invariant direction is normal to the page.

value of the parent cell; in a cell unrefinement step, the volume average of child cells' cell-centered values is set on the parent cell-center. However, mapping of surface fields during the refinement step is more demanding and critical since most solvers in OpenFOAM are flux based and fluxes are represented as surface fields. Values at refined faces are set with the value of their corresponding parent face, called master face, which is the face of the parent cell that is split into four new faces. New faces internal to the parent cells are however not related to any master face. A better value interpolation onto these faces is realized in this work by arithmetically averaging the value of the four adjacent master faces, as shown for one internal face in Figure 3.2a. The mapping of surface fields onto new internal faces has been implemented in the `dynamicRefineFvMesh` class (see Figure 3.1).

An implementation error dating back to 1.x OpenFOAM versions in the mesh cutter class `hexRef8` at the initialization of new faces has been corrected, which has invalidated the addressing of newly created internal faces, resulting in seemingly random values on new faces in the whole simulation domain.

The sign of fluxes depends on the face normal direction that is shared by up to two adjacent cells. This direction may change due to topological changes during refinement or unrefinement depending on a formal ownership. Thus a sign-flip of the flux values becomes necessary. Sign-flipping is done for all types of surface fields, even though they may not represent fluxes. Wrong sign-flipping has been corrected in numerous places within the OpenFOAM library.

Incompressible flow solvers in OpenFOAM rely on conservative flux fields, corresponding to a divergence-free velocity field. Due to the nonconservative mapping of surface fields, the flux field needs to be corrected after each AMR step (see 3.2.1). Using the mentioned correction of face addressing, the enhanced surface field mapping and the correction in sign-flipping significantly reduces the necessary correction to ensure a divergence-free field, and improves runtime performance, accuracy and stability (Deising et al., 2018).

The relation between child and parent cells is maintained in the form of a `refinementHistory`, which also stores the refinement level for each cell. Cells are only unrefined if the criteria for unrefinement is matched in all sibling cells, which is taken care of in the `dynamicRefineFvMesh` class. Otherwise, the level of cells at the border of the refined volume may switch back and forth between two levels at each refinement and unrefinement step, unnecessarily consuming computational resources.

Quadtree refinement

For 2D cases, OpenFOAM uses 3D meshes with the additional constraint of a single cell layer in the invariant direction. At runtime, the boundary type `empty` is automatically detected as an indication of a 2D case in order to reduce the number of dimensions in which to solve. Octree refinement breaks the invariance condition since it introduces cells in the invariant direction. For two-dimensional cases, the standard octree refinement must therefore be replaced by a quadtree refinement. The implementation of quadtree refinement is based on the octree refinement, with the difference that internal cells are not split to introduce new cells in the invariant direction. The two faces on the `empty` boundaries are split at their center into four new faces each. This step introduces new points at the middle of all boundary edges, used to split faces in the acceptable direction. Therefore, cell refinement produces four child cells and introduces four internal faces in the parent cell (see Figure 3.2b).

For axisymmetric cases, the implementation uses another type of boundary, the `wedge` type. The mesh still has a thickness of one cell but takes the form of a wedge with one edge along the axis of symmetry. Quadtree refinement can be applied as described above for hexahedral cells. However, special care needs to be taken in the refinement of prism cells at the axis. Triangular faces of these cells are detected at refinement to be split into triangular and quadrangular faces, so that

prism cells are refined into two prisms and two hexahedra (see Figure 3.2b).

The extension of the 3D mesh cutter to 2D and axisymmetric cases is based on work by Baniabedalruhman (2015), which is further abstracted and refined in this study. In order to limit code duplication, the `hexRef8` class is replaced with a base `hexRef` class with three derived classes, `hexRef8`, `hexRef4`, and `hexRef4Axi`, which implement octree refinement, quadtree refinement and quadtree refinement including prisms on the axis, respectively (see Figure 3.1). The `hexRef` classes make use of the runtime selection mechanism so that the `dynamicRefineFvMesh` selects the appropriate *n*-tree refinement based on the number of dimensions of the mesh and the number of dimensions of the solution. The number of dimensions is also used at runtime to determine whether prism cell refinement is allowed.

Combining multiple refinement criteria

For greater flexibility, OpenFOAM's single criterion refinement was extended to multiple different criteria. The criteria include uniquely selectable fields, their gradients and curls, interfaces, geometrical features such as boxes or domain boundaries as well as the maximum and minimal refinement levels on each individual criterion. All settings are modifiable at runtime and the use exemplarily demonstrated in tutorials of the repository. Figure 3.1 shows the multi-criterion refinement class as a modular plug-in to `dynamicRefineFvMesh`.

Buffer layers

Buffer layers are the number of cell layers between two refinement levels. In meshes with more than two refinement levels it is important to ensure a smooth transition between the different levels in order to sufficiently decrease discretization errors due to mesh skewness at refinement transitions and to provide a buffer between two refinement levels for the computed flow to adapt to the new mesh level. The one-irregularity constraint restricts the refinement level difference to neighboring cells to one, so the minimum number of buffer layers is one. However, more buffer layers are recommended.

The calculation of the target refinement level for each cell is performed as follows. First, all cells with the highest refinement level are marked to preserve their level. In a second step, their level, decremented by one, is propagated to neighboring cells sharing a cell corner point. The propagation operation is iterated from neighbor to neighbor as often as the number of buffer layers prescribed by the user. The procedure is then repeated for each refinement level, from the finest to the coarsest.

The propagation of target refinement levels is performed by marking all points used by cells of the level performing the propagation. All cells using these marked points then receive the target refinement level being propagated. The choice of points for propagation compared to faces is motivated by the larger directional preference exhibited by face based propagation.

Figure 3.3 shows examples of refined meshes using respectively two and six buffer layers. The number of effective buffer layers may exceed the specified number by one, since refining a cell creates two cells in each refined direction. A minimum of two layers is recommended.

Flux correction in OpenFOAM

The `interFoam` solver family, in particular, relies on a divergence-free volumetric flux field that corresponds to a divergence-free velocity field. Due to non-conservative mapping of surface fields, the flux field needs to be corrected

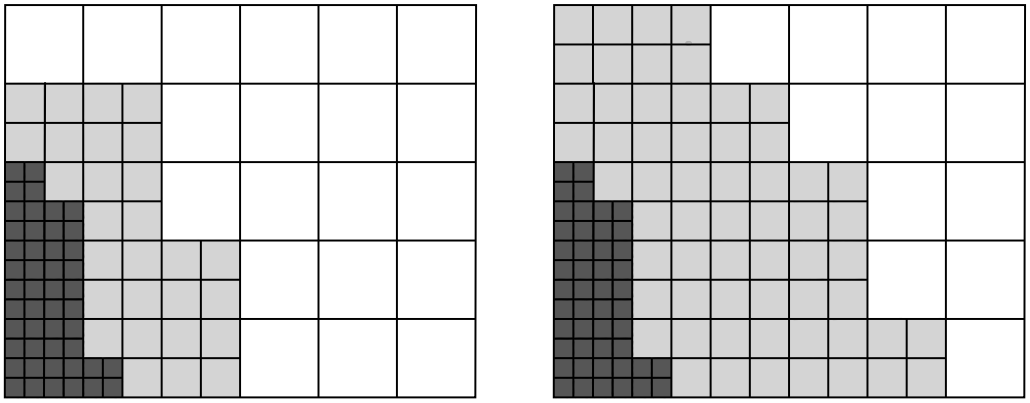

$N_{\text{Buff}} = 2$ cells $N_{\text{Buff}} = 6$ cells

Figure 3.3: Example of two buffer layer enforcing a minimum of two (left) and six (right) buffer cells between two different cell layers.

after each AMR step. This correction applies to the entire flux field even in cells not changed by the AMR mesh update. Good initial fluxes ensure convergence and minimize the correction. To start with, a flux estimate F_f^* is calculated extrapolating the flux of the last time step $F_f^{(-1)}$ using the with cell face-values interpolated velocity field $\mathbf{u}_{f(CD)}^{(-1)}$

$$F_f^* = \mathbf{u}_f \cdot \mathbf{S}_f \,, \tag{3.5}$$

with

$$\mathbf{u}_f = \left(\mathrm{I} - \mathbf{n}_f \otimes \mathbf{n}_f\right) \mathbf{u}_{f(CD)}^{(-1)} + \frac{F_f^{(-1)}}{|\mathbf{S}_f|} \mathbf{n}_f \,. \tag{3.6}$$

Hereby $\mathbf{S}_f$ denotes the surface area vector and $\mathbf{n}_f = \mathbf{S}_f / |\mathbf{S}_f|$ the face normal. Face-centered values are marked with the subscript f. Using this flux estimate F_f^*, the pressure Laplace equation is solved iteratively

$$\sum_f \left[\frac{1}{A_f} \nabla_f \, p_{\text{corr}}^n \, |\mathbf{S}_f| \right] = \sum_f F_f^* \,. \tag{3.7}$$

In the above equation, A_f is the central coefficient of the discretized momentum equation and ∇_f the surface normal gradient. Finally, the estimated flux is updated by the pressure correction term to obtain the divergence-free flux

$$F_f^n = F_f^* - \frac{1}{A_f} \nabla_f \, p_{\text{corr}}^n \, |\mathbf{S}_f| \,. \tag{3.8}$$

Using the different improvements namely the addressing fix, the enhanced surface field mapping, and the correction in sign-flipping as mentioned in Section 3.2.1, significantly reduces the necessary correction iteration to ensure a divergence-free field, while improving solver performance, robustness and accuracy (Deising et al., 2018).

3.2.2 Dynamic Load Balancing

In OpenFOAM, parallelism is based on domain decomposition. The simulation domain is decomposed into sub-domains, each being assigned to a different processor. Whenever AMR is used on a transient problem in parallel, the changing load on processors may significantly reduce the efficient use of computational resources. The processor with the largest load becomes a bottleneck when processed data is required by other waiting processors. Several methods to estimate the load

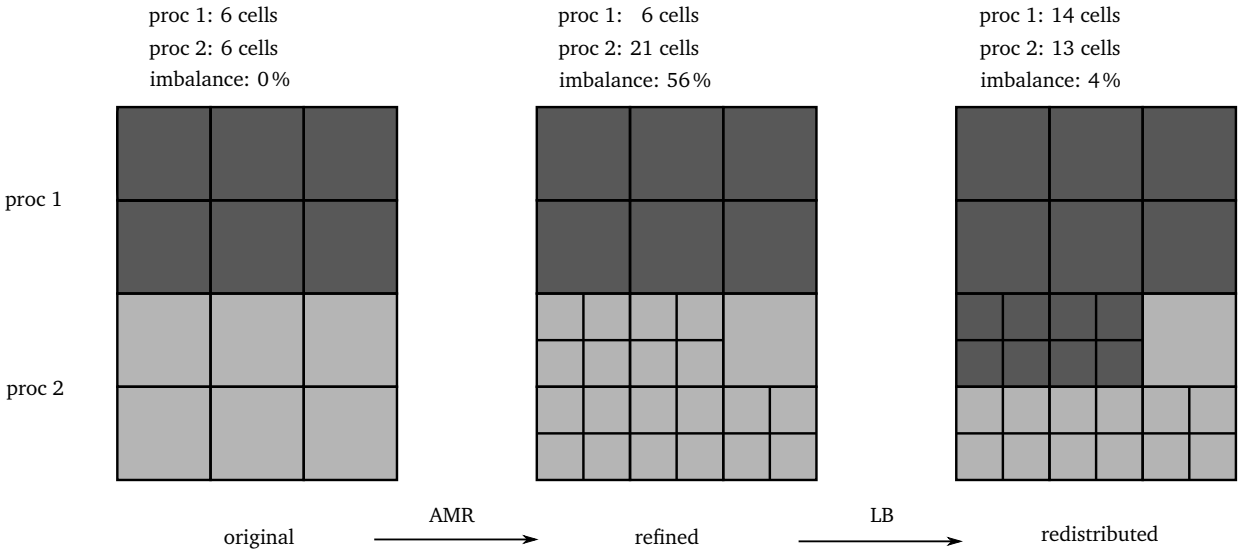

Figure 3.4: A mesh is refined on only one processor creates a load imbalance. To ease the imbalance, cells are redistributed between the processors.

balance can be thought of. Here the load balance is calculated as the ratio of the largest difference in cell number on each sub-domain to the average number of cells per sub-domain. This approach assumes the same computational cost for each cell, which is not generally true. An example of a load imbalance is given in Figure 3.4. After a refinement of a set of cells, the domain distribution is imbalanced by 56 %, clearly a significant amount. After redistribution, a load imbalance of only 4 % is achieved.

Several DLB algorithms based on OpenFOAM libraries are already in use, such as the one found in Batzdorf (2015) for version 2.1.x or another in Mooney (2015) based on the solution by Voskuilen (2014) for version 2.3.x, which also serves as a base for this study. The algorithms of all these authors rely on the redistribution functionality of OpenFOAM, which exchanges cells and their field values between processors given an old and a new domain decomposition. This algorithm needs some changes as outlined by Voskuilen to enable redistribution of fields with physical dimensions and this study further adds to that list with changes regarding surface field flipping and implement additional functionality to allow for the combination with 2D refinement.

Apart from Voskuilen's list, a problem was found in `fvMeshDistribute` related to the flux-flipping issue explained in Section 3.2.1, where non-flux surface fields are flipped while redistributing the cells on different processors. Wrongly flipped fields cause solver crashes. Furthermore, the default mapping of values on boundaries during an AMR mesh update is not sufficient in combination with DLB.

During DLB, stability issues appear using boundaries that hold a value such as for general Neumann or Dirichlet boundary conditions. Similarly to the mapping issue explained in Section 3.2.1, a proper mapping of values from parent to child cells is required. At boundaries, this mapping is not provided by default in the basic boundary conditions such as for Neumann boundary conditions (`fixedGradientFvPatchField`) from which contact angle boundary class (`alphaContactAngleFvPatchScalarField`) is derived. This contact angle boundary condition is necessary for the capillary rise test case in Section 3.2.3. During refinement and DLB, the boundary field size is updated, but new faces lack proper initialization. This issue leads to either incorrect gradient values or to exceptions. To prevent interruptions in our specific application, new faces are assigned with a zero normal gradient boundary condition. This corresponds to a contact angle of 90°. It is recommended that cells containing part of the three-phase contact line are never refined nor

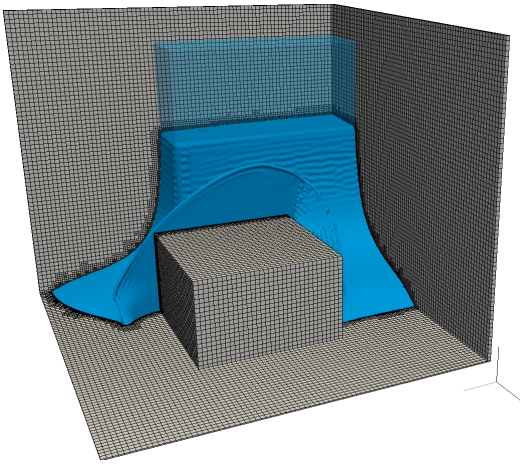

Figure 3.5: Simulation result of a dam break with a two-level refinement at the interface. The iso-surface of the liquid is shown at the initial state and for $t = 0.24\,\mathrm{s}$.

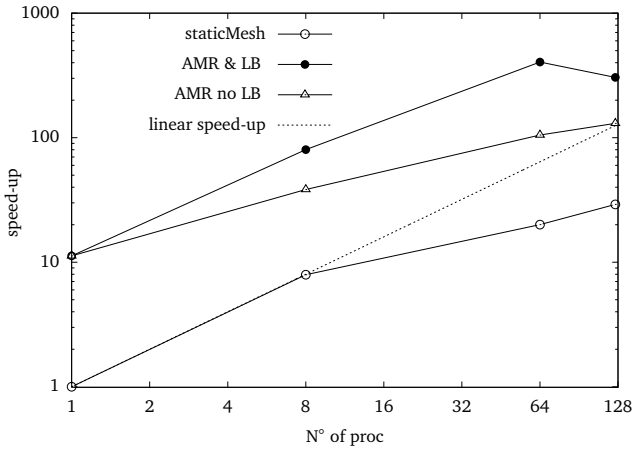

Figure 3.6: The 3D dam-break case shows the speed-up comparing a uniform mesh without refinement as a reference to adaptive mesh refinement in two levels. The refined case is calculated with and without dynamic load balancing. The static mesh matches the resolution of the finest refined cells. The octree-AMR provides a speed-up related to the reduction in cells and DLB helps to maintain the speed-up for an increasing number of processors.

unrefined to ensure that the boundary condition and field mapping acts as expected.

Both structured and unstructured domain decomposition strategies are available in OpenFOAM. Representative examples are the `simple` structured decomposition method, which subdivides the mesh to a user-defined number of sub-domains in each direction, and the unstructured `scotch` (`ptscotch` in parallel) decomposition, which aims at minimizing the size of inter-processor boundaries (see OpenFOAM User Guide). The `scotch` (`ptscotch`) decomposition tends to generate new domains from scratch at redistribution, resulting in a large quantity of cell data exchange between processors, and a large memory consumption.

Regardless of the chosen decomposition strategy, refined sibling cells should not be assigned to different sub-domains to preserve unrefinement capabilities. In Batzdorf (2015), this limitation was overcome by introducing a new `clustered` decomposition method. However, since OpenFOAM version 4.x, decomposition constraints allow selecting the `refinementHistory` class in the user-specified dictionary `decomposeParDict` to enforce cell families to remain on the same sub-domain. This restriction allows the use of any decomposition strategy while keeping unrefinement capabilities. The process of AMR, DLB and flux correction is summarized in Figure 3.29.

3.2.3 Validation

Two typical cases are presented to highlight the performance gains and reduction in necessary computational resources due to AMR and DLB in 2D and 3D. The 3D case is a dam break with an obstacle and the 2D case a capillary rise. Both cases are calculated with 2.5 GHz “Intel® Xeon® E52680 v3” processors, using the `interDyMFoam` solver, which captures the interface using an algebraic Volume of Fluid method (Hirt and Nichols, 1981, Ubbink, 1997, Muzaferija and Perić, 1997). The main advantage of AMR and DLB is the reduced number of cells, while maintaining parallel efficiency by re-balancing the computational load between processors.

The simulation of dam break flow is used to understand catastrophic dam-break incidents, promote dam safety and also used as a validation case in many CFD solvers (Biscarini et al., 2010, Fondelli et al., 2015, Gada et al., 2017). The domain

consists of a cube with a base length of 1 meter with a centered obstacle measuring 0.4 m × 0.4 m × 0.25 m. The water is initialized as a rectangle measuring 0.6 m × 0.19 m × 0.75 m as shown in Appendix A.1. Two meshes are compared, one with a uniform static mesh with a spatial resolution of $3.06 \cdot 10^{-3}$ m, resulting in 33.6 million cells and the second one with two-level AMR around the interface, matching the static mesh resolution and resulting in a total cell count only 2.6 million cells. The simulation is done with and without DLB. The maximum allowed imbalance is set to 20 %. Between the results with and without AMR no difference of the outcome is visible since the equally resolved interface dominates the flow field.

In the following, speed-up relates the reduction of total core-hours used in respect to a reference simulation. The speed-up of the simulation is shown in Figure 3.6, using the simulation with a static mesh on a single processor as a reference. A speed-up of one order of magnitude is achieved using AMR and DLB for 2, 8, 64 and 125 processors. Because of the communication overhead for increasing numbers of processors, only sub-linear speed-up is achieved. Note that the optimal number of processors is smaller for a setup with fewer cells using AMR.

To outline the necessity of DLB when using AMR, simulations are performed with and without DLB. Simulation times are halved for 125 processors when using DLB compared to a non-balanced simulation. It can be argued that for highly dynamic cases, where the region of interest migrates through the entire domain, the bottleneck originating from load imbalance may even result in lower parallel performance than with the statically refined case.

The capillary rise between plates is a two-dimensional case used in literature as a benchmark for curvature calculation and validation for contact angle models (Fath and Bothe, 2015, Xu and Guetari, 2004) since an analytic solution for prescribed constant contact angles is known (Fries and Dreyer, 2008). The liquid-gas interface is initialized horizontally between the plates and rises or falls over time depending on the applied contact angle, here chosen as 40°. The material parameters of air and the liquid are set as presented in Fath and Bothe (2015). In order to cover the rise of the two-phase interface, the entire domain is covered by a fine static mesh. As only the interface evolution requires high accuracy (see Figure 3.7), this test case is a good candidate to apply AMR and DLB.

The static discretization of the domain given in the Appendix A.3, uses a uniform hexahedral mesh resolving the half width of $R = 0.625$ mm between the two plates with 128 cells and the height of $17R$ with 2176 cells, in total 5.6×10^5 cells. The dynamically refined mesh is set with two refinement levels around the interface, matching the resolution of the static mesh at the interface (see Figure 3.7). The resulting cell count using AMR is only 4.3×10^4 cells.

As for the dam break case, the speed-up with 2D-AMR achieved for the capillary rise case is around one order of magnitude, which directly relates to the reduction in cell count (see Figure 3.8). AMR with DLB still produces a two-fold increase in performance compared to simple AMR. To point out the benefit of having a true two-dimensional refinement in two-dimensional cases, additional simulations are performed using octree refinement instead of quadtree refinement. In this case, octree refinement is about five times slower than quadtree refinement, due to the larger number of child cells per parent as well as the introduction of parasitic flow in the invariant direction.

The dam-break and capillary rise test cases both show a significant speedup using adaptive mesh refinement by reducing the cell count. The benefit of a quad-tree refinement versus an octree refinement in 2D cases is quantified. A number of issues in the current OpenFOAM mesh related libraries have been solved obtaining stable and accurate calculations.

3.3 Interface representation - Volume of Fluid Method

To categorize the here used Volume of Fluid (VOF) method, different available two-phase interface descriptions are mentioned first. The interface is distinguished either by an explicit (*interface tracking*) or implicit (*interface-capturing*) description. *Interface tracking* methods (Muzaferija and Perič, 1997, Tukovic and Jasak, 2012) represent the interface by

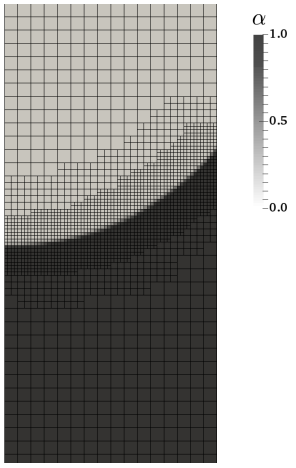

Figure 3.7: Two-level refinement at the interface and a contact angle of 40°. For better visualization, the resolution of the half width is reduced to $R/\Delta x = 64$. The volume fraction α indicates which cells are filled with liquid.

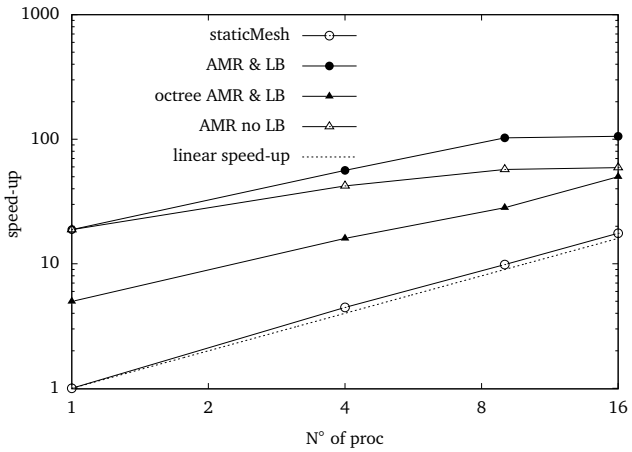

Figure 3.8: 2D capillary rise between plates case showing the speed-up when using AMR in two levels with and without DLB versus uniform mesh without refinement, matching the resolution of the finest refined cells. Using octree-AMR provides a speed-up related to the reduction in cells which is even further reduced using quadtree AMR. DLB helps to maintain the speed-up for an increasing number of sub-domains.

cell-faces. For moving interfaces, the spatial discretization has to be adapted in each time step. The high accuracy of the method is contradicted by an expensive re-meshing. Another method class with explicit interface representation are *Front tracking* methods (Tryggvason et al., 2001, M. van Sint Annaland et al., 2006, Dijkhuizen et al., 2010), where marker points are advected on a fix Eulerian mesh. The interface is reconstructed each time step from the marker points. This approach allows an easier description of dynamic interface motion compared to the interface tracking approach. However, the description is not per se conservative. On the other hand, *Interface capturing* methods rely on the advection of a marker field discretized by an Eulerian mesh, which provides the best capabilities to describe highly dynamic interface motion. The marker field can either be a Level-Set (Sussman et al., 1994, Sethian and Smereka, 2003) representing the distance to the interface, or a volumetric phase fraction used in the VOF method (Hirt and Nichols, 1981, Ubbink, 1997, Muzaferija and Perič, 1997). The VOF methods can be further categorized into geometrical and algebraic approaches. Geometrical VOF methods reconstruct the interface in each cell e.g. as piecewise linear functions (PLIC) used to calculate the volumetric fluxes of the volume fraction (Rider and Kothe, 1998). This approach ensures a sharp interface but is yet limited to structured mesh representations. Recently, this approach has been generalized for unstructured meshes (Maric et al., 2013). However, his demanding algorithm has not yet been coupled to Navier-Stokes equations. On the other hand, in the here used algebraic approach an advection equation for the volume fraction is solved where the diffusion of the interface and the accurate advection are the major challenges. It's robustness, conservativeness and applicability on unstructured meshes are the main reasons for its popularity.

The volume fraction $\alpha = V_{\mathrm{L}}/V_{\mathrm{cell}}$ reflects the ratio of the liquid volume in a cell to the volume of the cell. The gas and liquid phases can be distinguished locally by the value of α. If a cell is totally filled by liquid, α equals one and vice versa α is zero for a cell completely filled with gas

$$\alpha(x,t) = \begin{cases} 1, & \text{inside liquid phase (L)}, \\ 0, & \text{inside gas phase (G)}, \\ 0 < \alpha < 1, & \text{inside transitional region}. \end{cases} \tag{3.9}$$

For the transitional region, the values of viscosity and density are interpolated linearly from the values of the pure phases, allowing a one-fluid formulation of the Navier-Stokes equations

$$\rho = \alpha\rho_{\mathrm{L}} + (1-\alpha)\rho_{\mathrm{G}}\,, \tag{3.10}$$

$$\mu = \alpha\mu_{\mathrm{L}} + (1-\alpha)\mu_{\mathrm{G}}\,. \tag{3.11}$$

The α field is linked with the velocity field of the fluids by the transport equation

$$\frac{\partial \alpha}{\partial t} + \nabla\cdot(\boldsymbol{u}\alpha) = 0, \tag{3.12}$$

which is challenging to solve because of the requirement of the field α to remain as sharp as possible and to always be bounded between zero and one. To counteract the diffusion of the sharp interface, Weller (2006) proposed an additional term into the transport equation (3.12) within the so-called MULES advection algorithm used in the multi-phase VOF solver `interFoam` of OpenFOAM

$$\frac{\partial \alpha}{\partial t} + \nabla\cdot(\boldsymbol{u}\alpha) + \nabla\cdot\left\{c_\alpha \max\left[|\boldsymbol{u}|, u_{\mathrm{compr}}\right]\boldsymbol{n}_\Sigma[\alpha(\alpha-1)]\,\alpha\right\} = 0\,. \tag{3.13}$$

In this equation, $\boldsymbol{n}_\Sigma$ is the normal vector of the liquid-gas interface and c_α is the compression factor which is set equal to 1 in all simulations of this study. The compression depends linearly on the magnitude of the velocity $|\boldsymbol{u}|$. In dynamic cases that counter-gradient diffusion term is sufficient, in contrast to cases with a quasi-static interface, where the compression is to lax. This way interface smears out especially near the wall where the velocity is small, and moreover, by reducing parasitic currents as later explained in Section 3.4, this effect increases. Therefore, where necessary, a minimal compression velocity $u_{\mathrm{compr}} = 0.001\,\mathrm{m/s}$ is applied in this study. A validation of the MULES algorithm can be found in Deshpande et al. (2012).

The Courant number Co restricts the simulation time step Δt, depending on the velocity $\boldsymbol{u}$ of the fluid and on the cell size Δx, in such a way that an imaginary particle, moving within the fluid, is only transported a certain distance

$$Co = \frac{U\Delta t}{\Delta x}\,. \tag{3.14}$$

For an explicit time discretization, the simulation is only stable at $Co < 1$, whereas for implicit discretizations there is no general limit in respect to the simulation stability. Although, the handling of multi-phase flows with a segregating transient solution technique, as implemented in *OpenFOAM*, is critical for Courant numbers above $Co = 1$, therefore values of about $Co = 0.4$ and smaller are recommended to minimize discretization errors. The time step is dynamically maximized in each time step according to the Courant number to reduce computational effort.

In addition to the Courant number, another time step restriction is given by Brackbill et al. (1992) and Denner and van Wachem (2015) as a capillary wave stability constraint

$$\Delta t < \sqrt{\frac{(\varrho_{\mathrm{L}} + \varrho_{\mathrm{G}})\Delta x^3}{2\pi\sigma}}\,. \tag{3.15}$$

Typical resolutions of $\Delta x = 50\,\mu$m with water and air yield a maximum time step of $\Delta t < 1.6\times10^{-5}\,$s which is always ensured in this study.

3.4 Curvature and surface tension

An accurate calculation of the surface tension is key in surface tension dominated flows. A summary of the review on surface tension models by Popinet (2018) is given here, who distinguishes between two existing approaches to calculate the surface tension force $\boldsymbol{f}_\sigma$, the integral and the volumetric formulation.

Two fluids in an elementary volume Ω are intersected by the curve between two points A and B (see Figure 2.5). The surface tension force per unit length expressed by $\sigma \boldsymbol{t}$ acts tangentially to the curve s and reads for a constant surface tension as

$$\int_\Omega \boldsymbol{f}_\sigma = \oint_A^B \sigma \, \mathrm{d}\boldsymbol{t} = \sigma \left(\boldsymbol{t}_B - \boldsymbol{t}_A \right) . \tag{3.16}$$

Numerically, this integral formulation only involves low-order derivatives of the geometry which leads to accurate numerical estimates. Contributions of surface tension forces to neighboring control volumes cancel each other out exactly, ensuring a local and global momentum conservation of the surface tension. This methodology is often used with Lagrangian interface representations such as in Popinet and Zaleski (1999). However, a combination of the integral formulation with an interface capturing methods is not practical, which leaves the volumetric formulation as an alternative approach.

The volumetric formulation uses the formula of Frenet for parametric curves $\mathrm{d}\boldsymbol{t} = \kappa \boldsymbol{n}_\Sigma \mathrm{d}s$, where s is the curvilinear coordinate, $\boldsymbol{n}_\Sigma$ the unit interface normal and δ_Σ the surface Dirac function, which is nonzero only at the interface

$$\int_\Omega \boldsymbol{f}_\sigma = \oint_A^B \sigma \, \mathrm{d}\boldsymbol{t} = \oint_A^B \sigma \kappa \boldsymbol{n}_\Sigma \, \mathrm{d}\boldsymbol{s} = \int_\Omega \sigma \kappa \boldsymbol{n}_\Sigma \delta_\Sigma . \tag{3.17}$$

All volumetric formulations differ in the numerical approximation of the surface Dirac function δ_Σ. The idea can be traced back to the original immersed boundary method of Peskin (1972). A generalized form reads as

$$\boldsymbol{f}_\sigma = \sigma \kappa \delta_\Sigma \boldsymbol{n}_\Sigma = \sigma \kappa \nabla H(\boldsymbol{x} - \boldsymbol{x}_\Sigma), \tag{3.18}$$

with the Heaviside function H and the position of the interface $\boldsymbol{x}_\Sigma$. In this formulation the specific surface tension force calculation can be expressed by the Continuum Surface Force (CSF) method (Brackbill et al., 1992), the Level-Set method (Sussman et al., 1994) or the Ghost Fluid Method (GFM) (Fedkiw et al., 1999).

Concerning the widely used volumetric formulations, two challenges have to be dealt with: unbalanced solutions of physical equilibrium states that should be recovered by discrete schemes, and the inaccuracy of the curvature estimate. Both lead to parasitic currents at the interface.

For a spherical ($\kappa = \text{const.}$) static ($\boldsymbol{u} = 0$) drop in equilibrium the momentum equation of Navier-Stokes equations simplifies to

$$-\nabla p + \sigma \kappa \boldsymbol{n}_\Sigma \delta_\Sigma = 0 . \tag{3.19}$$

This way, the pressure jump at the interface results to $[\![p]\!] = \sigma\kappa$. A well-balanced discretization of (3.19) leads to

$$-\nabla p + \sigma \kappa \nabla H = 0 , \tag{3.20}$$

where the discretization errors of ∇p and $\kappa \nabla H$ cancel out (Renardy and Renardy, 2002), otherwise discretization errors lead to parasitic currents. To get canceled out, both terms have to be discretized the same way. Popinet (2018) points out that the use of a surface tension force averaged from cell centers onto face centers and a direct evaluation of the pressure gradient at face centers, as done in `interFoam`, breaks the well-balanced property. Nevertheless, Yamamoto et al. (2016) suggest using the same scheme for the pressure gradient ∇p and the Heaviside function ∇H as "pseudo"-balanced in `interFoam`, which is ensured in this study. The curvature accuracy obtained by the second derivative of ∇H is usually poor. Popinet (2018) advises, that when improving the curvature accuracy, ideally, the estimate of $\boldsymbol{n}_\Sigma \delta_\Sigma$ and of κ should be decoupled to keep the discretization of $\boldsymbol{n}_\Sigma \delta_\Sigma$ equal with the pressure gradient ∇p maintaining well-balancedness. The following sections reveal more details on the CSF method and modifications to it, which are validated afterward.

3.4.1 Continuum surface force

Brackbill et al. (1992) proposed the Continuum Surface Force method (CSF), a volumetric formulation converting the surface tension force into a volumetric force, which is necessary if no explicit representation of the interface exists such as in interface capturing approaches. In the VOF method, the Heaviside function $H = \alpha$ is set as an either sharp or diffused volume fraction

$$\boldsymbol{f}_\sigma = \sigma \kappa \nabla \alpha \,. \tag{3.21}$$

Sharp interface representations adapted in this study omit the difficulty of differentiating a discontinuous function by keeping the interface smeared out over several cells. Brackbill et al. approximated the curvature using

$$\kappa = -\nabla \cdot \boldsymbol{n}_\Sigma = -\nabla \cdot \frac{\nabla \alpha}{|\nabla \alpha|} \,. \tag{3.22}$$

Several studies show, however, that with this formulation curvature errors increase with spatial resolution (see Williams et al. (1998), Cummins et al. (2005), Tryggvason et al. (2011)). This is an indicator for an inconsistent curvature estimation which consequently leads to strong parasitic currents on fine meshes. The gradient information of $\nabla \alpha$ is an approximation of the interface normal direction. Small inaccuracies introduce a tangential force component that results in parasitic currents. Despite of this shortcoming and the balancing discretization issues, this method is still widely used and also implemented in `interFoam`. Second-order accurate curvature estimates, which would be possible with Height functions (Poo and Ashgriz, 1989, Sussman, 2003) are not efficiently implementable on unstructured grids. An improved curvature calculation for unstructured grids by Kunkelmann (2011) is presented in the next section. Better accuracy is also achieved in Level-Set frameworks, which however, are not per se mass conservative. Furthermore, a hybrid VOF Level-Set formulation based on the work of Albadawi et al. (2013) will be outlined, which combines the mass conservative VOF advection with the improved curvature calculation of a Level-Set formulation. The CSF model used in the `interFoam` solver has been modularized in this study to a solver called `interFoamExtended` to implement the named approaches selectable by the user. Their improvement in the curvature calculation is quantified after being introduced.

3.4.2 Iso-surface reconstruction

To improve the curvature estimate with regard to the CSF model and thus reduce the parasitic currents, which are required to be much smaller than the characteristic problem-related velocities, an iso-surface reconstruction algorithm is presented. It was first proposed by Kunkelmann (2011), further developed by Batzdorf (2015) and has been reimplemented more flexible and modularly in this study. The iso-surface calculation yields more accurate interface normals and provides the surface area of the interface. The surface area will be necessary to calculate shear forces at the two-phase interface. The algorithm has been implemented for unstructured grids and provides a continuous iso-surface in contrast to PLIC algorithms. Note that the reconstructed interface normals are not used to advect the interface.

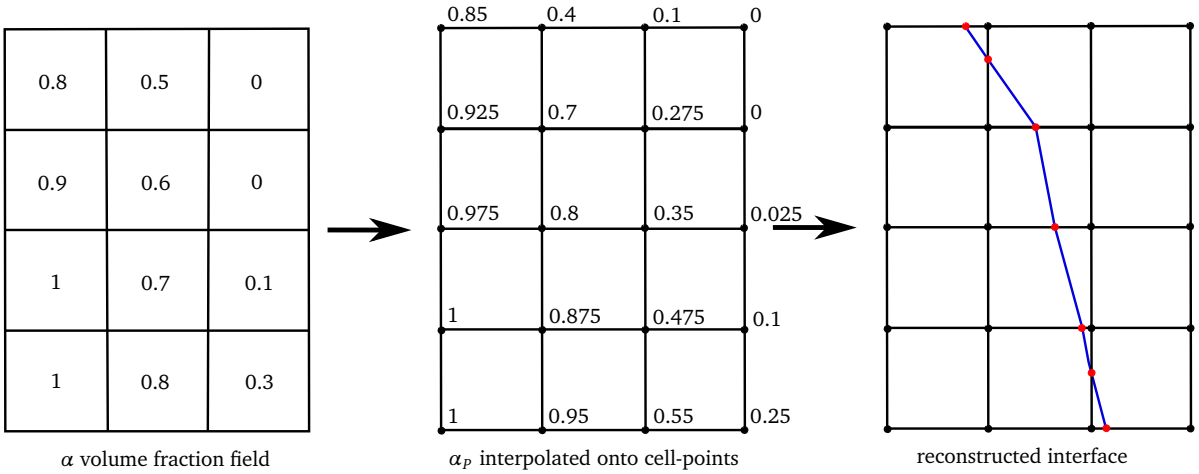

Figure 3.9: Iso-surface reconstruction of the volume fraction field α by interpolating cell-centered values on cell points and by linear interpolation of the edge cutting $\alpha = 0.5$ iso-surface (redrawn from Batzdorf (2015)).

To calculate the iso-surface, the volume fraction field α is interpolated from the cell centers onto the *cell points*. If the sign of $(\alpha - 0.5)$ at the two points of one *cell edge* differ, then the point where the iso-surface cuts the edge is calculated by linear interpolation. Two different interpolation methods from cell centers onto the cell points can be chosen. The point weighted interpolation is fast but lacks in accuracy when interpolating non-uniform meshes. A distance weighted approach is more accurate but more expensive to calculate. The first one is used throughout this study, even though adaptive mesh refinement is used which leads to hanging nodes. Care has been taken to avoid any hanging nodes at the interface at which the mesh is always regular.

Following the geometrical considerations of López and Hernández (2008), the cutting points on the cell edges are combined to a not necessarily plane polygon that forms part of the reconstructed interface. The center $\boldsymbol{x}_\Sigma$ of the polygon is calculated via triangulation and the surface normal vector and area are calculated as

$$\boldsymbol{S}_\Sigma = \sum_{i=1}^{N_\mathrm{p}} \frac{1}{2} \left(\boldsymbol{x}_{\mathrm{p},\Sigma} \times \boldsymbol{x}_{\mathrm{p},i+1} \right), \tag{3.23}$$

where $\boldsymbol{x}_{\mathrm{p},i}$ are the polygon points ordered clockwise and where the unit normal vector

$$\boldsymbol{n}_\Sigma = \frac{\boldsymbol{S}_\Sigma}{|\boldsymbol{S}_\Sigma|} \tag{3.24}$$

points into the denser fluid. If necessary, a distance field d_Σ to the reconstructed interface can be calculated by

$$d_\Sigma = (\boldsymbol{x}_\mathrm{c} - \boldsymbol{x}_\Sigma) \cdot \boldsymbol{n}_\Sigma \tag{3.25}$$

which is positive on the side of the denser liquid. The cell center point is denoted with $\boldsymbol{x}_\mathrm{c}$. A distance threshold can be set to stop the iterative distance-information propagation away from the interface containing cells to reduce computational costs.

To calculate the curvature it is necessary to spread the interface normal information to cells in a band around the interface since it is first only calculated in interface containing cells. The distribution algorithm propagating the interface normal and the interface distance information away from the interface is described in Batzdorf (2015) pp. 68, and outlined here. It iteratively propagates the information cell layer-wise via the cell faces and performs simple averaging if a receptor cell

receives from more than one donor cell. Instead of being averaged, the minimum distance to the interface is selected.

Finally, the curvature is calculated as $\kappa = -\nabla \cdot \boldsymbol{n}_\Sigma$. Note that the curvature accuracy is improved uncoupled of the gradient of the Heaviside function $\nabla H = \nabla \alpha$ which remains discretized in the same manner as the pressure gradient ∇p to keep the pseudo-well-balancedness as pointed out by Popinet (2018) and Yamamoto et al. (2016).

To obtain a smooth curvature field after the calculation, it is only kept at iso-surface containing cells, averaged with neighbor interface cells, propagated away from the interface and then again averaged with neighbor cells. Both averaging operations are performed N_{av} times. The choice of Kunkelmann and Batzdorf who used $N_{\text{av}} = 2$ has also been adopted here. Cells being part of a symmetry boundary or a wall boundary can be protected from averaging. However, even with average protected wall cells, the curvature at wall adjacent cells will not be as accurate, since cell-centered volume fraction values have to be extrapolated beyond the wall boundary to reconstruct the interface in wall adjacent cells. Further considerations on this topic are presented in Section 3.5.2.

3.4.3 S-CLSVOF a VOF Level-Set hybrid

The Level-Set method was invented by Osher and Sethian (1988) to calculate propagating fronts under the influence of surface tension and was first applied on multi-phase flows by Sussman et al. (1994). To distinguish between two fluids it relies on a signed distance function ψ with a positive value in one and a negative value in the other fluid. The interface is defined by the iso-contour $\psi = 0$. To advect the interface a transport equation for ψ is solved which couples the Level-Set with the velocity of the momentum balance. A review on Level-Set methods can be found in Losasso et al. (2006). Hybrid methods aim to combine the advantages of the Level-Set method, that are interface sharpness and an accurate curvature estimate, with the conservative formulation of the Volume of Fluid method. Sussman and Puckett (2000) proposed the Coupled Level-Set Volume of Fluid method (CLSVOF) in which the interface is advected conservatively by the volume fraction α and the interface normal is calculated using the Level-Set function. The material properties are updated to conform with a smoothed Heaviside function. Albadawi et al. (2013) provide an implementation in OpenFOAM suggesting a less expensive simple coupling (S-CLSVOF) in which the material properties of the VOF approach are kept. The Level-Set is initially approximated by the VOF field and then re-initialized to obtain the signed distance function, solely for a better estimate of the curvature and consequently the surface tension. Yokoi (2013) proposes a density scaled balanced continuum surface force (DSB-CSF) that combines with the S-CLSVOF model to mitigate parasitic forces towards the denser liquid to reduce parasitic currents. Both the S-CLSVOF and the DSB-CSF model have been combined (S-CLSVOF(DSB)) by Yamamoto et al. (2016) and are outlined in the following.

The Level-Set ψ is calculated by

$$\frac{\partial \psi}{\partial \tau_{\text{art}}} = \text{Sign}(\psi_0)(1 - |\nabla \psi|) \quad \text{with} \quad \psi(\boldsymbol{x}, 0) = \psi_0(\boldsymbol{x}), \tag{3.26}$$

where τ_{art} is an artificial time and ψ_0 the initial Level-Set function

$$\psi_0 = (2\alpha - 1)\Gamma. \tag{3.27}$$

The non-dimensional number Γ, the artificial time step $\Delta\tau_{\text{art}}$, and the interface thickness ϵ are defined by the grid size according to Albadawi et al. (2013)

$$\Gamma = 0.75\Delta x, \quad \Delta\tau_{\text{art}} = 0.1\Delta x, \quad \epsilon = \epsilon_{\text{c}}\Delta x, \tag{3.28}$$

with ϵ_c as the interface thickness coefficient for which Yamamoto et al. (2016) proposes an optimal value between two and three. The re-initialization equation (3.26) is solved in $10\epsilon_c$ iterations to obtain a continuous distribution of the Level-Set function. The surface tension force of the S-CLSVOF method combined with the CSF model reads as

$$\boldsymbol{f}_\sigma = \sigma \kappa_\psi \underbrace{\delta_\psi \nabla \psi}_{=\nabla H_\psi} \tag{3.29}$$

with the smoothed Dirac delta δ_ψ

$$\delta_\psi = \begin{cases} \frac{1}{2\epsilon}\left(1+\cos\frac{\pi\psi}{\epsilon}\right) & \text{for } |\psi| < \epsilon \\ 0 & \text{else}\,. \end{cases} \tag{3.30}$$

As presented by Yokoi (2013) the Heaviside function for the S-CLSVOF(DSB) combination reads as

$$H_{\psi,\mathrm{DSB}} = \begin{cases} 0 & \text{if } \psi < -\epsilon\,, \\ \frac{1}{2}\left[\frac{1}{2}+\frac{\psi}{\epsilon}+\frac{\psi^2}{2\epsilon^2}-\frac{1}{4\pi^2}\left(\cos\frac{2\pi\psi}{\epsilon}-1\right)+\frac{\epsilon+\psi}{\epsilon\pi}\sin\frac{\pi\psi}{\epsilon}\right] & \text{if } |\psi| \le \epsilon\,, \\ 1 & \text{if } \psi > \epsilon\,, \end{cases} \quad , \tag{3.31}$$

and the density-scaled balanced CSF model as

$$\boldsymbol{f}_\sigma = \sigma \kappa_\psi \nabla H_{\psi,\mathrm{DSB}}\,. \tag{3.32}$$

Both S-CLSVOF and S-CLSVOF(DSB) have been integrated in the framework of this study, but are limited to an use of only equidistant cells. The distance or Level-Set function, calculated for each time step is not accurate enough at mesh refinement jumps. The desired slope of one cannot be achieved by the number of iterations given in (3.28) even though the values for Γ, $\Delta\tau_{\mathrm{art}}$, and ϵ are local values recalculated after each mesh refinement operation. For cells near a refinement step the slope of the level-set is unequal to one, which changes the curvature and consequently the surface tension, and thus, distort the flow field significantly. Despite this limitation, a contact angle can be applied for the Level-Set, which increases the accuracy of the contact angle representation significantly. This method has been successfully used in an automotive water management background in Dianat et al. (2017a). The validation of the CSF model, the iso-surface reconstruction and the Level-Set VOF hybrid follows in the next section.

3.4.4 Validation of surface tension implementations

The accurate estimation of the surface tension is key to describe the capillary dominated flows of drops and rivulets. The different curvature estimates of this section are validated based on literature by simulation of a static drop and a capillary rise between two plates.

Static Drop

A statical and spherical drop with and without viscosity is a benchmark test case that was already used by Brackbill et al. (1992) to validate the CSF model. The used setup is described in Appendix A.2 and follows Francois et al. (2006) in order to compare their very accurate results with simulations using the three presented surface tension models. The magnitude of the maximum velocity $|\boldsymbol{u}|_{\max}$ in the domain after one time step, and up to 1000 time steps, is a measure of the parasitic currents. The influence of several parameters is investigated: The density ratio ϱ_1/ϱ_2, the time step length Δt, the end time T, the viscosity ratio ν_1/ν_2 and the resolution $R/\Delta x$.

ϱ_1/ϱ_2	interFoam exact curvature	CSF cell-centered Francois et al. (2006)	SSF face-centered Francois et al. (2006)
1	$1.26e-11$	$5.19e-5$	$5.42e-19$
10^3	$1.24e-8$	$6.15e-3$	$4.44e-18$
10^5	$9.92e-7$	$6.91e-3$	$2.71e-19$

Table 3.1: Magnitude of the maximum domain velocity simulating a stationary inviscid drop over one time step of $\Delta t = 10^{-6}$ s with a prescribed analytical curvature κ

First, the influence of increasing *density ratios* $\varrho_1/\varrho_2 = 1, 10^3, 10^5$ is evaluated after one time step $\Delta t = 10^{-6}$ s for an inviscid drop resolved with $R/\Delta x = 10$ cells per radius. The curvature is set as the analytical one of a 2D case $\kappa = 1/R_0 = 0.5\,\mathrm{m}^{-1}$. This *manufactured solution* provides insight into the force balance, which depends on the discretization as described in equation (3.19). Francois et al. (2006) present a *well-balanced* algorithm that calculates the surface tension based on either the *cell-centered* CSF method or a *face-centered* Sharp Surface tension Force (SSF) as part of the Ghost Fluid method. Table 3.1 compares the magnitude of the maximum domain velocity for different density ratios. For the density ratio of one, the result using the manufactured solution for the curvature κ is still better than the cell-centered model of Francois et al.. However, both `interFoam` and the CSF cell-centered approach by Francois et al. show a decrease in accuracy with increasing density ratio, a known yet unsolved methodological problem of `interFoam`.

As described in Section 3.4 parasitic currents occur due to a force imbalance and poor curvature estimates. The manufactured curvature solution shown in Table 3.1 reveals that the pseudo balancedness of the `interFoam` algorithm is surprisingly good, leaving the curvature estimate as the major problem to tackle. With the goal to improve the curvature calculation, the earlier presented iso-surface reconstruction, the hybrid Level-Set VOF method and the density scaling formulation are compared to the height function approach by Francois et al. (2006) in Table 3.2. An increasing *mesh resolution* reveals no convergence because the curvature estimate does not reach the required third or fourth order accuracy. The exception, showing second-order convergence, is the height function approach, which is, however, only efficiently implementable in parallel on structured meshes. Comparing the remaining methods, the iso-surface reconstruction is about an order of magnitude better than the standard CSF method. The S-CLSVOF method also shows a reduction in parasitic currents, which are further reduced by using the density scaling. The magnitude of the maximum domain velocity reduces insignificantly with finer time steps Δt and a constant simulation end time as shown in Table 3.3. The height functions approach remains about two orders of magnitude better than the iso-surface reconstruction.

In the following the two fluids are simulated *with a viscosity* ratio of ($\nu_1/\nu_2 = 10$) and $\nu_1 = 10^2\,\mathrm{kg/(m\,s)}$. For the given increasing *density ratios* in Table 3.4 the parasitic currents increase within the same order of magnitude for all methods. Tests performed within this study reveal an improvement between the OpenFOAM versions 2.4.x and the here used 5.x. The S-CLSVOF(DSB) method shows the smallest increase of parasitic currents and the iso-surface reconstruction shows the smallest parasitic currents excluding the work of Francois et al.. Table 3.5 shows results for different decreasing simulation *time steps* Δt. A linear increase of parasitic currents over the simulation time can be observed as reported among others by Francois et al.. Finally, the dependency on changing *viscosities* with a constant viscosity ratio of $\mu_1/\mu_2 = 10^2$ is investigated and results are presented in Table 3.6. The parasitic currents are almost invariant to changing viscosities.

To sum up, the `interFoam` algorithm is almost force balanced for a prescribed exact curvature, with comparable results to the force balanced algorithm presented by Francois et al. (2006). That leads to the conclusion that the major cause of parasitic currents is a poor estimate of the curvature. For finer meshes, none of the methods used to improve the curvature that are implemented in `interFoam` on unstructured meshes, converges. In contrast to that, on structured meshes, the use of height functions by Francois et al. is accurate enough to converge with second-order accuracy. Nevertheless, the results using the iso-surface reconstruction reduces the parasitic currents by about an order of magnitude. An increasing

R/h	interFoam exact curvature	interFoam CFS	interFoamExtended CFS - isoSurface	interFoamExtended S-CLSVOF	interFoamExtended S-CLSVOF(DSB)	Francois et al. (2006) CSF height functions
5	$2.03e-7$	$8.99e-5$	$8.21e-6$	$6.00e-5$	$3.92e-5$	$2.05e-6$
10	$1.24e-8$	$4.27e-4$	$6.58e-5$	$3.22e-4$	$1.84e-4$	$1.21e-7$
20	$1.50e-8$	$2.00e-3$	$2.70e-4$	$2.35e-3$	$1.47e-3$	$6.12e-8$
40	$2.33e-8$	$7.42e-3$	$6.60e-4$	$2.59e-2$	$1.06e-2$	$1.53e-8$

Table 3.2: Influence of the cell size on the magnitude of the maximum domain velocity simulating a stationary inviscid drop after one time step of $\Delta t = 10^6$ s and a density ratio of $\varrho_1/\varrho_2 = 10^3$.

Δt	interFoam exact curvature	interFoam CFS	interFoamExtended CFS - isoSurface	interFoamExtended S-CLSVOF	interFoamExtended S-CLSVOF(DSB)	Francois et al. (2006) CSF height functions
$1e-3$	$1.32e-7$	$1.86e-1$	$3.69e-2$	$1.53e-1$	$1.37e-1$	$4.35e-4$
$1e-4$	$1.95e-8$	$1.74e-1$	$3.52e-2$	$1.45e-1$	$1.20e-1$	$3.92e-4$
$1e-5$	$1.88e-8$	$1.66e-1$	$3.40e-2$	$1.40e-1$	$1.06e-1$	$3.64e-4$
$1e-6$	$6.17e-8$	$1.61e-1$	$3.32e-2$	$1.37e-1$	$1.01e-1$	$3.53e-4$

Table 3.3: Influence of the time step on the magnitude of the maximum domain velocity simulating a stationary inviscid drop with a simulation end time of 0.001 s and a density ratio of $\varrho_1/\varrho_2 = 10$.

ϱ_1/ϱ_2	interFoam exact curvature	interFoam CFS	interFoamExtended CFS - isoSurface	interFoamExtended S-CLSVOF	interFoamExtended S-CLSVOF(DSB)	Francois et al. (2006) CSF height functions
$1e1$	$1.32e-10$	$1.86e-4$	$3.69e-5$	$1.53e-4$	$1.37e-4$	$4.40e-7$
$1e3$	$1.23e-8$	$4.27e-4$	$6.59e-5$	$3.22e-4$	$1.37e-4$	$6.22e-7$
$1e5$	$9.92e-7$	$4.49e-4$	$8.20e-5$	$3.34e-4$	$1.84e-4$	$6.25e-7$

Table 3.4: Influence of the density on the magnitude of the maximum domain velocity simulating a stationary viscous drop ($\mu_1/\mu_2 = 10$) for one time step of $\Delta t = 10^{-6}$ s.

Δt	interFoam exact curvature	interFoam CFS	interFoamExtended CFS - isoSurface	interFoamExtended S-CLSVOF	interFoamExtended S-CLSVOF(DSB)	Francois et al. (2006) CSF height functions
$1e-3$	$1.04e-5$	$4.27e-1$	$6.58e-2$	$3.21e-1$	$1.84e-1$	$6.22e-4$
$1e-4$	$1.25e-6$	$4.27e-2$	$6.58e-3$	$3.22e-2$	$1.84e-2$	$6.22e-5$
$1e-5$	$1.23e-7$	$4.27e-3$	$6.58e-4$	$3.22e-3$	$1.84e-3$	$6.22e-6$
$1e-6$	$1.23e-8$	$4.27e-4$	$6.58e-5$	$3.22e-4$	$1.84e-4$	$6.22e-7$

Table 3.5: Influence of the time step on the magnitude of the maximum domain velocity simulating a stationary viscous drop ($\mu_1/\mu_2 = 10$) after one time step and a density ratio of $\varrho_1/\varrho_2 = 10^3$.

μ_1	μ_2	interFoam exact curv.	interFoam CFS	interFoamExtended CFS - isoSurface	interFoamExtended S-CLSVOF	interFoamExtended S-CLSVOF(DSB)	Francois et al. (2006) CSF height functions
a) after 100 time steps							
1	$1e-1$	$1.83e-7$	$3.80e-2$	$5.63e-3$	$2.76e-2$	$1.43e-2$	$4.73e-5$
$1e-2$	$1e-3$	$1.82e-7$	$3.82e-2$	$5.65e-3$	$2.77e-2$	$1.45e-2$	$4.83e-5$
$1e-4$	$1e-5$	$1.82e-7$	$3.82e-2$	$5.65e-3$	$2.77e-2$	$1.45e-2$	$4.83e-5$
b) after 1000 time steps							
1	$1e-1$	$6.15e-6$	$3.52e-1$	$1.25e-2$	$2.60e-1$	$1.33e-1$	$4.28e-4$
$1e-2$	$1e-3$	$6.17e-6$	$3.77e-1$	$1.26e-2$	$2.70e-1$	$1.38e-1$	$4.56e-4$
$1e-4$	$1e-5$	$6.17e-6$	$3.77e-1$	$1.26e-2$	$2.70e-1$	$1.38e-1$	$4.58e-4$

Table 3.6: Influence of the viscosity ratio μ_1/μ_2 on the magnitude of the maximum domain velocity simulating a stationary drop with after a) 100 and b) 1000 time steps of $\Delta t = 10^{-6}$ and a density ratio of $\varrho_1/\varrho_2 = 10^3$

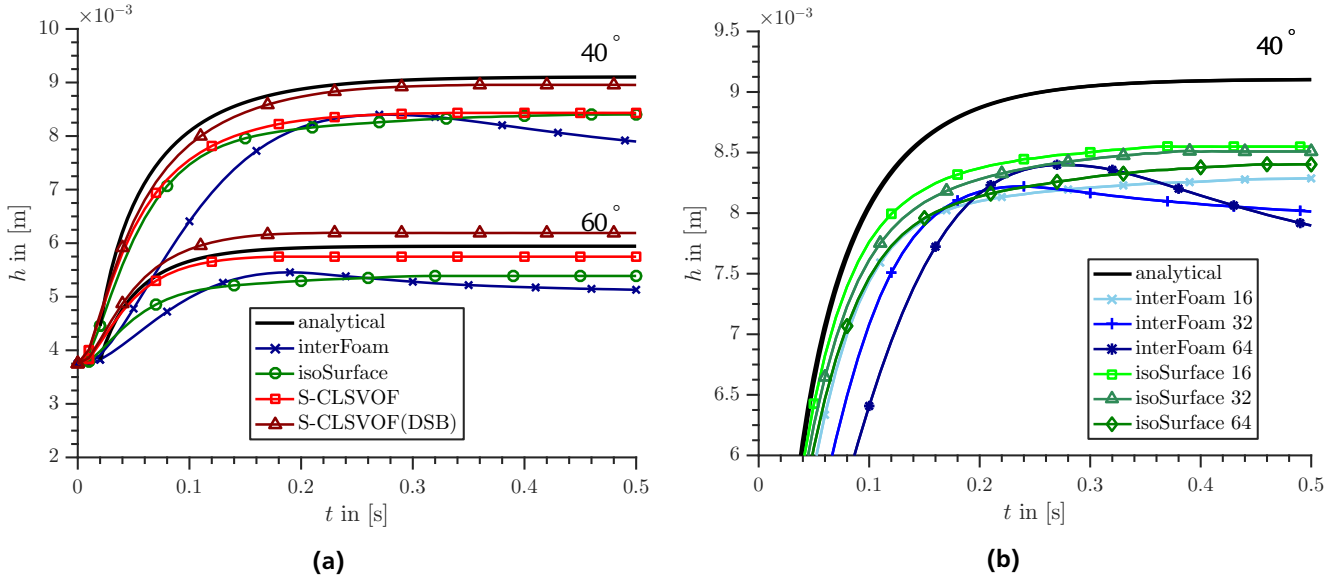

Figure 3.10: Capillary rise height between two plates: a) for a constant contact angle of $\theta_e = 40°$ and $\theta_e = 60°$ the surface tension force models, CSF, CSF-isoSurface, S-CLSVOF and S-CLSVOF(DSB) are compared with a resolution of $R/\Delta x = 64$. b) using the CSF-isoSurface model the rise height h is compared for three mesh resolutions.

density ratio leads to an increase of parasitic currents. The parasitic currents increase linearly in time and with increasing surface tension but remain invariant for a constant viscosity ratio but changing viscosities as found by Francois et al..

Capillary rise between two plates

For this study, it is relevant to validate the combinations of the different curvature estimations models with a contact angle model. Note at this point, that the contact angle is realized and adjusted by applying a surface tension force. And thus, the curvature calculation is of importance. An in-depth introduction to the numerical realization of the contact angle will follow in the next section. The capillary rise is often used as a benchmark for curvature calculations (Fath and Bothe, 2015, Xu and Guetari, 2004), since a transient analytical solution for the rise height is described by Fries and Dreyer (2008), which reads as

$$h(t) = \frac{a}{b}\left\{1 + W\left(\frac{-a + bh_0}{a}\exp\left(-1 + \frac{b}{a}(bt_0 + h_0 - bt)\right)\right)\right\}. \tag{3.33}$$

The height h_0 for a given time $t_0 > 0$ is taken from the simulation results after a few time steps. The constant a and b are given in a two-dimensional case as

$$a = \frac{\sigma R\cos\theta_e}{3\mu}, \quad b = \frac{\varrho g R^2}{3\mu}, \tag{3.34}$$

where ϱ and μ correspond to the denser fluid. The Lambert function W is implicitly defined as

$$x = W(x)\exp(W(x)). \tag{3.35}$$

The dimensions and material parameters are presented in Appendix A.3.

Figure 3.10a shows the analytical solution by Fries and Dreyer (2008) and results using the different surface tension force models CSF with `interFoam` and the iso-surface reconstruction, the S-CLSVOF and S-CLSVOF(DSB) hybrid methods, which show an increased accuracy in the named order. The gain in accuracy with the enhanced curvature estimates

is significant. Even though the parasitic currents are smallest with the iso-surface reconstruction, the most accurate rise height is attributed to the S-CLSVOF(DSB) method. Because of the limitation of the S-CLSVOF(DSB) method to equidistant meshes and the better reduction of parasitic currents by the iso-surface reconstruction, the latter is chosen for all further simulations of this study.

Similarly to the static drop simulations, the mesh study of the capillary rise shows no convergence using the `interFoam` solver. Even though the surface tension of the iso-surface reconstruction does not converge formally for finer meshes, the quasi-static rise height seems to converge the given range of mesh sizes. Furthermore, the contact line motion is dampened with finer meshes, which is due to the reduced effective slip length, an issue explained in detail in Section 3.5.4.

In synthesis, the iso-surface reconstruction reduces parasitic currents by about a magnitude compared to the standard CSF method implemented in `interFoam`. The S-CLSVOF(DSB) yields better results in combination with a contact line since the contact angle is also set as a boundary for the Level-Set. However, because of its limitation to equidistant meshes the iso-surface reconstruction is a better fit to solve the multi-scale problems in the applications of complex automotive surfaces.

3.5 Contact line models

The contact line represents the line at which three phases e.g. solid, liquid and gas meet. The accurate modeling of the contact line motion is to this day a demanding challenge since it depends on local hydrodynamic and thermodynamic flow conditions and many material parameters. The influence of the different parameters has yet to be conclusively investigated even though first modeling approaches exist since Young (1805). Different models regarding the contact angle, the contact angle hysteresis and the dependency of the contact angle on the contact line velocity are presented in the following with a focus on their numeric implementation, and are validated with simplistic test-cases. The contact line description in OpenFOAM is extended by an object oriented and a modular class hierarchy developed in this study to formalize and combine research of several colleagues working on wetting simulations.

3.5.1 Contact angle models and implementation

The contact angle is measured between the solid surface and the liquid-gas interface. As explained in Section 2.4, different model classes exist which differ in the spatial resolution between micro, meso- and apparent contact angles and their dependency on the contact line velocity for which again different approaches exist as presented in Section 3.5.2. A wide variety of contact angles models exist of which a selection is implemented in this VOF framework.

In OpenFOAM, the adjustment of the current to the target contact angle is done as follows. The current contact angle θ_0 can be represented by the inner product of the wall normal $\boldsymbol{n}_\mathrm{w}$ and to the current normal of the interface at the wall boundary $\boldsymbol{n}_{\Sigma,\mathrm{w},0} = \nabla\alpha_\mathrm{w}/|\nabla\alpha_\mathrm{w}|$ which is calculated by the normalized gradient of the volume fraction

$$\cos\theta_0 = \boldsymbol{n}_{\Sigma,\mathrm{w},0} \cdot \boldsymbol{n}_\mathrm{w} \,. \tag{3.36}$$

To correct the current contact angle with a given target contact angle θ the current interface normal vector at the wall is changed to $\boldsymbol{n}_{\Sigma,w}$. Thereby, the target interface normal vector has to lie in the plane defined by the current interface normal and the normal of the wall

$$\boldsymbol{n}_{\Sigma,\mathrm{w}} = a\boldsymbol{n}_{\Sigma,\mathrm{w},0} + b\boldsymbol{n}_\mathrm{w} \,. \tag{3.37}$$

empirical	Jiang et al. (1979)	$\frac{\cos\theta_e - \cos\theta_{app}}{\cos\theta_e + 1} = \tanh\left(4.96 Ca^{0.702}\right)$	(3.41)
	Bracke et al. (1989)	$\frac{\cos\theta_e - \cos\theta_{app}}{\cos\theta_e + 1} = 2\sqrt{Ca}$	(3.42)
	Kistler (1993)	$\theta_{app} = f_{Hoff}\left(Ca + f_{Hoff}^{-1}(\theta_e)\right)$, with $f_{Hoff}(Ca) = \arccos\left\{1 - 2\tanh\left[5.16\left(\frac{Ca}{1+1.31Ca^{0.99}}\right)^{0.706}\right]\right\}$	(3.43)
hydrodynamic theory	Voinov (1976)	$\theta_d^3 = \theta_m^3 + 9Ca\ln\left(\frac{\epsilon_d}{\epsilon_m}\right)$, for $\theta_d < 135°$, else: $(\pi - \theta_d)^3 + 2.25\pi\ln\left(\frac{1-\cos\theta_d}{1+\cos\theta_d}\right) = \theta_m^3 + 9Ca\ln\left(\frac{\epsilon_d}{\epsilon_m}\right)$.	(3.44)
	Hoffman-Voinov-Tanner	$\theta_d = \left(\theta_m^3 + 72Ca\right)^{1/3}$	(3.45)

Table 3.7: Contact angle models based on empirical correlations and on hydrodynamic theory.

The coefficients a and b can be calculated with equations (3.36) and (3.37)

$$a = \frac{\cos\theta - \cos\theta_0\cos(\theta_0 - \theta)}{1 - \cos^2\theta_0} \tag{3.38}$$

$$b = \frac{\cos(\theta_0 - \theta) - \cos\theta_0\cos\theta}{1 - \cos^2\theta_0} \tag{3.39}$$

Both the contact angle and the interface normal have no explicit representation in the standard implementation of `interFoam`. Therefore, the volume fraction gradient normal to the wall $\nabla\alpha_{w,n}$ is set to

$$\nabla\alpha_{w,n} = \underbrace{(\boldsymbol{n}_{\Sigma,w}\cdot\boldsymbol{n}_w)}_{\cos\theta}|\nabla\alpha_w|\,. \tag{3.40}$$

After the new interface normal is set at the wall, the curvature and the surface tension are calculated. The difference between the current and the target interface normal leads to a local surface tension force which will adapt the interface near the wall boundary in the next time step.

Different contact angle models are selectable to calculate the target contact angle. The simplest form is a so-called constant contact angle θ_e. Dynamic contact angle models, however, depend on the contact line velocity often expressed in terms of the Capillary number $Ca = \eta U_{cl}/\sigma$. The choice of contact angle models and their presentation in this study is inspired by Lippert (2016). Only macroscopic and apparent contact angles are treated here, due to the scales of the investigated flow problems and the resolution limits. The mesoscopic contact angle models are derived from hydrodynamic considerations, whereas for the apparent contact angles empirical correlations are used. A selection of models is presented in Table 3.7.

The empirical models by Jiang et al. (1979), Bracke et al. (1989) and by Hoffman (1975) related to Kistler (1993) are given in terms of an out-of-balance Young's force or the Hoffman function. These models are to be applied with spatial resolutions similar to these in experiments, which is about $\approx 100\,\mu$m. The microscopic contact angle θ_m in the hydrodynamic models is the only necessary parameter to describe a dynamic mesoscopic contact angle θ_d (Voinov (1976), Tanner (1979) and generalized by Cox (1986)). The hydrodynamic models are denoted as sub-grid models that only require a resolution down to the mesoscopic length scale (Dussan, 1976), which according to Dupont and Legendre (2010) and Sui et al. (2014) is of the order of $10\,\mu$m for most wetting processes.

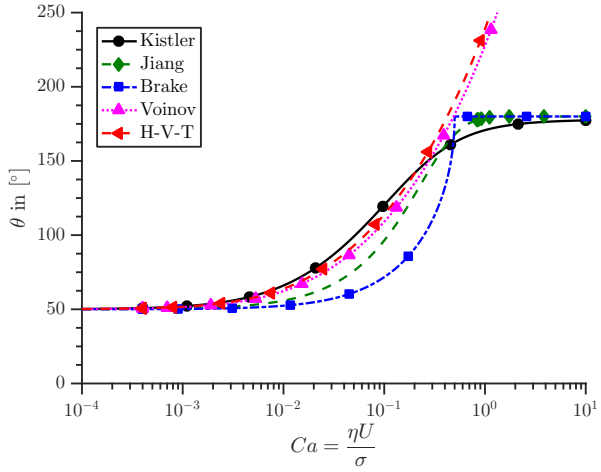

Figure 3.11: Comparison of different dynamic contact angle models based on both empirical data and hydrodynamic theory on the Capillary number. The equilibrium contact angle is set to $\theta_e = 50°$.

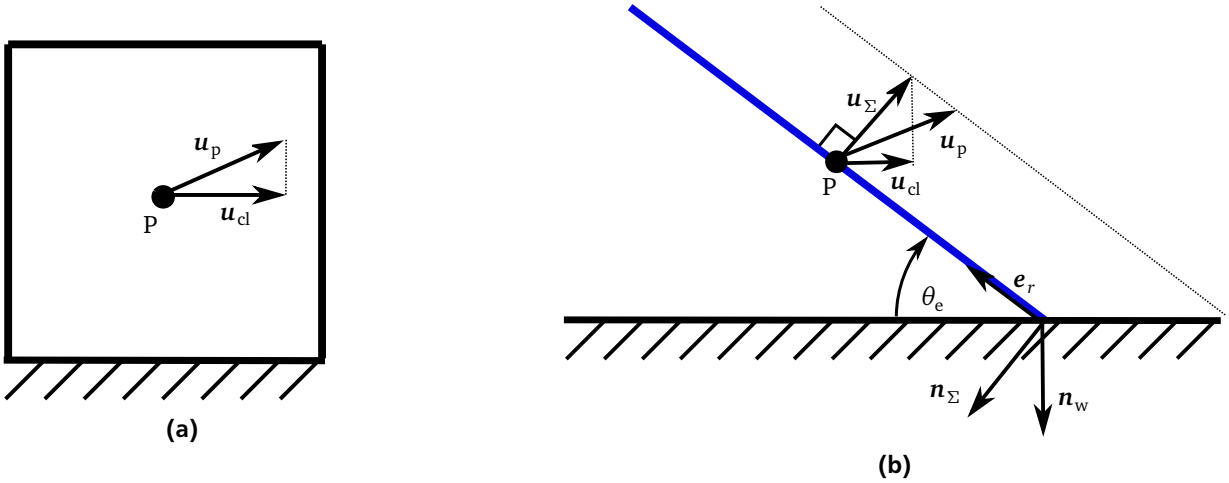

Figure 3.12: Approaches to calculate the contact line velocity using the cell-centered velocity. a) The projection of the wall adjacent velocity parallel to the wall. b) The wall adjacent velocity is first projected onto the two-phase interface and then to the wall (redrawn from Linder et al. (2015)).

The dependence of the contact angle on the Capillary number is shown in Figure 3.11 for the dynamic contact angle models of Table 3.7 and an equilibrium contact angle of $\theta_e = 50°$. Their shared range of validity is $Ca \leq 0.1$ for which all perform very similar. An application-oriented model validation and selection for this study follows in the next section.

The validation of surface tension models together with a constant contact angle model has already been shown in Section 3.4.4 in the case of a capillary rise between two plates, for which an analytical solution is known. To validate the dynamic contact angles the calculation of the contact line velocity is first introduced.

3.5.2 Contact line velocity

Applying a dynamic contact angle poses the challenge of an accurate approximation of the contact line velocity. In the VOF approach the interface is smeared out and no explicit representation of the interface or the contact line exists, which could be taken to calculated the contact line velocity knowing its position over time. Three different approaches to calculate the contact line velocity have been implemented.

Simple approach

The simplest approach to estimate the contact line velocity is to take the material point velocity $\boldsymbol{u}_p$ in the vicinity of the contact line and define the component parallel to the wall as the contact line velocity u_{cl} (see Figure 3.12a).

$$u_{\mathrm{cl,S}} = \frac{\boldsymbol{n}_\Sigma - (\boldsymbol{n}_\mathrm{w} \cdot \boldsymbol{n}_\Sigma)\boldsymbol{n}_\mathrm{w}}{|\boldsymbol{n}_\Sigma - (\boldsymbol{n}_\mathrm{w} \cdot \boldsymbol{n}_\Sigma)\boldsymbol{n}_\mathrm{w}|} \cdot \boldsymbol{u}_\mathrm{p} \,. \tag{3.46}$$

This simple contact line velocity model using the first cell center next to the wall as a reference point is widely used in literature for the simulation of wetting phenomena with interface capturing methods and is also implemented in OpenFOAM.

Roisman et al. (2008) and Linder et al. (2015) argue that this simple model sets the propagation velocity of the contact line equal to the velocity of the material point, which is not physical. This assumption only holds for contact angles of about $\theta \approx 90°$. Both propose a new model which we refer to as `LinderRoisman` model.

Projection onto the interface by Roisman et al. and Linder et al.

Based on geometrical considerations shown in Figure 3.12b and assuming a nearly planar interface near the wall, they consider the contact angle rate $\dot{\theta}$ and the distance r from the point P at the interface to the contact line and write for the interface velocity u_Σ

$$u_\Sigma - r\dot{\theta} \approx u_\mathrm{cl} \sin\theta \,. \tag{3.47}$$

If the value $r\dot{\theta}$ is much smaller than u_cl, the equation can be discretized as

$$u_{\mathrm{cl,LR}} = \frac{\boldsymbol{u}_\mathrm{P} \cdot \boldsymbol{n}_\Sigma}{\sqrt{1 - (\boldsymbol{n}_\mathrm{w} \cdot \boldsymbol{n}_\Sigma)^2}} \,. \tag{3.48}$$

The authors emphasize that for this approximation no creeping flow condition is required since it is only based on geometrical considerations. A more in-depth derivation can be found in Linder et al. (2015). The discretized value of the contact line velocity (3.48) has been corrected in this study with a necessary square, which is missing in the derivation and implementation by Linder which was also adapted by Lippert (2016).

Via contact line position

Šikalo et al. (2005) also used a VOF framework to simulate drop impact and they calculated the contact line velocity in an axisymmetric case by differentiation of the drop spreading radius. This application-oriented approach is similar to the more generic approach by Batzdorf (2015) who uses the volume fraction iso-surface reconstruction to estimate the position of the contact line in each time-step. In this approach the contact line velocity can be calculated knowing the position of the current and the last time step (see Figure 3.13a). This study adapts this approach following the steps outlined by Batzdorf.

The iso-surface reconstruction at the wall is a challenge since the volume fraction is a cell-centered field and not properly defined at the wall boundary. To reconstruct the contact line position, the volume fraction at the wall needs a correction. The gradient of the volume fraction at the wall boundary expressed by the contact angle is used to extrapolate a necessary value of $\alpha_\mathrm{w}^\mathrm{corr}$. This is possible since the gradient of any scalar field in a specific point is orthogonal to its iso-surface,

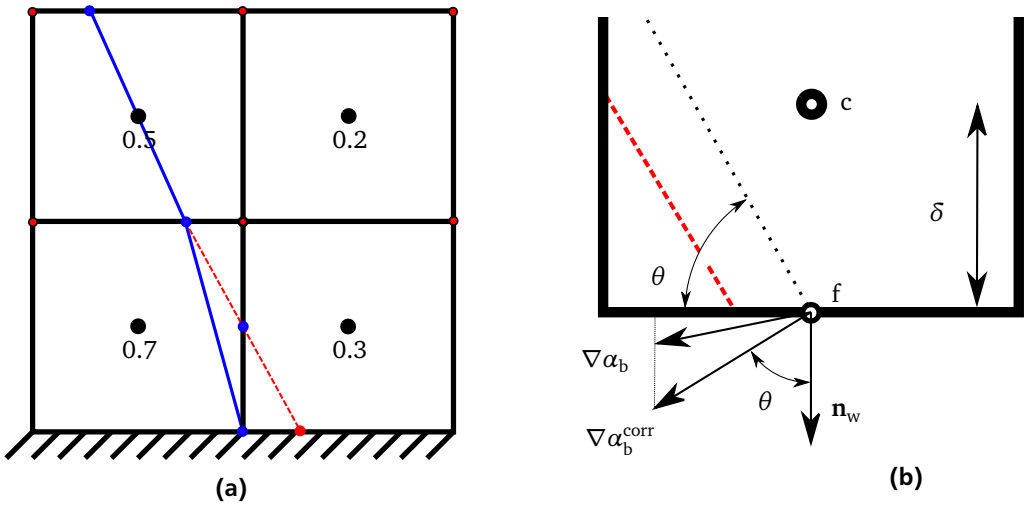

Figure 3.13: a) The contact line position is reconstructed as an iso-line and by comparing its position in two time steps the contact line velocity is calculated. b) The gradient information of the cell center and the contact angle are used to extrapolate and correct the volume fraction at the boundary face in order to determine the position of the contact line.

which means, the volume fraction extrapolated onto the wall by the contact angle will lead to iso-lines parallel to the contact line. Batzdorf stresses that this is not equivalent to setting the slope of the iso-surface inside the wall adjacent cell.

The extrapolation via the contact angle requires a correction of the volume fraction gradient $\nabla\alpha_{\mathrm{w}}^{\mathrm{corr}}$ as shown in Figure 3.13b that complies with two conditions. First, the gradient and the wall normal encloses the contact angle

$$\cos\theta = \frac{\nabla\alpha_{\mathrm{w}}^{\mathrm{corr}}}{|\nabla\alpha_{\mathrm{w}}^{\mathrm{corr}}|} \cdot \boldsymbol{n}_{\mathrm{w}}\,, \tag{3.49}$$

and secondly, the wall tangential component should remain untouched, in particular, be the same as given by the cell-centered volume fraction gradient $\nabla\alpha_c$ assuming a homogeneous Neumann boundary condition. This condition holds fulfilling

$$\nabla\alpha_{\mathrm{w}}^{\mathrm{corr}} \times \boldsymbol{n}_{\mathrm{w}} = \nabla\alpha_c \times \boldsymbol{n}_{\mathrm{w}}\,. \tag{3.50}$$

These equations combine to

$$\nabla\alpha_{\mathrm{w}}^{\mathrm{corr}} \cdot \boldsymbol{n}_{\mathrm{w}} = \frac{|\nabla\alpha_c \times \boldsymbol{n}_{\mathrm{w}}|\cos\theta}{\sin\theta}\,, \tag{3.51}$$

and provide the ingredient to extrapolate the cell-centered volume fraction α_c onto the wall face $\alpha_{f,\mathrm{w}}$

$$\alpha_{f,\mathrm{w}} = \alpha_c + \left(\nabla\alpha_{\mathrm{w}}^{\mathrm{corr}} \cdot \boldsymbol{n}_{\mathrm{w}}\right)\delta_{f\to c}\,. \tag{3.52}$$

The face-centered volume fraction $\alpha_{f,\mathrm{w}}$ is not bounded by zero or one, which is no issue since the flux through the wall is zero and the tangential component to the wall is preserved. To maintain a bounded volume fraction field α limiters are often used on wall boundary conditions. Consequently, the use of limiters should be avoided in combination with this method.

To obtain a smeared out contact line velocity, the distance to the reconstructed contact line is propagated to neighbor cells analogously to the algorithm explained in Section 3.4.2. The current contact line position vectors $\boldsymbol{x}_{\mathrm{cl}}^{n}$ and the position one from the last time step $\boldsymbol{x}_{\mathrm{cl}}^{n-1}$ define the contact line velocity

$$u_{\mathrm{cl,pos}} = -\frac{1}{\Delta t}\left(\boldsymbol{x}_{\mathrm{cl}}^{n} - \boldsymbol{x}_{\mathrm{cl}}^{n-1}\right) \cdot \frac{\boldsymbol{n}_{\Sigma} - (\boldsymbol{n}_{\mathrm{w}} \cdot \boldsymbol{n}_{\Sigma})\boldsymbol{n}_{\mathrm{w}}}{|\boldsymbol{n}_{\mathrm{I}} - (\boldsymbol{n}_{\mathrm{w}} \cdot \boldsymbol{n}_{\Sigma})\boldsymbol{n}_{\mathrm{w}}|}. \tag{3.53}$$

The contact line position is extrapolated using the current contact angle which itself depends on the contact line velocity and therefore also on the current contact line position itself. This circular dependency is solved by a fix-point iteration in which the value of the contact angle is under-relaxed to promote convergence and the iteration process is stopped if the contact angle change is less then 0.01° per iteration. This approach is the most accurate implemented here, however, using this method the iteration for almost static contact lines does not converge always due to the contact angle hysteresis and contact line pinning implementation in combination with parasitic currents as will be shown in Section 3.5.5. This model is later referred to as `cLVelocityViaCLPosition`.

3.5.3 Contact angle hysteresis and contact line pinning

The adhesion force acting at the contact line can be interpreted similarly to a friction force, which counteracts the acceleration of a static contact line. Small droplets stick to a window despite the gravitational force acting on the drop. Modeling this basic behavior of the contact line is crucial for an accurate description of contact line motion and is of major interest in this study. In experiments two critical contact angles are measured, which if locally exceeded, allow the contact line to move. The advancing and receding contact angle θ_{A} and θ_{R} are material parameters depending on both the solid and the liquid. The difference between both angles is called the contact angle hysteresis. The importance of the contact angle hysteresis is known since Frenkel (1948).

The contact line velocity is directly related to the velocity imposed by the momentum balance in the first cell center of the wall adjacent cells, since the advection of the volume fraction is directly coupled to the velocity. The adhesion force inhibits the motion of the contact line similar to a friction force, as long as the local contact angle does not exceed the contact angle hysteresis (θ_{A}, θ_{R}). To describe the contact line motion correctly two models, the contact angle hysteresis and the contact line pinning, are necessary.

Hysteresis effects are already modeled in various numerical methods like Lattice Boltzmann (Wang et al., 2013, Bommer et al., 2014), Level-Set (Spelt, 2005), Diffusive Interface (Ding and Spelt, 2008) and Front-Tracking (Duquennoy et al., 2001). To realize an immobile contact line while hydrodynamic forces act within the wall adjacent cells in a VOF framework three different approaches are known.

Dupont and Legendre (2010) suggest the cancellation of the velocity near the contact line if the current contact angle is in the range of the advancing and receding contact angle by altering the surface tension to cancel out the calculated acceleration. Their approach is implemented in the code framework JADIN and also adapted by Lippert (2016) in FS3D. This technique is, in general, applicable to algebraic VOF methods. A similar model is proposed by Park and Kang (2012) named Deceleration Feedback Technique, where the contact angle is changed by an increment such that the resulting curvature and thus the surface tension create a force that counteracts the contact line velocity in the next simulation step. By changing the contact angle directly the momentum equation remains untouched in contrary to Dupont's approach. Fang et al. (2008) developed an algorithm for geometrical VOF approaches only, where the contact line is immobilized for given conditions by only allowing a rotation of the PLIC interface plane around the contact line. The here followed approach, applicable for geometrical as well as algebraic VOF methods, is developed by Linder et al. (2015).

```
for all Wall faces do
    calc θ_cur
    calc Ca
    if    (θ_curr > θ_A && Ca > 0)
       || (θ_curr < θ_R && Ca < 0) then
        Neumann BC
        ∇α ← contact angle model
    else
        Dirichlet BC
        α fixed
    end if
end for
```

Algorithm 1: Pinning of the contact line is realized with the Robin boundary condition by Linder (2015).

The contact angle is, in general, imposed by a Neumann boundary condition for the volume fraction α. However, such a Neumann condition only imposes the gradient and allows for a changing volume fraction value at the boundary implying a moving contact line. To realize an immobile contact line for contact angles within the contact angle hysteresis, Linder suggests the use of a mixed boundary type fixing the volume fraction value or imposing the contact angle as a gradient. This so-called Robin boundary condition can be written for the volume fraction at the wall boundary α_w as

$$\alpha_w = s\alpha_w + (1-s)(\alpha_w + \nabla\alpha_w \cdot \boldsymbol{d}_w), \tag{3.54}$$

where $\boldsymbol{d}_w$ denotes the distance vector from the cell midpoint to the face center at the wall and s the blending factor that switches between zero, if the contact line should pin, and one if it is free to move. To determine whether pinning applies different cases are to be considered.

- The contact line is allowed to move if the current contact angle exceeds the advancing contact angle $\theta_{curr} > \theta_A$ and the interface velocity near the contact line $\boldsymbol{u}_p$ directs into the lighter fluid $\boldsymbol{u}_P \cdot \boldsymbol{n}_\Sigma > 0$ (advancing motion).
- Analog to the first case the contact line is allowed to move if $\theta_{curr} < \theta_R$ falls short of the receding contact angle and the interface velocity near the contact line $\boldsymbol{u}_p$ directs into the denser fluid $\boldsymbol{u}_P \cdot \boldsymbol{n}_\Sigma < 0$ (receding motion).
- in all other cases the contact line remains pinned.

Another way to express the direction of the interface velocity near the contact line $\boldsymbol{u}_p$ is the Capillary number calculated from the contact line velocity. If the contact line is free to move the dynamic contact angle model applies. The Algorithm 1 sums up the pinning boundary condition as used in this study.

The advantages of this methodology are the simplicity and applicability on unstructured meshes of general topology, as well as the localized formulation allowing for an application in 2D and 3D.

3.5.4 Cell-size dependence of the contact line velocity and the contact angle

The volume fraction α is coupled to the velocity calculated from the momentum and the continuity equations. At a wall the tangential velocity is set to zero. A strictly continuous approach would fix the contact line at the wall without the possibility of movement. However, in interface capturing methods such as VOF, the implicitly given contact line moves with the velocity of the wall adjacent cell center leading to a method-inherent numerical slip with a slip length $l_\lambda = 0.5\Delta x$ equal to half the mesh size (see Figure 2.6). By refining the mesh, the slip length will reduce, thus the contact line velocity is mesh size dependent.

For explicitly resolved contact lines the Navier-Slip model by Navier (1823) is often used to allow for slippage, which is proportional to the strain rate at the wall

$$u|_{y=0} = -\boldsymbol{u}_{\mathrm{w}} = l_\lambda \frac{\partial u}{\partial x}\bigg|_{y=0}, \tag{3.55}$$

where $\boldsymbol{u}_{\mathrm{w}}$ is the velocity at the wall and u parallel to the wall. The slip length is expected to be of molecular length scales near the contact line (Cox, 1986), which is much smaller than the here used typical mesh resolutions of the order of $\Delta x = 10 \mu m$. However, the Navier-Slip model could also be applied to reduce mesh dependence of the contact line velocity in the VOF context. The contact line velocity mesh dependency has a direct effect on the applied contact angle.

In addition to the contact line velocity mesh dependency, the application of the contact angle is also mesh dependent considering the macro, meso and micro contact angle scales. In this study, only meso to macroscopic/apparent contact angles are resolved with mesh resolutions at a minimum of $\Delta x = 10\,\mu$m and a maximum of $\Delta x = 100\,\mu$m. Afkhami et al. (2009) states that by resolving the slip length together with the Navier-Slip condition the contact line motion converges. Since such a resolution is out of scope in technical applications, they reuse the Cox contact angle model which connects the microscale θ_{m} to the mesoscale θ_{dyn} contact angle and apply the model bridging the apparent θ_{app} in an outer region to a numerical θ_{num} inner region contact angle. This approach is limited to a mesh resolution smaller than the outer or macro region of the order of $100\,\mu$m and accounts for both the mesh dependent contact line velocity and contact angle. The mesh dependent contact angle by Afkhami et al. reads as

$$G(\theta_{\mathrm{num}}) = G(\theta_{\mathrm{app}}) + Ca \ln \frac{\Delta x/2}{r_0}, \tag{3.56}$$

in which r_0 represents a length scale of the outer region. The function $G(\theta)$ is defined in Cox (1986) and also presented in Afkhami et al. (2009). An approximation for equation 3.56 is given by Voinov (1976)

$$\theta^3_{\mathrm{num}} = \theta^3_{\mathrm{app}} - 9Ca \ln\left(\frac{K}{\Delta x/2}\right), \quad \text{for } \theta_{\mathrm{app}} < 135°, \quad \text{else} \tag{3.57}$$

$$\theta^3_{\mathrm{num}} = (\pi - \theta_{\mathrm{app}})^3 + 2.25\pi \ln\left(\frac{1-\cos\theta_{\mathrm{app}}}{1+\cos\theta_{\mathrm{app}}}\right) - 9Ca \ln\left(\frac{K}{\Delta x/2}\right), \tag{3.58}$$

$$\tag{3.59}$$

which is comparable to the inverted equation (3.44). The model by Afkhami et al. has been implemented in this study and a validation will be shown in the next chapter.

3.5.5 Validation of contact line models

The validation of the different contact line models and their combinations, as well as a suitable selection in respect to their application on drops and rivulets in shear flow, is presented next. Where possible, experimental or analytical results are compared with simulation results.

Dynamic contact angle models

The validation of the different contact angle models is performed with three different test cases. To validate dynamic contact angle models a drop deposition simulation is compared to experiments by Lavi and Marmur (2004). Lavi and Marmur describes the evolution of a wetted surface area over time by the exponential power law

$$\frac{A}{A_f} = 1 - \exp\left(-\frac{K_{\mathrm{LM}}}{A_f}\tau^n\right) \quad \text{with } \tau = \frac{\sigma t}{\mu V^{1/3}}, \tag{3.60}$$

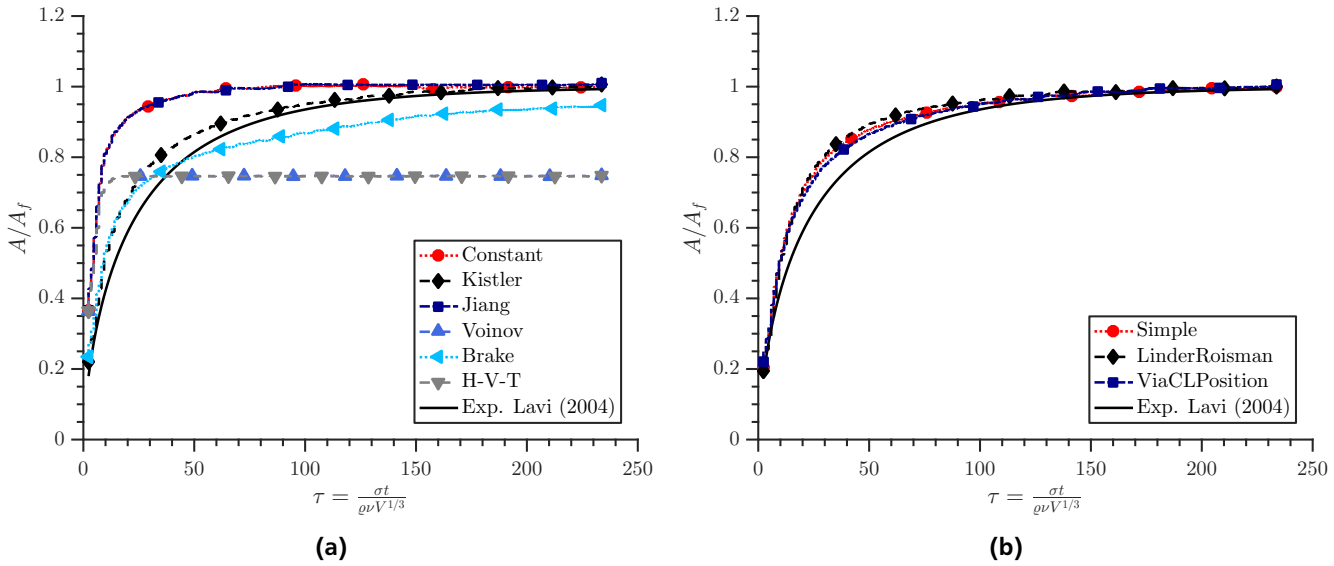

Figure 3.14: Comparison of the wetted area of a simulated droplet deposition of a squalane drop on a coated silicon wafer with an experiment described by Lavi and Marmur (2004). a) Comparison of different dynamic contact angle models using `LinderRoisman` as contact line velocity model. b) Comparison of different contact line velocity models using the Kistler model.

where V describes the drop volume and $\tau = \sigma t/(\varrho \nu V^{1/3})$ a dimensionless time. The constants $K_{\mathrm{LM}} = 0.471$ and $n = 0.699$ are known by experiments for the fluid Squalane and the solid, a Dodecyltrichlorosilane-coated silicon wafer. The droplet radius is $R_0 = 1\,\mathrm{mm}$ and the equilibrium contact angle is measured to be $\theta_{\mathrm{e}} = 41.5°$. The maximum Capillary number $Ca < 0.01$ well within the valid range of all models. The cell size is chosen to be $\Delta x = 10\,\mu\mathrm{m}$ to comply with the requirement of the contact angle models derived from hydrodynamic theory to resolve the intermediate contact angle region. The setup is further described in Appendix A.4.

The contact line velocity model to calculate the Capillary number is set to `LinderRoisman` which is presented in Section 3.5.2. Using this model, Figure 3.14a reveals the performance of different contact angle models compared to the experiment by Lavi and Marmur. Using the constant contact angle the drop reaches its maximum wetting area first. The dynamic contact angle models slow down the spreading rate of the drop. Nevertheless, the model by Jiang et al. performs almost identically to the constant model. The model by Voinov and Hoffman-Voinov-Tanner does not reach the final experimental wetting area. Kistler's model is closest to the experiment with a good approximation of the spreading dynamic and is therefore chosen in all further studies. The Kistler model has two additional advantages. First, the contact angle is bound by 180° for high Capillary numbers. Even though they are outside the valid Capillary number region of this model it provides robustness in simulations as the Capillary number is calculated on all wall boundary faces regardless of the presence of a contact line. And secondly, the empirical models are applicable for higher mesh resolutions in a range of $10\,\mu$m up to $100\,\mu$m which is exactly the range used in this study.

Contact line velocity models

Validation results of the three contact line velocities models are shown in Figure 3.14b using Kistler's contact angle model. All three models perform equally well. Interestingly, the difference between the `Simple` and the `LinderRoisman` models is not substantial even though the contact angle of $\theta_{\mathrm{e}} = 41.5°$ is far away from the optimal $\theta_{\mathrm{e}} = 90°$ for the `Simple` model. As expected the closest match with the experimental data is achieved by the most involved approach `cLVelocityViaCLPosition` which reconstructs the iso contact line. A final model selection is done only after adding pinning capabilities to the contact line.

Pinning and contact line velocity models

Drop impact receives huge attention due to its importance in many industrial applications such as spray coating, printing or combustion, and spray cooling. The test case presented here is categorized as a spherical drop impacting on a dry, horizontal, smooth and unyielding surface (Rein, 1993) for Weber numbers $We = \varrho u^2 L/\sigma$ in the drop deposition regime (Rioboo et al., 1999). To validate the pinning boundary condition as well as the combination of pinning with the different contact line velocity models, drop impact simulations are compared to experiments described by Šikalo et al. (2005) (see Appendix A.5). A glycerin drop with radius $R_0 = 1.225\,\text{mm}$ impacts with Weber numbers of $We = 802$ and $We = 93$ on wax $\theta_e = 93°$ and glass $\theta_e = 15°$.

The fast-spreading regime is dominated by inertial forces, for which the contact angle model plays an insignificant role (see Figure 3.15a and 3.15c). Reaching the maximum spreading radius, the constant contact angle overshoots the experiments the most and retraces the fastest until reaching its equilibrium state. As expected both impact velocities yield the same spreading radius d/D after the receding phase. The use of the dynamic contact angle comes with a slower receding. However, only when using the pinning boundary condition, the characteristic receding as shown by experiments is recovered. The drops impinging on glass do not even recede after spreading. In the transition between the spreading phase and the receding phase, the interface needs to adapt from the advancing θ_A to the receding contact angle θ_R. While for the pure dynamic contact angle the contact line is already receding during this change the contact line stays immobile using the pinning boundary condition. More complex cases regarding the pinning boundary are presented in Chapters 4 and 5.

Validation of the different contact line velocity models together with the pinning boundary condition shows similar results for the `Simple` and `LinderRoisman` models (see Figure 3.15b and 3.15d). The `ViaCLPosition` model, on the contrary, shows rather unphysical results after the spreading phase. This behavior stems from the extrapolation of the contact line position with the gradient information of the cell adjacent to the wall by assuming a pure Neumann boundary condition. Besides that, a point to ponder on is the handling of the incipient motion of a contact line using the contact line Capillary number to decide if the interface is in advancing or receding motion. If the contact line is not moving the Capillary number is zero in contrast to the contact line velocities retrieved from the velocity from the wall adjacent cell in the `Simple` or `LinderRoisman` model. This case should be handled separately.

Even though the `ViaCLPosition` model showed promising results, recalling the drop spreading in Figure 3.14b, it is not fit for an application with the pinning boundary condition. The experiments by Šikalo et al. (2005) are very well matched by simulations using the pinning boundary conditions. With regards to the velocity model, the `LinderRoisman` model is selected for all subsequent simulations, which performs slightly better than the `Simple` model.

Convergence and effective slip mesh dependence correction

The mesh dependence of both, the contact line velocity and the contact angle is shown in Figure 3.16a with results of the drop impact case described by Šikalo et al. (2005) and in Appendix A.5 for a glycerin drop on wax and a Weber number of $We = 802$. The maximum spreading radius and in the receding phase, the contact line converges for the simulated resolutions of 9.7, 19.5, 39.1, 78.1 μm even though further refinement would increase the surface tension force imbalance outlined in Section 3.18. By applying the correction model by Afkhami et al. (2009) the mesh dependence reduces the variation of the maximum spread. However, the mesh dependency cannot be corrected completely which is in line with Afkhami's observations.

Further results applying the pinning boundary condition as described in Section 3.5.3 are shown in Figure 3.16b. The experimental data is in very good agreement with simulations for different mesh sizes. A mesh dependence is visible

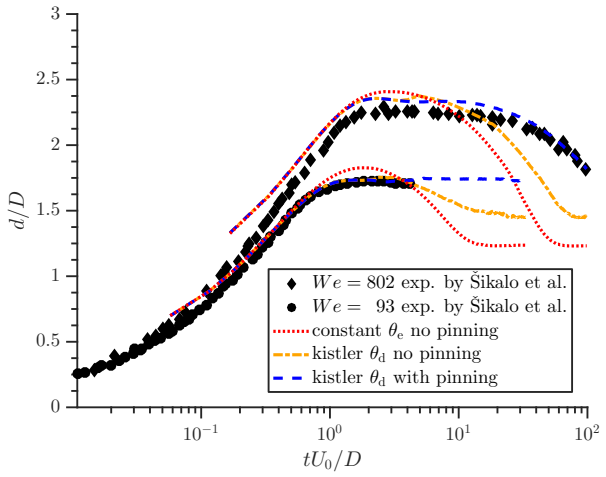

(a) Wax

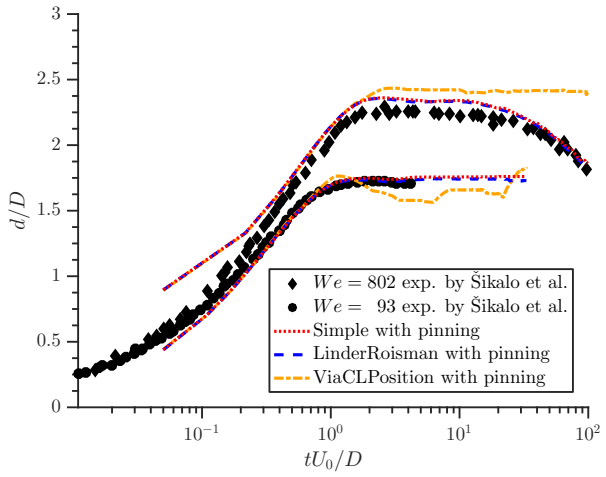

(b) Wax

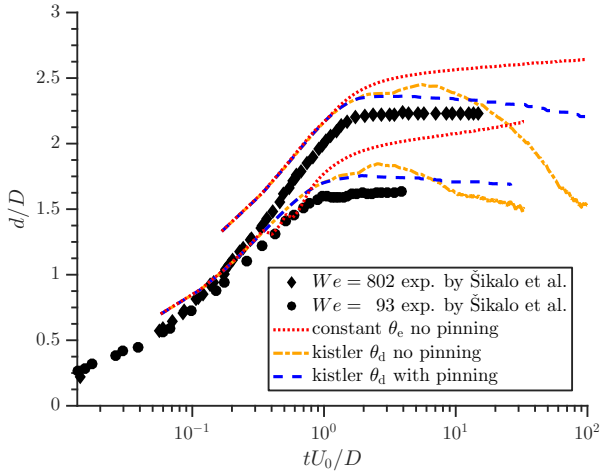

(c) Glass

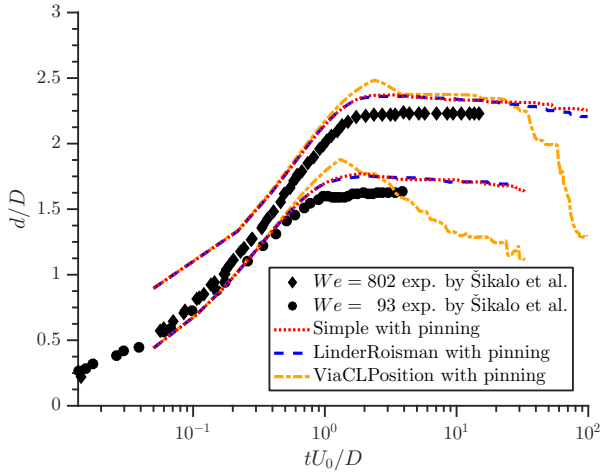

(d) Glass

Figure 3.15: Comparison of drop impact simulations onto a wax and a glass surface with experiments by Šikalo et al. (2005). a) and c) Difference between a constant contact angle model and the dynamic contact angle model by Kistler with and without pinning. b) and d) Comparison of three contact line velocity models using the Kistler model with pinning.

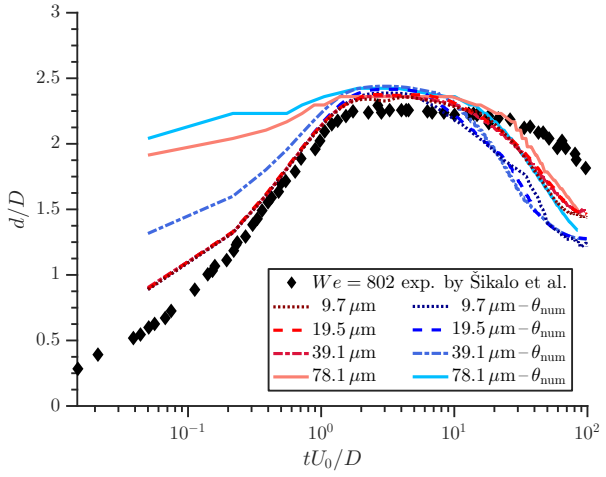

(a) no pinning

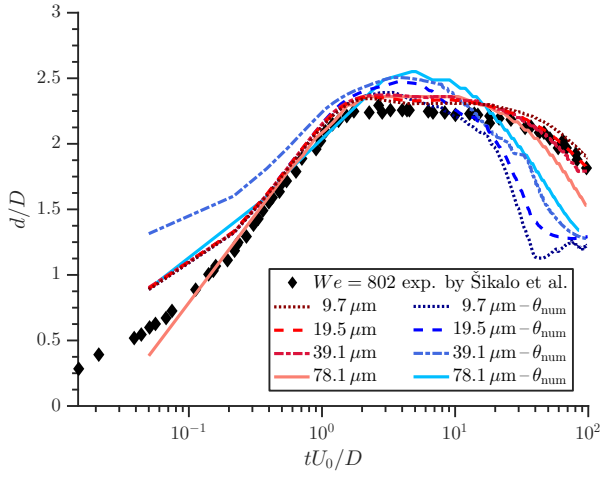

(b) with pinning

Figure 3.16: Convergence study with four mesh resolutions to observe the dependency between the contact line velocity and contact angle and the grid size. a) With and without the correcting contact angle model θ_{num} by Afkhami et al. (2009) and no pinning boundary condition. b) As a) but including the pinning boundary condition.

and convergence can be shown for the receding part of the drop impact within the range of the used spatial resolutions. Applying the correction by Afkhami et al. the mesh dependence increases noticeably leading to the conclusion that his model and the contact line pinning boundary condition implementation by Linder (2015) are not compatible.

The problem is, in fact, the fixed critical advancing θ_A and receding θ_R contact angles which are compared to the current velocity dependent corrected contact angle θ, which was set to be the numerical contact angle θ_{num} of the last time step. The corrected angle θ_{num} is, in general, higher (advancing) or lower (receding) than the calculated dynamic contact angle θ_d. Consequently, the pinning of the contact line will apply less often, which is clearly visible in Figure 3.16b. Note that even in stationary cases the contact line velocity will not be zero because of parasitic currents. To circumvent this problem one could change the reference contact angles θ_A and θ_R according to Afkhami's correction of the last time step. Such an approach would require some involved changes in the contact line handling, which are not in the scope of this study. All further simulations are performed without the contact line velocity dependent contact angle correction. The mesh dependence comes into play in dynamic cases, yet the results of the highly dynamic drop impact for finer meshes are all in very good agreement with experiments.

3.6 Boundary conditions

To realize simulations of drop and rivulets on tilted plates and in turbulent shear flow, several new boundary conditions had to be implemented in OpenFOAM. A short but technical description of these is necessary to be able to recreate the simulations in the Chapters 4 and 5.

3.6.1 Time variant gravitational acceleration

Instead of tilting a surface in respect to the gravitational acceleration, it is easier in simulations to change the orientation of the gravitational acceleration itself. In OpenFOAM this acceleration is realized as a constant vector. Linder (2015) changed the dictionary entry after a number of simulation time steps introducing small unwanted vibrations to a drop on a tilting surface. To allow for a smooth orientation change over time, a modular approach has been implemented in this study. The presence of a dictionary file `constant/gTimeDependent` activates a flag in the solver to recalculate the gravitational acceleration each time step. The data interpolation utility `Function1` is used to change the values linearly over time. A simple linear change of vector entries in Cartesian coordinates cannot recreate a linear change of a tilting angle of a plate. Thus, the user specifies the orientation in spherical coordinates for two or more points in time between which values are interpolated linearly (see Figure 3.17). The spherical coordinates are transformed within the solver in each time step to Cartesian coordinates.

3.6.2 Time variant pressure driven turbulence generator

In the review of Tabor and Baba-Ahmadi (2010) two approaches for the generation of turbulent inflow are described: a synthetic eddy prescription and a precursor simulation. The latter is used in this study to generate a natural turbulence field by mapping the flow field back onto the channel inlet. Since a drop or rivulet forms an obstacle creating a wake, the mapped flow fields are taken upstream of the liquid obstacles. To force a constant velocity, a pressure gradient is applied as a source term in selected cells, which is a feature provided by OpenFOAM called `meanVelocityForce`. This source term has been enhanced to allow for a time-dependent pressure gradient interpolated between given time steps. A typical dictionary entry is shown in Figure 3.18. The cell selection requires a defined `cellZone`, which in contrast to the `cellSet`, is updated with dynamic mesh changes. To obtain a fully developed turbulent flow the precursor channel has to be passed through by a total length of minimum ten channel heights, which defines the necessary simulation time to create a fully developed turbulence field. The minimum precursor channel length should be determined as a multiple of the largest eddy structures to avoid periodic eddies and allow for a natural turbulence field. Chaudhari (2014) suggest a minimum length of three times the channel height $l \geq 3\delta$.

```
gTimeTable
{
      outOfBounds clamp;
      g           table
      (     //Spherical coordinate system in degree!
            // t   r    θ   ϕ
            (0.0 (9.81 90 270)) // in −y-direction
            (0.1 (9.81 90 180)) // in −x-direction
      );
}
```

Figure 3.17: Dictionary entry for the time-dependent gravitational acceleration.

```
momentumSource
{
      type        meanVelocityForceTimeVar;
      active      yes;
      meanVelocityForceTimeVarCoeffs
      {
            selectionMode     cellZone;
            cellZone          fvCellZone;
            fields            (U);
            UbarVar           table
                  (
                  ( 0.0 ( 3.0 0 0))
                  ( 2.6 ( 15.4 0 0))
                  );
      }
}
```

Figure 3.18: Dictionary entry for the time-dependent velocity-forcing pressure gradient source term.

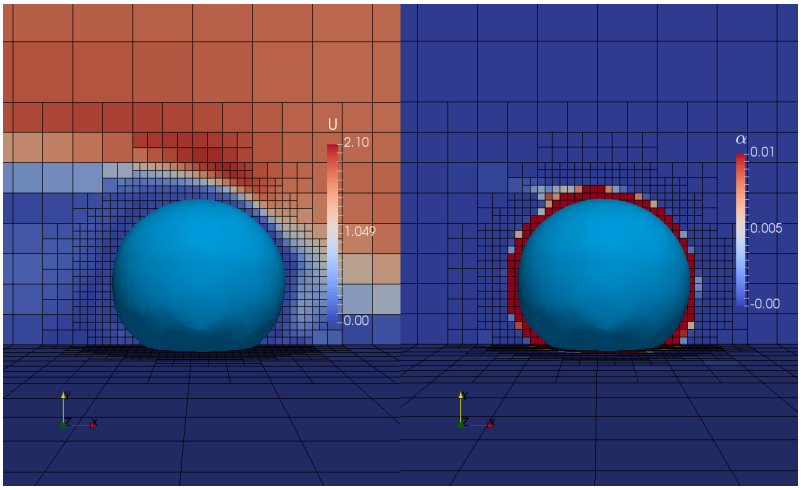

Figure 3.19: A drop in shear flow shown on the left picture and the according volume fraction capped at $\alpha = 0.01$ at the right to show the diffusive interface around the $\alpha = 0.5$ iso contour. A small part of the diffusive interface is constantly blown away by the shear flow (from right to left).

3.6.3 Drop refuel

One of the great challenges using the algebraic Volume of Fluid method is the numerical diffusion due to the gradient of the volume fraction field α. Although the diffusion is counteracted by a compression term, presented in Section 3.3, and small Courant numbers, the interface will always be smeared out over some cells. Thus, in shear flow, parts of the interface will be blown away continuously as shown by a small flag downstream of the drop in Figure 3.19. Important to note is the scaling of the volume fraction cut off at $\max(\alpha) = 0.01$ in the Figure. The continuous mass loss of the drop is comparable with evaporation and is not related to mass conservation problems often found in Level-Set methods. In relatively long simulations with a high shear rate, this evaporation becomes an issue as the drop might lose more than 5% of its mass. To counteract this method inherent problem, the drop is refueled over time in long simulations with shear flow. Therefore, the mass outflux of the domain is measured each time step and pumped back into the drop through the wall in boundary faces that meet the following conditions. First, the volume fraction needs to be $\alpha \geq 0.95$ and secondly, the face has to be marked as pinned, using the Robin boundary condition introduced in Section 3.5.3. As the sheared off mass per time step is relatively small and per average more than 100 faces meet that condition in typical setups, the inflow velocity is small ($< 10^{-3}\,\mathrm{m/s}$) compared to parasitic currents ($< 10^{-2}\,\mathrm{m/s}$) and very small compared to the channel flow ($\ll 10^{1}\,\mathrm{m/s}$). Consequently, the influence on the flow field is negligible.

3.6.4 Wall-functions for turbulent flow

The use of wall functions relaxes the requirement of a cell resolution at the wall of $y^+ = 1$. The distance between the midpoint of the wall adjacent cell to the wall is important to correctly apply wall functions in the three regions, the viscous sublayer, the buffer layer, and the logarithmic region as introduced in Section 2.2. In many CFD codes including OpenFOAM, no specific model for the buffer layer is included. Therefore in this study, the minimal resolution of $y^+ \leq 5$ at the wall is ensured in terms of average channel velocity to avoid the buffer layer, in which the asymptotic solutions for the viscous sublayer and the logarithmic region does not hold. An attempt to incorporate the Compound Wall Treatment by Popovac and Hanjalic (2007) was made, who suggest an exponential blending of both asymptotic regimes. However, only simulations with a sub-viscous resolution have shown satisfactory results. In the viscous sublayer, wall functions are already provided in OpenFOAM for the turbulent viscosity ν_t as suggested by Spalding (1961), prescribing a velocity profile down to $y^+ = 0$

$$y^+ = u^+ + \frac{1}{E}\left[\exp(\kappa u^+) - 1 - \kappa u^+ - 0.5(\kappa u^+)^2 - \frac{1}{6}(\kappa u^+)^3\right], \tag{3.61}$$

with $E = 9.8$ and $\kappa = 0.41$. The turbulent viscosity is calculated using equation (3.61) and (2.13) as

$$\nu_t = u_\tau^2 - \nu \frac{\partial u}{\partial y}\bigg|_{\mathrm{w}}. \tag{3.62}$$

In the RANS model, introduced in the next section, a boundary condition for the dissipation rate ϵ and the production P is required and implemented as

$$\epsilon = 2\frac{k\nu}{y_{\mathrm{p}}^2}, \tag{3.63}$$

with the kinetic energy k and

$$P = (\nu_{\mathrm{t}} + \nu)\left|\frac{\partial u}{\partial y}\right|_{\mathrm{w}} C_\eta^{1/4} \frac{\sqrt{k}}{\kappa y_{\mathrm{p}}} \tag{3.64}$$

with $C_\eta = 0.09$. Simulation results using these boundary conditions in combination with two different turbulence models are shown in Figures 3.20 and 3.21. The turbulence models are set out in the next section.

3.7 Turbulence models

In this section, the basic concepts and implementation details of turbulence models as used in this study are described. As already introduced in Chapter 2.2, turbulence covers multiple scales. Three general techniques exist to predict turbulent flows, each with a different range of resolved scales.

When even the smallest length and time scales are resolved as in the Direct Numerical Simulation (DNS), there is no need of turbulence models since all eddies are properly resolved. Naturally, the number of required grid cells is very high and scales with $Re^{9/4}$. Because of the cell size dependent time step restrictions, the overall computational cost increases even faster with $Re^{11/4}$ (Nieuwstadt et al., 2016). Hence, the use of DNS is and will be restricted to small domains and low Reynolds numbers for the coming years.

Smagorinsky (1963) proposed the first Large Eddy Simulation (LES) model. Only large eddies are resolved, which contain most of the kinetic energy. The energy cascade in Figure 2.1 suggests that the smallest eddies are of isotropic nature, which can be modeled accurately. All the small scales which contain a total of approximated 20 % of the kinetic energy are cut off by spatial filtering. Hence, the computational cost reduces significantly (Pope, 2000). Nevertheless, for many industrial applications a pure LES approach is not yet affordable. The Wall Adaptive Local Eddy (WALE) model by Nicoud

and Ducros (1999) is a state of the art LES model explained in further detail in Section 3.7.2.

The Reynolds-Averaged Navier-Stokes (RANS) model describes the whole turbulent energy spectrum statistically. Based on the work of Reynolds (1895), flow quantities are averaged such that small fluctuations are canceled out. This is by far the cheapest approach in terms of computational costs, but also the least accurate. Nevertheless, it is a widely used approach and applicable in simple turbulent flow conditions. The $\zeta-f$ model by Hanjalić et al. (2004) is a four-equation RANS model used in this study which is introduced in Section 3.7.1.

Hybrid models combine RANS and LES to reduce computational cost where possible. RANS lacks in an accurate description of flows dominated by large-scale anisotropic flow structures, while LES wall-bounded flows are very expensive due to grid requirements resolving the small structures at the wall. Combining both approaches these and other shortcomings can be circumvented. An overview of hybrid models is provided by Fröhlich and von Terzi (2008). Speziale (1998) introduced the Very Large Eddy Simulation (VLES), which blends seamlessly between RANS and DNS depending on the flow condition. Together with further changes by Han and Krajnović (2013) and Chang et al. (2014) this robust and highly efficient hybrid model is also used in the present study and outlined in Section 3.7.3.

After presenting these different models a validation and comparison follow. Section 3.7.5 concludes with a discussion of the combination of turbulence models with two-phase interface models.

3.7.1 RANS - $k-\epsilon-\zeta-f$

The $\zeta-f$ model by Hanjalić et al. (2004) is a four-equation eddy-viscosity RANS model, which accounts for the near-wall Reynolds stress anisotropy that represents a good compromise between numerical robustness and physical accuracy near the wall. It is based on the elliptic relaxation concept of Durbin (1991), according to which instead of the wall normal velocity scale $\overline{v^2}$ the velocity scales ratio $\zeta = \overline{v^2}/k$ is used, which makes the model more robust and less sensitive to grid non-uniformities. Besides the equation for ζ, further transport equations are solved for the kinetic energy $k = \overline{u_i u_i}/2$ which includes the production $P = \nu_t \overline{S_{ij} S_{ij}}$, and for the dissipation rate ϵ. Additionally, an equation for the elliptic relaxation parameter f is used to sensitize $\overline{v^2}$ to wall blocking effects:

$$
\begin{aligned}
\frac{\partial k}{\partial t} + u_j \frac{\partial k}{\partial x_j} &= P - \epsilon + \frac{\partial}{\partial x_j}\left[\left(\nu + \frac{\nu_t}{\sigma_k}\right)\frac{\partial k}{\partial x_j}\right], \\
\frac{\partial \epsilon}{\partial t} + u_j \frac{\partial \epsilon}{\partial x_j} &= \frac{C_{\epsilon 1} P - C_{\epsilon 2}\epsilon}{T} + \frac{\partial}{\partial x_j}\left[\left(\nu + \frac{\nu_t}{\sigma_\epsilon}\right)\frac{\partial \epsilon}{\partial x_j}\right], \\
\frac{\partial \zeta}{\partial t} + u_j \frac{\partial \zeta}{\partial x_j} &= f - \frac{\zeta}{k} P + \frac{\partial}{\partial x_j}\left[\left(\nu + \frac{\nu_t}{\sigma_\zeta}\right)\frac{\partial \zeta}{\partial x_j}\right], \\
L^2 \nabla^2 f - f &= \frac{1}{T}\left(c_1 + C_2' \frac{P}{\epsilon}\right)\left(\zeta - \frac{2}{3}\right),
\end{aligned}
\tag{3.65}
$$

where L and T are length and time scales, which are bound by the Kolmogorov scales and the realizability constraints of Durbin (1996)

$$
\begin{aligned}
T &= \max\left[\min\left(\frac{k}{\epsilon}, \frac{a}{\sqrt{6} C_\eta |\overline{S}| \zeta}\right), C_\tau \left(\frac{\nu}{\epsilon}\right)^{1/2}\right], \\
L &= C_L \max\left[\min\left(\frac{k^{3/2}}{\epsilon}, \frac{\sqrt{k}}{\sqrt{6} C_\eta |\overline{S}| \zeta}\right), C_\eta \left(\frac{\nu^3}{\epsilon}\right)^{1/4}\right].
\end{aligned}
\tag{3.66}
$$

C_η	$C_{\epsilon 1}$	$C_{\epsilon 2}$	c_1	C_2'	σ_k	σ_ϵ	σ_ζ	C_τ	C_L	C_η
0.22	$1.4(1+0.012/\zeta)$	1.9	0.4	0.65	1	1.3	1.2	6.0	0.36	85

Table 3.8: Constants that define the $\zeta - f$ RANS model.

The magnitude of the rate of strain $|S|$ is calculated by $|S| = \sqrt{2S_{ij}S_{ij}}$ with

$$S_{ij} = \frac{1}{2}\left(\frac{\partial u_i}{\partial x_j} + \frac{\partial u_j}{\partial x_i}\right). \tag{3.67}$$

Finally, the turbulent viscosity can be written as

$$\nu_t = C_\eta \zeta k T\,. \tag{3.68}$$

All model related constants are found in Table 3.8.

3.7.2 LES - WALE

In this section, first, the concept of LES is explained, and then the WALE model is presented. The energy cascade and the energy spectrum implicate that small turbulent structures are of local and isotropic nature and carry only a small amount of the total kinetic energy (see Figure 2.1). These characteristics lead to the concept behind LES, which is to resolve only the large eddies and model the remaining. The separation of these scales is done by spatial filtering, which can be subdivided into two classes (Sagaut, 2006):

- explicit filtering: has to be explicitly calculated and provides a well-defined filter shape for grid independent results. The effective filter width is greater than the grid size.

- implicit filtering: the grid size Δ_x is used as a cut-off measure and thus, no sub-filter scale term needs to be calculated.

In this study, implicit filtering is used on all fields $\phi = \overline{\phi} + \phi^{\mathrm{SGS}}$ separating resolved scales $\overline{\phi}$ and sub-grid scales ϕ^{SGS} where $\overline{\phi}$ reads as

$$\overline{\phi} = G * \phi = \int \phi(r_i)\, G(x_i - r_i)\, \mathrm{d}\boldsymbol{r}\,, \tag{3.69}$$

which corresponds to a convolution with a filter kernel G. Application of the filter operation to the Navier-Stokes equations 2.6 yields the one-fluid LES equation (Labourasse et al., 2007):

$$\frac{\partial \overline{u_i}}{\partial x_i} = 0\,, \tag{3.70}$$

$$\frac{\partial \overline{u_i}}{\partial t} + \overline{u_j}\frac{\partial \overline{u_i}}{\partial x_j} = \frac{1}{\varrho}\frac{\partial \overline{p}}{\partial x_i} + \frac{\partial}{\partial x_j}\left(\nu \frac{\partial \overline{u_i}}{\partial x_j} - \tau_{ij}^{\mathrm{SGS}}\right) + \overline{\sigma}\,\overline{n_i}\,\overline{\kappa}\,\overline{\delta_S} + \Xi\,. \tag{3.71}$$

The additional terms due to spatial filtering at the two-phase interface are denoted by the symbol Ξ. They will be further discussed in Section 3.7.5. The residual stress tensor

$$\tau_{ij}^{\mathrm{SGS}} = \overline{u}_i\overline{u}_j - \overline{u_i u_j} \tag{3.72}$$

represents the influence of the sub-filter motion in the filtered momentum equation. The variety of LES models emerges from different approaches to close the sub-grid stress tensor. Many of them are based on the eddy viscosity assumption to model the sub-grid scale tensor as already proposed in 1877 by Boussinesq (Schmitt, 2007)

$$\tau_{ij}^{\mathrm{SGS}} = -2\nu_{\mathrm{t}}^{\mathrm{SGS}}\overline{S}_{ij} + \frac{1}{3}\tau_{kk}\delta_{ij}\,, \tag{3.73}$$

$$\overline{S}_{ij} = \frac{1}{2}\left(\frac{\partial\overline{u_i}}{\partial x_j} + \frac{\partial\overline{u_j}}{\partial x_i}\right), \tag{3.74}$$

where $\overline{S}_{ij}$ is the deformation tensor of the resolved field. Smagorinsky (1963) was the first to model the sub-grid scale turbulent viscosity $\nu_{\mathrm{t}}^{\mathrm{SGS}} = (C_S\Delta_x)^2\sqrt{2\overline{S}_{ij}\,\overline{S}_{ij}}$ with the shortcoming that $\sqrt{2\overline{S}_{ij}\,\overline{S}_{ij}}$ incorrectly remains finite at the wall.

The Wall Adaptive Local Eddy Viscosity (WALE) model by Nicoud and Ducros (1999) is much more accurate at the wall. Here, the turbulent sub-grid viscosity is calculated with the traceless symmetric part of the squared velocity gradient tensor $\overline{g}_{ij}^2 = \frac{\partial\overline{u_i}}{\partial x_j}\frac{\partial\overline{u_i}}{\partial x_j}$

$$\nu_{\mathrm{t}}^{\mathrm{SGS}} = (C_{\mathrm{W}}\Delta_x)^2\frac{(S_{ij}^{\mathrm{d}}S_{ij}^{\mathrm{d}})^{\frac{3}{2}}}{(\overline{S}_{ij}\,\overline{S}_{ij})^{\frac{5}{2}} + (S_{ij}^{\mathrm{d}}S_{ij}^{\mathrm{d}})^{\frac{5}{4}}} \tag{3.75}$$

with

$$S_{ij}^{\mathrm{d}} = \frac{1}{2}\left(\overline{g}_{ij}^2 + \overline{g}_{ij}^2\right) - \frac{1}{3}\delta_{ij}\overline{g}_{ij}^2\,. \tag{3.76}$$

C_{w} is set to 0.325 for all simulations. To this day, the WALE model is a suitable choice to calculate complex wall-bounded flows such as the flow around a vehicle.

3.7.3 Very Large Eddy Simulation

The Very Large Eddy Simulation (VLES) is a hybrid methodology proposed by Speziale (1997, 1998) combining the RANS and LES approaches. VLES reduces dynamically to a pure RANS formulation on a relatively coarse mesh and to a pure DNS formulation on a fine mesh.

VLES shares the main idea with LES to simulate all large scales and to filter unresolved scales and model them accordingly using an appropriate RANS model. The big advantage of VLES is an improved accuracy compared to pure unsteady RANS models while being very flexible in the choice of the grid resolution. On the other side of the spectrum VLES is bridged seamlessly to a fully resolved DNS using very fine grids. Furthermore, it is a so-called “non-zonal” approach, which implies that use of RANS, VLES, LES or DNS is dynamically matched in this model especially for dynamically changing mesh resolution.

Speziale (1998) outlines three requirements for a hybrid turbulence model:

- Test filters and double-filtered fields contaminating larger scales should be avoided in subgrid-scale models.
- A strain dependent anisotropic eddy viscosity should be implemented, that allows for direct integration of subgrid-scale models up to a solid boundary without the need of ad-hoc wall damping functions.
- For the coarse mesh and infinite Reynolds number limit, a Reynolds stress model must be recovered, which allows an LES to be bridged continuously to a RANS computation.

Following these requirements, the turbulent viscosity of the unresolved motion reads as $\nu_t = F_{\mathrm{r}}\nu_t^{\mathrm{RANS}}$, where ν_t^{RANS} is calculated by the RANS-based sub-scale model, which relies on the underlying unsteady flow field (Krumbein et al.,

2017). VLES can be based on a variety of RANS models. Kondratyuk (2017) gained insights combining the $k-\epsilon$, $k-\omega$ and $\zeta-f$ models with VLES. In this study, the more accurate $\zeta-f$ model is used for which the turbulent viscosity reads:

$$\nu_t = F_\mathrm{r} C_\eta^\zeta \zeta_\mathrm{us} k_\mathrm{us} T_\mathrm{us}\,. \tag{3.77}$$

The subscript $[\cdot]_\mathrm{us}$ refers to unsteady quantities obtained from the RANS model. In this context, the variables k, ϵ, ζ, f, P, L and T of equations (3.65) and (3.66) will thus gain this subscript. The resolution function F_r dampens the influence of the RANS model for an increasing mesh resolution:

$$F_\mathrm{r} = \min\left[\left(\frac{\Delta_x}{l_\mathrm{K,us}}\right)^{\frac{4}{3}}, 1\right] = \min\left[\left(\frac{\Delta_x}{\frac{k_\mathrm{us}^{3/2}}{\epsilon_\mathrm{us}}}\right)^{\frac{4}{3}}, 1\right]. \tag{3.78}$$

Hereby, $\Delta_x = (\Delta^x, \Delta^y, \Delta^z)^{1/3}$ is implemented as the local grid spacing used as cut-off length and $l_{0,\mathrm{us}}$ represents the energy-containing turbulent length scales. Depending on the cut-off length in comparison with the Kolmogorov length scales the resolution function varies between $F_\mathrm{r} \to 1$ for the pure RANS and $F_\mathrm{r} \to 0$ for a theoretical DNS. F_r has an independent value in each computational cell. A detailed derivation can be found in Chang et al. (2014).

The original implementation in OpenFOAM by Chang et al. (2014) was enhanced in this study to account for multiphase flows within a Volume of Fluid framework, which can be done analog to the already in a one-fluid formulation implemented and related v^2-f model by Durbin (1991).

3.7.4 Validation and comparison of turbulence models

The validation of the WALE and the $\zeta-f$-VLES models in single-phase flows ensures a correct handling and a better understanding of their capabilities. Simulation results of the earlier presented turbulence models and DNS data of Moser et al. (1999) are quantitatively compared by characteristic values such as the averaged normalized velocity $\langle u^+ \rangle$ and the averaged resolved components of the Reynolds stresses $\langle u'u' \rangle / u_\tau^2$, which are normalized by the squared shear velocity u_τ.

In Chapter 5.1.2 a two-dimensional Hagen-Poiseuille channel flow with fully developed turbulence is simulated with a channel height of $H = 15\,\mathrm{mm}$. The domain used for validation has the dimensions $80 \times 15 \times 30\,\mathrm{mm}$. The grid resolution is set as suggested by Choi and Moin (2012) to $N_i = 160 \times 40 \times 60$ in combination with wall-functions to cope with the maximal wall resolution of $y^+ = 5$. The used wall functions described in Section 3.6.4 are valid in the viscous sub-layer and are applied for ν_t and ϵ in the $\zeta-f$-VLES model and ν_t in the WALE model. A cell grading towards the walls is applied with a total aspect ratio of two, measuring from the channel midst to the walls, in order to account for the smaller near-wall turbulent length scales. Thereby, the cell aspect ratio of two is chosen to keep the interface thickness in the VOF simulation justifiable. The inlet and outlet boundary conditions are periodic and the average channel velocity is kept constant at different Reynolds numbers by applying a pressure gradient. The Reynolds numbers of $Re_\tau = 180$ and $Re_\tau = 395$ are the extrema found in this study. All simulations are initialized with a fully developed turbulent flow that is simulated with 50 through-flow times.

WALE vs $\zeta-f$-VLES

Figure 3.20a shows the performance of the WALE and the $\zeta-f$-VLES turbulence models at $Re_\tau = 395$. Both underpredict the velocity in the near-wall region $y^+ < 20$ and overpredict it slightly for $y^+ > 20$ compared to DNS data, showing an overall good agreement with respect to the wall resolution of y^+. The mean Reynolds-stress-components in Figure 3.20b

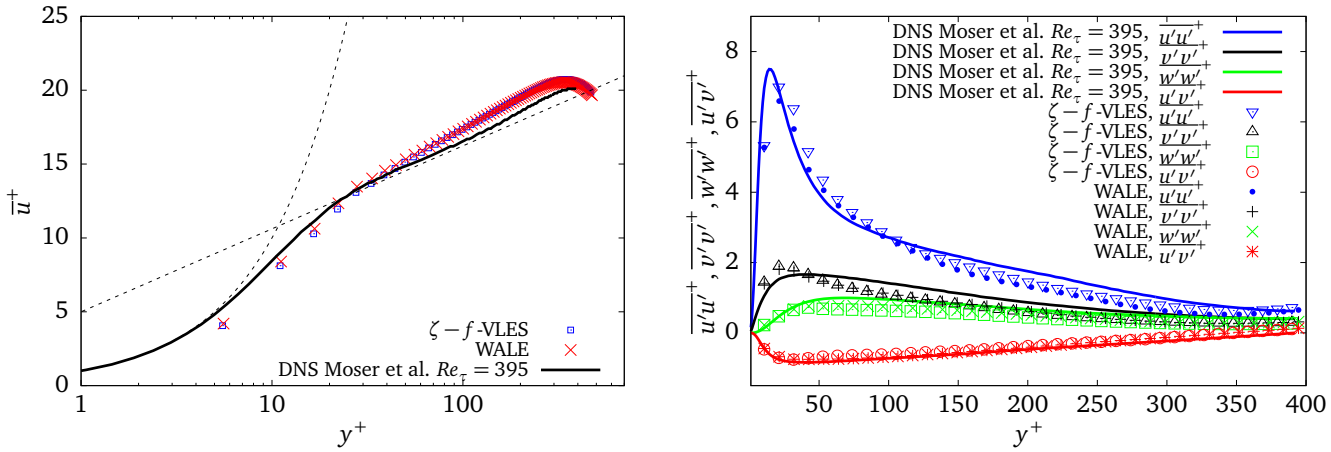

(a) Mean velocity profile

(b) Mean Reynolds-stress components

Figure 3.20: Comparison of the $\zeta - f$-VLES and the WALE turbulence models with DNS data by Moser et al. (1999) at $Re_\tau = 395$.

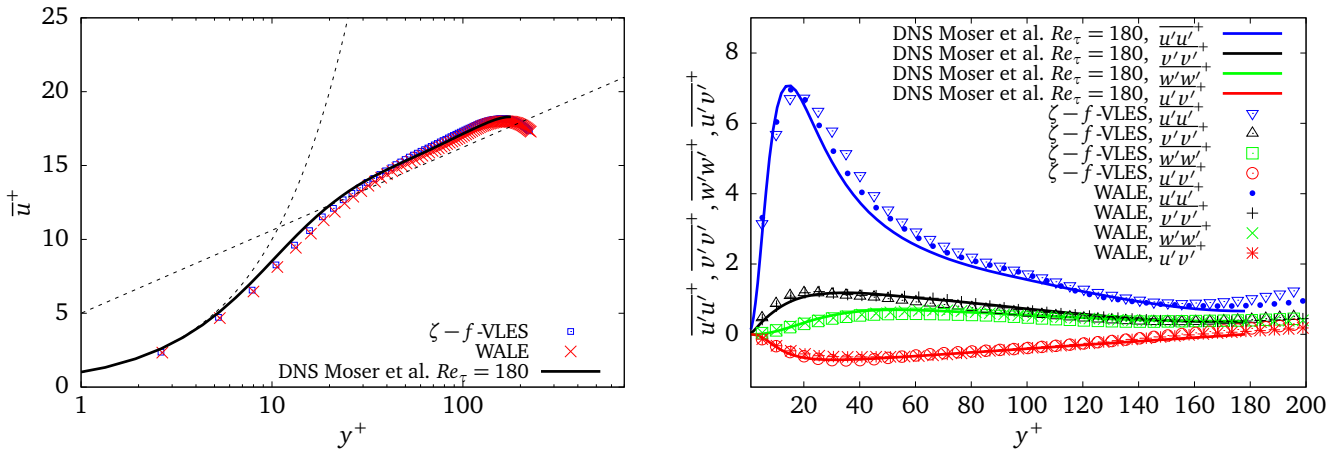

(a) Mean velocity profile

(b) Mean Reynolds-stress components

Figure 3.21: Comparison of the $\zeta - f$-VLES and the WALE turbulence models with DNS data by Moser et al. (1999) at $Re_\tau = 180$.

follow the DNS characteristics nicely for both turbulence models. The $\zeta - f$-VLES model follows the DNS data a bit better. Again, both models perform considerably well compared to DNS data regarding the under-resolved wall and application of wall functions. They provide an almost identical accuracy in this particular setup. However, the calculations of the $\zeta - f$-VLES are found to be about 10 % faster.

To simulate the incipient drop motion of in shear flow, the Reynolds number is linearly ramped up over time. Using the same mesh as for $Re_\tau = 395$, a validation at $Re_\tau = 180$ is shown in Figure 3.21. The overall quality with the same mesh is, as expected, even better since the turbulence scales are bigger and therefore better resolved with a minimal wall distance of $y^+ \approx 2$.

Influence of mesh refinement on turbulence modeling

Refining the cells at the two-phase interface is key to obtain the necessary resolution at the drop and at the same time obtain a cost-efficient computation of the less demanding spatial turbulent resolution for the here used channel Reynolds numbers of up to $Re = 13000$ utilizing wall functions. De Villiers (2007) argues that an abrupt cell refinement creates a non-equilibrium of the turbulent flow since resolved turbulent scales change slowly while modeled sub-scales change abruptly because of their direct relation to the cell size. Hence, the influence of the refinement on the turbulence prop-

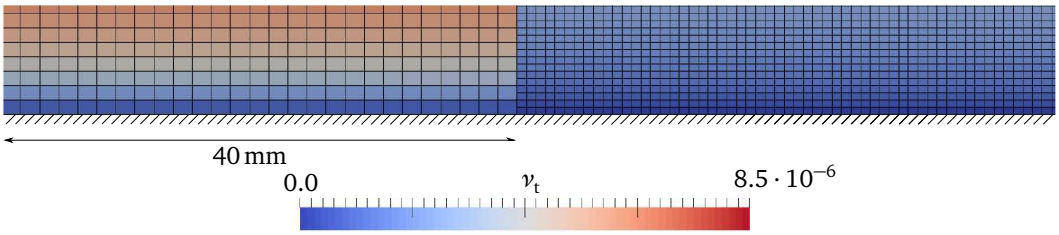

Figure 3.22: The change of the turbulent kinematic viscosity ν_t at a mesh refinement with $Re_\tau = 395$ is simulated with the $\zeta - f$-VLES model. The abrupt change is caused by a higher resolution where less turbulent viscosity is required to model the turbulence. The cell-center next to the refinement border are located at $x = 39.5\,\text{mm}$ and $x = 40.25\,\text{mm}$, respectively.

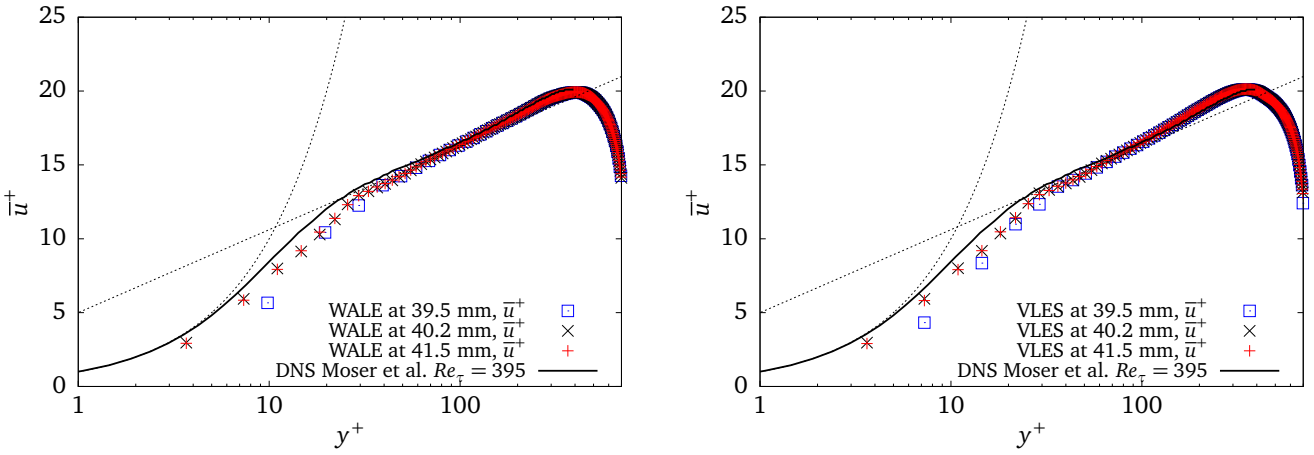

(a) WALE **(b)** $\zeta - f$-VLES

Figure 3.23: Velocity profile before, at and after a mesh refinement for $Re_\tau = 395$.

erties is investigated next.

The same settings for the domain and resolution of the test cases before are used with a Reynolds number of $Re_\tau = 395$. However, the domain is statically refined by one level from the middle of the channel at $x = 40\,\text{mm}$ up to the end. Cells in this area have half of the length width and height with respect to the base mesh.

The abruptly changing sub-grid fields, as mentioned by De Villiers, are observed at the location of the mesh size change, which is exemplarily shown for ν_t in Figure 3.22. The resolved fields are evaluated at $x = 39.5\,\text{mm}$ and $x = 40.2\,\text{mm}$ at the cell centers right before and after the refinement. Another probe is set at $x = 41.4\,\text{mm}$ since the minimum distance from the interface to a cell with another refinement level is set to 1.5 mm in this study. The averaged normalized velocity $\overline{u}^+$ of these probe locations is shown for both turbulence models in Figure 3.23. The increased mesh accuracy at the refined area results in a closer match between the normalized velocity and the DNS data, which is to be expected in the buffer and viscous sub-layer. Far from the wall the mesh resolution does not change results. Interestingly, the values in the cells right after the refinement at $x = 40.2\,\text{mm}$ are almost the same as the ones 1.5 mm or 8 cells away from the refinement leading to the conclusion, that also the resolved scales adapt rather quickly to the new mesh. The data of the averaged resolved components of the normalized Reynolds stresses $\overline{u'u'}/u_\tau^2$, shown in Figure 3.24, leads to the same conclusion.

Considering multiple refinement layers, the results for only one layer leave no doubt that the same quick adaption will take place for further refinements. Although, it is always important to keep a minimal number of buffer layers cells between refinement layers that ensure a smooth transition of flow fields. The number of buffer layers is set to ten.

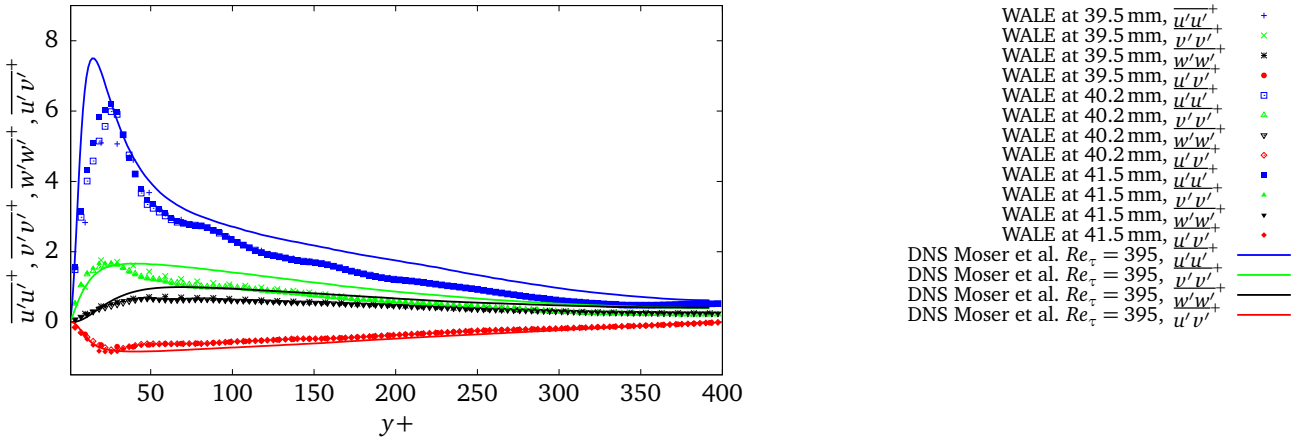

(a) WALE

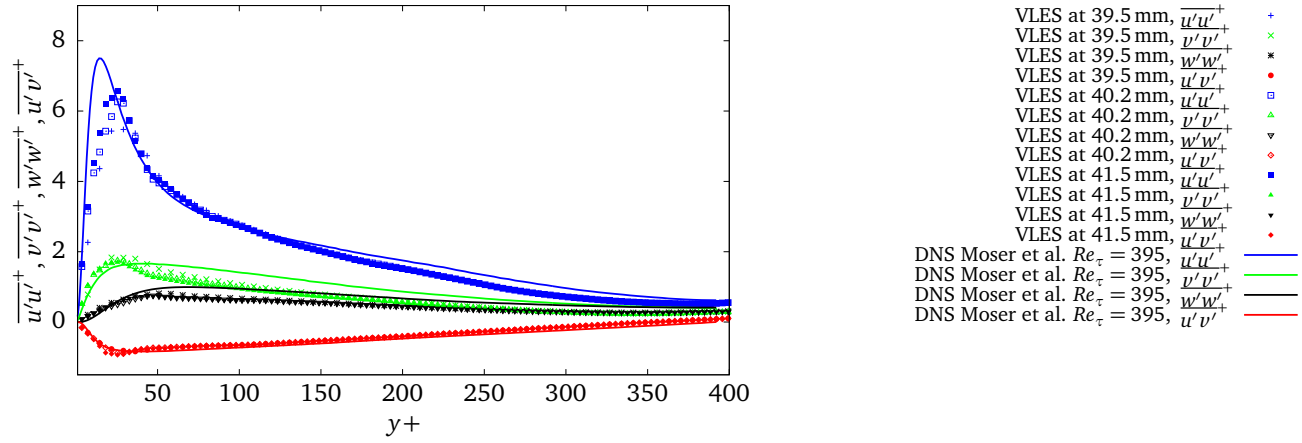

(b) $\zeta - f$-VLES

Figure 3.24: Reynolds-stress components before, at and after a mesh refinement for $Re_\tau = 395$.

The quick adaption of resolved scales after a mesh refinement approves the use of dynamic refinement in combination with the turbulence models even for multiple refinement layers. It even increases the accuracy in the region near the wall.

3.7.5 Combining turbulence models with VOF

The combination of turbulence models (not DNS) with VOF has been avoided for many years and has often been treated without the necessary diligence, mainly because of a lack of understanding and, subsequently, a lack of applicable models. In this study, RANS, VLES, LES and DNS are paired with VOF. First, the different pairings will be discussed including a short literature review. It is shown that in the specific VLES setup introduced earlier no special turbulence-interface treatment is necessary, whereas the WALE model shows nonphysical results at the interface.

RANS

Although RANS models have been steadily improved, they are not expected to give very accurate results. However, because of the high computational cost, this method is often the only option when simulating large time or length scales such as in ship and wave simulations. A few examples of RANS-VOF simulations in literature imply that no particular research focuses on turbulence at the interface in the context of RANS modeling.

- Yejun et al. (2010): evaporating oil spray: with a Re-Normalization Group $k-\epsilon$ turbulence model combined with VOF in OpenFOAM. They use additional source terms in the k and ϵ equation to account for the amount of turbulent energy that is dissipated because of the work performed on the droplets by turbulent velocity fluctuations. Unfortunately, these terms are not specified nor a validation is shown. It is expected that the influence of the fluctuations is much higher in sprays than in large drops such as those considered in this study.
- Bortolin et al. (2014): condensation in a square mini-channel using the $k-\omega$ SST model with VOF. They state that no special treatment is necessary at the interface since all scalar values are shared by both phases in the one fluid formulation.
- Vyzikas et al. (2017): oscillating water column simulated with a $k-\epsilon$ - VOF approach with no mention of special interface treatment.

Since RANS is not applied in this study at the interface, it is not necessary here to further investigate the influence of the averaged velocity fluctuations at the interface.

LES

The combination of LES with multi-phase flows is known in literature as Large Eddy Interface Simulation (LEIS). Labourasse et al. (2007), Toutant et al. (2008), Toutant et al. (2009), Liovic and Lakehal (2007) and Liovic and Lakehal (2012) provided the mathematical basis and a priori tests. By applying the filtering operation on the flow fields at the two-phase interface additional terms emerge, which are gathered in Ξ of equation (3.71):

$$\Xi = \tau_{nn,i} - \frac{\partial \tau_{tt,i}}{\partial t} - \frac{\partial \tau_{vS,ij}}{\partial x_j} \tag{3.79}$$

Additionally, the volume fraction transport equation gains a source term:

$$\frac{\partial \overline{\alpha}}{\partial t} + \frac{\partial}{\partial x_i}(\overline{\alpha}\,\overline{u_i}) = -\frac{\partial}{\partial x_i}\tau_{\alpha u,i} \tag{3.80}$$

In total one gets five unclosed sub-grid terms of which one is the already known and modeled sub-grid stress τ_{ij}^{SGS}. The remaining read as:

$$\tau_{\nu S,ij} = \overline{\nu\left(\frac{\partial u_i}{\partial x_j} + \frac{\partial u_j}{\partial x_i}\right)} - \overline{\nu}\left(\frac{\partial \overline{u_i}}{\partial x_j} + \frac{\partial \overline{u_j}}{\partial x_i}\right) \tag{3.81}$$

$$\tau_{nn,i} = \sigma\overline{n_i \kappa \delta_S} - \sigma\overline{n_i}\,\overline{\kappa}\,\overline{\delta_S} \tag{3.82}$$

$$\tau_{tt,i} = \overline{\varrho u_i} - \overline{\varrho}\,\overline{u_i} \tag{3.83}$$

$$\tau_{\alpha u,i} = \overline{\alpha u_i} - \overline{\alpha}\,\overline{u_i} \tag{3.84}$$

The diffusive $\tau_{\nu S,ij}$, and the temporal $\tau_{tt,i}$ SGS terms arise due to the discontinuity of ϱ, ν and α at the interface, which is smeared out over several cells using the algebraic Volume of Fluid method. The density ϱ as well as the kinematic viscosity ν are mixed using the volume fraction α (see equation 3.13). The diffusive term is found to be very small and can be neglected (Chesnel et al., 2011). $\tau_{\alpha,u,i}$ is the interfacial SGS term that represents the unresolved mass transfer due to filtering. $\tau_{nn,i}$ denotes the unresolved surface tension force at the phase boundary. Ketterl and Klein (2018) review all up to date interface related sub-grid scale closure models and evaluates them with explicitly filtered DNS data through correlation and magnitude analysis in the context of the multi-phase primary breakup.

However, in many recent publications the introduced errors by filtering fields at the interface are neglected, to mention a few:

- Bianchi et al. (2007): liquid jet atomization using LES with VOF. Additional sub-grid scales are neglected because of a lack of accurate models.
- Roohi et al. (2013): airfoil cavitation using LES with VOF. No consideration nor mention of the here reviewed terms.
- Moghtadernejad et al. (2015a): rivulets in shear flow using Smooth Particle Hydrodynamics with LES. No consideration nor mention of the here reviewed terms.
- Strasser et al. (2015): primary atomization of liquid jets with a dynamic hybrid RANS-LES approach in a VOF framework neglecting all sub-grid scales related to the interface since they are, still part of discussion, not always important, partially offsetting with unresolved interface curvature, often ignored and complex regarding the many other problems that have to be solved.
- Rek et al. (2017): gas jet in liquid cross-flow using LES with VOF. The unresolved surface tension is neglected following the argument by Liovic and Lakehal (2007) that the used discretization scheme is not very accurate on the sub-grid surface tension force, introducing even larger errors when sub-grid effects are considered.

On the contrary, some authors suggest that depending on the flow conditions, interfacial structures smaller than the grid size might carry a lot of momentum. The small structures naturally come with high curvatures and could have a significant effect on larger scales (Herrmann and Gorokhovski, 2009, Desjardins et al., 2010).

In this study, the additional terms are not implemented into the WALE nor the VLES model. This decision is discussed in the following. For an a-priori quantification of the error made by neglecting the terms would require a DNS which is out of scope. Furthermore, simulating Weber numbers between one and five, the surface tension is of high influence.

First, the observed length and time scales are analyzed in respect to unresolved sub-grid scales. Figure 3.25 shows a regime map for the free surface shape disturbed by turbulence. Typical length scales of the here simulated drops lie between 1 mm for the minimum drop height and 7 mm for the maximum wetting length. The typical turbulent velocity is measured as the oscillation of the drop height over time limited by 0.04 m/s. According to Brocchini and Peregrine (2001)

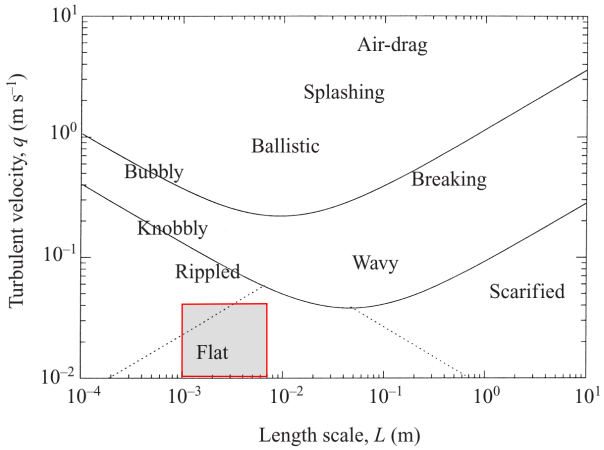

Figure 3.25: Free surface flow regimes (picture taken from Brocchini and Peregrine (2001)).

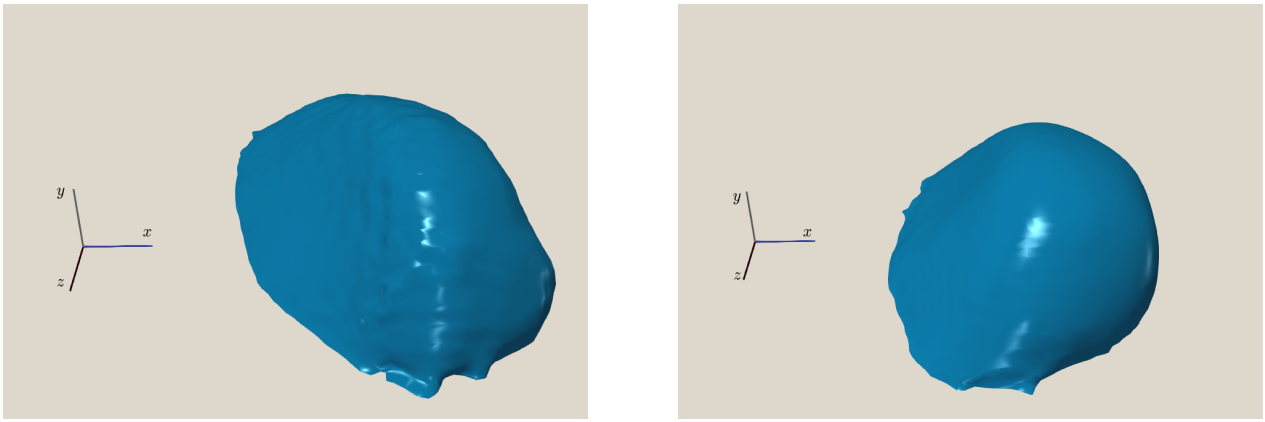

(a) WALE **(b)** $\zeta - f$–VLES

Figure 3.26: Comparison of the two-phase interface of a 25 μl drop shown in an iso-contour in turbulent channel flow with $Re = 13000$ and $\theta_{A,R} = 105°, 46°$.

the surface of the drop is expected to remain flat in the here investigated flow regimes.

The simulation of the incipient motion of a 25 μl water drop in turbulent channel flow with WALE shows unphysical dimples at the liquid-gas interface, which are shown in Figure 3.26a. They are attributed to a wrongly calculated turbulent viscosity ν_t at the highly resolved interface. The magnitude of the modeled sub-grid viscosity should vanish for a finer grid resolution down to the Kolmogorov scales. The results presented in the next sub-section suggest that the here used grid, in fact, resolves the smallest turbulent scales at the interface. The direct dependence of ν_t on the velocity gradient might not be converging at the two-phase interface far from the wall. It remains unclear if the closure of the additional emerging LES terms would help. Fact is, the turbulent viscosity ν_t is overpredicted at the interface as shown in Figure 3.27a, and is an order of magnitude higher than in the VLES framework shown in Figure 3.27b.

Regardless of the sufficient performance of the WALE model in our validation without a drop in Section 3.7.2, the unphysical turbulent viscosity leading to dimples at the interface cannot be ignored. It is to be expected, that the forces at the interface leading to dimples also act near and at the contact line, disturbing the most important area of the simulation. Therefore, an alternative turbulence model has to be chosen for further parameter studies.

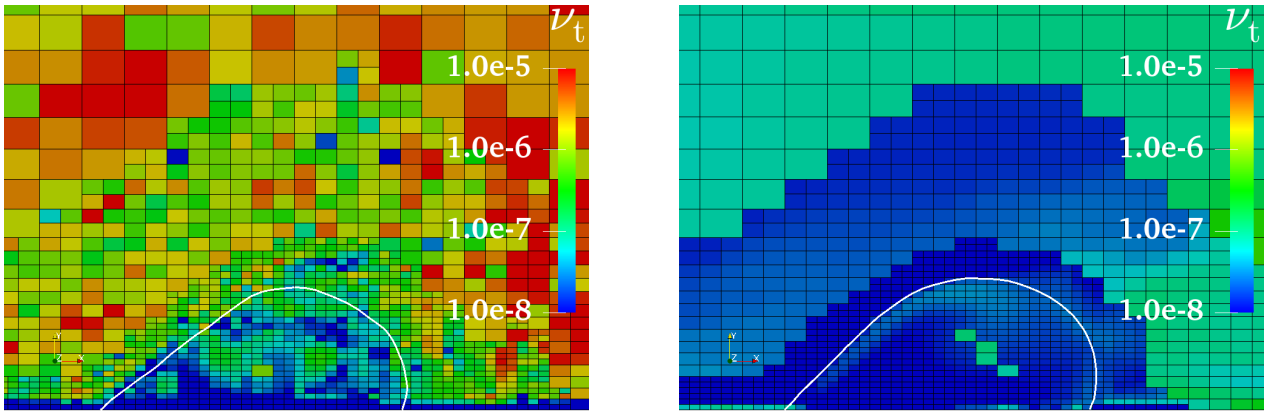

(a) WALE **(b)** $\zeta - f$–VLES

Figure 3.27: Turbulent kinetic velocity of a 25 μl drop in a turbulent channel flow with $Re = 13000$ and $\theta_{A,R} = 105°, 46°$.

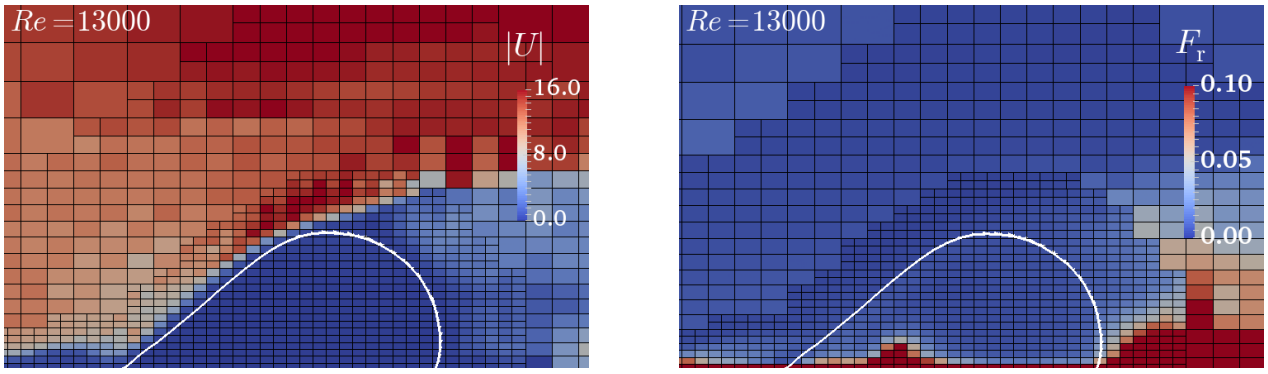

(a) Velocity profile **(b)** F_r function

Figure 3.28: The velocity profile and the blending function F_r of the $\zeta - f$-VLES model. $F_r \to 0$ DNS, $F_r \to 1$ RANS. A 25 μl drop in turbulent channel flow with $Re = 13000$ and $\theta_{A,R} = 105°, 46°$.

VLES and DNS

Up to date, the VLES method by Chang et al. (2014) was never used for multi-phase flows. However, hybrid RANS-LES models have already been used to simulate the primary atomization of liquid jets by Strasser et al. (2015). As mentioned in Section 3.7.2, they do not consider unclosed terms due to filtering at the interface. Besides that, an LES-DNS hybrid has been proposed by Herrmann and Gorokhovski (2009) and Herrmann (2010), where turbulence is resolved with LES and only interface cells are refined up to a DNS level. Thereby, the interface advected in a Level-Set approach, a so-called dual scale approach. Since in this approach only interface containing cells have DNS resolution, the missing sub-grid velocity fluctuations in the sharp transition between the LES and the DNS grid are seeded randomly at the interface.

As opposed to the sharp transition of the mesh resolution, buffer layers between mesh refinement levels ensure a better adoption of the turbulent scales to the finer grid resolution as validated in Section 3.7.4. A typical flow field around the here simulated 25 μl drop at a channel Reynolds number $Re = 13000$ is shown in Figure 3.28a. The drop moves much slower than the shear velocity, which enhances the turbulence production in the gas phase, decelerating the gas. The gas itself experiences the slow drop interface similar to a wall, at which a boundary layer forms (Liovic and Lakehal, 2007).

VLES switches to (a theoretical) pure DNS depending on the relation between the turbulent length scales and the grid resolution. The function $F_r < 0.025$ is almost zero for typical settings at the two-level dynamically refined interface, indicating a very low necessity to model sub-grid scales (see Figure 3.28b). In terms of turbulent scales, the interface is resolved with DNS where implicit LES filtering is damped to zero. Consequently, the modeled viscosity ν_t is almost zero

(Figure 3.27b), which leads to a smooth interface in contrast to the WALE model explained in the previous section, of which results are shown in Figure 3.26b. Furthermore, all additional sub-grid terms emerging due to the filtering will be negligible applying an analog reasoning.

The important results of this section are summed up in the following. Because of the seamless blending between RANS - VLES - LES and DNS the model by Chang et al. (2014) provides a high flexibility in meshing. An optimal condition to combine turbulence modeling with dynamic mesh refinement and furthermore, the option to reduce the computational cost even further than typical LES models with acceptable accuracy. Comparing WALE and $\zeta - f$-VLES the quality of both models is almost identical in simulations without drops or rivulets (see Section 3.7.4), whereas the VLES model is about 10% more efficient using identical meshing, while being more robust to time-step restrictions. At the two-phase interface the WALE model leads to unphysical dimples in contrast to $\zeta - f$-VLES. These reasons lead to the decision for VLES over WALE for all further parameter studies.

3.8 Summary of the simulation procedure and final model selection

The numerical framework developed in the present study consists of submodules featuring physical models as well as high-performance techniques. All of them are validated separately as well as in combination with cases of increasing complexity. This section gives an overview of the solver in which the different models are selected during run-time according to the simulation case specifics given by the user. The final model selection is summarized and further details on the simulation process are presented.

The `interFoam` solver is based on FVM and enables the simulation of two phases with an implicit interface using the VOF method. This solver is significantly enhanced with libraries that plug in seamlessly into the structure of `interFoam`. Features of `interFoam` have been abstracted to allow additional models e.g. for the interface handling while also maintaining basic functionality to fall back to the original `interFoam` code. A walkthrough of one simulation time step will summarize the different enhancing models and will explain their dependency (see Figure 3.29).

Assuming the simulation is already running on several processors, the incremental time step is adjusted to its maximum, which is restricted by the Courant number separately in the bulk flow and at the interface by the capillary wave stability criterion. If AMR or DLB is set, a time interval can be selected after which adaptive mesh refinement and re-balancing is performed. With multiple possible refinement criteria, the target refinement level of each cell is calculated, which also includes the specified buffer layers between refinement levels. If the target cell levels differ from the current, cells are (un)refined according to the domain boundaries in 3D, 2.5D or 2D. The surface and volume fields are mapped onto the new mesh. If DLB is selected, the number of cells on each processor is compared and the imbalance calculated. If the imbalance exceeds an user specified threshold a new decomposition is created. Using the refinement history as a constraint to ensure refined sibling cells to remain on the same processor, any decomposition method can be selected. In this study, the only the `hierarchical` decomposition method is used. All fields are then distributed according to the new decomposition. With the named bug-fixes in Section 3.2.1 and 3.2.2, the necessary flux correction reduces to a minimum.

The α equation (3.13) is solved ensuring a sharp interface with a counter-gradient compression scheme. In this study, the advection and compression of the volume fraction α is calculated exclusively with the MULES algorithm, because of its laxer time step restriction compared to other compressive advection schemes. To increase accuracy, the transport equation is solved in two sub-cycles in combination with the implicit Euler scheme, which is selected for the interpolation in time. For the turbulence simulations, the Crank Nicholson scheme is selected for which no sub-cycling is possible due to implementation restrictions in OpenFOAM.

All cells within a near band to the interface are first selected by either the gradient or the direct value of the volume fraction α. For long simulation times, the author recommends the gradient method, since over time, small amounts

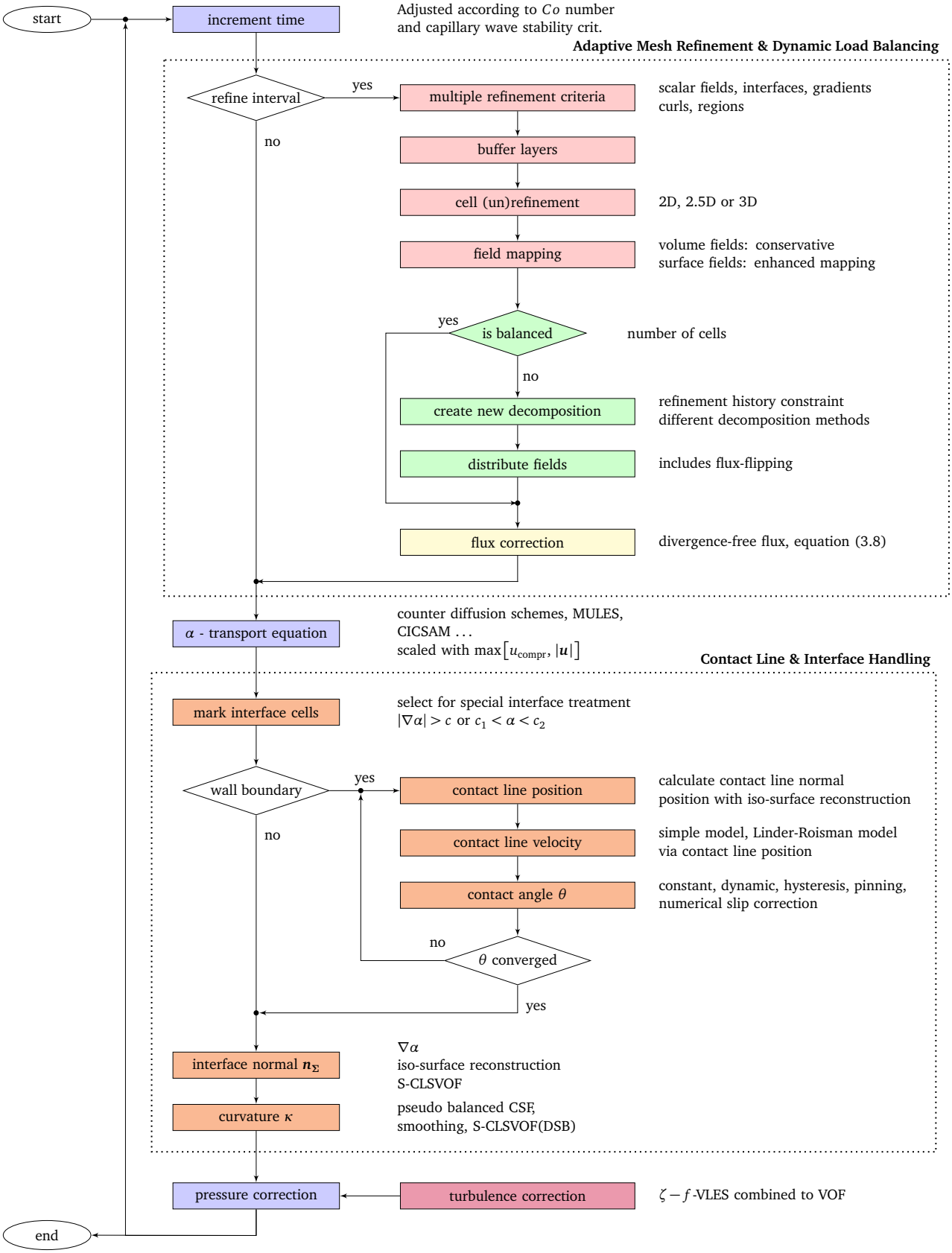

Figure 3.29: Flowchart of the `interFoamExtended` solver with user selectable models regarding high-performance techniques such as Adaptive Mesh Refinement and Dynamic Load Balancing, enhanced interface and contact line handling, as well as a turbulence model fit for multi-phase flows within the VOF method.

of the volume fraction $\alpha < 10^{-6}$ || $\alpha > (1 - 10^{-6})$ tend to smear out over the whole simulation domain even though a counter-gradient compression is used. In cells adjacent to a wall boundary the contact line normal is calculated. If selected, the contact line position is explicitly extrapolated using the iso-surface reconstruction algorithm and the contact angle. Because of the contact angle dependency on the velocity and the dependency of the velocity on the contact line position, an iterative correction is mandatory. The contact line velocity can be calculated in three ways as presented in Section 3.5.2. The `LinderRoisman` model has been found to work best with the necessary mixed α boundary condition to realize the pinning of the contact line for contact angles within the contact angle hysteresis. Besides the constant contact angle, a variety of dynamic models are implemented of which the Kistler (1993) model is found to work best for the here investigated length scales. To trigger rivulet meandering, a statistical contact angle variation can be applied which is inspired by the description of a rough surface. The contact angle correction to reduce mesh dependency of the contact line motion (Afkhami et al., 2009) cannot be applied straight-forward with the mixed boundary condition of Linder et al. (2015), and thus it is not selected in further simulations of this study.

The target contact angle applied at the wall and the interface will adjust in the next time-step via the surface tension force. The interface normal can be calculated either via the gradient of the volume fraction $\nabla\alpha$, the iso-surface reconstruction or a Level-Set VOF hybrid called S-CLSFVOF. The choice of the model dictates the application of the curvature model as well. The iso-surface reconstruction was found to be the most appropriate choice for unstructured meshes and is used in the following.

The velocity and pressure fields are strongly coupled in the continuity and momentum equations. To solve these, the *Pressure Implicit with Splitting of Operators* (PISO) method is used, which has been developed by Issa et al. (1986). In the PISO loop, an intermediate velocity field is first calculated via the momentum equation using the currently known fields. With the intermediate velocity a new pressure field is calculated via the continuity equation. The new pressure field is in turn used to calculate the velocity. Iterating these steps leads to a converging solution. The converged solution is then used for the calculations within the next time step. This short explanation may encourage further reading additional literature, e.g. in Schäfer (2006) or Hirsch (2007). Within the PISO loop the turbulent fields are calculated. Two models have been compared in combination with VOF. The WALE turbulence model shows unphysical turbulent viscosities at the interface leading to dimples, whereas the $\zeta - f$-VLES model yields a smooth interface as observed in experiments. The $\zeta - f$-VLES turbulence model shows similar accuracy in single field simulation compared to the WALE model and is, in addition, much more flexible due to its mesh dependent turbulence modeling that bridges seamlessly between RANS, LES and DNS.

To complete the description of the numerical setup, it shall be mentioned that a *Preconditioned Conjugate Gradient* (PCG) solver is used with a multi-grid preconditioner *Geometric Algebraic Multi Grid* (GMAG) to solve the linear algebraic equations of the form $\boldsymbol{A} \cdot \boldsymbol{x} = \boldsymbol{b}$. These solvers are well explained in Saad (2003).

4 Drops and rivulets wetting tilted plates

For simulations with contact angle hysteresis and contact line pinning, drops wetting tilted plates serve as a basic validation test-case, before increasing the complexity by introducing shear flow in the next chapter. Several experiments of drops and rivulets on tilted plates in literature will be compared with simulation results. Both, the incipient motion of drops and the evaluation of fast-moving drops that form a cornered receding contact line shape, show good agreement with experiments, which paves the way for simulations of rivulets running down inclined plates. Rivulets tend to meander in a certain range of volume flow rates. Simulations in this range show similar meander characteristics to cases in literature. A novelty is the simulation of sliding and corner forming drops, as well as the simulation of meandering rivulets, both using the VOF method and including the contact angle hysteresis.

4.1 Incipient motion

To understand the incipient motion of drops on tilted surfaces a closer look at the force balance is given. A sessile drop on a horizontal plate forms the equilibrium contact angle θ_e. By slowly tilting the plate, the contact line of the drop remains pinned and the drop shape adapts with the tilting angle (see Figure 4.1a). The contact angles at the highest and the lowest point of the drop form the minimum and the maximum contact angles θ_{min} and θ_{max}. The difference in both angles results in a so-called adhesion force, which counteracts the weight pulling the drop down. Both forces are in equilibrium up to a critical tilting angle β_{crit} where the contact angles match the characteristic receding and advancing contact angles, $\theta_{min} = \theta_R$ and $\theta_{max} = \theta_A$. In a quasi-static case, at this point, the maximum adhesion force is reached and further tilting leads to the incipient motion of the drop.

The maximum adhesion force acting on the drop at the critical tilting angle can be derived theoretically from a force balance. Frenkel (1948) and Dussan V. and Chow (1983) considered two-dimensional drops for which the adhesion force can be written as

$$F_{ad,max} = \sigma R k(\cos\theta_{min} - \cos\theta_{max}), \tag{4.1}$$

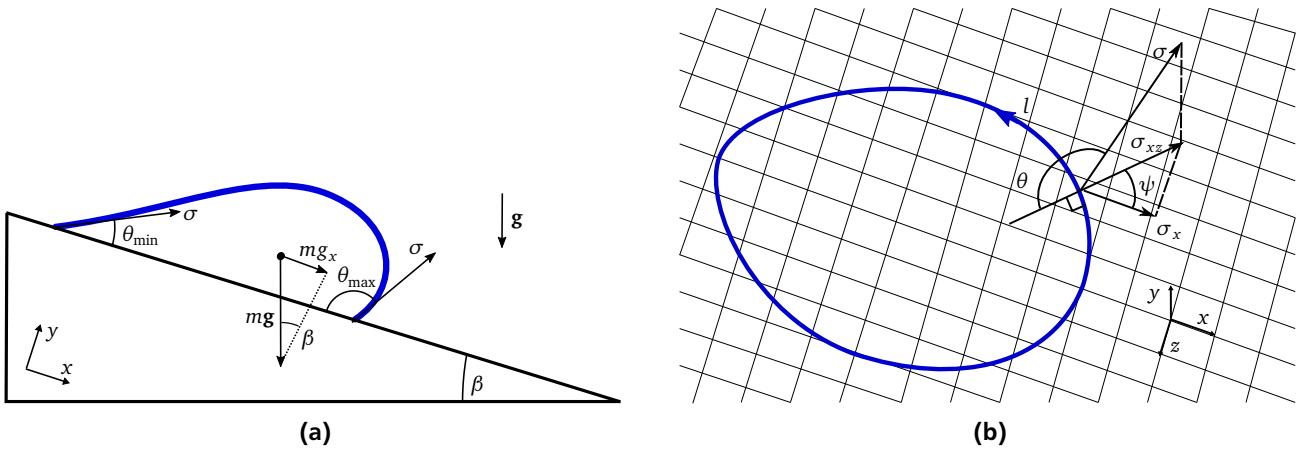

Figure 4.1: a) Profile of a drop on an inclined surface under the influence of gravity, and the adhesion force due to surface tension. b) View on the contact line with the normal direction that encloses the angle ψ with the x-axis, and the surface tension vector by $\boldsymbol{\sigma}$. The surface tension vector is projected on the xz-plane and on the x-axis (Antonini et al., 2009).

where R is the length of the drop footprint on the tilted plate and k an adjustable parameter measured in experiments (Pierce et al., 2008, Antonini et al., 2009). The force balance up to the critical tilting angle can be written as

$$m\boldsymbol{g}\sin\beta = \sigma R k(\cos\theta_{\text{min}} - \cos\theta_{\text{max}}) \tag{4.2}$$

with the drop mass m and a gravitational acceleration $\boldsymbol{g}\sin\beta$ in x-direction g_x. Similar to a static friction force the adhesion force always counteracts the disequilibrating force. Even though the formulation does not account for the three-dimensional shape of the contact line, it is also used in three dimensions calibrating k accordingly. In literature, the angles θ_{min} and θ_{max} are often considered to be the characteristic receding and advancing contact angles θ_{R} and θ_{A}, respectively, defining the contact angle hysteresis.

In three dimensions, the adhesion force is the integrated interfacial tension σ, which acts at the contact line for arbitrary contact line shapes as an integrated surface tension projected here in x-direction according to Figure 4.1b (Antonini et al., 2009)

$$\mathrm{dF_x} = \sigma_x \,\mathrm{d}l\,, \tag{4.3}$$

$$F_{\text{ad}} = F_x = \int_0^L \sigma_x \,\mathrm{d}l = -\sigma \int_0^L \cos\theta(l)\cos\psi(l)\,\mathrm{d}l\,. \tag{4.4}$$

The angle ψ is defined by the x-axis and the contact line normal, which in this case points into the gas phase (see Figure 4.1b). The component of the adhesion force in y-axis is absorbed by the rigid surface and is therefore negligible in contrary to drops on soft matter. Drops on tilted surfaces tend to form axis-symmetrical shapes because of which a resulting force in the z-direction is not considered.

To measure the characteristic advancing and receding contact angles, the setup of drops on tilted surfaces is used in experiments since Bikerman (1950). Both angles are essential as boundary conditions for numerical simulations which date back to Brown et al. (1980). For an overview for experimental studies we refer to Maurer et al. (2016). A selected literature overview focusing on simulations of drops on inclined plates is given in Table 4.1.

Most of the studies listed in Table 4.1 have used a surface optimization tool such as Surface Evolver, which is suited only for studying quasi-static problems. For dynamic cases such as drops rolling on tilted planes, one has to resort the conventional techniques such as interface tracking or interface capturing schemes. VOF is one of the commonly used interface capturing method for studying multi-phase flows. So far, Dupont and Legendre (2010) used VOF in two dimensions and limited to a structured mesh. In this study, the motion on the tilted plate is studied in three dimensions. The method adopted to realize pinning is an extension of an earlier work by Linder et al. (2015).

From a numerical point of view, two major challenges have to be dealt with using the framework of this study. First, parasitic currents lead to inaccuracies of the velocity field near the interface introducing a slight oscillation of the interface especially in quasi-static setups. The advancing and receding contact angle might be exceeded leading to an unphysical local pinning or de-pinning of the contact line. Because of the quasi-static drop scenario, the time step is limited by the parasitic currents via the Courant number limitation. The here used iso-surface reconstruction introduced in Section 3.4.2 reduces the parasitic currents significantly by about one order of magnitude which is essential for this type of simulation. Second, the diffusion of the interface becomes problematic for long simulation times of a static drop as discussed in Section 3.3. This diffusion is counteracted using a minimum compression scaling velocity.

Literature	Dim.	Methodology	Note
Brown et al. (1980)	3D	Surface mesh in spherical coordinates with a Galerkin-FEM	Prescribed contact line position
Iliev (1997)	3D	Surface mesh with FEM minimizing the potential energy of the drop with step by step virtual displacements	The position of the contact line is no longer prescribed
Dimitrakopoulos and Higdon (1999)	3D	Surface mesh with the spectral boundary element method minimizing the free surface energy	Only quasi-static solutions possible
Dupont and Legendre (2010)	2D	Structured staggered mesh with the VOF method in the JADIM framework	Accounts for drop motion and a dynamic contact angle
Chou et al. (2012)	3D	Surface Evolver, a tool based on the liquid-induced defect model	Only quasi-static solutions
Prabhala et al. (2013)	3D	Surface Evolver	Focusing on drop shapes on horizontal and vertical surfaces only
Janardan and Panchagnula (2014)	3D	Surface Evolver	Only quasi-static solutions
Semprebon and Brinkmann (2014)	3D	Surface Evolver	Only quasi-static solutions
Bommer et al. (2014)	2D	Lattice Boltzmann Model	Also investigates on structured surfaces.
Linder et al. (2015)	3D	VOF method on an unstructured mesh in OpenFOAM	Accounts for drop motion and a dynamic contact angle
Lippert (2016)	3D	VOF method on structured mesh	Several pinning strategies, no extensive parameter study for tilted plates
This study	3D	Unstructured mesh with the VOF method using an iso-surface reconstruction to improve the surface tension accuracy.	Similar to Linder et al. (2015), with reduced parasitic currents

Table 4.1: Literature overview of the simulation of incipient motion of drops on tilting plates.

4.1.1 2D drop on a tilting plate

Increasing the level of complexity step by step, the numerical framework is first validated for incipient motion of a drop with the 2D cases suggested by Dupont and Legendre (2010), who compare their critical tilting angle with theoretical results of Dussan V. and Chow (1983). A hemicircle drop with a diameter of $D_0 = 5.4\,\mathrm{mm}$ is initialized with a density of $\varrho_\mathrm{L} = 1000\,\mathrm{kg/m^3}$, a viscosity $\mu_L = 10^{-2}\,\mathrm{Pa\,s}$ and the surrounding gas with $\varrho_g = 1\,\mathrm{kg/m^3}$ and $\mu_G = 2.1 \times 10^{-2}\,\mathrm{Pa\,s}$. The drop is resolved with about 90 cells per initial diameter. The Bond number $Bo = \varrho_\mathrm{L} g (D_0/2)^2/\sigma$ calculates to $Bo = 0.5$, 1.0 or 2.0 for different surface tensions $\sigma = 0.036\,\mathrm{N/m}$, $\sigma = 0.072\,\mathrm{N/m}$ and $\sigma = 0.144\,\mathrm{Nm/m}$ and a gravitational acceleration of $g = 9.81\,\mathrm{m/s^2}$. For each of the three surface tensions, a simulation with the contact angle hysteresis of $(\theta_\mathrm{A}, \theta_\mathrm{R}) = (100°, 80°)$, $(120°, 60°)$ and $(140°, 40°)$ is performed. The plate is tilted by $\dot{\beta} = 5.625°\mathrm{s}^{-1}$ as suggested by Linder et al. (2015). Linder (2015) also elaborates on different mesh resolutions and the initial shapes of the drop for which he finds an indifferent point of incipient motion.

Figure 4.2a shows the position of the receding and advancing contact line for an increasing tilting angle and three different contact angle hysteresis pairs. The larger the contact angle hysteresis, the longer the contact line remains pinned. The receding and advancing contact lines start to move independently. The critical contact angle is measured at the time both contact lines moved further than $80\,\mu\mathrm{m}$ which is of the order of the cell width.

The critical tilting angle of all surface tension and hysteresis pairs are shown in Figure 4.2b. They are in very good agreement with the static theory (equation 4.2). Even the two configurations with high surface tension and large hysteresis stay pinned as expected up to a tilting angle of $\beta = 90°$. Comparing the simulation results with those published by Linder et al. one can observe an overall improvement mainly due to the iso-surface reconstruction which reduces parasitic currents by improving the interface curvature estimation (see Section 3.4).

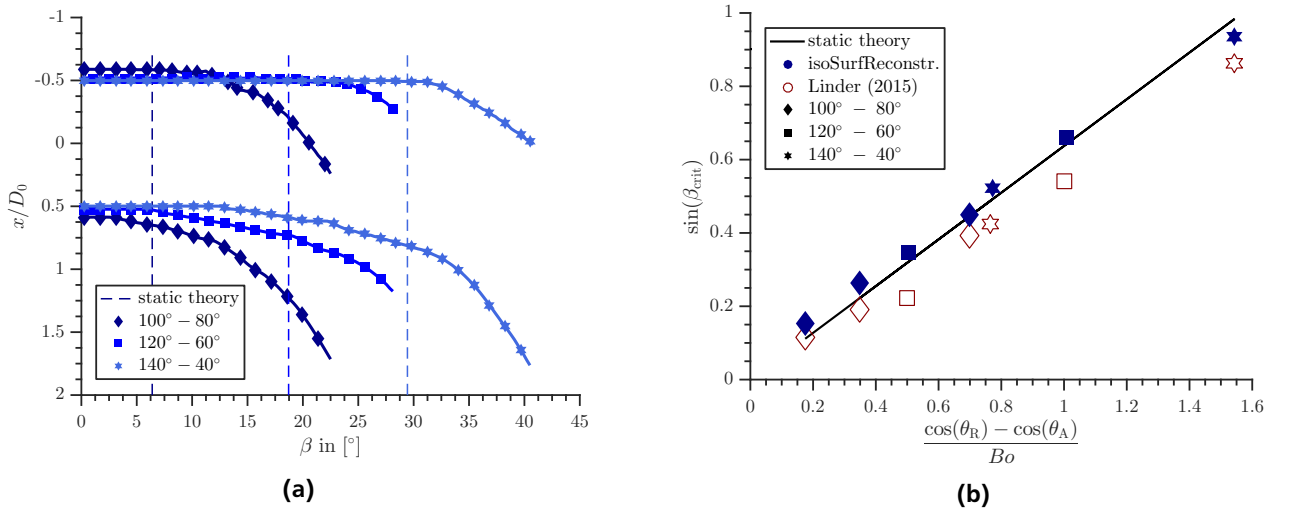

Figure 4.2: a) Advancing and receding contact line of a simulated 2D drop on a tilting plate with a surface tension of $\sigma = 0.036\,\mathrm{N/m}$ and three contact angle hysteresis pairs. The critical tilting angles for incipient motion by the static theory of Dussan V. and Chow (1983) are marked. b) Comparison of the critical tilting angle with static theory and the simulations by Linder et al. (2015) (empty symbols) and simulations of this study using the iso-surface reconstruction technique (filled symbols).

4.1.2 3D drop on a tilting plate

In this section, we increase the complexity by simulating the tilted drop case in three dimensions. The comparison of the experiments of Pierce et al. (2008) and Bommer et al. (2014) with simulation results validates the numerical framework in three dimensions. The drop is initialized as a spherical cap with radius R_0 specified by the given volume V and initial contact angle θ_I

$$R_0 = \left(\frac{3V}{\pi(1-\cos\theta_\mathrm{I})^2(2+\cos\theta_\mathrm{I})} \right)^{(1/3)} . \tag{4.5}$$

The diameter of the drop's contact line can be calculated as

$$L_\mathrm{b} = 2R_0 \sin(\theta) \tag{4.6}$$

and the height of the drop as

$$H_0 = R_0(1-\cos(\theta)) . \tag{4.7}$$

To save computational resources the interface is dynamically refined by two levels down to a resolution of $\Delta x = 50\,\mu\mathrm{m}$. The inclination angle rate is set to $\dot{\beta} = 5.625°/\mathrm{s}$ by changing the direction of the gravitational acceleration $g = 9.81\,\mathrm{m/s^2}$. The liquid and material properties are used as provided in Table 4.2.

The definition of the critical tilting angle for incipient motion is controversially discussed in literature. Several different ways are followed, e. g. a minimum distance threshold has to be surpassed by the receding and the advancing contact line (Milne, 2013), which is a robust and easily measurable value. Because of the stick-slip contact line motion, Linder et al. (2015) suggest the last tilting angle for which both angles are pinned at the same time. However, this characterization is very much dependent on the temporal resolution and therefore not practical. A more complex method is suggested here, which considers the last angle at which the force balance of adhesion and mass hold. Experimentally, this approach is rather difficult since for an evaluation of the adhesion force the local contact angle of each point of the contact line is to be measured. This kind of measurements is possible with an experimental setup shown in Antonini et al. (2009), that has a camera rotating on the tilting plane around the drop. In simulations, on the contrary, such local measurements are easily accessible. The critical tilting angle measured with the distance threshold method $\beta_{\mathrm{crit,d}}$ and the force balance

	Liquid	Surface	σ [N/m^2]	θ_A [°]	θ_R [°]	θ_I [°]	Vol [μL]	Exp. β_{crit} [°]	Sim. $\beta_{crit,d}$ [°]	Sim. $\beta_{crit,F}$ [°]
Pierce et al. (2008)	Water	Silicon	0.0728	128 ±0.2	115 ±0.2		20	14.8 ±1.7	14.1	15.1
							30	12.2 ±1.6	11.1	11.5
							40	9.0 ±1.3	9.4	9.0
							50	8.0 ±1.2	8.5	8.4
							60	7.5 ±1.1	7.5	7.6
							70	6.5 ±1.0	6.7	6.1
Bommer et al. (2014)	Water	OTS monol.	0.0728	110.9	102.0	104.9	10	20.4	19.1	17.6
		OTS monol.	0.0728	110.6	101.9	104.7	20	13.2	12.5	11.4
		OTS monol.	0.0728	112.4	95.8	104.7	50	8.9	13.4	12.7
	Ethylene	OTS monol.	0.0484	86.0	76.9	83.4	10	15.3	15.4	15.4
		OTS monol.	0.0484	86.1	76.3	82.5	20	12.8	10.8	10.3
		OTS monol.	0.0484	87.8	73.3	83.5	50	7.8	8.9	8.6
	Ethylene	OTS + plasma	0.0634	37.0	20.6	27.3	10	26.2	19.4	22.2
		OTS + plasma	0.0634	37.7	16.7	27.3	20	18.9	15.2	21.5
		OTS + plasma	0.0634	36.1	16.2	27.2	50	14.1	9.1	12.0

Table 4.2: The critical tilting angle comparison between experiments and 3D simulations of incipient motion of drops on tilting plates. The surface used by Bommer et al. (2014) is an octadecyltrichlorosilane monolayer, which is exposed to oxygen plasma in three of the cases.

$\beta_{crit,F}$ are compared in Table 4.2.

Figure 4.3a shows the motion of the contact line position in dependence of the tilting angle for a 10 μl ethylene drop on a plate with an OTS mono layer surface as measured by Bommer et al. (2014). Furthermore, the calculated mass force and the adhesion force both increase over time up to a point where the adhesion force is surpassed. In this case, the critical tilting angles measured via the distance threshold method and the critical force balance method are in line. However, it is important to mention that the adhesion force measurement is a result of post-processing and therefore, not as accurate as the contact line position. Overall, this method yields good results with a maximum difference to the distance threshold of about 2°.

Contact angle measurements are known to be very demanding due to the many influential parameters of all involved materials and the measuring procedure, which is carefully investigated by Pierce et al. (2008). Their well defined and controlled setup yields reproducible measurements of very high accuracy. Water drops of different volumes are placed on a horizontal silicon plate which is then inclined over time. The distance threshold is set to be 250 μm, for which the simulated critical tilting angles are in very good agreement with the experimental data. All critical angles lie within the rather small accuracy tolerance of the experiments.

Bommer et al. (2014) measured the contact angle hysteresis of different substrates and various liquids of which a selection is given in Table 4.2. The differing measurements of their advancing and receding contact angle for one liquid-solid pair with changing drop volumes give reason to the assumption that these measurements are not statistically averaged since the advancing and receding contact angle are purely material parameters and should not depend on the drop volume. The biggest hysteresis discrepancy between different drop volumes and the same solid-liquid pair is $\Delta\theta_R = 7.9°$. Because of the ever-present difficulties in contact angle measurements, this is still an acceptable accuracy often found in similar literature. The simulations are within an error of ±3° very close to the experimental results with an exception for the 50 μl drops. The simulations are nonetheless in line with the differing contact angle hysteresis. The measurement quality is visualized in Figure 4.4. The data of Pierce et al. is linearly interpolated and taken as a reference for the results of Bommer et al. (2014). Direct comparison of both experiments is valid assuming a similar shape of the contact line, which is not accounted for in this representation.

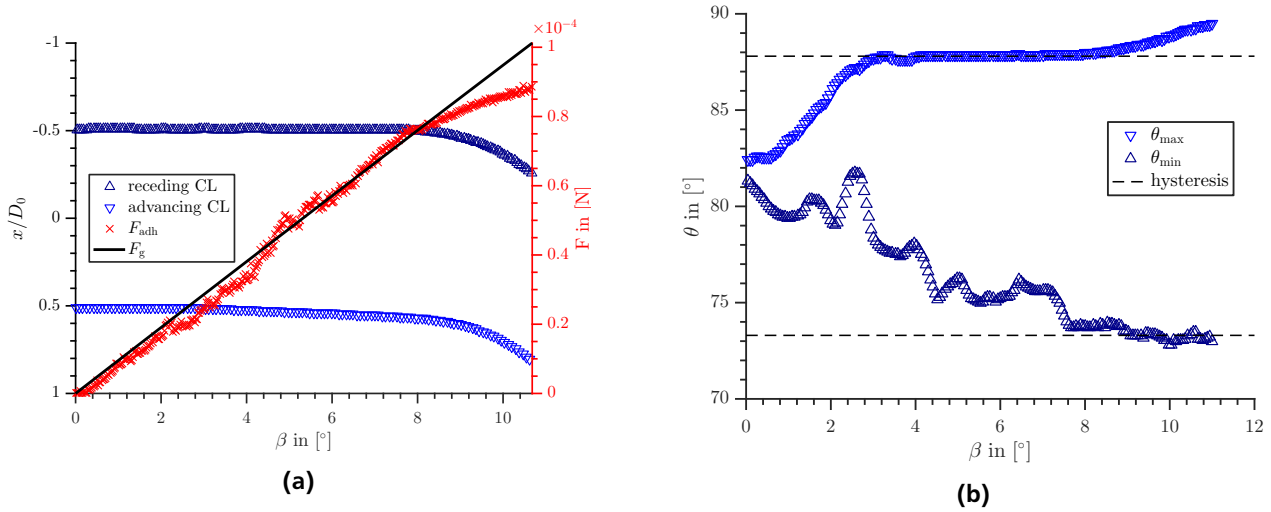

Figure 4.3: Simulation results of the incipient motion of a 50 μl Ethylene Glycol drop on an OTS monolayer as described by Bommer et al. (2014). a) Contact line position over a tilting angle for a critical tilting angle of $\beta = 8.9°$ measured when the front and rear contact line position moved a distance of 250 μm. The adhesion force is surpassed by the increasing mass force at $\beta = 8.6°$. b) Dependence of the contact angles at the advancing and receding front on the tilting angle. The drop starts to move when both contact angles exceed the contact angle hysteresis.

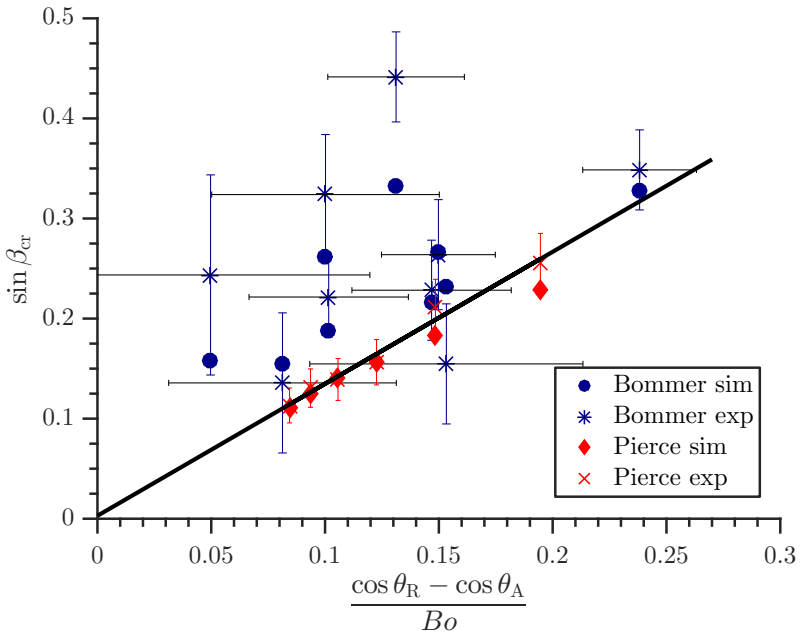

Figure 4.4: Critical tilting angles for the incipient motion of drops with different liquids, volumes and on a variation of surfaces. Experimental results of Pierce et al. (2008) and Bommer et al. (2014) are compared to simulation results. The measurement tolerance of contact angle experiments is critical for a good comparison with simulation results. The solid line is a linear approximation of the experimental results by Pierce et al. (2008).

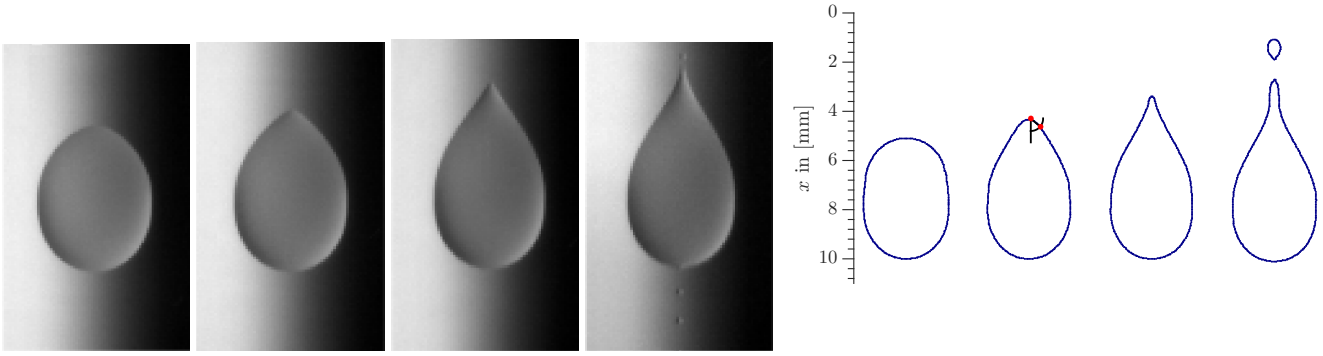

(a) Experimental results of a sliding drop on a tilted plate for a variety of constant inclination angles. (pictures from and experiments by Podgorski (2000)).

(b) Simulation results using an increasing tilting angle β at the rate of $\dot{\beta} = 5°/\mathrm{s}$. The contact line shape is shown for different time steps that correspond to increasing tilting angles.

Figure 4.5: Shape of a PMMA drop ($V_D = 6\,\mu\mathrm{l}$; $\nu = 10.68\times10^{-6}\,\mathrm{m}^2/\mathrm{s}$) sliding down a glass plate ($\theta_{\mathrm{A,R}} = 55°, 45°$). For an increasing Capillary number, from left to right, the contact line shape changes from spherical to oval and, then, to a rounded corner at the rear of the drop. The rounded corner forms to a cusp eventually emitting smaller droplets.

To conclude, the exceptional accordance of the simulation data with the experiments of Pierce et al. (2008) validates the here used framework for the incipient motion of drops on tilted plates. Considering the measurement uncertainties of Bommer et al. (2014), the simulation results are as well promising for different liquid-solid pairs. Post-processing of the adhesion force is verified and the definition of the critical tilting angle via the force balance of mass and adhesion forces is found to be valid.

4.2 Cornered drops

After studying the incipient motion of a drop, the continuous motion of a drop on tilted plates is analyzed in this section. Even though sliding drops are often found in nature and in industrial processes such as coating, this setup received much less attention than the critical tilting angle for incipient motion. Podgorski et al. (2001) show experiments of millimeter-sized drops sliding down for different tilting angles and observe a transition from almost spherical contact lines to oval or elliptical shapes. The aspect ratio increases with the Capillary number. At a critical Capillary number Ca_{cr} a corner forms at the rear of the drop. For even higher Capillary numbers these corners transform to cusp tails emitting smaller drops. All regimes are also observed in simulations of which snapshots of contact line shapes for an increasing Capillary number are shown in Figure 4.5.

The experiments of Podgorski et al. have been revisited by Le Grand-Piteira et al. (2005) and the contact line shape is modeled in the different regimes by Snoeijer et al. (2007) and Ahmed et al. (2014) and simulated by Thiele et al. (2002) as well as Schwartz et al. (2005), all of which used models based on long-wave or lubrication approximations. A variational method is proposed by Xu et al. (2016) to describe the temporal change of the contact line shape. Engelnkemper et al. (2016) simulate three-dimensional droplets employing a thin-film equation and analyzes relevant eigenmodes of the pearling regime. Maglio and Legendre (2014) simulated the incipient motion and sliding drops on inclined solids based on VOF in the research code JADIM. This study differs by using an unstructured underlying mesh and a different model to account for the contact angle hysteresis (see Section 2.4.2). The most recent related publication by Solomenko et al. (2017) uses the level-set method to capture the interface and recovers all drop shape regimes from an oval contact line to pearling in experiments. This study aims to validate the models involved in contact line motion and sets the possibility of further investigations on cornered drops and the transition to drop breakup and forming of rivulets.

In the experiments of Le Grand-Piteira et al. (2005), PDMS drops with a kinematic viscosity of $\nu = 10.68\times10^{-6}\,\mathrm{m}^2/\mathrm{s}$, a density of $\varrho = 936\,\mathrm{kg/m}^3$, a surface tension of $\sigma = 0.201\,\mathrm{kg/s}^2$ and a contact angle hysteresis of $\theta_{\mathrm{A,R}} = 55°, 45°$ slide down an inclined glass plate. This case is simulated with a linearly increasing inclination angle of $\beta = 10°$ up to $\beta = 70°$.

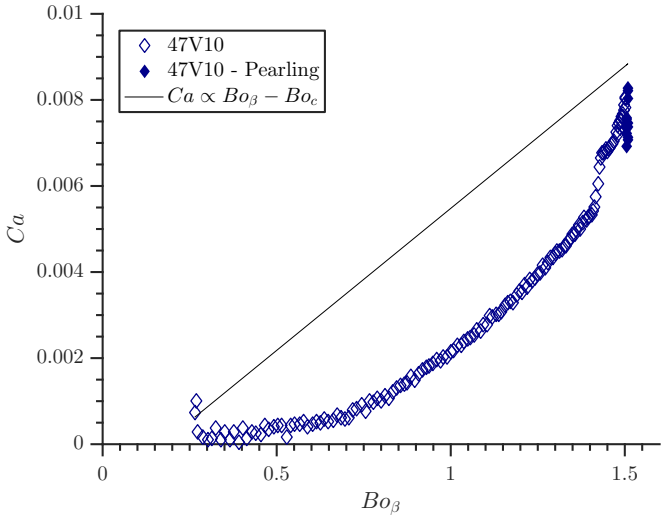

Figure 4.6: Simulated drop velocity over the inclination Bond number similar to the experiments by Le Grand-Piteira et al. (2005). The simulation is performed with increasing tilting angle $\dot{\beta} = 5°/s$ versus different but constant tilting angles in experiments. The drop acceleration apparently plays a significant role in the simulations.

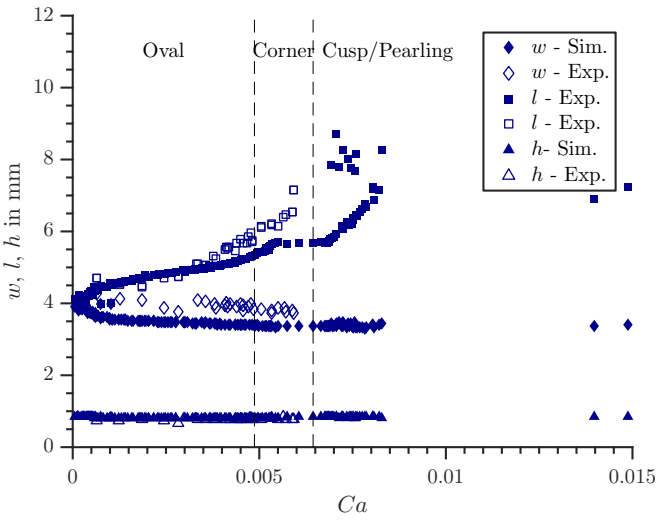

Figure 4.7: The drop shape measured in terms of height, width and length for an increasing drop velocity. The experimental and simulation results are of similar character.

Single experiments are performed at a constant inclination angle whereas in the simulation a tilting rate of $\dot{\beta} = 5°/s$ is used to cover the whole Ca range in one simulation. The drop is refined in three levels down to $\Delta x = 50\,\mu$m. Note that in this section the Capillary number is calculated using the global drop velocity instead of the local contact line velocity.

The drop velocity and the plate inclination can be expressed in terms of the Capillary number and the Bond number. Three forces act on the drop in quasi-static motion: a viscous drag on the glass plate, the interfacial forces and the weight of the drop. They scale with $-\eta U V^{1/3}$, $-\sigma V^{1/3}\Delta$ and $\varrho V g \sin\beta$ respectively. The Bond number based on the component of gravity parallel to the tilted plate is defined as $Bo_\beta = Bo \sin\beta = V^{2/3}\rho g/\sigma$. Figure 4.6 shows the Capillary number over the inclination Bond number Bo_β. Le Grand-Piteira et al. suggest a scaling law as a result of a force balance

$$Ca \propto Bo_\beta - Bo_c\,, \tag{4.8}$$

where Bo_c is a constant depending on the wetting hysteresis $\Delta\theta$ given by Dussan V. (1985) as

$$Bo_c = \left(\frac{24}{\pi}\right)^{1/3} \frac{(\cos\theta_R - \cos\theta_A)(1+\cos\theta_A)^{1/2}}{(2+\cos\theta_A)^{1/3}(1-\cos\theta_A)^{1/6}}\,. \tag{4.9}$$

The comparison of the scaling law with the simulation results indicates that the drop acceleration due to the continuous tilting rate of $\dot{\beta} = 5°/s$ still has a strong influence. Consequently, a much lower tilting rate would be recommended for a quantitative comparison to the experiments.

Despite the differences in the case setup, a comparison of the drop geometry is still insightful. In Figure 4.7, the length L, width W, and maximum drop height H are compared with experimental results. The drop height stays almost constant for increasing Capillary numbers and the drop width decreases slightly, whereas the length of the drop almost doubles reaching a maximum before the breakup of the droplet at the cusp.

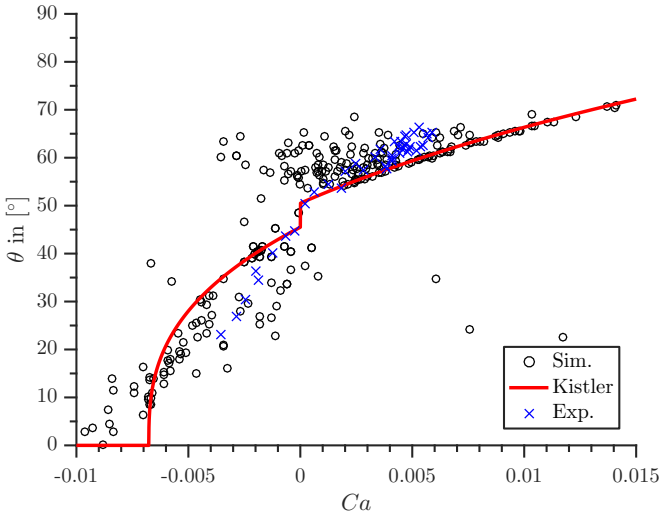

Figure 4.8: Comparison of dynamic contact angle distribution using the Kistler model (see equation 3.43) in simulations and experimental measurements.

The dynamic contact angle model by Kistler (1993) used in simulations leads to contact angles at the receding contact line down to zero for high receding Capillary numbers as described in Section 2.4. The contact angles are shown in Figure 4.8. This stands in contrast to a finite contact angle found in experiments by Le Grand-Piteira et al. of $\theta_{\text{min}} = 21°$.

The formation of the corner at the rear end of the drop was first explained theoretically by Blake and Ruschak (1979), where they postulate that a maximum receding contact line speed Ca_{cr} exists. When Ca_{cr} is exceeded, the contact line inclines to maintain the speed normal to the contact line constant at the maximum contact line speed

$$Ca = \frac{Ca_{\text{cr}}}{\sin\phi}\,, \tag{4.10}$$

wherein ϕ is defined between the drop motion direction and the tangent of the contact line. This speed normal to the contact line increases with the drop speed and plateaus at an almost constant level while forming a corner. This behavior is recovered in simulations shown in Figure 4.9 as well as in experiments.

In simulations, the tangent of the contact line is estimated by two points, of which one is defined at the rear tip of the drop. The tip serves as the center of a circle with radius 0.5 mm which cuts the contact line in the second point, as indicated in Figure 4.5. To define the beginning of the corner regime, a threshold of $\sin\phi > 0.98$ is set which coincides well with the transition shown in Figure 4.9 as well as Figure 4.10. In the corner regime, the dependence of ϕ is proportional to $1/Ca$ law as already suggested by Podgorski et al. (2001).

A transition between the corner and the cusp regime is naturally set at $\phi = 45°$ which is in line with the saddle point corner tip description by Amar et al. (2001). Differently to Podgorski et al., Le Grand-Piteira et al. suggested a separate cusp and pearling regime distinguishable not only by the emitted small drops but also by the Capillary number. In simulations, however, the drop slows down when emitting droplets which is in accordance with the reduced mass of the main drop. In contrary to the simulations, the experiments are fed with new drops at a frequency of 0.5 Hz, such that the main drop collects the droplets from the predecessor drop.

To summarize, in our simulations all regimes shown in experiments by Le Grand-Piteira et al. (2005) are recovered. The simulation setup expands the experimental results by an increasing tilting angle to cover a wide range of Capillary numbers versus many quasi-static experiments with fixed tilting angles. Because of an additional drop acceleration in the simulation, the transitions from an oval to a corner and from a corner to a cusp-shaped contact line appear for higher

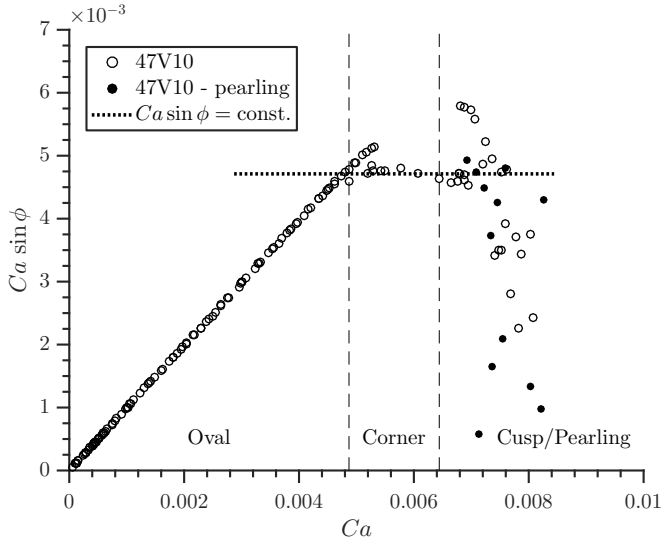

Figure 4.9: The simulated contact line velocity in drop motion direction remains almost constant in the corner regime.

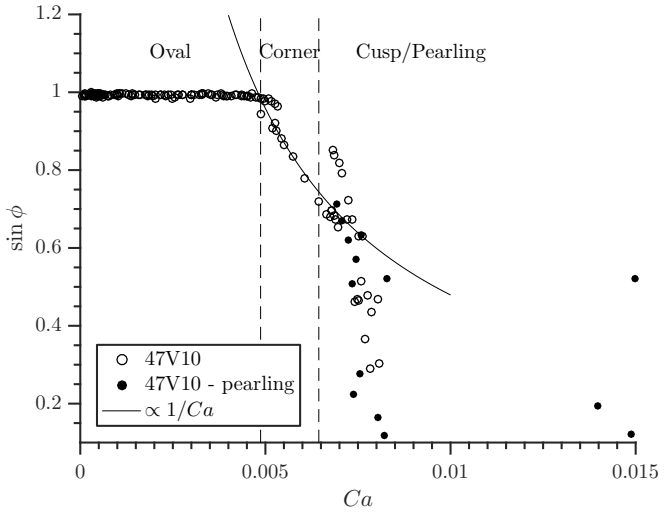

Figure 4.10: The contact line corner opening angle ϕ experiences a sharp transition in the corner regime in order to keep the Capillary number of the receding contact line constant.

Capillary numbers. Despite the setup difference, the constant plateau of $Ca \sin\phi$ is comparable and in line with the theoretical maximum receding speed postulated by Blake and Ruschak (1979). Also, the aspect ratio of the drop is similar to experiments. These observations lead to the conclusion that the receding motion of the contact line, in particular, is well described by this computational framework. Unlike shown in experiments, the pearling regime is not distinguishable from the cusps regime via the Capillary number, because of the differences in the setup.

As this study focuses on the drop motion in turbulent shear flow, the insight on the validity of the receding contact line motion is sufficient for this study. However, a further detailed investigation by simulations of the transition from corners to cusps and the break-up of droplets might be as well insightful. Moreover, it would help to understand the formation of rivulets from large drops.

4.3 Meandering rivulets

Rivulets form in many circumstances under partial wetting conditions. They can emerge from a tail of a moving drop, from a thin film or simply due to a steady stream of liquid. As often observed on vehicle surfaces while driving in rain, drops merge on surfaces and form a film. Under the influence of shear forces and gravity these films form rivulets. With this motivation, rivulets are investigated, yielding a better understanding of the formation of rivulets and their motion. These findings are also vital to understand sediment transport in rivers or in trickle bed reactors and structured packings (Herrada et al., 2015). In this section, the formation of rivulets is investigated considering a steady stream on a tilted surface. In experiments by Culkin and Davis (1982), Nakagawa and Scott (1984) and Le Grand-Piteira et al. (2006), different regimes are found for an increasing volumetric flux $\dot{Q}$ and increasing tilting angle.

- Individual drops: the volumetric flux is not sufficient to form a closed rivulet.
- A straight rivulet: forms along the direction of the steepest descent.
- Meandering rivulet: Above a critical volumetric flux $\dot{Q}_\mathrm{m}$ the straight stream becomes unstable. Perturbations are triggered by surface defects, injection-noise, or air movement and amplify laterally and downwards on the plate. After some time the rivulet path becomes stable. A typical meandering rivulet path is shown in Figure 4.11.

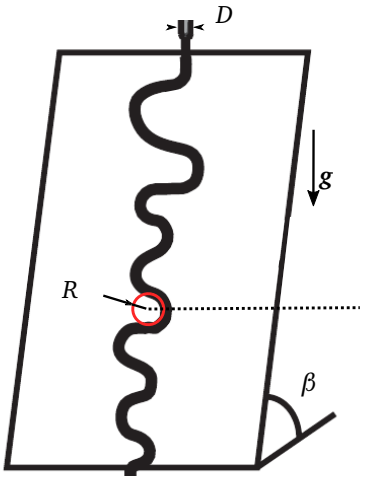

Figure 4.11: Experimental setup used by Le Grand-Piteira et al. (2006). The inflow nozzle has a diameter $D = 1\,\text{mm}$ and the tilting angle β is varied between $9° < \beta < 90°$. The plate is covered with Mylamar with contact angles of $\theta_{A,R} = 70°, 35°$.

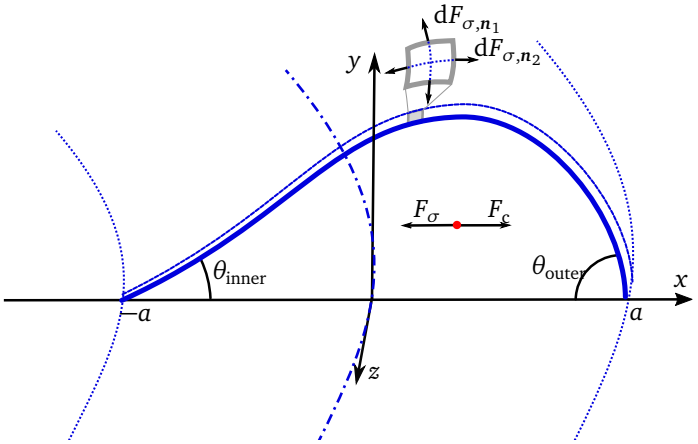

Figure 4.12: Cross-section of a meandering rivulet. The asymmetry of the rivulet is due to a balance between the inertial force F_c and the surface tension force F_σ that consists of two components: one due to the curved shape of the cross-section and the other due to the curved rivulet path. Furthermore, the adhesion force due to the difference of the inner and outer contact angles is a reacting force that counteracts the motion of the contact line.

- Dynamic meandering: Above a second critical volumetric flux $\dot{Q}_{dm}$ the rivulet path remains unstable even after a settling time of 24 hours as described by Le Grand-Piteira et al. (2006).
- Restable regime: the inertia of the volume flow dominates and no meandering is found. The shape of the rivulet is not straight but forms braids.

To understand quasi-static meandering, a force balance of adhesion force, surface tension, and gravity as shown in Figure 4.12 is to be considered. The surface tension scales with the curvature, which varies in the cross-section and along the longitude of the rivulet. It tries to minimize the surface of the rivulet targeting a symmetrical cross-section and a straight rivulet path. The adhesion force is a reactive force restricting the motion of the contact line. In a curved rivulet, centrifugal forces depend on the volumetric flux and counteract the surface tension and adhesion forces. Couvreur and Daerr (2012) propose a force balance of a rivulet cross-section which includes these forces and is able to predict the transition from the straight rivulet regime to the static meandering regime by increasing the volumetric flux. However, Fathi et al. (2014) claim that assumptions made by Couvreur and Daerr have substantial deficits, albeit proposing a final form. As the critical conditions for a transition between the meandering regimes are still under discussion, the reader is referred to the literature cited above.

Even though the experimental setup for meandering rivulets on tilted plates is rather simple (see Figure 4.11), many influential parameters must be controlled very carefully. To give some examples from preliminary investigations that led to the presented study, a dependence on the rivulet inflow geometry, an oscillatory volume inflow, and a statistical contact angle distribution have been found. In literature, several groups show that small perturbations, as well as the flow history, influence the rivulet path (Nakagawa and Scott, 1984, Daerr et al., 2011, Couvreur and Daerr, 2012, Fathi et al., 2014). The dependence on the flow history is easily accessible in a thought experiment. The flow rate of a *straight* rivulet is increased to form a *stable meandering* path and then reduced again to the flow rate of the beginning. The rivulet still follows the stable meandering path even though the reduced volume flow rate would correspond to a straight meandering path. The adhesion force restricts the contact line to remain immobile.

Literature on simulations of rivulets is very sparse since an accurate description of the different regimes is either trivial for straight rivulets or rather demanding for meandering rivulets. Simulations of meandering rivulets require models for the dynamic contact lines and contact line pinning. Ramaswamy et al. (1997) simulated the formation of rivulets

from a heated film using the Finite Element Method, including temperature-dependent surface tension. Moghtadernejad et al. (2015a) simulated rivulets fed from a hole in the wall of a channel with turbulent flow. Moghtadernejad used the Smoothed Particle Hydrodynamic technique for numerical simulations and compared results with experiments. Meredith et al. (2011) simulated rivulet formation from a thin film with a specific thin 2D film model. Iso and Chen (2011), Cooke et al. (2012) and Singh et al. (2016) also simulated the rivulet formation from a film with the VOF method and a constant contact angle model. Their goal is to improve the CO_2 absorption in packed columns by delaying the formation of rivulets using surface structures and thereby increasing the wetted area by a closed thin film. Rivulet breakup is studied in Singh et al. (2017), who show pictures of meandering rivulets simulated with a dynamic contact angle model. So far in the literature there is no numerical study focusing on the effects of contact line pinning to recover quasi-static meandering paths.

Rivulet cross-section of a straight rivulet

Duffy and Moffatt (1995) present an analytical solution of a rivulet cross-section which is valid within the straight rivulet regime. According to them, a Bond number

$$Bo_\mathrm{r} = a\sqrt{\frac{\varrho\, g\,|\cos(\beta)|}{\sigma}} \tag{4.11}$$

can be introduced for which the rivulet height reads as

$$h_\mathrm{r}(z) = \tan(\theta)\sqrt{\frac{\sigma}{\varrho\, g\,|\cos(\beta)|}}\,\frac{\cosh(Bo_\mathrm{r}) - \cosh\left(Bo_\mathrm{r}\frac{z}{a}\right)}{\sin(Bo_\mathrm{r})}\,. \tag{4.12}$$

Thereinf, the half of the rivulet width is denoted as a and is measured in z-direction as shown in Figure 4.13. The analytical solution serves as a first point for validation. According to this analytical solution, the theoretical rivulet shape is given as an inlet boundary condition of $a = 3\,\mathrm{mm}$, a constant contact angle $\theta_\mathrm{e} = 60°$ and a plate tilting angle of $\beta = 60°$. The resolution at the rivulet is $\Delta x = 150\,\mu\mathrm{m}$ and the cross-section is evaluated after $T = 1\,\mathrm{s}$ with a distance of $d = 70\,\mathrm{mm}$ downstream the inlet. The simulation result matches the analytical solution very well.

Straight, quasi-static meandering and dynamic meandering

To compare experiments by Le Grand-Piteira et al. (2006) with simulations, the setup shown in Figure 4.11 is discretized with a domain $48 \times 6 \times 250\,\mathrm{mm}^3$ and refined at the rivulet interface in five levels down to a cell size of $\Delta x = 100\,\mu\mathrm{m}$. Different from the previous setup, the rivulet is initialized with a spherical inlet with a diameter of $D = 1\,\mathrm{mm}$. The surface is reported to have advancing and receding contact angles of $\theta_\mathrm{A} = 70°$ and $\theta_\mathrm{R} = 35°$. The volumetric flow rate $\dot{Q}$, as well as the inclination angle β, are chosen to recover three regimes: straight, meandering and dynamic meandering with flow rates of $\dot{Q} = 0.8,\ 1.2,\ 2.5\,\mathrm{ml/s}$ and tilting angles of $\beta = 9°,\ 20°, 32°$, as shown in Figure 4.14.

Figure 4.15 shows the evolution of a rivulet in the straight regime. At the circular inlet a so-called braid forms, where gravity flattens the rivulet. The rivulet flows down the plate completely straight. After a short time, the perturbation caused by numerical inaccuracies near the inlet triggers the meandering instability. Further down the plate, the path straightens again, which is also observed in experiments by Le Grand-Piteira et al. (2006). If a meandering path is established, the adhesion force due to the contact angle hysteresis counteracts the surface tension force, which tries to straighten the path again. For the chosen boundary conditions, a meandering wavelength of about $\lambda = 4\,\mathrm{cm}$ and a meandering radius of about $R_c = 1.3\,\mathrm{cm}$ is observed in experiments, which matches the simulated rivulet path very well.

This exact effect should be recovered by the volume rate and plate inclination used in the simulations of Figure 4.16. Other than in the straight regime, the amplitude of the meandering path grows far from the inlet, which indicates the

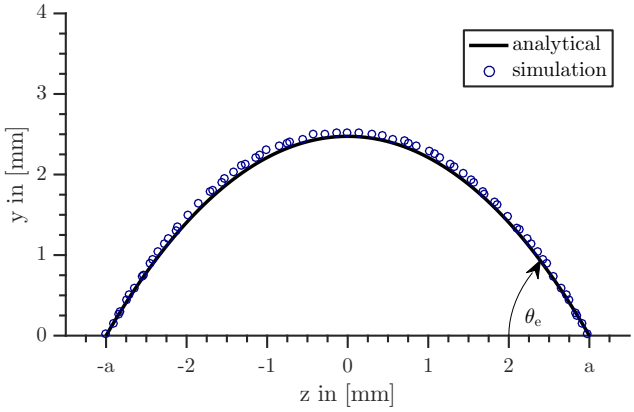

Figure 4.13: Comparison of an analytical (Duffy and Moffatt, 1995) rivulet cross-section of a straight rivulet to simulations. The constant contact angle is $\theta_e = 60°$, the inclination angle $\beta = 60°$ and the rivulet half-width $a = 3\,\text{mm}$.

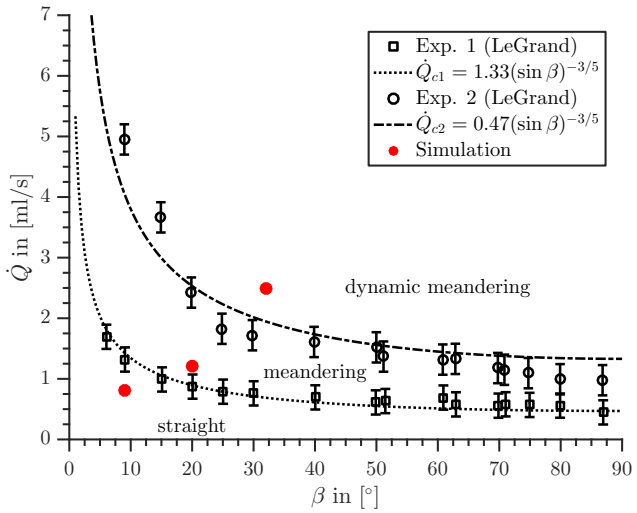

Figure 4.14: Rivulet regimes in experiments with $\theta_{A,R} = 70°, 35°$ by Le Grand-Piteira et al. (2006) for an increasing flow rate $\dot{Q}$ and an inclination angle β: straight - no meandering, static meandering state which is eventually reached after up to 24 hours, dynamic meandering - the rivulet path changes constantly.

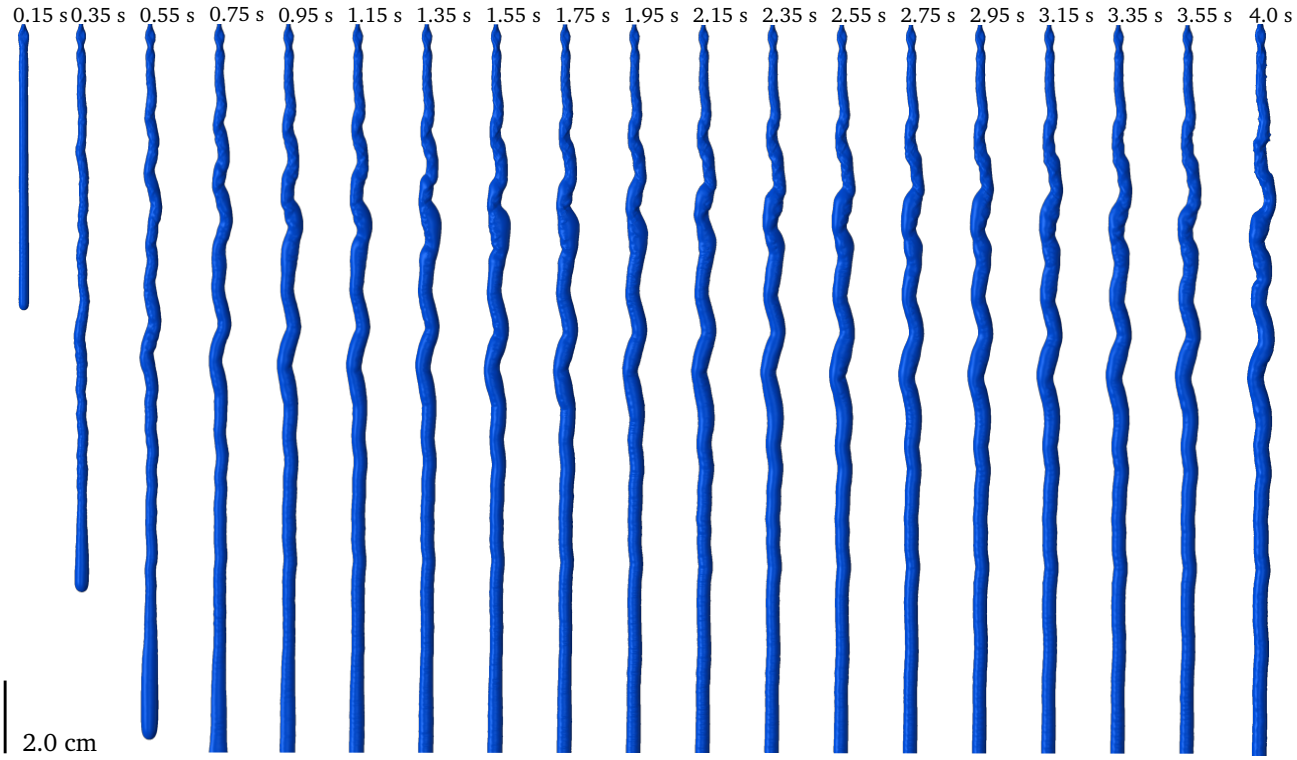

Figure 4.15: Simulated rivulet evolution on a plate with an inclination angle of $\beta = 9°$ and a constant flow rate of $\dot{Q} = 0.8\,\text{ml/s}$. The perturbation at the inlet, caused by small numerical errors, induces a static meandering path with very small amplitude. The meandering is dampened and the rivulet continues straight, which matches well with the experimental observations by Le Grand-Piteira et al. (2006).

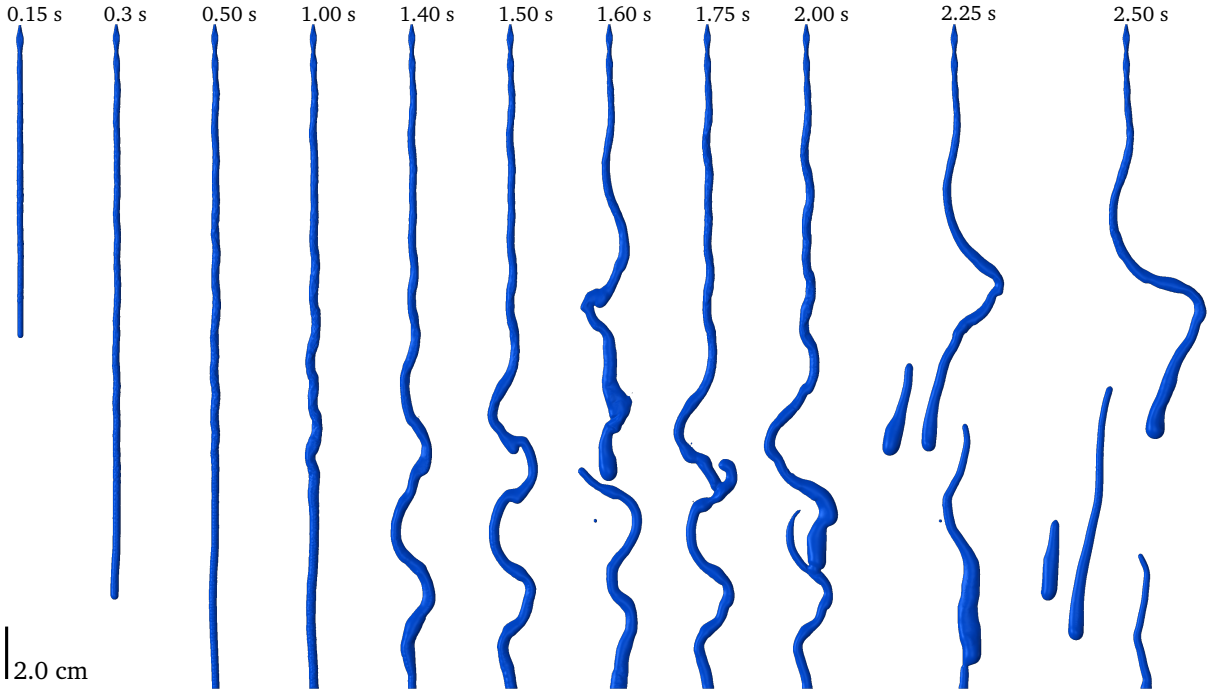

Figure 4.16: Rivulet evolution on a plate with an inclination angle of $\beta = 20°$ and a constant flow rate of $\dot{Q} = 1.2\,\mathrm{ml/s}$. From an initially straight rivulet, an instability shapes a dynamic meandering path with growing amplitude. Exceeding a certain radius the rivulet breaks up, to find a new path. The dynamic rivulet will at some point find a quasi-static path, which in experiments by Le Grand-Piteira et al. (2006) is observed after up to 24 hours.

existence of a more natural evolving path. The meandering amplitude grows over time until exceeding a case-specific threshold at which point the rivulet forms a second path. While the flow rate of the original path decreases, the new path forms a nose, which due to gravity follows a straighter path down the plate. Eventually, the leftover of an old path is crossed, where both merge again, to follow the already established older path. Experiments show that in the static meander regime the meander path will become quasi-static after up to 24 hours. Naturally, computational resources limit the simulation time. However, the static meander path of the case shown in Figure 4.15 gives reason to believe that a quasi-static path would be established after some more simulation time. For the chosen boundary conditions a meandering wavelength of about $\lambda = 6.5\,\mathrm{cm}$ and a meandering radius of about $R_c = 1.6\,\mathrm{cm}$ is observed in experiments, which matches the simulated rivulet path very well.

A much more dynamic rivulet is shown in Figure 4.17. First, a much longer braid is observed after the inlet, which is followed by another smaller one. The higher flow rate makes the inertial forces dominant compared to the previously described rivulets. The meandering path is observed to be much more dynamic, showing an increasing meandering wavelength and many breakups occur, leaving old paths behind. In experiments, no quasi-static meandering path could be observed even after 24 hours. For the chosen boundary conditions no experiments have been performed. Extrapolating the trends given in Le Grand-Piteira et al. (2006), a wavelength of about $\lambda = 17\,\mathrm{cm}$ and a radius of about $R_c = 3.6\,\mathrm{cm}$ are to be expected.

To sum up, the theoretical rivulet cross-section described by Duffy and Moffatt (1995) are matched very well by simulations. Furthermore, all three regimes described in experiments by Le Grand-Piteira et al. (2006) are recovered in simulations, even though the simulation time is rather limited due to computational costs. The accurate description of rivulets on tilted plates in general will serve as a basis for future investigations on rivulets in cross-flow. Experimental and numerical references of rivulets in shear flow are given by Marshall and Ettema (2004), Tivert et al. (2007), Cheverda et al. (2013), and Herrada et al. (2015).

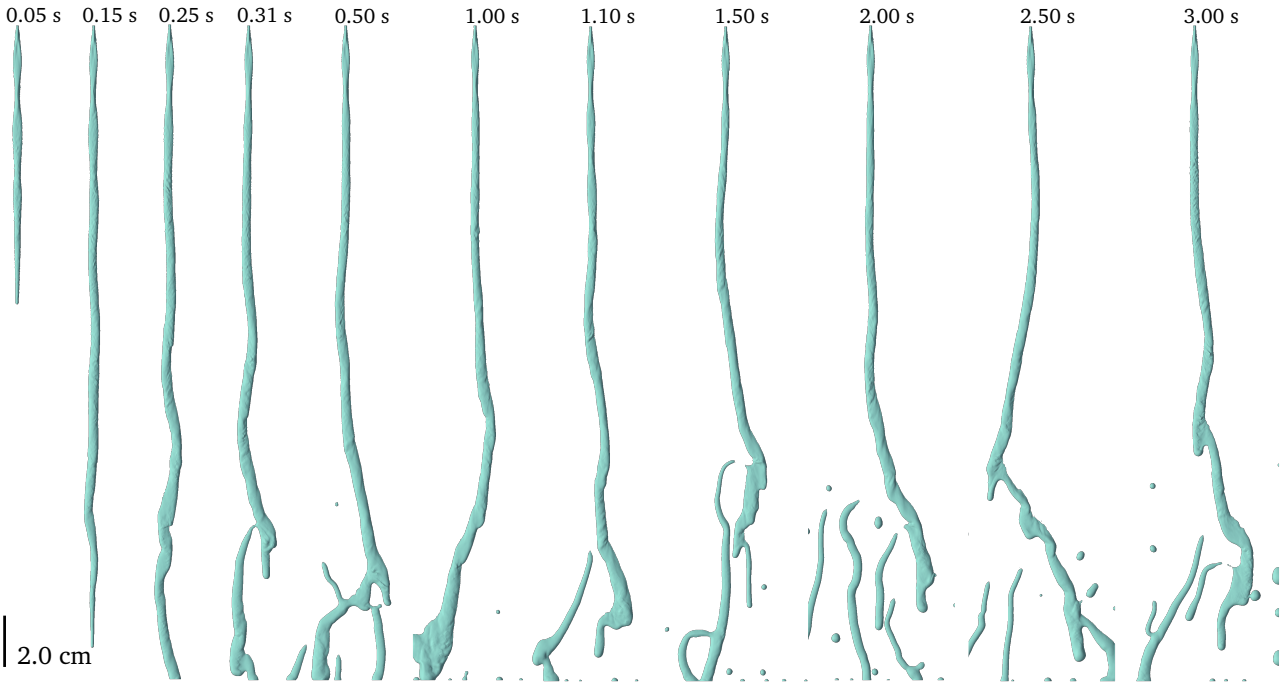

Figure 4.17: Rivulet evolution on a plate with an inclination angle of $\beta = 32°$ and a constant flow rate of $\dot{Q} = 2.5\,\mathrm{ml/s}$. The rivulet path meanders dynamically as described in experiments by Le Grand-Piteira et al. (2006).

4.4 Summary

The nature of the adhesion force to act similar to a friction force has been shown for drops on tilted surfaces. At a critical inclination angle, an incipient motion of the drop is observed in experiments. The simulations of such cases in 2D and 3D using the numerical framework introduced in Chapter 3 show improved results to previous work by Linder et al. (2015) and match experiments very well, which validates the pinning boundary condition by Linder once again. Thereby, it has been shown that accurate measurements of advancing and receding contact angles in experiments are of utmost importance.

Experiments of a drop sliding down a tilted plate by Le Grand-Piteira et al. (2005) are compared with simulations to validate the continuous motion of the advancing and receding contact line. At a certain drop speed, a small sliding drop changes its receding contact line shape from oval to a corner, with a finite curvature. As observed by Blake and Ruschak (1979), the speed of the receding contact line has a limit. By changing the receding contact line shape forming a corner, the velocity normal to the contact line is maintained constant. Consequently, the corner opening angle decreases with increasing drop velocity. At a threshold of about 45° the corner transforms into a cusp, which eventually emits droplets at even higher velocities. All these regimes are recovered in simulations performed in this study. Larger drops might form a crescent-shaped receding contact angle or even more complex shapes. Large drops sliding down a plate can leave a rivulet trace.

Rivulet dynamics are studied next. The theoretical shape of a rivulet cross-section described by Duffy and Moffatt (1995) has been compared with simulations with a very promising match. The evolution of rivulets on tilted plates are categorized by Le Grand-Piteira et al. (2006) among others into a straight, a quasi-static meandering and a dynamic meandering regime. Simulations using the VOF method that recover all three regimes are a novelty, as far as known to the author. This might be due to the necessity of an accurate description of the surface tension force, the contact angle hysteresis and a contact line pinning model in combination with a highly efficient calculation for which the enhanced AMR and DLB are essential. As a proof of concept, rivulets in all three regimes are simulated with a very good agreement to experiments.

5 Forced wetting of drops in shear flow

This study encompasses the simulation of drops and rivulet motion in turbulent channel flow. First, the incipient motion is investigated, in both, laminar and turbulent shear flow to establish references for the validation of the numerical framework with and without turbulence. The simulation results of incipient drop motion are compared to experiments and to a theoretical approach, with a very good agreement. Then the oscillation of droplets is described. Finally, the interaction of drops with complex geometry is exemplarily shown for drops crossing a microchannel oriented perpendicular to the drop motion. The microchannel width is varied and the simulation results are compared to experiments.

5.1 Incipient motion

Similar to the incipient motion on a tilting plate, a wall-bounded drop in shear flow starts moving if the adhesion force $\boldsymbol{f}_{\mathrm{adh}}$ is overcome by the shear/drag $\boldsymbol{f}_{\mathrm{s}}$ force, assuming the absence of net body forces on the drop (no drop oscillation and gravity balanced by normal surface reaction (Milne and Amirfazli, 2009)). Simple models will be compared to simulation results in Section 5.1.4. In general, the height of the drop with respect to the velocity boundary layer δ is of importance to model the shear force.

In contrast to experiments, simulations allow a direct measurement of the shear force on the drop surface. Taking advantage of the iso-surface reconstruction algorithm introduced in Section 3.4.2, the shear force projected in x-direction is calculated in a post-processing step as

$$F_{\mathrm{s}} = \sum_{c}^{N_{\mathrm{cell}}} \left[p_c S_{\Sigma,c} - \sigma \kappa_c \nabla \alpha_c V_{\mathrm{cell}} \,\mathrm{pos}\left(S_{\Sigma,c} - \epsilon\right) \right] \boldsymbol{e}_x \,. \tag{5.1}$$

The pressure force pS_Σ is calculated with the surface area S_Σ of the reconstructed iso-surface, which is non-zero only in cells that include the volume fraction value of $\alpha = 0.5$. The pressure jump at the interface due to the surface tension is comparable in magnitude with the dynamic pressure due to shear forces at the point of incipient motion. Since the interface is smeared out over a few cells, small inaccuracies in the iso-surface reconstruction might lead to improper integral values of the shear force. Furthermore, the exact values of the pressure are only known at cell centers. Therefore, the surface tension volume force calculated with the CSF method (see Section 3.4) is subtracted from the total pressure force $p_c S_{\Sigma,c}$ only in cells containing parts of the reconstructed interface.

5.1.1 Laminar shear flow

Drops in laminar shear flow can be found for low Reynolds numbers or for small drops within the viscous turbulent sublayer. An accurate description of drops in laminar shear flow is a mile-stone to tackle turbulent shear flow. Table 5.1 gives an overview of selected literature describing incipient motion in laminar shear flow experimentally, theoretically and in simulations. Most relevant here is the work by Milne and Amirfazli (2009) and Milne (2013), who present incipient motion for a wide range of drop volumes $V_{\mathrm{D}} = 0.5 - 100\,\mu\mathrm{l}$. The drops are placed on an elliptic profile within a channel which operates with mean velocities of up to $U_{\mathrm{Channel}} \leq 30\,\mathrm{m/s}$. The corresponding drop Reynolds numbers of $Re_{\mathrm{D}} \leq 3000$ and the Reynolds numbers calculated by the curved boundary layer length of up to $Re \leq 2 \times 10^5$ are well below the turbulent transition of a flat plate or a cylinder in free stream conditions. The dimensions of the channel are given in Figure 5.1a. The water drops are placed on three different surfaces, PMMA ($\theta_{\mathrm{A}} = 76.3° \pm 3.3°$, $\theta_{\mathrm{R}} = 53.1° \pm 3.8°$), Teflon ($\theta_{\mathrm{A}} = 124.3° \pm 0.7°$, $\theta_{\mathrm{R}} = 108.2° \pm 3.4°$) and SHS ($\theta_{\mathrm{A}} = 161.4° \pm 0.8°$, $\theta_{\mathrm{R}} = 129.8° \pm 8.9°$). Refer to Milne and Amirfazli (2009) for details on the surface preparation. The drops are exposed to both the boundary layer and the free

Literature	Methodology	Note
Schleizer and Bonnecaze (1999)	Experiments Simulation	2D Boundary Element Method simulations of drops in Stokes shear flow ($Re = 0.01 - 0.03$)
Dimitrakopoulos and Higdon (2001)	Simulation	3D simulations with Spectral Boundary Element method minimizing the free surface energy of drops for low Reynolds numbers.
Spelt (2005)	Simulation	2D Level-Set simulation of shear flow ($Re \leq 25$) of the setup by Schleizer and Bonnecaze (1999)
Ding and Spelt (2008)	Simulation	3D Diffusive Interface simulation for moderate shear flow ($Re \leq 222.5$). Focuses on the influence of the Weber number and also on the difference between 2D and 3D solutions
Milne and Amirfazli (2009)	Experiments Theory	Investigation of drops ($0.5 - 100\,\mu$l) incipient motion on an elliptical profile within a channel ($0 - 30\,$m/s, $Re \leq 2 \times 10^5$)
Dupont and Legendre (2010)	Simulation	2D VOF simulation of a Couette-Stokes-Flow ($Re = 0.01 - 0.03$) of the setup by Schleizer and Bonnecaze (1999) and a Poiseuille-Stokes-Flow
Seevaratnam et al. (2010)	Experiments Simulation	3D Diffusive Interface method simulating drops in cross-flow $Re \leq 700$ for very low Bond numbers $Bo \leq 10^{-4}$. Three different drop motions are found: sliding, crawling, and detachment
Fan et al. (2011)	Experiments Theory	Drops ($\leq 50\,\mu$l) in channel flow ($0 - 10\,$m/s)
Milne (2013)	Experiments Theory	In addition to the first publication of this table, the drag force on the drop is measured
Linder (2015)	Simulation Experiments	3D VOF simulation of drop ($50\,\mu$m) incipient motion on a spherical profile within a channel ($0 - 10\,$m/s)
Roisman et al. (2015)	Theory	A force balance for drops of the height of the viscous boundary layer yields a relation between wetting properties, the drop volume, and the velocity gradient at the wall.
This study	Simulation	3D VOF simulation with enhanced interface handling of the setup described by Milne and Amirfazli (2009)

Table 5.1: Literature selection on experiments, theory and simulations of incipient drop motion in laminar shear flow and laminar boundary layers.

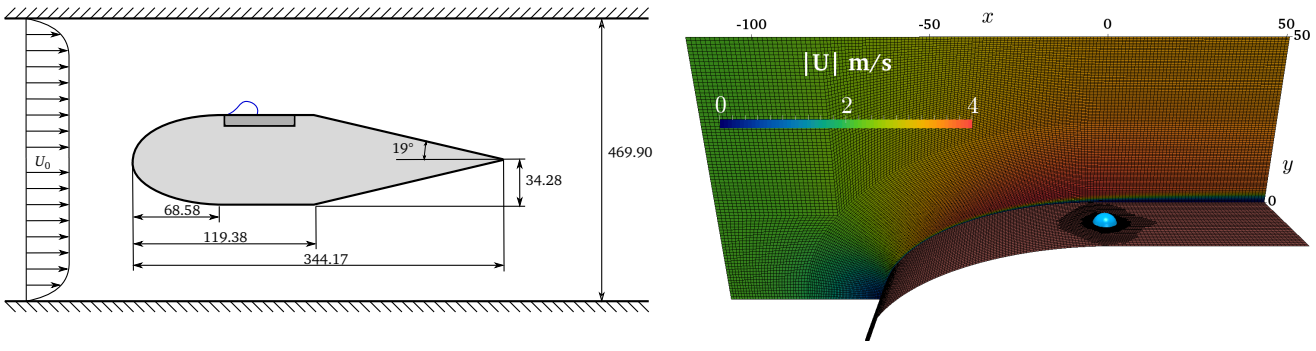

(a) Dimensions **(b)**

Figure 5.1: a) A drop sits on a surface probe enclosed by a profile with an elliptical nose that is placed in the center of a channel. The mean channel velocity U_0 is increased over time to investigate the incipient motion of the drop. Experiments with water drops on three surfaces with this setup are performed by Milne and Amirfazli (2009) used for the validation of the simulation framework. b) Simulation domain initialized with a velocity profile ($U_0 = 2\,$m/s) and a drop volume of $V_D = 58\,\mu$l. The drop is refined in three levels down to $\Delta x = 250\,\mu$m. The numerical domain-depth measures 30 mm.

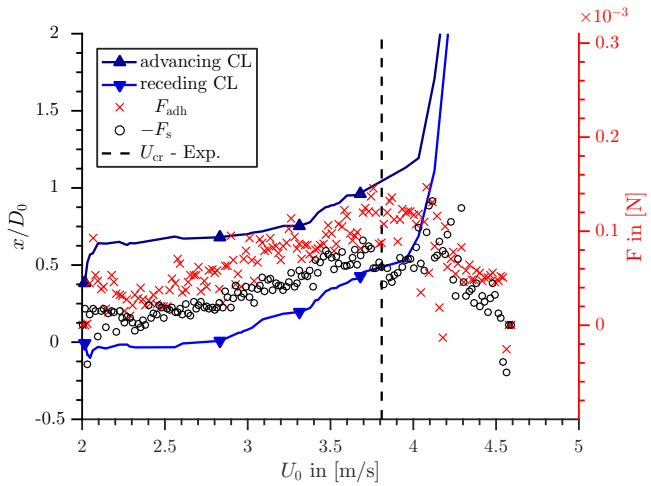

Figure 5.2: The incipient motion of a water drop ($V_D = 30\,\mu$l) on SHS in laminar shear flow. The contact line position is shown over the ramped inlet velocity as well as the magnitude of the adhesion and shear force.

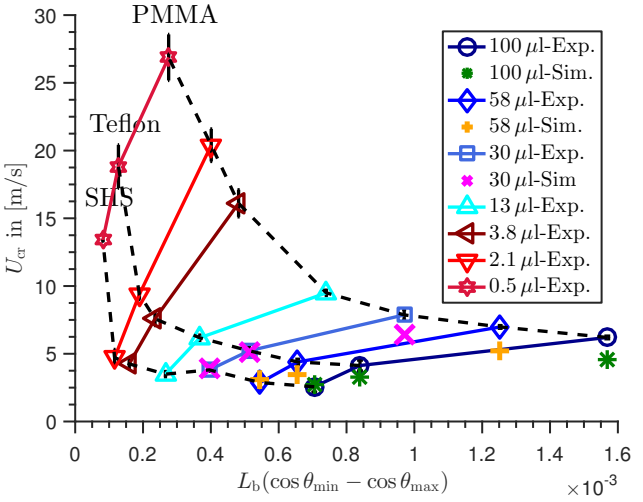

Figure 5.3: The critical velocity of water drops of different sizes and the three surfaces (PMMA, Teflon, SHS) is compared between experiments by Milne and Amirfazli (2009) and simulations.

stream. Their height ranges from approximately 0.9 to 2.5 times the boundary layer thickness δ.

Besides the wall boundary and the in and outflow conditions, a free flow condition is set at the top patch of the domain and symmetry at the bottom patch. The numerical discretization is realized with a block-mesh of high quality which is refined dynamically at the drop in three levels. At the drop, the resolution reaches $\Delta x = 125\,\mu$m which leads to a total of about one million cells. In contrast to Linder et al. (2015), the drop is fully resolved in 3D to account for asymmetric effects at the receding contact line of large drops. A velocity profile is initialized with an inflow velocity of 2.0 m/s. The drop is placed with the shape of a spherical cap (see equations (4.5) - (4.7)) according to the drop volume and the initial contact angles of $\theta_{init} = 76°,\ 124°,\ 161°$ for the surfaces PMMA, Teflon and SHS, respectively. In contrast to an acceleration of 0.5 m/s^2 in the experiment, the velocity is ramped up in simulations by 2 m/s^2 to avoid high computational costs. Most challenging is the time-step restriction by the Courant number of $Co = 0.4$, which limits the time step to $\Delta t = 2 \times 10^{-7}$ s for higher velocities. The Courant number couples the mesh size with the time step. Therefore, in this study drop volumes of $V_D = 100\,\mu$l, 58 μl and 30 μl are simulated, avoiding the smaller drops for which a higher resolution would be necessary due to the higher curvature.

In Figure 5.2 the displacement of the drop is shown exemplarily in terms of the contact line position at both extrema of the drop in up- and downstream direction while ramping up the velocity. At the beginning, the drop adjusts from the initialized state to an equilibrium in the flow field. With increasing velocity the adhesion and the shear force increase. Both, the advancing and receding contact lines move, when the integral shear force on the drop surpasses the counteracting adhesion force.

In Figure 5.3 the critical channel velocities U_{cr} for the three surfaces and different drop volumes are compared between experimental results by Milne and Amirfazli (2009) and simulations. As given in equation (4.1), the contact line diameter of the initialized spherical cap L_b, combined with the difference of the cosine of advancing and receding contact angle, are a measure of the adhesion force acting on the drop which increases with drop volume and hysteresis. For PMMA there is a larger discrepancy between simulations and experiments. Since the simulation results match very well for the two other surfaces, the contact angle measurement in the experiments could be a reason for this discrepancy. For instance, an earlier incipient motion of the drop in simulation suggests that the advancing contact angle is expected to be much greater than that measured by Milne and Amirfazli. In Figure 2 of Milne and Amirfazli (2009) a downstream contact

Literature	Methodology	Note
White and Schmucker (2008)	Exp.	Incipient motion of drops in stagnation-point boundary layer flow inspired by aircraft foils.
Moghtadernejad et al. (2013, 2015a,b)	Exp./Sim.	Experiments on drops moving in shear flow of up to $U_0 \leq 90\,\mathrm{m/s}$. Simulations with Smooth Particle Hydrodynamics method. No study on a critical shear velocity.
Maurer and Janoske (2015)	Exp.	Drops ($V_D = 5-12\,\mu\mathrm{l}$) in turbulent shear flow $Re = 6000-16000$ in a channel with variable height. Includes critical shear velocities.
Maurer (2017)	Exp./Sim.	Drops ($V_D = 5-20\,\mu\mathrm{l}$) in turbulent shear flow $Re = 6000-16000$ in a channel. VOF simulation without specification of the used turbulence model. Focus on the influence of surface vibration on the incipient motion.
Barwari et al. (2018)	Exp.	Water and glycerin drops ($V_D = 8-40\,\mu\mathrm{l}$) in turbulent shear flow $Re = 2000-14000$ in a channel with variable height. Includes critical shear velocities.
Seiler et al. (2018a,b)	Exp.	Experiments with water and glycerin drops ($V_D = 5-40\,\mu\mathrm{l}$) in turbulent shear flow $Re = 3000-32000$ on flat and complex surfaces.
This study	Sim.	3D VOF simulation using the $\zeta-f$-VLES hybrid turbulence model. Water drops ($V_D = 15-30\,\mu\mathrm{l}$) in turbulent shear flow $Re = 3000-15000$.

Table 5.2: Literature on experiments and simulations of incipient drop motion in turbulent shear flow.

angle of about $\theta_{\mathrm{max}} = 76°$ is visible in the third row depicting a drop at the critical velocity U_{cr} for incipient motion. In the fourth row, however, a contact angle above $\theta_{\mathrm{max}} = 90°$ is unmistakable for a drop that just started moving and has consequentially a relatively low contact line velocity. Hence, the current dynamic contact angle should not be much apart of the advancing contact angle, which is stated to be $\theta_{\mathrm{max}} = 76°$ and simulated here as such. In conclusion, the real advancing contact angle for PMMA is expected to be much higher. Despite this discrepancy, the simulation results using PMMA, the simulations on Teflon and SHS match the experiments very well, following the characteristic dependencies on wetting properties and the drop volume.

Oscillations of drops in laminar shear flow are observed by Milne and Amirfazli as well as predicted by Thoroddsen et al. (2008) who relate the natural oscillation frequency to density, surface tension and drop size. An analysis of oscillations for drops in turbulent shear flow is given in Section 5.2. Oscillations also occur hand in hand with the independent contact line movement of the advancing and receding front, manifested also in the caterpillar-like motion of the drop for shear velocities higher than the critical value. After having validated the methodology by a good match of experiments and simulations, the next level of complexity, embodied by turbulent shear flow, is analyzed in the following.

5.1.2 Turbulent channel flow

Although forced wetting in turbulent shear flow is found in many industrial applications, no literature simulating the incipient motion of drops in turbulent shear flow exists besides the study of Maurer (2017) who works with the VOF method in OpenFOAM. However, no turbulence model is specified in his work, which focuses on the influence of surface vibration at the point of incipient motion. A list of relevant literature with experimental results is given in Table 5.2. While in experiments a higher shear flow automatically leads to a turbulent flow, in simulations the necessary turbulence model is very challenging unless a DNS is affordable. The $\zeta-f$-VLES hybrid RANS-LES-DNS model introduced in Section 3.7.3 is used here as a turbulence model. As one novelty of this study, it is adapted to the VOF method and yields a stable interface handling as shown in Section 3.7.5.

To cover incipient motion, a single drop is placed in a fully turbulent, two-dimensional Hagen-Poiseuille channel flow with a linearly increasing Reynolds number. The discretization is shown in Figure 5.4 with a channel height of $H = 15\,\mathrm{mm}$. Although the depth is simulated with $B = 30\,\mathrm{mm}$, the boundary conditions imply an infinite depth. The mean inflow is

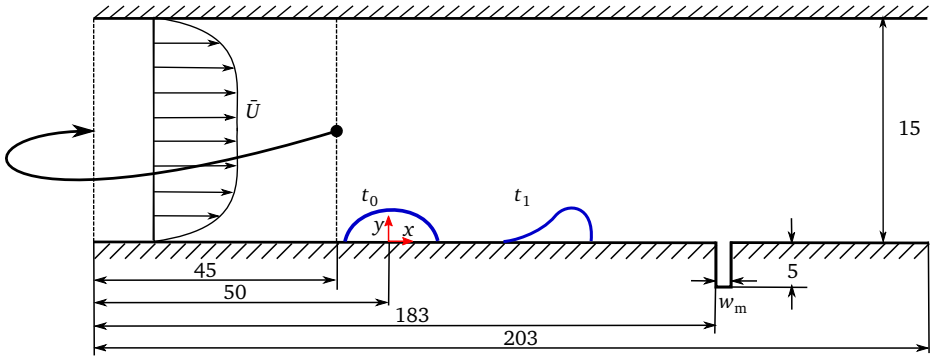

Figure 5.4: The discretized channel for a Hagen-Poiseuille flow. The flow field is mapped back into the inlet to create a constant and natural turbulent flow field. The drop is initialized as a spherical cap according to the drop volume and contact angle and interacts with a gap while running down the channel. The channel depth measures 30 mm in the simulations with boundary conditions implying an infinite depth. The setup is in accordance with Seiler et al. (2018a).

initialized with a Reynolds number of $Re = 3000$, which is ramped up with $\dot{Re} = 3758\,\mathrm{s}^{-1}$ with a novel boundary condition described in Section 3.6.2. The drop with different volumes of $V_D = 15, 20, 25, 30\,\mu$l is initialized as a spherical cap according to the initial contact angles of different surfaces, represented by their respective advancing and receding contact angles. At the drop the mesh is refined in two levels, if not mentioned otherwise, down to a cell size of $\Delta x = 125\,\mu$m in x-direction and $\Delta y = 93\,\mu$m in y-direction. Additionally to this base mesh, a simple grading with a factor of two towards the walls is applied to resolve the wall effectively with $\Delta y = 46.5\,\mu$m, which corresponds to a wall resolution of $2 \leq y^+ \leq 5$ in areas without dynamic refinement around the drop for the simulated Reynolds numbers.

In Figure 5.5 a 25 μl drop with a hysteresis of $\theta_{\mathrm{A,R}} = 105°, 46°$ is shown in comparison to the shear velocity profile at a Reynolds number of $Re = 13000$. Half of the channel height defines the boundary layer thickness in turbulent channel flow. However, the drop height of about $h = 2\,$mm corresponds to a dimensionless wall distance of $y^+ \approx 400$ which lies within the logarithmic region of the velocity profile (see Section 2.2).

For increasing drop volumes V_d, the drop height rises and consequently also the integrated shear velocity over the drop profile, such that the drop will move earlier in a linearly increasing shear flow as shown in Figure 5.6. There, the average of the advancing and receding contact line position is shown over the linearly increasing Reynolds number.

Increasing the contact angle hysteresis by keeping the receding contact angle constant for 25 μl drops delays the point of incipient motion, as shown in Figure 5.7. A change in the contact angle hysteresis is equal to a different surface in experiments. To show the influence of the contact angle boundary condition, the contact angle hysteresis of $\theta_{\mathrm{A,R}} = 85°, 46°$ is varied by two degrees to $\theta_{\mathrm{A,R}} = 87°, 46°$ and $\theta_{\mathrm{A,R}} = 85°, 44°$. Even such a small change exhibits a significant delay of the incipient motion. Once more, the importance of accurate boundary conditions shall be emphasized here.

Results for the case of a constant contact angle hysteresis width but an increasing position are shown in Figure 5.8. As the adhesion force scales with the cosine of the advancing and receding angle (see equation 4.1), it changes fastest for contact angles around 90°. Furthermore, drops with increasing contact angle hysteresis position have a smaller wetting area, a shorter contact line, and therefore less adhesion force. Together with the increasing height and the dependence on the nonlinear dependence of the cosine, the accelerated incipient motion for an increasing contact angle hysteresis position is very plausible. The evolution of the adhesion force and the shear force acting on the drop are similar to those shown for incipient motion in laminar shear flow (see Figure 5.2).

A *grid convergence study* has been performed by changing the number of refinement levels to one, two and three, for which the resolution at the drop in x-direction is given by $\Delta x = 250\,\mu$m, $\Delta x = 125\,\mu$m and $\Delta x = 62.3\,\mu$m. Thereby, the contact angle hysteresis is simulated as $\theta_{\mathrm{A,R}} = 108°, 30°$. The drop has a volume of $V_\mathrm{d} = 20\,\mu$l and the final channel

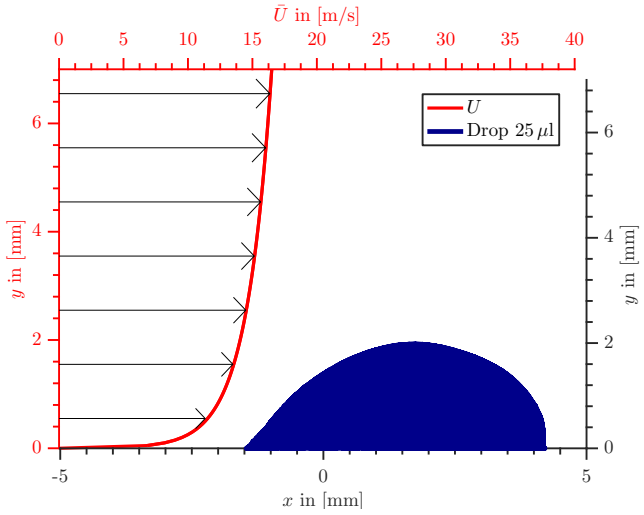

Figure 5.5: Turbulent velocity profile at $Re = 13000$ and drop profile of a drop with volume $V_d = 25\,\mu$l on a surface with (θ_A, $\theta_R = 105°$, 46°).

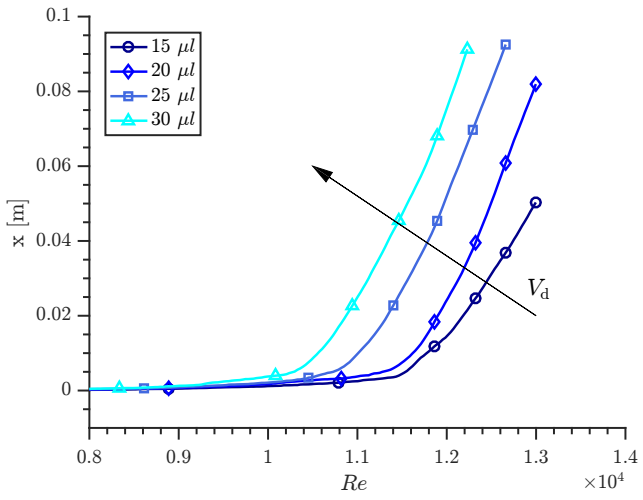

Figure 5.6: With increasing drop volume the point of incipient motion is found earlier for a linearly ramped up channel velocity. The surface is characterized by $\theta_{A,R} = 85°$, 46°.

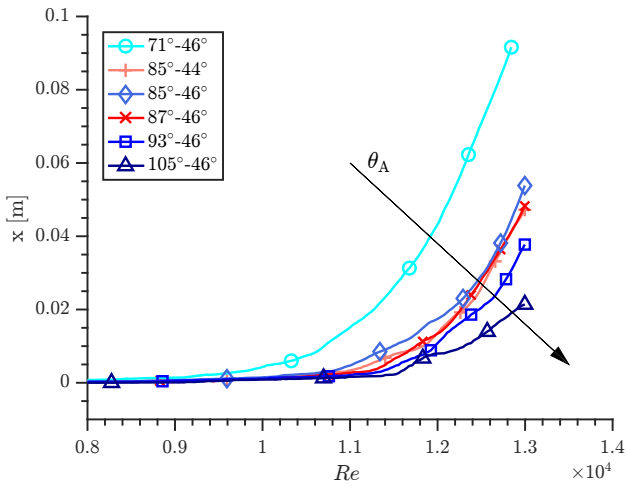

Figure 5.7: With increasing advancing and a constant receding contact angle, the point of incipient motion is delayed for a linearly ramped up channel velocity. The drop volume measures $V_d = 25\,\mu$l. Small changes of the contact angle hysteresis have a significant influence on the point of incipient motion.

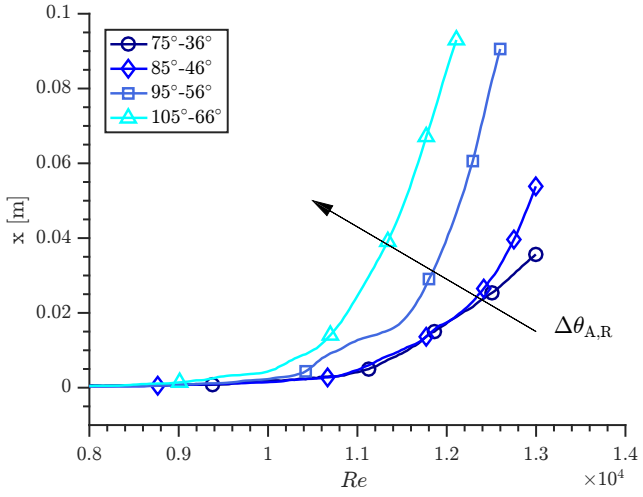

Figure 5.8: Elevating the constant contact angle hysteresis leads to an earlier incipient motion for a linearly ramped up channel velocity due to three reasons: an increasing drop height, a reduced contact line length, and a reduced adhesion force. The drop volume is set to $V_d = 25\,\mu$l.

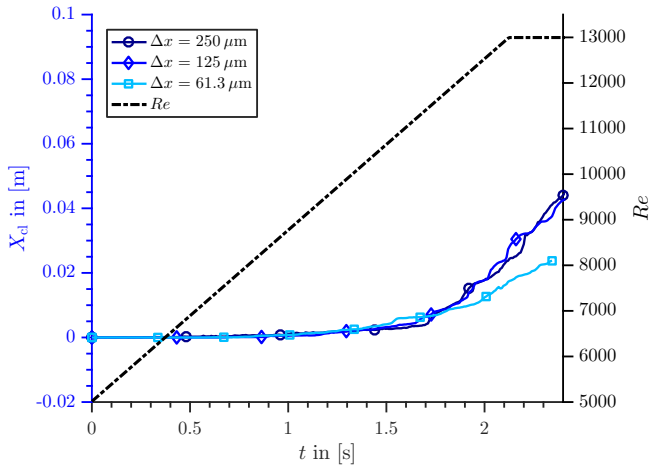

Figure 5.9: A grid convergence study with resolutions of $\Delta x = 250\,\mu$m, $\Delta x = 125\,\mu$m and $\Delta x = 62.3\,\mu$m at the drop with a volume of $V_d = 20\,\mu$l and a hysteresis of $\theta_{A,R} = 108°, 30°$. The drop trajectory converges towards the finest resolution.

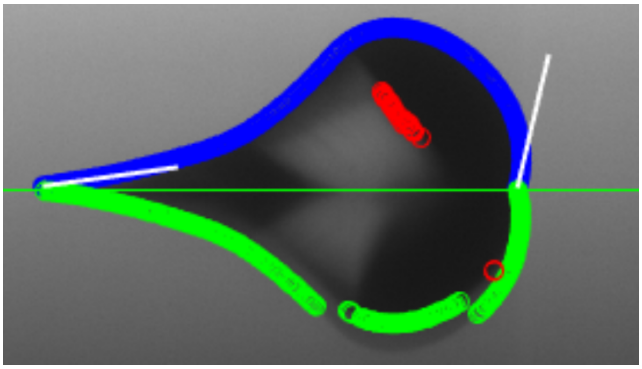

Figure 5.10: Shadowgraphy of a moving $10\,\mu$l drop on an aluminum surface. Using the grey-scale gradient the contour of the drop is extracted and the contact angles measured. The drop reflects on the aluminum surface (picture by P. Seiler).

velocity is set to $Re = 13000$, which is increased beginning with $Re = 3000$ at a rate of $\dot{Re} = 3758\,s^{-1}$. Figure 5.9 shows that for a finer discretization the characteristic point of incipient motion converges towards the finest grid resolution. Theses results do not contradict the increase in parasitic currents due to a diverging curvature for finer meshes shown in Section 3.4.4. In the investigated range of resolutions, the overall improvement by a finer mesh resolution outperforms the increasing parasitic currents, which furthermore, are very small compared to the shear flow. A second characteristic shown in Figure 5.9 is the evolving drop velocity. With a finer mesh the drop moves slower. This might be fully attributed to the contact line velocity mesh dependence explained in Section 3.5.4. Future work should address this point.

Despite the plausible simulation results, the complexity of the simulation mandates a careful comparison with experimental results for a final validation of this setup.

5.1.3 Comparison of the incipient motion in turbulent shear flow between simulations and experiments

Because of the high complexity of the interaction between the turbulence model in combination with the contact line and interface models, the validity of the simulation can only be confirmed with experiments. Therefore, simulations are compared with experimental data by Seiler et al. (2017) on the incipient motion of drops in turbulent channel flow.

In these experiments, the contact angle of a $25\,\mu$l water drop moving with constant velocity in turbulent shear flow on a PMMA surface is measured. Shadowgraphy pictures as shown in Figure 5.10 are analyzed with a temporal resolution of up to 4000 Hz and a spatial resolution of $20\,\mu$m. The contact angle hysteresis is measured to $\theta_{A,R} = 105°, 46° \pm 5°$ for water on PMMA. In the following, results of experiments with a temporal resolution of 150 Hz and a spatial resolution of $27.5\,\mu$m are presented.

The natural variation in experiments is analyzed in Figure 5.11. Even though the same initial conditions are provided in each experiment, the turbulence and the drop oscillation cause a variation in the incipient motion of the drop. Figure 5.11a shows the position of the drop mid-point over time. The critical Reynolds number for incipient motion is measured with a distance threshold of 1.5 mm to avoid most of the creeping regime of the drop after which a continuous motion is observed. The critical Reynolds numbers of the experiments range between $Re_{crit} = 9658$ and $Re_{crit} = 10528$, whereas the simulation yields $Re_{crit} = 10972$, which is only 4% above the most similar experiment.

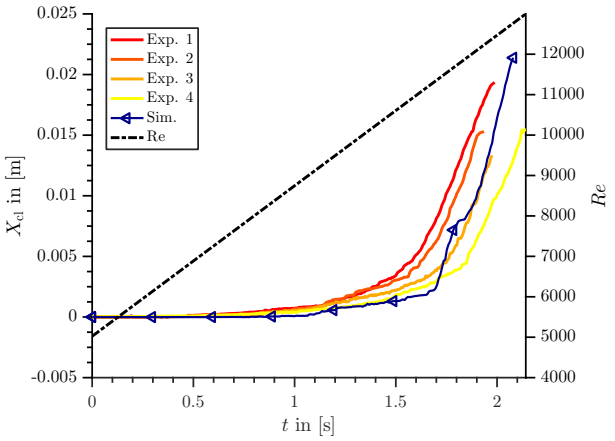

(a) The drop mid-point position over time. The experiments show a natural scatter which is due to the randomness of turbulence and the oscillation of the drop.

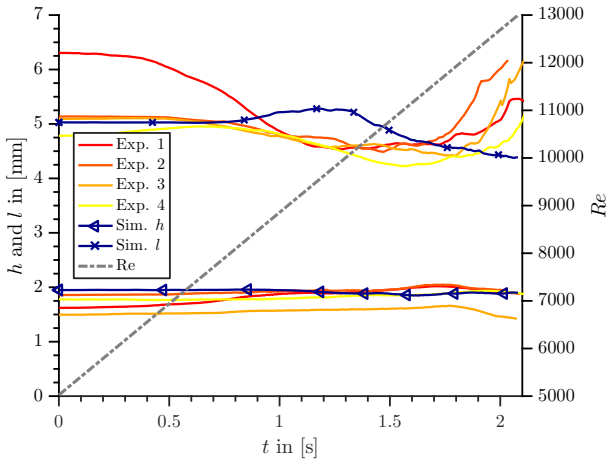

(b) The drop height and length (streamwise) are of the same magnitude in experiments and simulation.

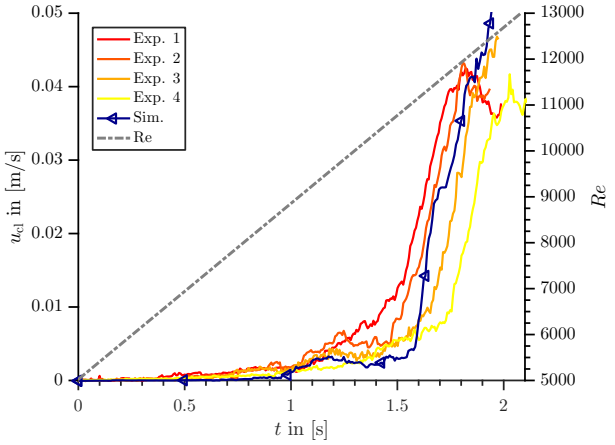

(c) The drop mid-point velocity over time with a moving average of 30 time steps at a data rate of 150 Hz. Experiments as well as the simulation show a plateau between 1 s up to 1.5 s after which the velocity increases rapidly.

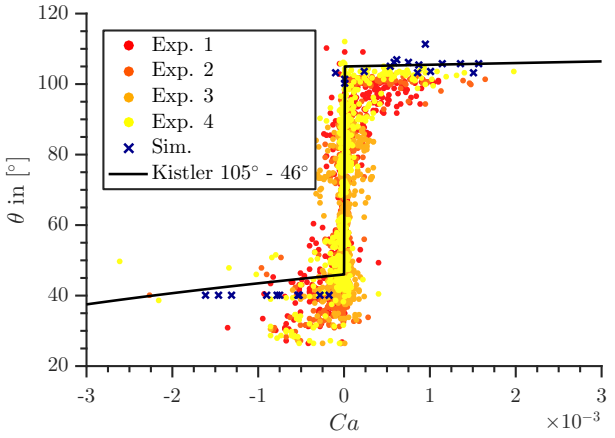

(d) The contact angles measured up and downstream of the drop shown over the Capillary number. In experiments the velocity is calculated by the contact line position movement measured at a rate of 150 Hz. For better visibility the contact angles of the simulation within the contact angle hysteresis are filtered out.

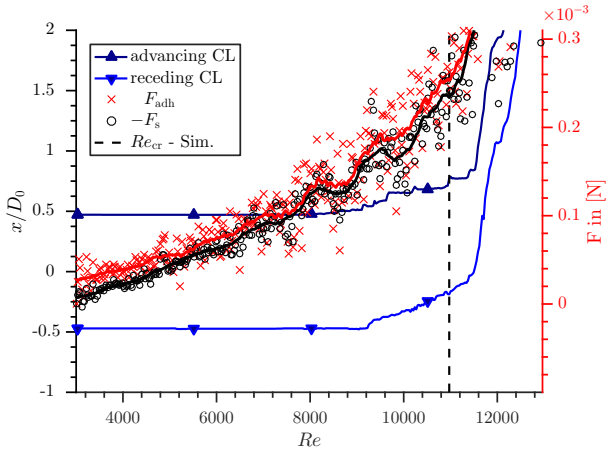

(e) Advancing and receding contact line motion with increasing Reynolds number from the simulation. The adhesion force and the shear force cancel each other out until a Reynolds number of about $Re = 9200$ after which the drop moves in a creeping motion. At $Re = 11300$ the drop accelerates rapidly.

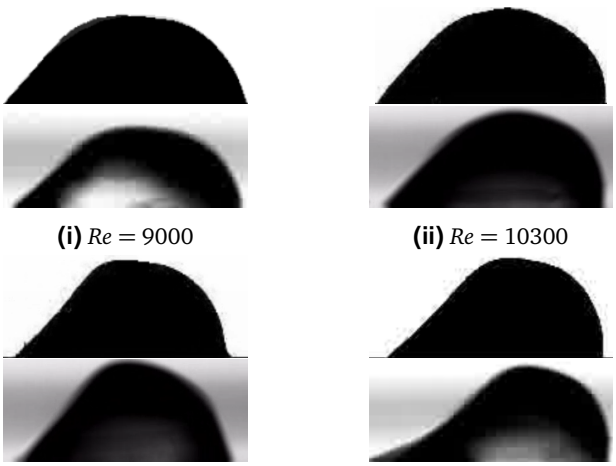

(i) $Re = 9000$ **(ii)** $Re = 10300$

(iii) $Re = 11300$ **(iv)** $Re = 12300$

(f) Shadowgraphy comparison of simulations (above) with experiments (below) at different Reynolds numbers

Figure 5.11: Comparison of experiments and a simulation of the incipient motion of a drop ($V_d = 25\,\mu$l) on PMMA $\theta_{A,R} = 105°, 46° \pm 5°$ in turbulent shear flow. Beginning with $Re = 3000$, the Reynolds number is increased at a rate of $\dot{Re} = 3758\,s^{-1}$.

The dynamic contact angle model by Kistler introduced in Section 2.4.1 in combination with the contact angle hysteresis model is shown in Figure 5.11d. For contact angles exceeding the contact angle hysteresis of $\theta_{A,R} = 105°, 46° \pm 5°$, Kistler's model serves as a boundary condition for simulations. Both, the simulation results and the measurements of the experiments show a similar behavior regarding the contact angle dependency on the Capillary number. A difficulty of the experiments are the high frequencies of the drop oscillation of up to 1000 Hz and the limited temporal resolution of 150 Hz as shown in the present results. The contact line velocity in experiments is calculated by the change of the contact line position, which is measured at a rate of 150 Hz. This average velocity is expressed in the Capillary number shown in Figure 5.11d with an instantaneous contact angle measured from the shadowgraphy. Therefore, both the average Capillary number might not match the current visible contact angle, which accounts for the large experimental scatter. However, in simulations, the exact contact line velocity is available in every simulated time step. For comparison the average simulation time step is about 5×10^{-6} s in these cases.

In Figure 5.11b the drop height h and length l are compared between experiments and simulation. Both are shown with a central moving average including 30 time steps at a data sampling rate of 150 Hz. They show the same order of magnitude and the simulation results lie in the range of experimental variance. The drop velocity presented in Figure 5.11c, again, match very well between experiments and simulation, exhibiting the same moving average of 30 time steps. Interesting are the velocity plateaus after about 1 s after the drop starts to move. This behavior is described by Barwari et al. (2018) as a creeping motion, after which the drop accelerates almost instantly. In Figure 5.11e the beginning of the creeping motion coincides with the first time the shear force overcomes the adhesion force for a short time, whereas, at the point of rapid acceleration, even the moving average of the shear force exceeds the adhesion force.

Before the point of incipient motion, the drop oscillates in the shear flow. This will be investigated in more detail in Section 5.2. Also after the incipient motion, the drop shape changes constantly. Even though the drop oscillation follows a characteristic pattern, the particular drop shape at an instance in time is random. Therefore, and because of the recording frequency of 150 Hz, Figure 5.11f compares similar drop shapes of experiments and simulations with a Reynolds number range of $\Delta Re \leq 300$.

The simulation result lies within the experimental error-bounds. The drop position, velocity, height, length as well as the measured dynamic contact angles are in good agreement. Furthermore, the calculated adhesion force and the counteracting shear force are accessible. The incipient motion of a drop can be separated into two regimes, namely the creeping regime and a subsequent continuous motion of the drop, as is shown in simulations and observed in experiments by Barwari et al. (2018). The excellent match of the incipient motion in turbulent channel flow between simulations and experiments is the most important result of this study. Even though only one contact angle hysteresis and drop volume is compared here, the close match of experimental, simulation, and theoretical results presented in the next section suggest a general validity of the numerical and modeling framework used in this study.

5.1.4 Modeling of incipient motion

Several authors provide suggestions on how to predict the point of incipient motion. Roisman et al. (2015) approximate the drop shape by a spherical cap and use the Blasius solution in *laminar* boundary layers to approximate the so-called attack velocity U_{attack} at half of the height of the spherical cap. With the attack velocity and the area of the projection of the spherical cap cross-section the drag force is approximated. To obtain the critical velocity, the adhesion force calculated with the advancing and receding contact angle, and the drag force are set equal. A comparison of Roisman's model and the experiments of Hu et al. (2013) and Milne and Amirfazli (2009) yield promising results. In a publication by Barwari et al. (2018) considering *turbulent* flow, an empirically fitted relation between the Laplace number $La = \sigma \varrho_L L_b \mu_L^{-2}$ and the critical Reynolds number $Re = U_{crit} h \nu_L^{-1}$ is given:

$$Re_{crit} = 51.04 La^{0.434}. \tag{5.2}$$

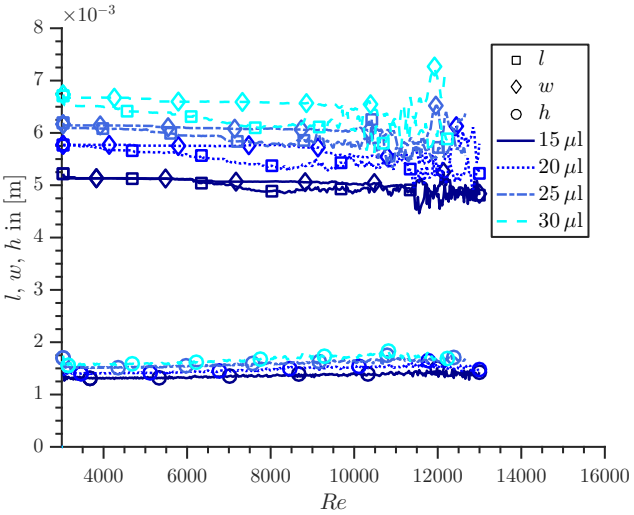

Figure 5.12: Wetting length, width and drop height for different drop volumes, a contact angle hysteresis $\theta_{A,R} = 71°, 46°$ and an over time linearly increasing Reynolds number.

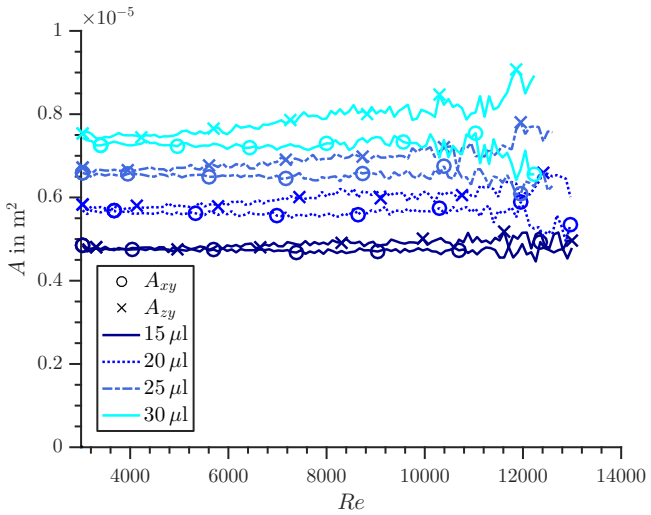

Figure 5.13: Comparison of the area of the drop cross-section in a plane streamwise (xy) and perpendicular to the flow (zy) for different drop volumes, a contact angle hysteresis $\theta_{A,R} = 71°, 46°$ and an over time linearly increasing Reynolds number.

Unfortunately, the fitting requires a calibration for each channel or free flow field and only partly includes the adhesion force due to the contact angle hysteresis by accounting for the drop shape with the wetting width L_b and the drop height h.

The model by Roisman et al. (2015) is analyzed in the following. Their approximations made about the drop shape and the attack velocity are verified here with the simulation data in *turbulent* shear flow. Roisman et al. (2015) assume the shape of a drop at its point of incipient motion to be similar to the shape of a sessile drop without the influence of shear flow. This assumption is first validated. The evolution of the drop height h, as well as the wetting length l, is given for several drop volumes with a contact angle hysteresis of $\theta_{A,R} = 71°, 46°$ and a linearly ramped up channel Reynolds number as reported in Figure 5.12. The drop height reaches its maximum at the point of incipient motion but differs less than 10 % from the initial value. Furthermore, the wetting width and length show a similar range of discrepancy of about 10 % between the initial values and the point of incipient motion. Up to the point of incipient motion, the drop is found to be wider than long (streamwise). Apart from that, the projected areas of the drop streamwise (xy-plane) as well as perpendicular to the flow (zy-plane) are assumed to be equal by Roisman et al. (2015). Figure 5.13 shows both areas for the same setup. According to the wider drops, the area A_{zy} is larger than A_{xy}. The discrepancy amplifies with the drop volume and can be estimated to be up to 15% in the case of a 30 μl drop. To approximate the attack velocity U_{attack} of a drop in shear flow by the attack velocity $U_{attack,0}$ at the height h_0 of a sessile drop without shear flow is a very good approximation as shown in Figure 5.14. The same figure also shows the relation between the channel mean velocity $\bar{U}_0$ to the lower attack velocity U_{attack} and the very small drop velocity after the point of incipient motion indicated by the contact line position. Finally, Roisman et al. leave the drag coefficient to be fitted by experiments. Being able to evaluate the drag force F_s in simulations directly at the drop with equation (5.1) and with the area of the cross-section of the drop A_{zy}, the drag coefficient c_D can be calculated by

$$c_D = \frac{2F_s}{\varrho_G U_{attack}^2 A_{zy}}. \tag{5.3}$$

The drag coefficient of all present simulation data is combined in Figure 5.15, which shows a dependency on the attack velocity U_{attack}, as well as on the contact angle hysteresis. With increasing adhesion force, the critical drag coefficient at the point of incipient motion also increases, as shown for three contact angle hysteresis values. In this section, a linear dependency of the critical drag coefficient on the contact angle hysteresis is assumed. All in all, the model assumptions

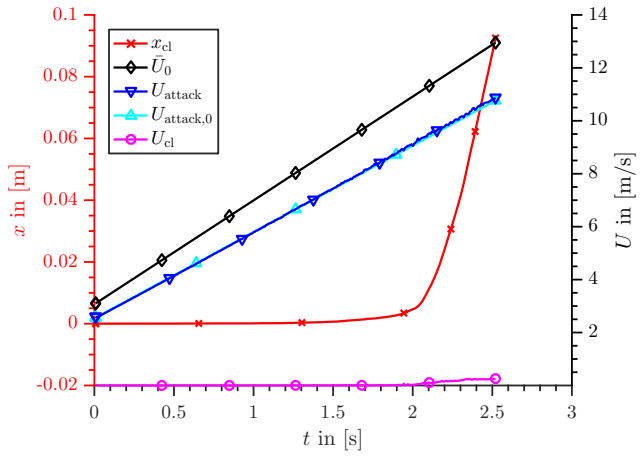

Figure 5.14: Comparison of the mean channel velocity $\bar{U}_0$, the attack velocity at the half height of a sessile drop $U_{attack,0}$ and a sheared drop U_{attack} of 25 μl on a surface with the contact angle hysteresis $\theta_{A,R} = 71°, 46°$. At the point of incipient motion the contact line mid x_{cl} increases together with the contact line velocity U_{cl}.

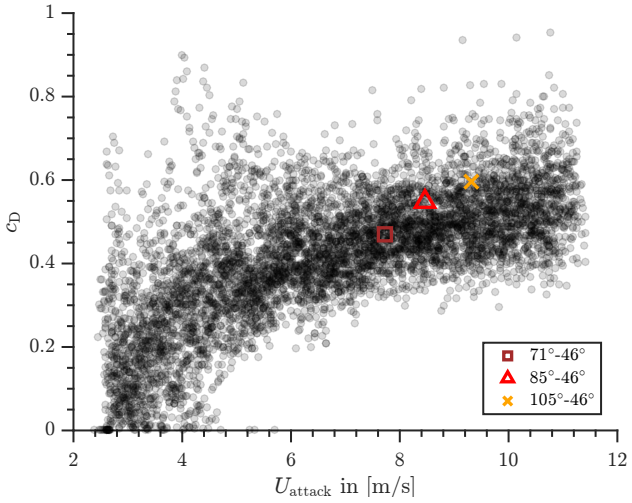

Figure 5.15: The drag coefficient c_D is plotted for each time step of all simulations over the attack velocity U_{attack}. The drag coefficient rises with increasing attack velocity as well as with the contact angle hysteresis. At the point of incipient motion the critical drag coefficient is shown for three contact angle hysteresis of a 25 μl drop.

made by Roisman et al. (2015) for laminar shear flow are analyzed, yielding reasonable results for turbulent flow. Moreover, the drag coefficient can be calculated from simulation results and requires no further fitting.

Inspired by the model of Roisman et al., a balance of the adhesion force and the shear force reads as

$$F_s = F_{adh}\,, \tag{5.4}$$

$$\frac{1}{2}\varrho_G U^2_{attack,crit} c_D A_0 = \sigma L_b (\cos\theta_R - \cos\theta_A)\,, \tag{5.5}$$

$$U_{attack,crit} = \sqrt{\frac{2\sigma L_b (\cos\theta_R - \cos\theta_A)}{\varrho_G c_D A_0}}\,, \tag{5.6}$$

where L_b and A_0 are given by the shape of a sessile drop in equilibrium with a certain volume and a contact angle of $\theta_e = (\theta_A + \theta_R)/2$ (see equations (4.5) - (4.7)). Figure 5.16 shows selected simulations, as well as the theoretical results given by the force balance in equation (5.4).

The simulation results match very well the theoretical model predictions, with a maximum offset of 1 m/s and a relative error smaller than 10%. The discrepancy is coincides with the assumptions made about the drop shape. However, simulation inaccuracies due to models describing surface tension, contact line dynamics and turbulence might also play a role. Note that no fitting factor is necessary here, because of the calculated drag coefficient. Since the definition of U_{attack} is independent of laminar or turbulent flow, the estimation given by Blasius in laminar flow, as well as the dimensionless velocity profile given for turbulent flow e.g. by Spalding (1961) in (3.61), connects the attack velocity to a global shear velocity U.

5.2 Oscillation of sessile drops in turbulent shear flow

When investigating the incipient motion of a drop in shear flow, oscillations of the drop are observed in experiments before and after the critical shear flow is reached. Zhi-Yong et al. (2006) found two oscillation modes, namely forward-backward and upward-downward. Chiba et al. (2012) give a practical overview of different oscillation modes and their

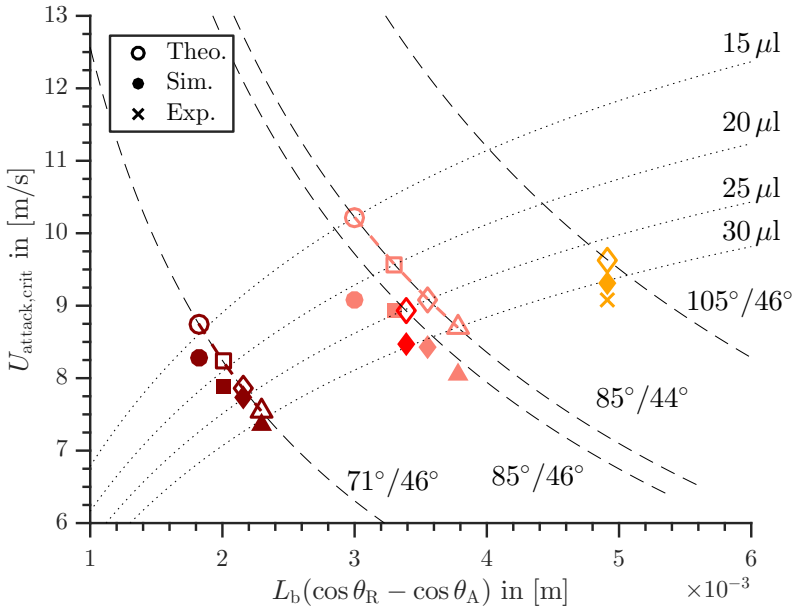

Figure 5.16: The critical attack velocity U_{attack} is plotted over the wetting characteristics of the drop. The theoretical approximation comes close to the simulation results and provides information about the influence of the drop volume and the characteristic contact angles.

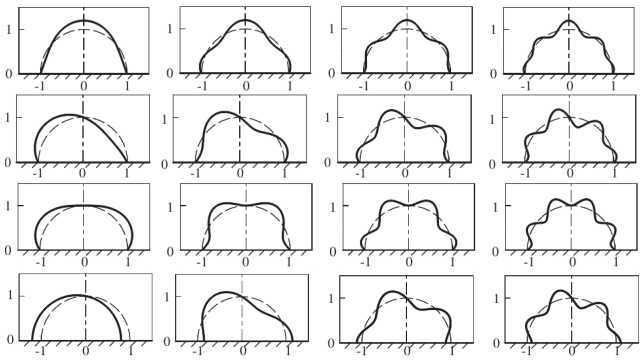

Figure 5.17: Oscillation modes (rows) and first four orders (columns) of drops in zero gravity (pictures from Chiba et al. (2012) Figure 4-8)

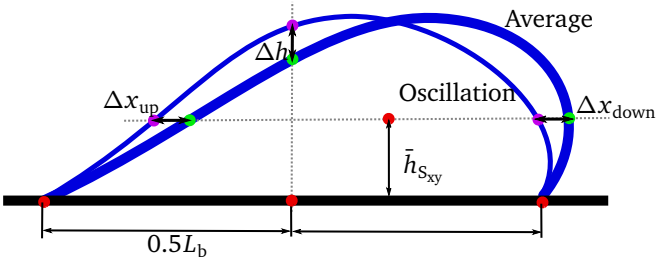

Figure 5.18: Characteristic measures Δh, Δx_{up} and Δx_{down} of the forward-backward and upward-downward modes. The oscillation is measured as the difference to the average drop shape.

higher order evolution without the effect of gravity or shear force (see Figure 5.17), which are in accordance with the modes found by Zhi-Yong et al. (2006). The oscillation characteristics depend on the surface tension, droplet size, air velocity, roughness, and viscosity (Burgmann et al., 2018). Zhi-Yong et al. also state that the oscillation has an effect on the incipient motion of a drop. In fact, the oscillation of the drop increases the drag coefficient (Clift et al., 2005) and influences the incipient motion by forcing the interface over the advancing or under the receding contact angle. Milne (2013) and Milne et al. (2014) present an in-depth experimental study on the oscillation of drops in laminar shear flow which are shown in Section 5.1.4.

The topic of oscillating drops deserves a thorough investigation, especially since the oscillation of sessile drops in turbulent shear flow has not yet been described systematically by simulations, as far as known to the author. Since this study focuses more on the validation of the entire numerical framework this section is considered a motivation for future work.

To capture the forward-backward and upward-downward modes, the oscillation of the drop is characterized by the drop height h_{cl} measured above the center between the advancing and receding contact line point as presented by Seiler et al. (2017). The length of the drop is measured at the height of the average mass center in up and downstream direction separately with x_{down} and x_{up} as shown in Figure 5.18. These measurements are averaged over all time steps, to describe the change with respect to the average value exemplarily shown for Δh:

$$\Delta h = |h_{\mathrm{cl}} - \bar{h}_{\mathrm{cl}}| \,. \tag{5.7}$$

With a Fast Fourier Transformation the frequency of the drop oscillations are identified and the corresponding amplitude peaks reveal the main frequencies that are related to the resonant frequency of the system. Figure 5.19 shows the oscillation frequencies of the three measures Δh, Δx_{down} and Δx_{up} for an increasing drop volume. With increasing drop volume, the peak frequencies remain almost the same. However, the overall amplitude increases, which also amplifies the frequencies of higher order modes. The contact angles in these cases are set to $\theta_{\mathrm{A,R}} = 71°, 47°$ and the sample time is 1 s at 1000 Hz for a range of Reynolds numbers between $Re = 6300$ and $Re = 9600$, which is linearly ramped up over time.

By increasing the contact angle hysteresis as shown in Figure 5.20, the peak frequency of the first mode reduces while its amplitude increases. Interestingly, the higher order modes are more pronounced for small hysteresis. These measurements are taken for a drop with volume $V_{\mathrm{d}} = 25\,\mu$l and for Reynolds numbers between $Re = 6300$ and $Re = 9600$.

The velocity ramp shown in Section 5.1.2 is evaluated for three velocity ranges with Reynolds numbers of $Re = 4000 - 6000$, $Re = 6000 - 8000$ and $Re = 8000 - 1000$. The oscillation amplitude increases with the Reynolds number and higher order modes become more pronounced, which is in line with observations by Burgmann et al. (2018).

To sum up, oscillations have an impact on the incipient motion, as the critical contact angles θ_{A} and θ_{R} might be exceeded earlier. Different oscillation modes are captured that can be qualitatively described by the forward-backward and upward-downward modes. The peak frequency increases with the contact angle hysteresis as well as the peak amplitude, which is comparable with experimental findings by Zhi-Yong et al. (2006), who varied the surface roughnesses. Also, higher shear velocity increases the oscillation amplitude. Moreover, the same dependency is found for an increasing drop volume. Further numerical studies are recommended to capture the influence of viscosity by using a higher sample time over a longer period. Both are limited in this study due to computational resource restrictions.

5.3 Drop interaction with complex geometry in turbulent shear flow

In many industrial applications, the complex geometry of wetted surfaces is functional or at least influential for which a detailed understanding of the wetting process is essential. Being able to model wetting of complex surfaces helps to improve the functionality of such surfaces. One can imagine a huge variety of grooves and micro channel geometries that are wetted by single drops, films, rivulets or a bulk flow. Thereby, the geometry, capillary forces as well as external forces

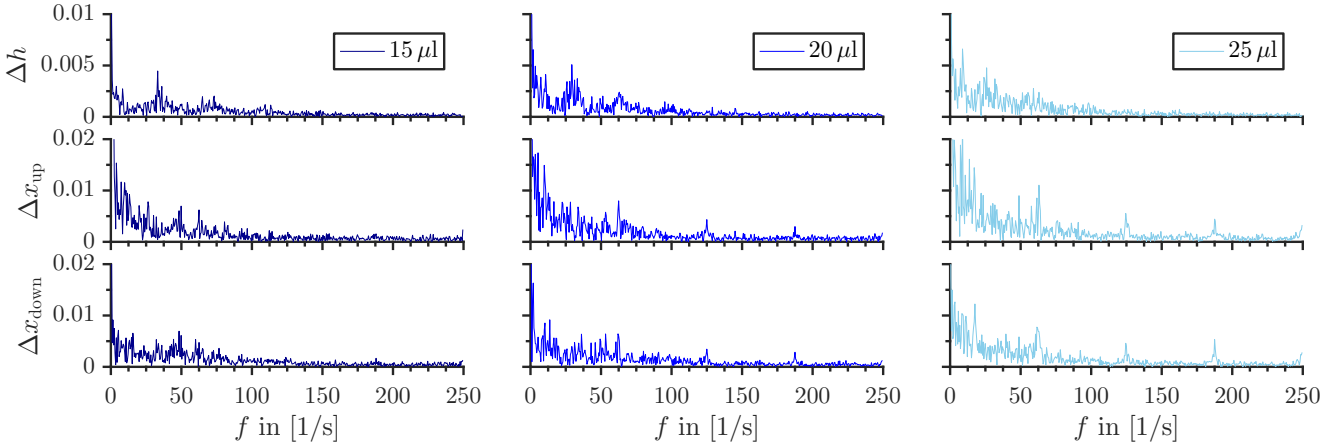

Figure 5.19: An increasing drop volume results in similar peak frequencies but also in an increase in amplitude, which amplifies the frequencies of higher order modes.

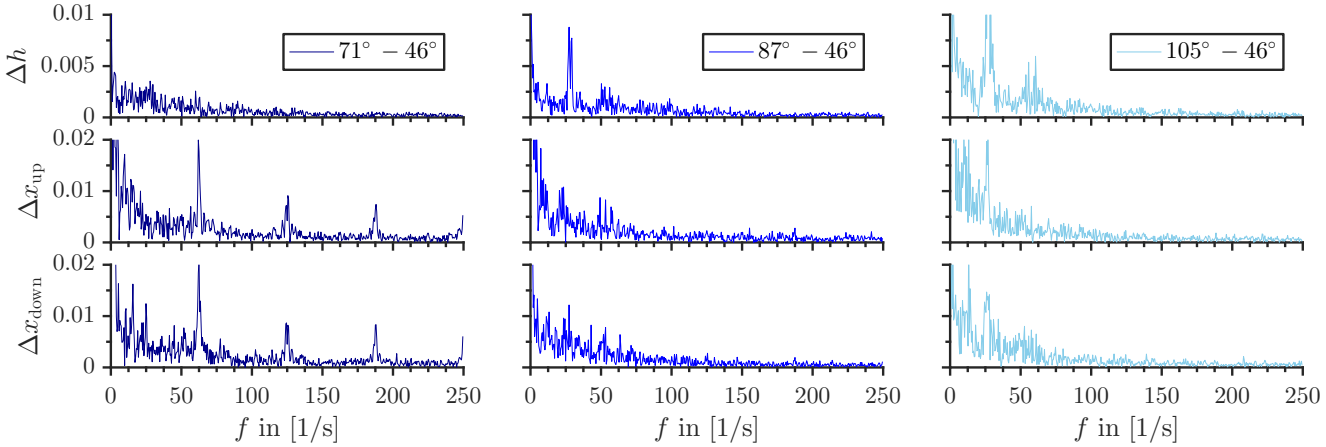

Figure 5.20: An increasing contact angle hysteresis shows different peak frequencies and an increase in amplitude. However the frequencies of higher order modes are more pronounced for a small hysteresis. The drop volume is kept at $V_d = 25\,\mu l$.

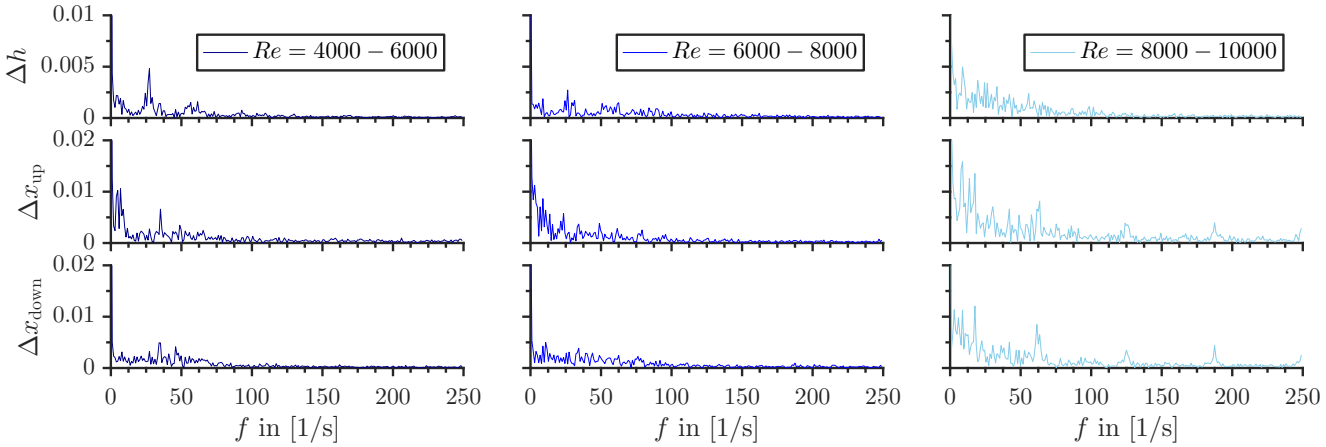

Figure 5.21: Increasing the shear flow velocity shows similar peak frequencies and an increase in amplitude. The drop volume is $V_d = 25\,\mu l$ and the contact angle hysteresis set to $\theta_{A,R} = 71°, 47°$.

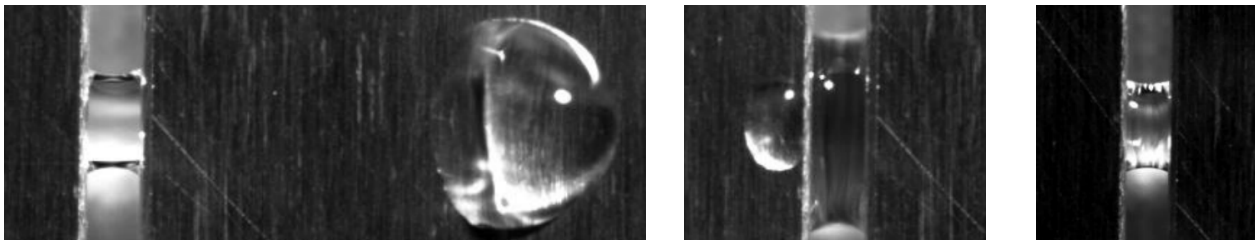

(a) Continuous drop motion (20 μl) **(b)** Satellite droplet (15 μl) **(c)** Absorption (5 μl)

Figure 5.22: Top view on a microchannel with a width $w_m = 10$ mm. Drops of increasing volume $V_D = 5\,\mu$l, 15 μl, and 20 μl move with an increasing velocity at a constant shear flow velocity (pictures by Seiler et al. (2018a) and Mayrhofer (2018))

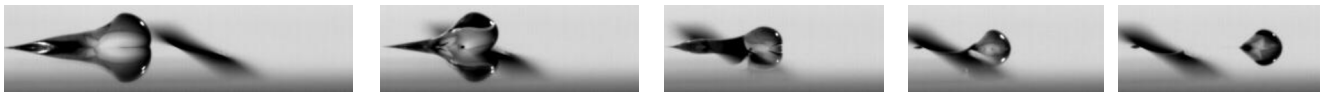

(a) $t = 0$ ms **(b)** $t = 56$ ms **(c)** $t = 80$ ms **(d)** $t = 120$ ms **(e)** $t = 344$ ms

Figure 5.23: Side view of a 20 μl drop on aluminum partly crossing a $w_m = 2.3$ mm microchannel. The drop is mainly absorbed by the microchannel but has enough volume left to keep moving in the channel flow. (pictures by Seiler et al. (2018a) and Mayrhofer (2018))

influence the wetting outcome.

As an introduction to the topic, the work of Shuttleworth and Bailey (1948) on wetting of rough surfaces is recommended. Seemann et al. (2005) and Herminghaus et al. (2008) present an overview on the possible static wetting morphologies of a liquid in simple linear solid micro-scale wedges and grooves without the influence of gravity. The morphology depends on the contact angle as well as the opening angles of the wedges that form the microchannel. Among many others, an experimental study of forced wetting of complex surfaces is the study on dip-coating of a pyramidal structured surface by Manukyan (2013) and their simulation presented in Linder (2015), who uses the Volume of Fluid method as well as a model for contact angle hysteresis and pinning of the contact line. In their work, as well as in Oliver et al. (1977) and Berthier et al. (2009), a geometrical pinning of the contact line is described. The contact line will stay immobile at an edge as long as the interface needs to adapt to the corner angle in relation to the given contact angle, which according to Thammanna Gurumurthy et al. (2018) also depends on the sharpness of the edge. Dianat et al. (2017a,b) present a numerical study of a drop forced by turbulent shear flow over a rounded edge, which is inspired by the exterior water management of cars. They use a hybrid VOF-LS method S-CLSVOF, that is introduced in Section 3.4, in combination with the ω-SST turbulence model. At the contact line, however, no hysteresis nor pinning model is used and the simulation results are not compared to experiments. The present study has a lot to add in terms of modeling the contact line, the interface, the turbulence to all of the mentioned studies (see Chapter 3).

In experiments by Seiler et al. (2018a) and Mayrhofer (2018) several outcomes are classified. For a given drop size and low drop velocities, the drop does not cross the edge of the micro channel. Increasing the drop velocity by a finite amount, the drop will be completely absorbed by the microchannel, as shown in Figure 5.22c. Higher velocities allow the drop to pass the microchannel partially. The microchannel will absorb the main part of the drop, leaving satellite droplets on one or both sides as shown in Figure 5.22b. Exceeding a drop velocity threshold, the main part of the drop surpasses the obstacle, leaving only a small liquid bridge (see Figure 5.22a). The contact line of the bridge pins at the side walls of the microchannel. Naturally, the reduction of the width w_m of the microchannel yields the same effect as increasing the drop velocity. The speed of the drop can be expressed in the Capillary number which depends directly on the shear velocity and the drop volume as shown in the last sections.

TProviding a proof of concept, this study is limited to a horizontal and rectangular micro-channel perpendicular to the shear flow as shown in Figure 5.4. The microchannel width $w_m = 1.7, 2.3, 3.0$ mm is varied, while the microchannel

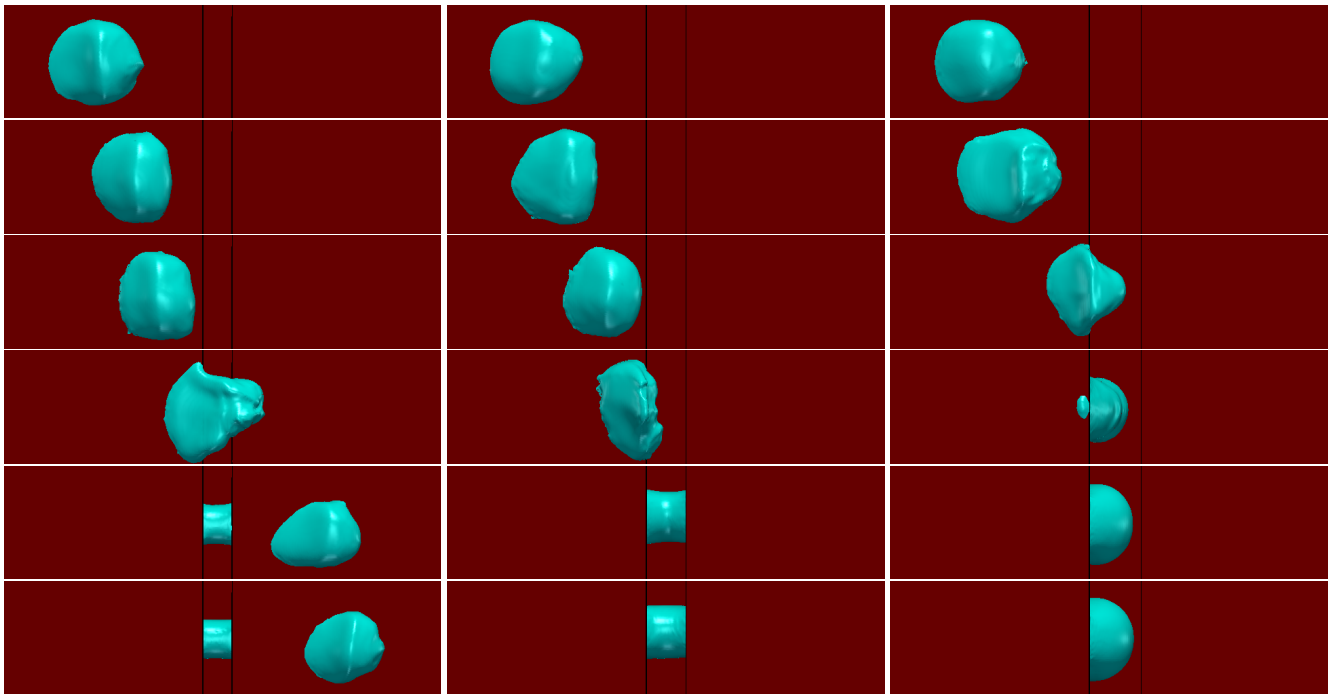

(a) Continuous motion ($w_m = 1.7\,\text{mm}$) **(b)** Complete absorption ($w_m = 2.3\,\text{mm}$) **(c)** Satellite droplets ($w_m = 3.0\,\text{mm}$)

Figure 5.24: Top view of a microchannel with $w_m = 1.7\,\text{mm}$, $2.3\,\text{mm}$, and $3.0\,\text{mm}$. A drop ($20\,\mu\text{l}$ moves with almost constant velocity $Ca = \eta_L U_D/\sigma \approx 1.06 \times 10^{-3}$ in constant shear flow $Re = 13000$ until it interacts with the microchannel. The contact angle hysteresis is set to $\theta_{A,R} = 108°, 30°$. With a larger gap, more of the drop gets absorbed. The snapshots correspond to $t = 0$, 80, 120, 160, 200, 240 ms.

height $h_h = 5\,\text{mm}$ is fixed. Similar to the conditions in Section 5.1.2, a $20\,\mu\text{l}$ drop is placed in a fully developed turbulent Hagen-Poiseuille flow with a Reynolds number of $Re = 3000$. The channel velocity is increased linearly over time until a Reynolds number of $Re = 13100$ is reached. The distance from the initial drop placement to the groove is long enough for the drop to develop a constant velocity in respect to the shear-flow Reynolds number.

Figure 5.24 shows all three regimes in simulations: A continuous motion where a small part of the drop is absorbed, a partly absorption leaving satellite droplets, and a complete absorption. The drop motion is almost constant until the advancing front hits the edge. As explained in Section 2.4.2, the interface needs to adapt to the new inclination angle of the microchannel before a motion downwards the microchannel side would be possible. Hence, the drop aligns at the edge until one of two scenarios apply. If the front nose of the drop reaches the surface of the downstream side *above* the microchannel, the drop attaches and forms a liquid bridge, after which continuous motion is possible. If the front nose only reaches the right side of the microchannel without contact to the main channel surface downstream of the microchannel, a complete absorption of the drop follows. Note that the satellite droplets in the simulations numerically diffuse over time since the compression of the volume fraction field α at the interface suffers from the under-resolved interface curvature. A proper resolution of such small length scales was not feasible in this study.

A qualitative comparison between simulation and experiments has been given, recovering all of the possible outcomes. A quantitative relation between wetting conditions, drop size, microchannel geometry, and drop velocity has yet to be found. Furthermore, the edge radius might play a role and the contact angle on the microchannel walls needs to be controlled properly during its manufacturing process. In the experiments shown in Figures 5.22, the main channel surface is a rolled surface, whereas the microchannel has a milled aluminum surface. Small changes in the contact angle hysteresis might significantly change the absorption rate of the drop. The predictive capabilities of the presented framework in combination with complex surfaces are promising and represents the first step to a highly anticipated systematic modeling of drop and rivulet interacting with complex geometry in shear flow.

5.4 Summary

In many industrial applications, the simulation of forced wetting by laminar and most importantly turbulent shear flow is envisioned to reduce the costs of product development and to increase productivity. The excellent results of Chapter 4 predicting the wetting of drops an rivulets on tilted plates encourage the increase in complexity towards the investigation of wetting under shear flow. Therefore, a step-wise validation of the simulation framework concerning shear flow is mandatory to ensure the predictive capabilities.

The simulation of incipient drop motion has been compared with experiments in laminar shear flow. The dependency of the critical shear velocity on different surfaces and on a variety of drop volumes matches experimental data very well. As a novelty, the incipient motion is simulated in turbulent shear flow using a sophisticated hybrid RANS-LES turbulence model (see Section 3.7) in combination with Adaptive Mesh Refinement and Load Balancing (see Section 3.2), which allows for the necessary accuracy at the drop interface and a high resolution of the turbulent flow. Again, the dependency of the critical shear velocity on different surfaces and for a variety of drop volumes with characteristic values found in the exterior water management of vehicles, show reassuring results. Furthermore, a convergence study on the incipient motion shows a reasonable outcome. The comparison with a set of experiments by Seiler et al. (2017) is exceptionally good and confirms the theoretical predictions of the point of incipient motion. The model of Roisman et al. (2015) for incipient motion in laminar shear flow is based on a force balance of the adhesion and the drag force. The model has been applied to turbulent flow and simplifying assumptions are analyzed with simulation results. The simulations naturally provide the drag coefficient of the drop at the point of incipient motion, which originally had to be fitted for each experiment. Simulations and theory, as well as the experiments, are in very good agreement. Hence, the model by Roisman et al. (2008) is expandable to turbulent flows if the turbulent velocity profile is known by experiments, by simulations or limited to simple geometries by the universal law of the wall. As one of the major achievements of this study, the selected models within the simulation framework have shown accurate predictive capabilities for the incipient motion of drops in turbulent shear flow.

Drop oscillations have an impact on drag force, the point of incipient motion and play a role in the caterpillar motion of drops in shear flow. An outline of the observed oscillations in simulations is given for a variation of drop volumes, hysteresis pairs, and different Reynolds numbers. The characteristic oscillation modes are comparable with findings in literature, which encourages future research.

Theoretical models for the interaction of forced wetting with complex geometry have yet to be developed. Hence, the ability to accurately simulate such demanding cases would help to understand the underlying phenomena, which are often not accessible by experimental measurements. The capability to handle complex geometries in simulations is dictated by the principal choice of the simulation framework and the underlying mesh representation. The use of an unstructured mesh is mandatory which, however, has implications on the implementation of many applied models such as e.g. the surface tension. In this study, great care has been taken to ensure the compatibility of all models with an unstructured mesh representation. To demonstrate the capability of the numerical framework in respect to complex geometry, the forced wetting of drops in turbulent shear flow over rectangular microchannels with variable width is investigated. The simulation results are match qualitatively with results of experiments by Seiler et al. (2018a) and Mayrhofer (2018). The comparison motivates future research on the topic of forced wetting on complex geometry in shear flow.

6 Summary and outlook

The capability to accurately predict forced wetting in shear flow is highly anticipated in industrial applications, e.g. for the optimization of vehicle soiling early on in the design process. This thesis is motivated by the necessity of a highly accurate simulation framework to cover complex industrial cases, as well as, to provide phenomenological insight complementary to experimental and theoretical analysis. To cover multi-phase flow, wetting, and turbulent shear flow in cases motivated by industry, high-performance techniques and the ability to handle complex geometries are required. Therefore, in each of this research areas novelties have been presented in this work. They have been combined in one solver based on OpenFOAM, which has been extensively validated and successfully applied to relevant cases.

To efficiently discretize multiple length scales with transient transport processes, such as moving two-phase interfaces and reduce computational effort, Adaptive Mesh Refinement represents a powerful tool. The respective refinement algorithm in OpenFOAM has been enhanced, abstracting the basic 3D refinement and the underlying single criterion refinement to a versatile application in 2D, 2.5D, and 3D and a multi-criterion refinement. Thereby, severe bugs have been found and fixed to ensure accurate and stable simulations. To maintain the benefits of Adaptive Mesh Refinement on highly parallelized computations, Dynamic Load Balancing is required. An existing algorithm has been consolidated, enhanced and combined with improved Adaptive Mesh Refinement. Both, the developments in Adaptive Mesh Refinement and Dynamic Load Balancing have been published in Rettenmaier et al. (2019).

In the analyzed characteristic length scales, the surface tension plays an important role at the multi-phase interface. Using the interface capturing Volume of Fluid method, in which no explicit interface representation exists, the accurate calculation of the curvature is a major challenge especially on an unstructured mesh. Inaccuracies of the curvature calculation affect the surface tension directly and cause parasitic currents near the interface. To reduce such currents and to increase the accuracy of the simulations, three models for improved surface tension have been implemented and validated in this study: the Continuum Surface Force model, an iso-surface reconstruction of the interface and a conservative hybrid of the Volume of Fluid and Level-Set methods called S-CLSVOF(DSB). For the applications of this study, the iso-surface reconstruction model has been found to be most suitable. The modular implementation structure allows for an easy incorporation of even better models developed in the future.

A major focus of this work are the many phenomena related to the dynamic three-phase contact line. A variety of models for the discretization of the position of the contact line, the contact line velocity, the dependence of the contact angle on the contact line velocity, the contact angle hysteresis, as well as to reduce the mesh size dependency, have been implemented. All these models are part of a unique contact line library which has been successfully validated.

Shear flow in industrial applications is often turbulent. For high Reynolds numbers, the small turbulent scales cannot be resolved with a reasonable computational effort, therefore, turbulence models are necessary. The combination of turbulence models with multi-phase flow is a field of ongoing research and requires a particular treatment at the two-phase interface. On this behalf, two models, the WALE model and the $\zeta - f$-VLES model have been analyzed. The results point out, that only the latter model yields satisfactory results at the interface.

Then the piecewise validated numerical framework has been applied, first on drops and rivulets on tilted plates and then for drops in laminar and turbulent shear flow. The point of incipient motion of a drop on a slowly tilting plate has been matched in 2D and 3D with theoretical and experimental results for different surfaces and drop volumes. The accurate simulation results indicate that the adhesion force has been modeled correctly but also point out, that experimental contact angle measurements are required to be very accurate. Simulations of the continuous motion of drops sliding down a tilted plate show the characteristic cornered tail of a drop, which forms to a cusp and eventu-

ally emits droplets. These regimes are equally found in experiments. The path of a rivulet on a tilted plate can be categorized as straight, quasi-static meandering and dynamic meandering for increasing volumetric flow and constant wetting conditions. As a novelty in literature, simulations of this study recover all three regimes. A quasi-static meandering path can only be achieved when accounting for the contact angle hysteresis and the related pinning of the contact line.

Shear flow has been validated first on a drop impact case, for which the receding phase is in exceptional good agreement with experiments using the pinning boundary condition. Also for the incipient motion of drops in laminar conditions. The critical shear velocity is accurately matched for different surfaces and drop volumes described in experiments in literature. A novelty of this study is the simulation of the incipient motion of drops in turbulent shear flow with the Volume of Fluid method and a Very Large Eddy Simulation modeling the turbulence. Experiments on incipient motion of drops in turbulent shear flow by Seiler et al. (2018a) have been compared with simulations with good accordance, which encouraged the expansion of a theoretical model for incipient motion in laminar shear flow to turbulent flows on the basis of simulation data. The characteristic drop oscillation, caterpillar-like motion have been compared qualitatively with experiments.

Great care has been taken to ensure the compatibility of the applied models with unstructured meshes to be able to handle complex geometries. To show the predictive capabilities of the framework even on complex geometries, a microchannel has been placed perpendicular to the drop motion in turbulent channel flow. The interaction of a moving drop with a microchannel as obstacle depends on the drop velocity, the drop volume, and the microchannel width are in qualitative agreement with experimental findings.

All in all, the numerical framework including high-performance techniques, interface, and dynamic contact line handling, as well as turbulence modeling in combination with multi-phase flows has been successfully validated with experiments. The trustworthy validation builds a water-proof step-stone for future work on drops and rivulets in turbulent shear flow and complex geometries.

There are two possible directions for future work research, the improvement of numerical models and the simulation of related application relevant cases as well as theoretical modeling. Numerical methods are being improved constantly. Currently, Adaptive Mesh Refinement is restricted to hexahedra and prisms, therefore the next step regarding Adaptive Mesh Refinement would be the incorporation of a polyeder (un)refinement as presented in Meredith and Vukčević (2018). Especially the surface tension model has great potential for game-changing improvements. Second-order accurate geometrical Volume of Fluid methods for unstructured meshes are currently developed, among others, by Maric et al. (2013). Handling the diffusion of the interface is an ongoing challenge with algebraic Volume of Fluid methods. An improvement is expected by incorporating the Ghost-Fluid method by Vukčević et al. (2017), which has yet to be combined with surface tension modeling within OpenFOAM. Besides that, an already available advection method is the so-called iso-advector, a geometrically based volume fraction transport scheme by Roenby et al. (2016). A stable combination of this model with Adaptive Mesh Refinement and Dynamic Load Balancing in OpenFOAM would be promising. Regarding the contact line velocity, the model of Afkhami et al. (2009) did not result in the expected reduction of mesh dependence for all contact line model combinations. An incorporation of the Navier-Slip model might help in that aspect.

On the application side, the complexity of cases is to be increased by simulation of rivulets in shear flow, interaction and shedding of drops and rivulets on complex geometry. A detailed analysis of merging and breakup of drops and rivulets could also give valuable insight. Moreover, the predictive capability of the presented framework with respect to the transitions between thin films, drops, and rivulets have yet to be proven. Furthermore, the influence of surface vibration on wetting as shown by Burgmann et al. (2018) should be included. Resolving large-scale industrial applications droplet by droplet might not always be practical. Therefore, further theoretical work is necessary, in particular on the interaction of the contact line with complex geometry. Such theoretical models might base on simulations using the presented well validated numerical framework.

A Test cases for the validation of the numerical framework

The test case setups for the validation of the numerical framework are given in the following to allow for a compact presentation of Chapter 3 and provide necessary details in a unified manner. A legend and the used units are given in Table A.2.

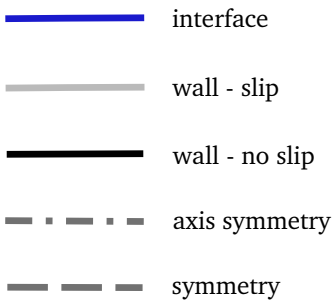

Table A.1: Legend

	Unit
ϱ	kg/m^3
ν	m^2/s
σ	$kg/(s^2m)$
θ	$^\circ$

Table A.2: Units of physical quantities

A.1 Dam break with an obstacle (3D)

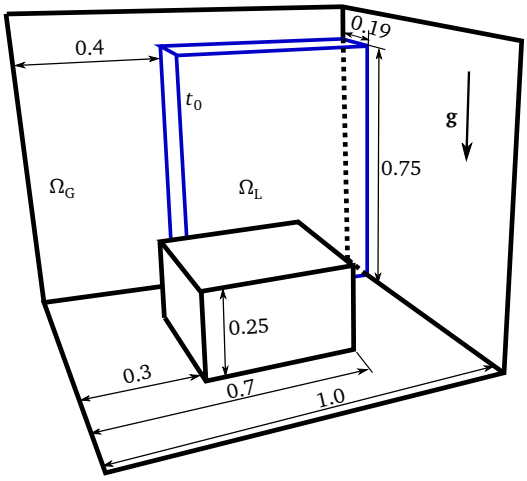

Figure A.1: 3D dam break

	Ω_L	Ω_G
ϱ	1000	1
ν	1.00×10^{-6}	14.8×10^{-6}
σ	0.070	
θ_e	90.0°	

Table A.3: Physical quantities

A dam break with a centric obstacle in 3D with measurements in Figure A.1 is given in meters. At time t_0 the liquid is initialized as a square. During the simulation the liquid is forced down due to the gravitational acceleration hitting the obstacle. The domain is cubic and surrounded by walls. For a better visualization the front and left wall are not shown.

A.2 Static drop without contact line (2D)

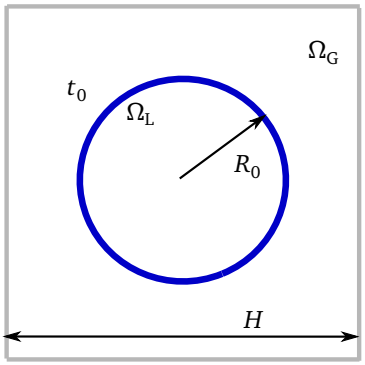

Figure A.2: 2D static drop

	Ω_L	Ω_G
ϱ	1	10^0, 10^{-1}, 10^{-3}, 10^{-5}
ν	0	0
σ	73	

Table A.4: Physical quantities

A static inviscid/viscous drop with a radius of $R_0 = 2.0\,\mathrm{m}$ is initialized in a domain measuring $H \times H = 8 \times 8\,\mathrm{m}^2$. The boundary is set to no slip for the velocity and the Courant number to $Co = 0.4$. The end time, time step, viscosity ratio, and density ratio are varied as presented in Francois et al. (2006).

A.3 Capillary rise between two plates (2D)

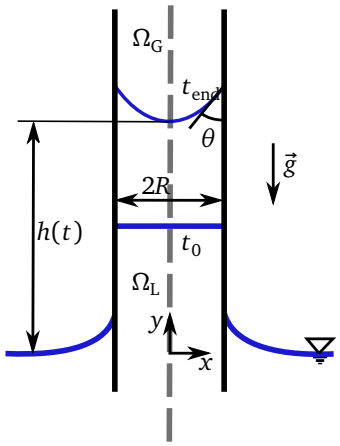

Figure A.3: Capillary rise case setup

	Ω_L	Ω_G
ϱ	998.2	1.188
ν	10.0×10^{-6}	15.35×10^{-6}
σ	0.0728	
θ_e	40.0°, 60.0°, 80.0°	

Table A.5: Physical quantities

The liquid is initialized horizontally between two plates. Due to capillary forces, the liquid forms a meniscus and rises up to a quasi-static height. The rise and final height are described analytically by Fries and Dreyer (2008). For comparability material properties and domain specs of Fath and Bothe (2015) have been used. The distance between the plates is $2R = 1.25\,\mathrm{mm}$ and the resolution $R/\Delta x = 16, 32, 64, 128$.

A.4 Drop deposition (2.5D)

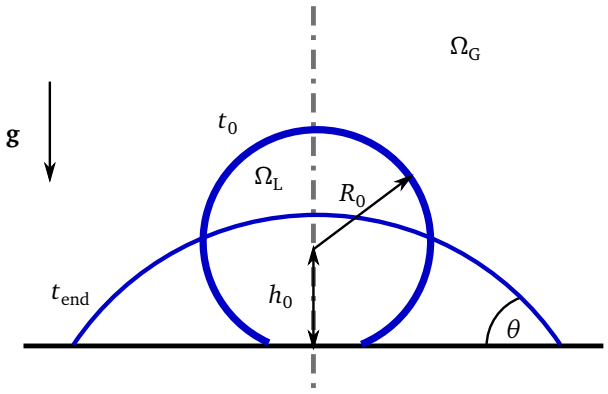

Figure A.4: Drop deposition case setup

	Ω_L	Ω_G
ϱ	809	1.20
ν	42.0×10^{-6}	150×10^{-6}
σ	0.032	
θ_e	41.5°	

Table A.6: Physical quantities

The drop is simulated in an axisymmetric domain with the dimensions $R_D \times H = 3.0 \times 3.0\,\text{mm}^2$ and a resolution of $\Delta x = 19.5\,\mu\text{m}$ at the drop, which is refined in five levels. The initial radius is $R_0 = 1.0\,\text{mm}$ and the offset to the drop center is $h_0 = 0.95\,\text{mm}$. The setup describes the experimental setup of Lavi and Marmur (2004) for the material combination of a squalane drop on a Dodecyltrichlorosilane-coated silicon wafer. This setup is used to validate the dynamic contact angle and contact line velocity models with experimental results.

A.5 Drop impact (2.5 D)

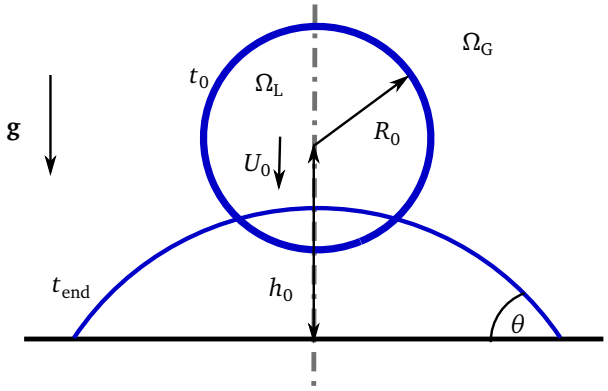

Figure A.5: Drop impact case setup

fluids	Ω_L	Ω_G
ϱ	1220	1.188
ν	95.1×10^{-6}	15.4×10^{-6}
σ	0.063	
surfaces	wax	glass
θ_e	93°	15°
θ_A	97°	17°
θ_R	90°	13°

Table A.7: Physical quantities

The drop impact case is discretized as an axisymmetric case with a domain radius of $R_D \times H = 5.0 \times 5.0\,\text{mm}^2$, a drop radius of $R_0 = 1.225\,\text{mm}$ and an offset of $h_0 = 5.0\,\text{mm}$. The case describes an experiment of Šikalo et al. (2005) of glycerin drops impacting with Weber numbers of $We = 802$ and $We = 93$ on glass and wax.

Bibliography

Adams, M., Schwartz, P. O., Johansen, H., Colella, P., Ligocki, T. J., Martin, D., Keen, N., Graves, D., Modiano, D., and Van Straalen, B. (2015). Chombo software package for AMR applications – design document. *Berkeley National Laboratory Technical Report LBNL-6616E*.

Ade, M., Jehle-Graf, E., and Duggirala, R. (2017). Multiphase simulation of external water management. In *STAR Global Conference, Berlin, March 2017*.

Afkhami, S., Zaleski, S., and Bussmann, M. (2009). A mesh-dependent model for applying dynamic contact angles to VOF simulations. *Journal of Computational Physics*, 228(15):5370 – 5389.

Ahmed, G., Sellier, M., Jermy, M., and Taylor, M. (2014). Modeling the effects of contact angle hysteresis on the sliding of droplets down inclined surfaces. *European Journal of Mechanics - B/Fluids*, 48:218 – 230.

Albadawi, A., Donoghue, D., Robinson, A., Murray, D., and Delauré, Y. (2013). On the analysis of bubble growth and detachment at low Capillary and Bond numbers using Volume of Fluid and Level Set methods. *Chemical Engineering Science*, 90:77 – 91.

Amar, M. B., Cummings, L., and Pomeau, Y. (2001). Points singuliers d'une ligne de contact mobile. *Comptes Rendus de l'Académie des Sciences - Series IIB - Mechanics*, 329(4):277 – 282.

Antonini, C., Carmona, F. J., Pierce, E., Marengo, M., and Amirfazli, A. (2009). General methodology for evaluating the adhesion force of drops and bubbles on solid surfaces. *Langmuir*, 25(11):6143 – 6154. PMID: 19408902.

Antonini, C., Innocenti, M., Horn, T., Marengo, M., and Amirfazli, A. (2011). Understanding the effect of superhydrophobic coatings on energy reduction in anti-icing systems. *Cold Regions Science and Technology*, 67(1):58 – 67.

Baniabedalruhman, A. (2015). *Dynamic meshing around fluid-fluid interfaces with applications to droplet tracking in contraction geometries*. PhD thesis, Michigan Technological University.

Barwari, B., Burgmann, S., and Janoske, U. (2018). Deformation and movement of adhering droplets in shear flow. In *5th International Conference on Experimental Fluid Mechanics 2018 in Munich*.

Batzdorf, S. (2015). *Heat transfer and evaporation during single drop impingement onto a superheated wall*. PhD thesis, Institut für Technische Thermodynamik, Technische Universität Darmstadt. PhD thesis, Technical University Darmstadt.

Berger, M. J. and Colella, P. (1989). Local Adaptive Mesh Refinement for shock hydrodynamics. *Journal of Computational Physics*, 82(1):64 – 84.

Berthier, J., Loe-Mie, F., Tran, V.-M., Schoumacker, S., Mittler, F., Marchand, G., and Sarrut, N. (2009). On the pinning of interfaces on micropillar edges. *Journal of Colloid and Interface Science*, 338(1):296 – 303.

Bianchi, G. M., Minelli, F., Scardovelli, R., and Zaleski, S. (2007). 3D large scale simulation of the high-speed liquid jet atomization. In *SAE Technical Paper*. SAE International.

Bikerman, J. (1950). Sliding of drops from surfaces of different roughnesses. *Journal of Colloid Science*, 5(4):349 – 359.

Biscarini, C., Di Francesco, S., and Manciola, P. (2010). CFD modelling approach for dam break flow studies. *Hydrology and Earth System Sciences*, 14(4):705.

Blake, T. and Ruschak, K. (1979). A maximum speed of wetting. *Nature*, 282(5738):489.

Blake, T. D. (2006). The physics of moving wetting lines. *Journal of Colloid and Interface Science*, 299(1):1 – 13.

Bommer, S., Scholl, H., Seemann, R., Kanhaiya, K., Sheraton M, V., and Verma, N. (2014). Depinning of drops on inclined smooth and topographic surfaces: Experimental and lattice Boltzmann model study. *Langmuir*, 30(37):11086 – 11095. PMID: 25154035.

Bonn, D., Eggers, J., Indekeu, J., Meunier, J., and Rolley, E. (2009). Wetting and spreading. *Reviews of Modern Physics*, 81(2):739 – 805.

Bortolin, S., Riva, E. D., and Col, D. D. (2014). Condensation in a square minichannel: Application of the VOF method. *Heat Transfer Engineering*, 35(2):193–203.

Boudaoud, A. (2007). Non-newtonian thin films with normal stresses: dynamics and spreading. *The European Physical Journal E*, 22(2):107 – 109.

Brackbill, J., Kothe, D., and Zemach, C. (1992). A continuum method for modeling surface tension. *Journal of Computational Physics*, 100(2):335 – 354.

Bracke, M., De Voeght, F., and Joos, P. (1989). The kinetics of wetting: the dynamic contact angle. In Bothorel, P. and Dufourc, E. J., editors, *Trends in Colloid and Interface Science III*, pages 142 – 149, Darmstadt. Steinkopff.

Bradshaw, P. (2013). *An introduction to turbulence and its measurement: thermodynamics and fluid mechanics series*. Elsevier.

Brennen, C. E. (2013). *Cavitation and bubble dynamics*. Cambridge University Press.

Brocchini, M. and Peregrine, D. H. (2001). The dynamics of strong turbulence at free surfaces. Part 1. Description. *Journal of Fluid Mechanics*, 449:225 – 254.

Brown, R., Orr, F., and Scriven, L. (1980). Static drop on an inclined plate: Analysis by the Finite Element Method. *Journal of Colloid and Interface Science*, 73(1):76 – 87.

Burgmann, S., Barwari, B., and Janoske, U. (2018). Oscillation of adhering droplets in shear flow. In *5th International Conference on Experimental Fluid Mechanics 2018 in Munich*.

Butt, H.-J., Graf, K., and Kappl, M. (2004). *Contact Angle Phenomena and Wetting*, pages 118 – 144. Wiley-VCH Verlag GmbH & Co. KGaA.

Chang, C.-Y., Jakirlić, S., Dietrich, K., Basara, B., and Tropea, C. (2014). Swirling flow in a tube with variably-shaped outlet orifices: An LES and VLES study. *International Journal of Heat and Fluid Flow*, 49(Supplement C):28 – 42. 8th Symposium on Turbulence & Shear Flow Phenomena (TSFP8).

Chaudhari, A. (2014). *Large-eddy simulation of wind flows over complex terrains for wind energy applications*. PhD thesis, Lappeenranta University of Technology.

Chen, Q., Ramé, E., and Garoff, S. (1997). The velocity field near moving contact lines. *Journal of Fluid Mechanics*, 337:49 – 66.

Chesnel, J., Menard, T., Reveillon, J., and Demoulin, F. (2011). Subgrid analysis of liquid jet atomization. *Atomization and Sprays*, 21(1):41 – 67.

Cheverda, V., Glushchuk, A., Queeckers, P., Chikov, S., and Kabov, O. (2013). Liquid rivulets moved by shear stress of gas flow at altered levels of gravity. *Microgravity Science and Technology*, 25(1):73 – 81. experiment, rivulet.

Chiba, M., Michiue, S., and Katayama, I. (2012). Free vibration of a spherical liquid drop attached to a conical base in zero gravity. *Journal of Sound and Vibration*, 331(8):1908 – 1925.

Choi, H. and Moin, P. (2012). Grid-point requirements for Large Eddy Simulation: Chapman's estimates revisited. *Physics of Fluids*, 24(1):011702.

Chou, T.-H., Hong, S.-J., Sheng, Y.-J., and Tsao, H.-K. (2012). Drops sitting on a tilted plate: Receding and advancing pinning. *Langmuir*, 28(11):5158 – 5166. PMID: 22372858.

Clift, R., Grace, J. R., and Weber, M. E. (2005). *Bubbles, drops, and particles*. Courier Corporation.

Cooke, J., Gu, S., Armstrong, L., and Luo, K. (2012). Gas-liquid flow on smooth and textured inclined planes. *World Academy of Science, Engineering and Technology*, 6(8):1449 – 1457.

Couvreur, S. and Daerr, a. (2012). The role of wetting heterogeneities in the meandering instability of a partial wetting rivulet. *EPL (Europhysics Letters)*, 99(2):24004.

Cox, R. G. (1986). The dynamics of the spreading of liquids on a solid surface. part 1. viscous flow. *Journal of Fluid Mechanics*, 168:169–194.

Culkin, J. and Davis, S. H. (1982). Meandering of water rivulets. *American Institute of Chemical Engineers Journal*, 30(2):263 – 267.

Cummins, S. J., Francois, M. M., and Kothe, D. B. (2005). Estimating curvature from volume fractions. *Computers & Structures*, 83(6):425 – 434. Frontier of Multi-Phase Flow Analysis and Fluid-Structure.

Daerr, A., Eggers, J., Limat, L., and Valade, N. (2011). General mechanism for the meandering instability of rivulets of newtonian fluids. *Physical Review Letters*, 106(18):4 – 7.

De Gennes, P. and Hervet, H. (1984). Dynamique du mouillage: films précurseurs sur solide sec. *Comptes rendus de l'Académie des sciences*, 299:499.

De Gennes, P. G. (1985). Wetting: statics and dynamics. *Reviews of Modern Physics*, 57:827 – 863.

De Villiers, E. (2007). *The potential of Large Eddy Simulation for the modelling of wall bounded flows*. PhD thesis, University of London.

Deising, D., Bothe, D., and Marschall, H. (2018). Direct Numerical simulation of mass transfer in bubbly flows. *Computers & Fluids*.

Denner, F. and van Wachem, B. G. (2015). Numerical time-step restrictions as a result of capillary waves. *Journal of Computational Physics*, 285:24 – 40.

Deshpande, S. S., Anumolu, L., and Trujillo, M. F. (2012). Evaluating the performance of the two-phase flow solver interFoam. *Computational Science & Discovery*, 5(1):014016.

Desjardins, O., Pitsch, H., et al. (2010). Detailed numerical investigation of turbulent atomization of liquid jets. *Atomization and Sprays*, 20(4):311.

Dianat, M., Skarysz, M., and Garmory, A. (2017a). A coupled Level Set and Volume of Fluid method for automotive exterior water management applications. *International Journal of Multiphase Flow*, 91:19 – 38.

Dianat, M., Skarysz, M., Hodgson, G., Garmory, A., and Passmore, M. (2017b). Coupled Level-Set Volume of Fluid simulations of water flowing over a simplified drainage channel with and without air coflow. *SAE International Journal of Passenger Cars - Mechanical Systems*, 10(1):369 – 377.

Dijkhuizen, W., Roghair, I., van Sint Annaland, M., and Kuipers, H. (2010). DNS of gas bubbles behaviour using an improved 3D front tracking model – Model development. *Chemical Engineering Science*, 65:1427 – 1437.

Dimitrakopoulos, P. and Higdon, J. J. L. (1999). On the gravitational displacement of three-dimensional fluid droplets from inclined solid surfaces. *Journal of Fluid Mechanics*, 395:181 – 209.

Dimitrakopoulos, P. and Higdon, J. J. L. (2001). On the displacement of three-dimensional fluid droplets adhering to a plane wall in viscous pressure-driven flows. *Journal of Fluid Mechanics*, 435:327 – 350.

Ding, H. and Spelt, P. D. M. (2008). Onset of motion of a three-dimensional droplet on a wall in shear flow at moderate Reynolds numbers. *Journal of Fluid Mechanics*, 599:341–362.

Duffy, B. R. and Moffatt, H. K. (1995). Flow of a viscous trickle on a slowly varying incline. *The Chemial Engineering Journal*, 60:141 – 146.

Dupont, J.-B. and Legendre, D. (2010). Numerical simulation of static and sliding drop with contact angle hysteresis. *Journal of Computational Physics*, 229(7):2453 – 2478.

Duquennoy, C., Lebaigue, O., and Magnaudet, J. (2001). A numerical model of gas-liquid-solid contact line. In King, A. C. and Shikhmurzaev, Y. D., editors, *IUTAM Symposium on Free Surface Flows*, pages 89 – 98, Dordrecht. Springer Netherlands.

Durbin, P. (1996). On the k-3 stagnation point anomaly. *International Journal of Heat and Fluid Flow*, 17(1):89 – 90.

Durbin, P. A. (1991). Near-wall turbulence closure modeling without “damping functions”. *Theoretical and Computational Fluid Dynamics*, 3(1):1 – 13.

Dussan, V. (1976). The moving contact line: the slip boundary condition. *Journal of Fluid Mechanics*, 77:665 – 684.

Dussan, V., B., E., and Davis, S. H. (1974). On the motion of a fluid-fluid interface along a solid surface. *Journal of Fluid Mechanics*, 65(1):71 – 95.

Dussan V., E. B. (1985). On the ability of drops or bubbles to stick to non-horizontal surfaces of solids. Part 2. Small drops or bubbles having contact angles of arbitrary size. *Journal of Fluid Mechanics*, 151:1 – 20.

Dussan V., E. B. and Chow, R. T.-P. (1983). On the ability of drops or bubbles to stick to non-horizontal surfaces of solids. *Journal of Fluid Mechanics*, 137:1 – 29.

Eick, J., Good, R., and Neumann, A. (1975). Thermodynamics of contact angles. II. Rough solid surfaces. *Journal of Colloid and Interface Science*, 53(2):235 – 248.

Engelnkemper, S., Wilczek, M., Gurevich, S. V., and Thiele, U. (2016). Morphological transitions of sliding drops: Dynamics and bifurcations. *Phys. Rev. Fluids*, 1:073901.

Eral, H. B., ’t Mannetje, D. J. C. M., and Oh, J. M. (2013). Contact angle hysteresis: a review of fundamentals and applications. *Colloid and Polymer Science*, 291(2):247 – 260.

Eres, M. H., Schwartz, L. W., and Roy, R. V. (2000). Fingering phenomena for driven coating films. *Physics of Fluids*, 12(6):1278 – 1295.

Fan, J., Wilson, M., and Kapur, N. (2011). Displacement of liquid droplets on a surface by a shearing air flow. *Journal of Colloid and Interface Science*, 356(1):286 – 292.

Fang, C., Hidrovo, C., min Wang, F., Eaton, J., and Goodson, K. (2008). 3-D numerical simulation of contact angle hysteresis for microscale two phase flow. *International Journal of Multiphase Flow*, 34(7):690 – 705.

Fath, A. and Bothe, D. (2015). Direct Numerical Simulations of thermocapillary migration of a droplet attached to a solid wall. *International Journal of Multiphase Flow*, 77:209 – 221.

Fathi, N., Mertens, K., Putkaradze, V., and Vorobieff, P. (2014). Comment on "The role of wetting heterogeneities in the meandering instability of a partial wetting rivulet" by Couvreur S. and Daerr A. *EPL (Europhysics Letters)*, 108(5):54002.

Fedkiw, R. P., Aslam, T., Merriman, B., and Osher, S. (1999). A non-oscillatory eulerian approach to interfaces in multimaterial flows (the ghost fluid method). *Journal of Computational Physics*, 152(2):457 – 492.

Feldmann, J., Roisman, I., and Tropea, C. (2018). Shear driven liquid film shapes on a solid substrate. In *Proceedings of the ICLASS 2018 Conference in Chicago*.

Flaherty, J., Loy, R., Shephard, M., Szymanski, B., Teresco, J., and Ziantz, L. (1997). Adaptive Local Refinement with octree Load Balancing for the parallel solution of three-dimensional conservation laws. *Journal of Parallel and Distributed Computing*, 47(2):139 – 152.

Fondelli, T., Andreini, A., and Facchini, B. (2015). Numerical simulation of dam-break problem using an adaptive meshing approach. *Energy Procedia*, 82:309 – 315.

Francois, M. M., Cummins, S. J., Dendy, E. D., Kothe, D. B., Sicilian, J. M., and Williams, M. W. (2006). A balanced-force algorithm for continuous and sharp interfacial surface tension models within a volume tracking framework. *Journal of Computational Physics*, 213(1):141 – 173.

Frenkel, Y. I. (1948). O povedenii zhidkikh kapel na poverkhnosti tverdogo tela. 1. skatyvanie kapel s naklonnoi poverkhnosti. *Zhurnal Eksperimentalnoi I Teoreticheskoi Fiziki*, 18(7):659 – 667. Translation by V. Berejnov: http://xxx.lanl.gov/abs/physics/0503051.

Fries, N. and Dreyer, M. (2008). An analytic solution of capillary rise restrained by gravity. *Journal of Colloid and Interface Science*, 320(1):259 – 263.

Fröhlich, J. and von Terzi, D. (2008). Hybrid LES/RANS methods for the simulation of turbulent flows. *Progress in Aerospace Sciences*, 44(5):349 – 377.

Gada, V. H., Tandon, M. P., Elias, J., Vikulov, R., and Lo, S. (2017). A large scale interface multi-fluid model for simulating multiphase flows. *Applied Mathematical Modelling*, 44:189 – 204.

Gao, N., Geyer, F., Pilat, D. W., Wooh, S., Vollmer, D., Butt, H.-J., and Berger, R. (2018). How drops start sliding over solid surfaces. *Nature Physics*, 14:191 – 196.

Gibbs, J. W. (1928). *The collected works of J. Willard Gibbs, volume I: thermodynamics*. Yale University Press.

Glasstone, S., Laidler, K. J., and Eyring, H. (1941). The theory of rate processes; the kinetics of chemical reactions, viscosity, diffusion and electrochemical phenomena. Technical report, McGraw-Hill Book Company,.

Güttler, A. (2017). *High accuracy determination of skin friction differences in an air channel flow based on pressure drop measurements*. PhD thesis, Karlsruhe Institute of Technology.

Hagemeier, T., Hartmann, M., and Thévenin, D. (2011). Practice of vehicle soiling investigations: A review. *International Journal of Multiphase Flow*, 37(8):860 – 875.

Han, X. and Krajnović, S. (2013). Validation of a novel Very Large Eddy Simulation method for simulation of turbulent separated flow. *International Journal for Numerical Methods in Fluids*, 73(5):436 – 461.

Hanjalić, K., Popovac, M., and Hadžiabdić, M. (2004). A robust near-wall elliptic-relaxation eddy-viscosity turbulence model for CFD. *International Journal of Heat and Fluid Flow*, 25(6):1047 – 1051.

Hao, L. and Cheng, P. (2009). Lattice Boltzmann simulations of liquid droplet dynamic behavior on a hydrophobic surface of a gas flow channel. *Journal of Power Sources*, 190(2):435 – 446.

Hasenzahl, M. T. (2018). Simulation of Drop Motion in Turbulent Channel Flow. Master thesis, Institut for Fluid Mechanics and Aerodynamics, Technical University Darmstadt.

Haspel, P. (2017). Simulation of Drops and Rivulets in Shear Flow. Master thesis, Institut for Fluid Mechanics and Aerodynamics, Technical University Darmstadt.

Herminghaus, S., Brinkmann, M., and Seemann, R. (2008). Wetting and dewetting of complex surface geometries. *Annual Review of Materials Research*, 38:101 – 121.

Herrada, M. A., Mohamed, A. S., Montanero, J. M., and Gañán-Calvo, A. (2015). Stability of a rivulet flowing in a microchannel. *International Journal of Multiphase Flow*, 69:1 – 7.

Herrmann, M. (2010). Detailed numerical simulations of the primary atomization of a turbulent liquid jet in crossflow. *Journal of Engineering for Gas Turbines and Power*, 132(6):10.

Herrmann, M. and Gorokhovski, M. (2009). A Large Eddy Simulation subgrid model for turbulent phase interface dynamics. In *11th Triennial International Annual Conference on Liquid Atomization and Spray Systems*, Vail Colorado USA.

Hirsch, C. (2007). *Numerical computation of internal and external flows – The fundamentals of Computational Fluid Dynamics*, volume 1. John Wiley & Sons, Ltd., second edition.

Hirt, C. and Nichols, B. (1981). Volume of Fluid (VOF) method for the dynamics of free boundaries. *Journal of Computational Physics*, 39(1):201 – 225.

Hocking, L. M. (1976). A moving fluid interface on a rough surface. *Journal of Fluid Mechanics*, 76(4):801 – 817.

Hoffman, R. L. (1975). A study of the advancing interface. i. interface shape in liquid—gas systems. *Journal of colloid and interface science*, 50(2):228 – 241.

Hu, H., Huang, S., and Chen, L. (2013). Displacement of liquid droplets on micro-grooved surfaces with air flow. *Experimental Thermal and Fluid Science*, 49:86 – 93.

Huh, C. and Mason, S. (1977). Effects of surface roughness on wetting (theoretical). *Journal of Colloid and Interface Science*, 60(1):11 – 38.

Huh, C. and Scriven, L. (1971). Hydrodynamic model of steady movement of a solid/liquid/fluid contact line. *Journal of Colloid and Interface Science*, 35(1):85 – 101.

Iliev, S. D. (1997). Static drops on an inclined plane: Equilibrium modeling and numerical analysis. *Journal of Colloid and Interface Science*, 194(2):287 – 300.

Iso, Y. and Chen, X. (2011). Flow transition behavior of the wetting flow between the film flow and rivulet flow on an inclined wall. *Journal of Fluids Engineering*, 133(9):091101.

Issa, R., Gosman, A., and Watkins, A. (1986). The computation of compressible and incompressible recirculating flows by a non-iterative implicit scheme. *Journal of Computational Physics*, 62(1):66 – 82.

Janardan, N. and Panchagnula, M. V. (2014). Effect of the initial conditions on the onset of motion in sessile drops on tilted plates. *Colloids and Surfaces A: Physicochemical and Engineering Aspects*, 456:238 – 245.

Jasak, H. (1996). *Error Analysis and Estimation for the Finite Volume Method with Applications to Fluid Flows*. PhD thesis, Imperial College of Science, Technology and Medicine, London.

Jasak, H. (2009). Openfoam: Open source CFD in research and industry. *International Journal of Naval Architecture and Ocean Engineering*, 1(2):89 – 94.

Jiang, T.-S., Soo-Gun, O., and Slattery, J. C. (1979). Correlation for dynamic contact angle. *Journal of Colloid and Interface Science*, 69(1):74 – 77.

Johnson, R. E. and Dettre, R. H. (1993). Hydrodynamics of wetting. In Berg, J. C., editor, *Wettability*, pages 1–74. Marcel Dekker, New York.

Juretic, F. and Gosman, A. D. (2010). Error analysis of the Finite-Volume Method with respect to mesh type. *Numerical Heat Transfer Part B-Fundamentals*, 57:414 – 439.

Ketterl, S. and Klein, M. (2018). A-priori assessment of subgrid scale models for large-eddy simulation of multiphase primary breakup. *Computers & Fluids*, 165:64 – 77.

Kim, J. (2007). Spray cooling heat transfer: The state of the art. *International Journal of Heat and Fluid Flow*, 28(4):753 – 767. Including Special Issue of Conference on Modelling Fluid Flow (CMFF 2006), Budapest.

Kistler, S. F. (1993). Hydrodynamics of wetting. In Berg, J. C., editor, *Wettability*, pages 311 – 429. Marcel Dekker, New York.

Knoche, M. (1994). Effect of droplet size and carrier volume on performance of foliage-applied herbicides. *Crop Protection*, 13(3):163 – 178.

Kolmogorov, A. N. (1941). The local structure of turbulence in incompressible viscous fluid for very large Reynolds numbers. In *Doklady Akademii Nauk SSSR*, volume 30, pages 299 – 303.

Kondratyuk, A. (2017). *Investigation of the Very Large Eddy Simulation Model in the Context of Fluid-Structure Interaction*. PhD thesis, Technische Universität, Darmstadt.

Krumbein, B., Forooghi, P., Jakirlić, S., Magagnato, F., and Frohnapfel, B. (2017). VLES modeling of flow over walls with variably-shaped roughness by reference to complementary DNS. *Flow, Turbulence and Combustion*, 99(3):685 – 703.

Kunkelmann, C. (2011). *Numerical Modeling and Investigation of Boiling Phenomena*. PhD thesis, Institut für Technische Thermodynamik, Technische Universität Darmstadt.

Labourasse, E., Lacanette, D., Toutant, A., Lubin, P., Vincent, S., Lebaigue, O., Caltagirone, J.-P., and Sagaut, P. (2007). Towards Large Eddy Simulation of isothermal two-phase flows: Governing equations and a priori tests. *International Journal of Multiphase Flow*, 33:1 – 39.

Lavi, B. and Marmur, A. (2004). The exponential power law: partial wetting kinetics and dynamic contact angles. *Colloids and Surfaces A: Physicochemical and Engineering Aspects*, 250(1):409 – 414. In honour of the 250th volume of Colloid and Surfaces A and the 25th Anniversary of the International Association of Colloid and Interface Scientists (IACIS).

Le Grand-Piteira, N., Daerr, A., and Limat, L. (2005). Shape and motion of drops sliding down an inclined plane. *Journal of Fluid Mechanics*, 541:293 – 315.

Le Grand-Piteira, N., Daerr, A., and Limat, L. (2006). Meandering rivulets on a plane: A simple balance between inertia and capillarity. *Physical Review Letters*, 96:254503.

Linder, N. (2015). *Numerical Simulation of Complex Wetting*. PhD thesis, Technische Universität Darmstadt.

Linder, N., Criscione, A., Roisman, I. V., Marschall, H., and Tropea, C. (2015). 3D computation of an incipient motion of a sessile drop on a rigid surface with contact angle hysteresis. *Theoretical and Computational Fluid Dynamics*, 29(5-6):373 – 390.

Liovic, P. and Lakehal, D. (2007). Interface–turbulence interactions in large-scale bubbling processes. *International Journal of Heat and Fluid Flow*, 28(1):127 – 144. The International Conference on Heat Transfer and Fluid Flow in Microscale (HTFFM-05).

Liovic, P. and Lakehal, D. (2012). Subgrid-scale modelling of surface tension within interface tracking-based large eddy and interface simulation of 3D interfacial flows. *Computers & Fluids*, 63:27 – 46.

Lippert, A. C. (2016). *Direct Numerical Simulations of Thermocapillary Driven Motions in Two-phase Flows*. PhD thesis, Technische Universität, Darmstadt.

Liu, Z., Hill, J. C., Fox, R. O., Passalacqua, A., and Olsen, M. G. (2019). A Delayed Detached Eddy Simulation model with low Reynolds number correction for transitional swirling flow in a multi-inlet vortex nanoprecipitation reactor. *Chemical Engineering Science*, 193:66 – 75.

Losasso, F., Fedkiw, R., and Osher, S. (2006). Spatially adaptive techniques for Level Set methods and incompressible flow. *Computers & Fluids*, 35(10):995 – 1010.

López, J. and Hernández, J. (2008). Analytical and geometrical tools for 3D Volume of Fluidmethods in general grids. *Journal of Computational Physics*, 227(12):5939 – 5948.

M. van Sint Annaland, W. D., Deen, N., and Kuipers, H. (2006). Numerical simulation of behaviour of gas bubbles using a 3-D front-tracking method. *American Institute of Chemical Engineers Journal*, 52(1):99 – 110.

Maglio, M. and Legendre, D. (2014). *Numerical Simulation of Sliding Drops on an Inclined Solid Surface*, pages 47–69. Springer International Publishing, Cham.

Manukyan, S. (2013). *Fundamental Investigation of Forced Wetting on Structured Surfaces*. PhD thesis, TU Darmstadt, Darmstadt.

Maric, T., Marschall, H., and Bothe, D. (2013). voFoam - A geometrical Volume of Fluidalgorithm on arbitrary unstructured meshes with local dynamic Adaptive Mesh Refinement using OpenFOAM. *ArXiv e-prints*.

Marschall, H. (2011). *Towards the Numerical Simulation of Multi-Scale Two-Phase Flows*. PhD thesis, Technische Universität München, Lehrstuhl I für Technische Chemie.

Marshall, J. S. and Ettema, R. (2004). Rivulet dynamics with variable gravity and wind shear. Technical report.

Maurer, T. (2017). *Experimentelle und numerische Untersuchung der Tropfenbewegung unter Einfluss von äußeren Kräften*. PhD thesis, Bergische Universität Wuppertal.

Maurer, T. and Janoske, U. (2015). Displacement of water droplets induced by the superposition of shear flows and mechanical vibrations. In *Proceedings of 2nd International Conference on Fluid Flow, Heat and Mass Transfer, Ottawa*.

Maurer, T., Mebus, A., and Janoske, U. (2016). Water droplet motion on an inclining surface. In *Proceedings of the 3rd International Conference on Fluid Flow, Heat and Mass Transfer (FFHMT'16), Ottawa, Canada–May*, pages 2 – 3.

Mayrhofer, A. (2018). Experimentelle Untersuchung des Verhaltens von durch Scherkräfte bewegte Tropfen an Spalten.

Meredith, K., Heather, A., De Vries, J., and Xin, Y. (2011). A numerical model for partially-wetted flow of thin liquid films. *Computational Methods in Multiphase Flow VI*, 70:239.

Meredith, K. and Vukčević, V. (2018). Resolving the near-field flow patterns of an idealized fire sprinkler with VOF modeling and Adpative Mesh Refinement. 13th OpenFOAM Workshop in Shanghai China.

Milne, A., Defez, B., Cabrerizo-Vílchez, M., and Amirfazli, A. (2014). Understanding (sessile/constrained) bubble and drop oscillations. *Advances in Colloid and Interface Science*, 203:22 – 36.

Milne, A. J. B. (2013). *Blown Away: The Shedding and Oscillation of Sessile Drops by Cross Flowing Air*. PhD thesis, University of Alberta.

Milne, A. J. B. and Amirfazli, A. (2009). Drop shedding by shear flow for hydrophilic to superhydrophobic surfaces†. *Langmuir*, 25(24):14155 – 14164.

Misaka, T., Sasaki, D., and Obayashi, S. (2017). Adaptive Mesh Refinement and Load Balancing based on multi-level block-structured cartesian mesh. *International Journal of Computational Fluid Dynamics*, 31(10):476 – 487.

Moghtadernejad, S., Jadidi, M., Dolatabadi, A., and Esmail, N. (2015a). Sph simulation of rivulet dynamics on surfaces with various wettabilities. *SAE International Journal of Aerospace*, 8(1):160 – 173.

Moghtadernejad, S., Mohammadi, M., Jadidi, M., Tembely, M., and Dolatabadi, A. (2013). Shear driven droplet shedding on surfaces with various wettabilities. *SAE International Journal of Aerospace*, 6(2):459 – 464.

Moghtadernejad, S., Tembely, M., Jadidi, M., Esmail, N., and Dolatabadi, A. (2015b). Shear driven droplet shedding and coalescence on a superhydrophobic surface. *Physics of Fluids*, 27(3):032106.

Mooney, K. (2015). Implementation of a moving immersed boundary method on a dynamically refining mesh with automatic Load Balancing. 10th OpenFOAM Workshop Ann Arbor MI.

Moser, R. D., Kim, J., and Mansour, N. N. (1999). Direct Numerical Simulation of turbulent channel flow up to $re_\tau = 590$. *Physics of Fluids*, 11(4):943–945.

Moukalled, F., Mangani, L., and Darwish, M. (2016). The Finite Volume Method in Computational Fluid Dynamics. *Springer International Publishing*, 113.

Müller, P. (2016). *Simulation von Tropfenbewegung auf schiefen Platten in Scherströmung*. Bachelor thesis, Technical University Darmstadt.

Muzaferija, S. and Perìc, M. (1997). Computations of free-surface flows using the Finite-Volume Method and moving grids. *Numerical Heat Transfer Part B-Fundamentals*, 32:369 – 384.

Nakagawa, T. and Scott, J. C. (1984). Stream meanders on a smooth hydrophobic surface. *Journal of Fluid Mechanics*, 149:89 – 99.

Navier, C. (1823). Mémoire sur les lois du mouvement des fluides. *Mémoires de l'Académie Royale des Sciences de l'Institut de France*, 6(1823):389 – 440.

Nicoud, F. and Ducros, F. (1999). Subgrid-scale stress modeling based on the square of the velocity gradient tensor. *Flow, Turbulence and Combustion*, 62(3):183 – 200.

Nieuwstadt, F. T., Westerweel, J., and Boersma, B. J. (2016). *Turbulence: introduction to theory and applications of turbulent flows*. Springer.

Oliver, J., Huh, C., and Mason, S. (1977). Resistance to spreading of liquids by sharp edges. *Journal of Colloid and Interface Science*, 59(3):568 – 581.

Osher, S. and Sethian, J. A. (1988). Fronts propagating with curvature-dependent speed: Algorithms based on Hamilton-Jacobi formulations. *Journal of Computational Physics*, 79(1):12 – 49.

Park, J. K. and Kang, K. H. (2012). Numerical analysis of moving contact line with contact angle hysteresis using feedback deceleration technique. *Physics of Fluids*, 24(4):042105.

Peskin, C. S. (1972). Flow patterns around heart valves: a numerical method. *Journal of Computational Physics*, 10(2):252 – 271.

Pierce, E., Carmona, F., and Amirfazli, A. (2008). Understanding of sliding and contact angle results in tilted plate experiments. *Colloids and Surfaces A: Physicochemical and Engineering Aspects*, 323(1):73 – 82. Bubble and Drop Interfaces.

Podgorski, T. (2000). *Ruissellement en conditions de mouillage partiel*. PhD thesis, Université Pierre et Marie Curie-Paris VI.

Podgorski, T., Flesselles, J.-M., and Limat, L. (2001). Corners, cusps, and pearls in running drops. *Physical Review Letters*, 87:036102.

Poo, J. and Ashgriz, N. (1989). A computational method for determining curvatures. *Journal of Computational Physics*, 84(2):483 – 491.

Pope, S. B. (2000). *Turbulent Flows*. Cambridge University Press.

Popinet, S. (2018). Numerical models of surface tension. *Annual Review of Fluid Mechanics*, 50(1):49 – 75.

Popinet, S. and Zaleski, S. (1999). A front-tracking algorithm for accurate representation of surface tension. *International Journal for Numerical Methods in Fluids*, 30(6):775 – 793.

Popovac, M. and Hanjalic, K. (2007). Compound wall treatment for RANS computation of complex turbulent flows and heat transfer. *Flow, Turbulence and Combustion*, 78(2):177.

Prabhala, B. R., Panchagnula, M. V., and Vedantam, S. (2013). Three-dimensional equilibrium shapes of drops on hysteretic surfaces. *Colloid and Polymer Science*, 291(2):279 – 289.

Ramaswamy, B., Krishnamoorthy, S., and Joo, S. (1997). Three-dimensional simulation of instabilities and rivulet formation in heated falling films. *Journal of Computational Physics*, 131(1):70 – 88.

Rein, M. (1993). Phenomena of liquid drop impact on solid and liquid surfaces. *Fluid Dynamics Research*, 12(2):61 – 93.

Rek, Z., Gregorc, J., Bouaifi, M., and Daniel, C. (2017). Numerical simulation of gas jet in liquid crossflow with high mean jet to crossflow velocity ratio. *Chemical Engineering Science*, 172:667 – 676.

Ren, L. (2017). Simulation of Drops in Turbulent Channel Flow. Master thesis, Institut for Fluid Mechanics and Aerodynamics, Technical University Darmstadt.

Renardy, Y. and Renardy, M. (2002). Prost: A parabolic reconstruction of surface tension for the Volume-Of-Fluid method. *Journal of Computational Physics*, 183(2):400 – 421.

Rettenmaier, D., Deising, D., Marschall, H., and Tropea, C. (2016). Kontaktlinien-Modellierung in einer algebraischen Volume-Of-Fluid Methode auf unstrukturierten Gittern mit OpenFOAM. In *Jahrestreffen der ProcessNet-Fachgruppen Agglomerations- und Schüttguttechnik, Computational Fluid Dynamics und Mehrphasenströmungen*.

Rettenmaier, D., Deising, D., Ouedraogo, Y., Gjonaj, E., De Gersem, H., Bothe, D., Tropea, C., and Marschall, H. (2018). Load balanced 2D and 3D Adaptive Mesh Refinement. In *6th OpenFOAM Conference 2018*.

Rettenmaier, D., Deising, D., Ouedraogo, Y., Gjonaj, E., De Gersem, H., Bothe, D., Tropea, C., and Marschall, H. (2019). Load Balanced 2D and 3D Adaptive Mesh Refinement in OpenFOAM. *SoftwareX*. under review.

Rettenmaier, D., Marschall, H., and Tropea, C. (2017). 3D simulation of pinning of droplets on tilted surfaces with openfoam. In *3rd International Conference on Numerical Methods in Multiphase Flows (ICNMMF-III)*.

Reynolds, O. (1883). I883: An experimental investigation of the circumstances which determine whether the motion of water shall be direct or sinuous, and of the law of resistance in parallel channels. *Philosophical Transactions of the Royal Society*, 17:935 – 982.

Reynolds, O. (1895). Iv. on the dynamical theory of incompressible viscous fluids and the determination of the criterion. *Philosophical Transactions of the Royal Society of London A: Mathematical, Physical and Engineering Sciences*, 186:123 – 164.

Richardson, L. F. (2007). *Weather prediction by numerical process*. Cambridge University Press.

Rider, W. J. and Kothe, D. B. (1998). Reconstructing volume tracking. *Journal of Computational Physics*, 141(2):112 – 152.

Rioboo, R., Marengo, M., and Tropea, C. (1999). Outcomes from a drop impact on solid surfaces. In *Proceedings of the Conference on Liquid Atomization and Spray Systems, Toulouse*. Also published in: *Atomization and sprays*. (2001) 11:155-165.

Roenby, J., Bredmose, H., and Jasak, H. (2016). A computational method for sharp interface advection. *Royal Society Open Science*, 3(11).

Roisman, I. V., Criscione, A., Tropea, C., Mandal, D. K., and Amirfazli, A. (2015). Dislodging a sessile drop by a high-Reynolds-number shear flow at subfreezing temperatures. *Physical Review E*, 92:023007.

Roisman, I. V., Opfer, L., Tropea, C., Raessi, M., Mostaghimi, J., and Chandra, S. (2008). Drop impact onto a dry surface: Role of the dynamic contact angle. *Colloids and Surfaces a-Physicochemical and Engineering Aspects*, 322(1-3):183 – 191.

Roohi, E., Zahiri, A. P., and Passandideh-Fard, M. (2013). Numerical simulation of cavitation around a two-dimensional hydrofoil using VOF method and LES turbulence model. *Applied Mathematical Modelling*, 37(9):6469 – 6488.

Saad, Y. (2003). Iterative methods for sparse linear systems. *Society for Industrial and Applied Mathematics*, Second Edition.

Sagaut, P. (2006). *Large eddy simulation for incompressible flows: an introduction*. Springer Science & Business Media.

Schäfer, M. (2006). *Computational Engineering — Introduction to Numerical Methods*. Springer-Verlag Berlin Heidelberg, Berlin, Heidelberg.

Schleizer, A. and Bonnecaze, R. (1999). Displacement of a two-dimensional immiscible droplet adhering to a wall in shear and pressure-driven flows. *Journal of Fluid Mechanics*, 383:29 – 54.

Schmitt, F. G. (2007). About boussinesq's turbulent viscosity hypothesis: historical remarks and a direct evaluation of its validity. *Comptes Rendus Mécanique*, 335(9):617 – 627.

Schwartz, L., Roux, D., and Cooper-White, J. (2005). On the shapes of droplets that are sliding on a vertical wall. *Physica D: Nonlinear Phenomena*, 209(1-4):236 – 244.

Schwing, A., Nompelis, I., and Candler, G. (2013). Implementation of adaptive mesh refinement in an implicit unstructured finite-volume flow solver. In *21st AIAA Computational Fluid Dynamics Conference, San Diego, CA*. American Institute of Aeronautics and Astronautics.

Seemann, R., Brinkmann, M., Kramer, E. J., Lange, F. F., and Lipowsky, R. (2005). Wetting morphologies at microstructured surfaces. *Proceedings of the National Academy of Sciences of the United States of America*, 102(6):1848 – 1852.

Seevaratnam, G., Ding, H., Michel, O., Heng, J., and Matar, O. (2010). Laminar flow deformation of a droplet adhering to a wall in a channel. *Chemical Engineering Science*, 65(16):4523 – 4534.

Seiler, P. M., Rettenmaier, D., Roisman, I. V., and Tropea, C. (2018a). Shear driven drop propagation and breakup on a solid substrate. In *32st Conference of the European Colloid and Interface Society, Ljubljana, Slowenia, September 2018*.

Seiler, P. M., Roisman, I. V., Matthes, S., and Tropea, C. (2017). Shear driven motion of a liquid drop on a smooth rigid substrate. In *ILASS-Americas 29th Annual Conference on Liquid Atomization and Spray Systems, North and South America*.

Seiler, P. M., Roisman, I. V., and Tropea, C. (2018b). Shear driven drop propagation and breakup on a solid substrate. In *14th International Conference on Liquid Atomization and Spray Systems, Chicago, IL, USA, July 2018*.

Semprebon, C. and Brinkmann, M. (2014). On the onset of motion of sliding drops. *Soft Matter*, 10(18):3325 – 3334.

Seppecher, P. (1996). Moving contact lines in the Cahn-Hilliard theory. *International Journal of Engineering Science*, 34(9):977 – 992.

Sethian, J. A. and Smereka, P. (2003). Level Set methods for fluid interfaces. *Annual Review of Fluid Mechanics*, 35(1):341 – 372.

Shen, C. and Ruth, D. W. (1998). Experimental and numerical investigations of the interface profile close to a moving contact line. *Physics of Fluids*, 10(4):789–799.

Shikhmurzaev, Y. (1993). The moving contact line on a smooth solid surface. *International Journal of Multiphase Flow*, 19(4):589 – 610.

Shikhmurzaev, Y. D. (1997). Moving contact lines in liquid/liquid/solid systems. *Journal of Fluid Mechanics*, 334:211 – 249.

Shikhmurzaev, Y. D. (2007). *Capillary flows with forming interfaces*. Chapman and Hall/CRC.

Shuttleworth, R. and Bailey, G. (1948). The spreading of a liquid over a rough solid. *Discussions of the Faraday Society*, 3:16 – 22.

Singh, M., Haverinen, H. M., Dhagat, P., and Jabbour, G. E. (2009). Inkjet printing—process and its applications. *Advanced Materials*, 22(6):673 – 685.

Singh, R. K., Galvin, J. E., and Sun, X. (2016). Three-dimensional simulation of rivulet and film flows over an inclined plate: Effects of solvent properties and contact angle. *Chemical Engineering Science*, 142:244 – 257.

Singh, R. K., Galvin, J. E., Whyatt, G. A., and Sun, X. (2017). Breakup of a liquid rivulet falling over an inclined plate: Identification of a critical weber number. *Physics of Fluids*, 29(5):052101.

Smagorinsky, J. (1963). General circulation experiments with the primitive equations. *Monthly Weather Review*, 91(3):99 – 164.

Snoeijer, J., Le Grand-Piteira, N., Limat, L., Stone, H., and Eggers, J. (2007). Cornered drops and rivulets. *Physics of Fluids*, 19(4):042104.

Solomenko, Z., Spelt, P. D., and Alix, P. (2017). A Level-Set method for large-scale simulations of three-dimensional flows with moving contact lines. *Journal of Computational Physics*, 348:151 – 170.

Spalding, D. B. (1961). A single formula for the “law of the wall”. *Journal of Applied Mechanics*, 28(3):455 – 458.

Spelt, P. D. (2005). A Level-Set approach for simulations of flows with multiple moving contact lines with hysteresis. *Journal of Computational Physics*, 207(2):389 – 404.

Speziale, C. (1997). *Computing non-equilibrium turbulent flows with time-dependent RANS and VLES*, pages 123 – 129. Springer Berlin Heidelberg, Berlin, Heidelberg.

Speziale, C. (1998). Turbulence modeling for time-dependent RANS and VLES: A review. *American Institute of Aeronautics and Astronautics Journal*, 36(2):173 – 184.

Sprittles, J. and Shikhmurzaev, Y. (2013). Finite element simulation of dynamic wetting flows as an interface formation process. *Journal of Computational Physics*, 233:34 – 65.

Spruß, I. (2016). *Ein Beitrag zur Untersuchung der Kraftfahrzeugverschmutzung in Experiment und Simulation*. Springer.

Spurk, J. (2013). *Strömungslehre: Einführung in die Theorie der Strömungen*. Springer-Verlag.

Strasser, W., Battaglia, F., and Walters, D. (2015). Application of hybrid RANS-LES CFD methodology to primary atomization in a coaxial injector. In *Proceedings of the International Mechanical Engineering Congress and Exposition, Paper# IMECE2015-53028*.

Sui, Y., Ding, H., and Spelt, P. D. (2014). Numerical simulations of flows with moving contact lines. *Annual Review of Fluid Mechanics*, 46(1):97 – 119.

Sussman, M. (2003). A second order coupled Level Set and Volume-Of-Fluid method for computing growth and collapse of vapor bubbles. *Journal of Computational Physics*, 187(1):110 – 136.

Sussman, M. and Puckett, E. G. (2000). A coupled Level Set and Volume-Of-Fluid method for computing 3D and axisymmetric incompressible two-phase flows. *Journal of Computational Physics*, 162(2):301 – 337.

Sussman, M., Smereka, P., and Osher, S. (1994). A Level Set approach for computing solutions to incompressible two-phase flow. *Journal of Computational Physics*, 114(1):146 – 159.

Tabor, G. and Baba-Ahmadi, M. (2010). Inlet conditions for Large Eddy Simulation: A review. *Computers & Fluids*, 39(4):553 – 567.

Tanner, L. H. (1979). The spreading of silicone oil drops on horizontal surfaces. *Journal of Physics D: Applied Physics*, 12(9):1473.

Thammanna Gurumurthy, R., Rettenmaier, D., Roisman, I. V., Tropea, C., and Garoff, S. (2018a). Spontaneous imbibition and forced wetting in closed square capillaries and open rectangular grooves. In *AIChE Annual Meeting in Pittsburgh, PA*.

Thammanna Gurumurthy, R., Rettenmaier, D., Roisman, I. V., Tropea, C., and Garoff, S. (2018b). Spontaneous rise of rivulets in square capillaries. In *14th Zsigmondy Colloquium of the German Colloid Society*.

Thammanna Gurumurthy, R., Rettenmaier, D., Roisman, I. V., Tropea, C., and Garoff, S. (2018c). Spontaneous rise of rivulets in square capillaries. In *93th American Chemical Society Colloid and Surface Science Symposium in Pennsylvania*.

Thammanna Gurumurthy, V., Rettenmaier, D., Roisman, I. V., Tropea, C., and Garoff, S. (2018). Computations of spontaneous rise of a rivulet in a corner of a vertical square capillary. *Colloids and Surfaces A: Physicochemical and Engineering Aspects*, 544:118 – 126.

The OpenFOAM Foundation (2016). OpenFOAM v5 User Guide. https://cfd.direct/openfoam/user-guide.

Thiele, U., Neuffer, K., Bestehorn, M., Pomeau, Y., and Velarde, M. G. (2002). Sliding drops on an inclined plane. *Colloids and Surfaces A: Physicochemical and Engineering Aspects*, 206(1-3):87 – 104.

Thoroddsen, S., Etoh, T., and Takehara, K. (2008). High-speed imaging of drops and bubbles. *Annual Review of Fluid Mechanics*, 40(1):257 – 285.

Tivert, T., Borg, A., Marimon, J., and Davidson, L. (2007). Wind-driven rivulet over an edge with break-up. In *In: 6th International Conference on Multiphase Flow, ICMF, Leipzig, Germany*.

Toutant, A., Chandesris, M., Jamet, D., and Lebaigue, O. (2009). Jump conditions for filtered quantities at an under-resolved discontinuous interface. Part 1: Theoretical development. *International Journal of Multiphase Flow*, 35(12):1100 – 1118.

Toutant, A., Labourasse, E., Lebaigue, O., and Simonin, O. (2008). DNS of the interaction between a deformable buoyant bubble and a spatially decaying turbulence: A priori tests for LES two-phase flow modelling. *Computers & Fluids*, 37(7):877 – 886. Special Issue of the "Turbulence and Interaction–TI2006" Conference.

Tryggvason, G., Bunner, B., Esmaeeli, A., Juric, D., Al-Rawahi, N., Tauber, W., Han, J., Nas, S., and Jan, Y.-J. (2001). A front-tracking method for the computations of multiphase flow. *Journal of Computational Physics*, 169:708 – 759.

Tryggvason, G., Scardovelli, R., and Zaleski, S. (2011). *Direct Numerical Simulations of gas–liquid multiphase flows*. Cambridge University Press.

Tukovic, Z. and Jasak, H. (2012). A moving mesh Finite Volume interface tracking method for surface tension dominated interfacial fluid flow. *Computers & Fluids*, 55(0):70 – 84.

Ubbink, O. (1997). *Numerical Prediction of Two Fluid Systems with Sharp Interfaces*. PhD thesis, Department of Mechanical Engineering, Imperial College of Science, Technology & Medicine.

Vandriessche, R. and Roose, D., editors (1995). *Load balancing computational fluid dynamics calculations on unstructured grids*. AGARD, Special Course on Parallel Computing in CFD (see N96-16247 04-60).

Voinov, O. V. (1976). Hydrodynamics of wetting. *Fluid Dynamics*, 11(5):714 – 721.

Voskuilen, T. (2014). Mesh balancing. `https://github.com/tgvoskuilen/meshBalancing`. [last accessed July 2018].

Šikalo, v., Wilhelm, H.-D., Roisman, I. V., Jakirlić, S., and Tropea, C. (2005). Dynamic contact angle of spreading droplets: Experiments and simulations. *Physics of Fluids*, 17(6).

Vukčević, V., Jasak, H., and Gatin, I. (2017). Implementation of the Ghost Fluid Method for free surface flows in polyhedral Finite Volume framework. *Computers & Fluids*, 153:1 – 19.

Vuong, A.-V., Boschert, S., and Simeon, B. (2008). Adaptive Finite Volume Methods for interfacial flows. Technical report. Available at http://www-m2.ma.tum.de/homepages/simeon/publica.html [last accessed July 2018].

Vyzikas, T., Deshoulières, S., Giroux, O., Barton, M., and Greaves, D. (2017). Numerical study of fixed oscillating water column with RANS-type two-phase CFD model. *Renewable Energy*, 102:294 – 305.

Wang, L., Huang, H.-b., and Lu, X.-Y. (2013). Scheme for contact angle and its hysteresis in a multiphase lattice Boltzmann method. *Physical Review E*, 87:013301.

Wayner, P. C. (1993). Spreading of a liquid film with a finite contact angle by the evaporation/condensation process. *Langmuir*, 9(1):294 – 299.

Weidner, D. E. and Schwartz, L. W. (1994). Contact-line motion of shear-thinning liquids. *Physics of Fluids*, 6(11):3535 – 3538.

Weller, H. G. (2005). A code independent notation for Finite Volume algorithms. Technical report, OpenCFD Limited.

Weller, H. G. (2006). A new approach to VOF-based interface capturing methods for incompressible and compressible flow. Technical report, OpenCFD Limited.

Weller, H. G., Tabor, G., Jasak, H., and Fureby, C. (1998). A tensorial approach to computational continuum mechanics using object-oriented techniques. *Computers in Physics*, 12(6):620 – 631.

Wenzel, R. N. (1936). Resistance of solid surfaces to wetting by water. *Ind. Eng. Chem.*, 28:988 – 994.

White, E. B. and Schmucker, J. A. (2008). A runback criterion for water drops in a turbulent accelerated boundary layer. *Journal of Fluids Engineering*, 130(6):0098 – 2202.

Williams, M., Kothe, D., and Puckett, E. (1998). Accuracy and convergence of continuum surface tension models. *Fluid Dynamics at Interfaces, Cambridge University Press, Cambridge*, pages 294 – 305.

Xu, H. and Guetari, C. (2004). The use of CFD to simulate capillary rise and comparison to experimental data. In *2004 International ANSYS Conference, Pittsburgh*.

Xu, X., Di, Y., and Doi, M. (2016). Variational method for liquids moving on a substrate. *Physics of Fluids*, 28(8):087101.

Yamamoto, T., Okano, Y., and Dost, S. (2016). Validation of the S-CLSVOF method with the density-scaled balanced continuum surface force model in multiphase systems coupled with thermocapillary flows: S-CLSVOF method in multiphase systems with thermocapillary flows. *International Journal for Numerical Methods in Fluids*, 83.

Yejun, G., Tilli, O. K. A., Larmi, M., and Tanner, F. (2010). A computational investigation of hydrotreated vegetable oil sprays using RANS and a modified version of the RNG k-epsilon model in OpenFOAM. *SAE International*, 2010-01-0739.

Yokoi, K. (2013). A density-scaled continuum surface force model within a balanced force formulation. *Journal of Computational Physics*, 278(C):221 – 228.

Young, T. (1805). Contact angle. *Philosophical Transactions of the Royal Society*, 95:65.

Zhi-Yong, L., Xiao-Feng, P., and Xiao-Dong, W. (2006). Oscillation characteristics of droplets on solid surfaces with air flow. *Heat Transfer Asian Research*, 35(1):13 – 19.